Sebastian Halsig

Atmospheric refraction and turbulence in VLBI data analysis

München 2018

Atmospheric refraction and turbulence in VLBI data analysis

Inaugural-Dissertation zur

Erlangung des Grades

Doktor-Ingenieur (Dr.-Ing.)

der Hohen Landwirtschaftlichen Fakultät

der Rheinischen Friedrich-Wilhelms Universität Bonn

vorgelegt im Dezember 2017 von

Sebastian Halsig, M.Sc.

aus Bonn

München 2018

Adresse der DGK:

Ausschuss Geodäsie der Bayerischen Akademie der Wissenschaften (DGK)

Alfons-Goppel-Straße 11 ● D – 80 539 München

Telefon +49 – 331 – 288 1685 ● Telefax +49 – 331 – 288 1759

E-Mail post@dgk.badw.de ● http://www.dgk.badw.de

Atmospheric refraction and turbulence
in VLBI data analysis

Summary

The progress in further improving the quality of results derived by space-geodetic techniques observing in the radio frequency domain, such as Very Long Baseline Interferometry (VLBI) or Global Navigation Satellite Systems (GNSS), is limited by rapid changes in the neutral part of the atmosphere. In particular, insufficient knowledge of the temporal and spatial refractivity variations restrict the attainable accuracy of the derived VLBI and GNSS target parameters. In the current model describing the additional propagation delay due to the neutral part of the atmosphere, only annual to hourly long periodic variations are taken into account. In contrast, small-scale fluctuations mainly originating from turbulent motions are generally neglected, although they form a serious error source for electromagnetic wave propagation. Dynamic processes in the neutral atmosphere additionally induce physical correlations in space and time, which are also largely ignored so far.

Particularly with regard to future requirements, as, for instance, defined within the framework of the Global Geodetic Observing System established by the International Association of Geodesy, the current tropospheric model is not sufficient and needs to be improved. High rate GNSS data of 1 Hz sampling and below, and the VLBI Global Observing System with faster telescopes result in a better sampling of the atmosphere. However, new challenges emerge with respect to improved and proper analysis strategies, in particular to model the stochastic properties of atmospheric refraction, which represents a crucial issue in research and the main objective of this thesis.

Quantifying and assessing the small-scale behavior of atmospheric refraction is extremely challenging, since small-scale characteristics of atmospheric refraction cannot be analyzed without sufficient knowledge of the stability of the VLBI observing system. An optimal experimental setup for both, investigations in atmospheric refraction and system stability issues, emerges from the commissioning phase of the twin radio telescope at the Wettzell Geodetic Observatory in Germany. Specially designed so-called WHISP sessions are scheduled, observed and analyzed within this thesis allowing to quantify the individual components of the observing system, in part for the first time. On this basis, refractivity fluctuations are quantified which are found to be in the range of 1-3 millimeters. A number of noteworthy conclusions has been drawn which would not have been possible without the novel observing approach.

Special emphasis is also given to the development of an atmospheric turbulence model, which stochastically describes small-scale refractivity fluctuations due to turbulent motions in the neutral atmosphere. The results have produced an important contribution to the modeling of refraction effects in the neutral atmosphere now considering temporal and spatial correlations between the observations in a physical and meteorological way. By analyzing 2700 VLBI sessions including traditional and local observing networks, it is demonstrated that the incorporation of the newly devised model into the VLBI data analysis leads to an improvement of the solutions compared to the standard strategies of the International VLBI Service for Geodesy and Astrometry, or other strategies refining the stochastic model of VLBI observations. Compared to other approaches addressing the issue of atmospheric turbulence, the model developed within this thesis has the advantage to be operationally efficient for routine mass analysis of VLBI observing sessions.

Since the current atmospheric model reveals severe deficiencies with respect to the estimation of atmospheric parameters, new modeling and adjustment strategies are introduced to better describe the behavior of the neutral atmosphere. It is demonstrated that, in particular, the least squares collocation method ensures an improved modeling of the stochastic properties of the neutral atmosphere, which allows a zenith wet delay estimation in more meaningful and appropriate sense.

The main achievements of this thesis are the development of an atmospheric turbulence model to improve the stochastic model of VLBI observations and the quantification of local atmospheric refraction variations in space and time. Both allows for new interpretations and model improvements in a stochastic and deterministic sense.

Atmosphärische Refraktion und Turbulenz in der VLBI-Auswertung

Zusammenfassung

Die stetige Weiterentwicklung und Qualitätsverbesserung von Ergebnissen aus weltraum-geodätischen Verfahren im Radiofrequenzbereich, wie beispielsweise VLBI (Very Long Baseline Interferometry) oder GNSS (Global Navigation Satellite Systems), ist durch schnelle Veränderungen in der neutralen Atmosphäre limitiert. Die zu erreichende Genauigkeit von Stationskoordinaten, Erdrotationsparametern oder anderen Zielparametern wird durch die unzureichende Kenntnis räumlicher oder zeitlicher Variationen in der Refraktivität maßgeblich begrenzt. Das aktuelle Atmosphärenmodell in der Auswertung weltraum-geodätischer Verfahren sieht ausschließlich die Berücksichtigung langperiodischer Signale vor. Kleinskalige, überwiegend durch turbulentes Verhalten in der Atmosphäre hervorgerufene Fluktuationen werden hingegen weitestgehend vernachlässigt, obwohl sie einen nicht unerheblichen Einfluss auf die Ausbreitung elektromagnetischer Wellen haben. Des Weiteren induzieren dynamische Prozesse in der neutralen Atmosphäre sowohl räumliche als auch zeitliche Korrelation zwischen den Beobachtungen, die ebenfalls weitestgehend ignoriert werden.

Insbesondere im Hinblick auf die von der IAG (International Association of Geodesy) formulierten GGOS (Global Geodetic Observing System) Ziele genügt das aktuelle Atmosphärenmodell nicht den zukünftigen Anforderungen. Zwar führen hoch aufgelöste GNSS-Daten mit Abtastfrequenzen von bis zu 1 Hz und eine neue Generation von schnelleren und präziseren sogenannten VGOS (VLBI Global Observing System) Radioteleskopen zu einer besseren Abtastung der Atmosphäre, jedoch entstehen auch neue Herausforderungen hinsichtlich einer verbesserten und geeigneteren Modellierung der stochastischen Eigenschaften atmosphärischer Refraktion, welche allgemein eine zentrale Fragestellung darstellt und folglich die wesentliche Aufgabe dieser Arbeit repräsentiert.

Die Quantifizierung und Bewertung des Verhaltens der atmosphärischen Refraktion stellt eine große Herausforderung dar. Da insbesondere das kleinskalige Verhalten der atmosphärischen Refraktion eng mit den Stabilitätseigenschaften des VLBI-Beobachtungssystems zusammenhängt, müssen diese ausreichend gut bekannt sein. Durch die Inbetriebnahme des weltweit ersten Twin-Teleskops am Geodätischen Observatorium Wettzell in Deutschland entstanden optimale Voraussetzungen für die Detektion der Stabilitätseigenschaften des Beobachtungssystems sowie der atmosphärischen Refraktion. In dieser Arbeit wurden spezielle WHISP-Experimente entworfen, die es erlauben, einzelne Komponenten des Beobachtungssystems zum Teil erstmalig zu quantifizieren. Auf dieser Grundlage wird auch der Einfluss von Variationen in der Refraktivität bestimmt, dem eine Größenordnung von 1-3 Millimetern zugerechnet wird.

Ein besonderer Fokus liegt außerdem auf der Entwicklung eines Turbulenzmodells, welches zum einen zeitliche und räumliche Korrelationen zwischen den Beobachtungen berücksichtigt und zum anderen kleinskalige Fluktuationen in der Refraktivität stochastisch sowie physikalisch und meteorologisch sinnvoll beschreibt. Auf Basis der Auswertung von 2700 VLBI-Beobachtungssessionen unterschiedlicher Netzwerkgröße wird gezeigt, dass die Einführung des neuen Turbulenzmodells in die VLBI-Auswertung für die operationelle Auswertung geeignet ist und zu Verbesserungen gegenüber der Standardlösung des IVS (International VLBI Service for Geodesy and Astrometry) sowie alternativer Ansätze zur Verfeinerung des stochastischen Modells führt.

Da das routinemäßig verwendete Atmosphärenmodell einige Defizite hinsichtlich der Schätzung atmosphärischer Parameter aufweist, werden in dieser Arbeit einige Modellierungs- und Ausgleichungsstrategien eingeführt, um die neutrale Atmosphäre besser zu charakterisieren. Es wird gezeigt, dass insbesondere die Kleinste-Quadrate-Kollokation eine verbesserte Modellierung der stochastischen Eigenschaften der neutralen Atmosphäre erlaubt und somit zu einer aussagekräftigeren und geeigneteren Schätzung der Atmosphärenparameter führt.

Die Haupterrungenschaften dieser Arbeit sind die Entwicklung eines Turbulenzmodells zur Verbesserung des stochastischen Modells sowie die verbesserte Quantifizierung lokaler Refraktionseigenschaften in Raum und Zeit. Beides resultiert in neuen Interpretationsmöglichkeiten und Modellverbesserungen in deterministischer und stochastischer Hinsicht.

Contents

1. Introduction

1.1   General Aspects

The Earth is a continually changing planet. The variability of the entire system Earth can be divided into three principle components: the figure of the Earth, the gravity field of the Earth, and Earth rotation (PLAG et al. 2009). In order to investigate these elements and to increase the knowledge on the complexity of the Earth's system, very precise geodetic measurements are required.

Space-geodetic techniques, such as Very Long Baseline Interferometry (VLBI), Global Navigation Satellite Systems (GNSS), Satellite and Lunar Laser Ranging (SLR/LLR) or the French system Doppler Orbitography by Radiopositioning Integrated on Satellite (DORIS), are generally able to measure the figure of the Earth in terms of terrestrial reference frames (TRF) or the Earth's rotation. In the following, the term space geodesy refers to observations of signals transmitted or received by natural or artificial sources in space.

VLBI is a technique based on radio interferometry. At least a pair of two radio telescopes simultaneously observes a radio signal emitted by extragalactic sources, preferably compact radio galaxies or quasi-stellar radio sources. The fundamental observable, the group delay, is the difference in arrival time between both telescopes obtained by cross-correlation (SCHUH and BÖHM 2013). VLBI is the only technique to realize the celestial reference frame (CRF) and to determine all Earth orientation parameters (EOP) without hypotheses.

GNSS encompasses the United States Global Positioning System (GPS), the Russian Globalnaja Nawigazionnaja Sputnikowaja Sistema (GLONASS), the European GALILEO, and the Chinese system BEIDOU. Microwave signals transmitted by satellites at orbital heights of about 20.000 km are either received by GNSS antennas on the Earth or on board of other artificial objects such as satellites in low Earth orbits (LEO).

The application fields of space-geodetic techniques are versatile. On the one hand, the demand for space-geodetic products can be found in science and research, for instance, in Earth sciences such as hydrology, meteorology, climatology or geophysics. On the other hand, space-geodetic products are also highly relevant for societal issues, particularly in positioning or navigation applications, but also for early warning systems for natural hazards or weather forecasts.

Due to the high requirements on the precision to measure the variability of the planet Earth, many components have to be taken into account, including effects occurring on the way through the solar system and the Earth's atmosphere as well as geophysical phenomena or instrumental effects. In particular, the Earth's atmosphere plays a crucial role due to its highly dynamic nature, and represents one of the major contributions to the error budget of space-geodetic observations in state-of-the-art data analysis. In space-geodesy, the Earth's atmosphere is generally divided into two main compartments. First, the ionosphere includes the atmospheric layer with contributions from charged electrons and ions, extending from about 60 to more than 1.000 km altitude with the largest electron density between 300 and 400 km (BÖHM et al. 2013). The ionosphere is a dispersive (frequency-depending) medium for radio frequency techniques. Thus, the ionospheric refraction due to the ionization by solar radiation can be accounted for, to first order, by observing at two different frequencies. Second, the neutral part of the atmosphere up to 100 km altitude

considers contributions from neutral (non-charged) molecules (Böhm et al. 2013). The troposphere defines the lowest layer of the neutral atmosphere with a vertical thickness of 10-12 km. Due to the highly variable water vapor content, the troposphere is responsible for the major contribution to the variability of the propagation delay of microwave signals in the neutral atmosphere, although about 25 % of the delay occurs above the troposphere (Davis et al. 1985). In contrast to the ionosphere, the neutral atmosphere is a non-dispersive medium and the radio signal is subject to an additional delay as well as to bending and attenuation effects relative to a theoretical path in vacuum, which have to be modeled in data analysis.

In the routine VLBI data analysis of the International VLBI Service for Geodesy and Astrometry (IVS, Nothnagel et al. 2016), the tropospheric propagation delay is generally divided into a hydrostatic and a wet component, and both are modeled as a delay correction in zenith direction and mapped to an arbitrary elevation angle by so-called mapping functions (Davis et al. 1985). While the mapping functions and the hydrostatic delays are considered to be modeled accurately enough, there are no sufficiently accurate models or direct measurements available for the wet component, which is, thus, the most uncertain factor. Consequently, an additional atmospheric zenith delay correction, also referred to as zenith wet delay (ZWD), is estimated within the geodetic data correction and parameter estimation process.

1.2 Motivation

The motivation of this thesis is that the state-of-the-art tropospheric model reveals some serious deficiencies. Without going into details here already, the areas of concern are briefly summarized.

The ZWD parameters are generally resolved in time by continuous piece-wise linear functions, i.e., linear splines (e.g., De Boor 1978), of suitable lengths between 30 minutes and 3 hours, and estimated in a classical least squares solution (e.g., Koch 1999). The pseudo-stochastic character of the piece-wise linear representation is, however, not optimal to model the highly dynamic nature of the atmosphere. Moreover, additional soft constraints in the form of pseudo observations are often needed to stabilize the solution due to missing observations in some piece-wise linear segments. In order to consider azimuthal asymmetries of the neutral atmosphere around the station, an additional model component of so-called atmospheric gradients is usually introduced, which is subject to similar conditions. Since the estimation of the model coefficients heavily depends on observations at low elevation angles, soft constraints are again necessary to stabilize the solution. Another issue concerns the mapping functions relating the zenith delays to an arbitrary elevation angle. The most accurate mapping functions are based on numerical weather models, which are, however, not optimal due to the rather coarse temporal resolution of only six hours (Böhm et al. 2006b). In order to completely avoid the mapping function as additional uncertainty source, it would be desirable to obtain atmospheric delays directly in slant direction (i.e., the direction from the radio telescope to the radio source), which, however, is only possible, if the number of observations is large enough. Finally, several parameter groups, such as atmospheric and clock parameters as well as the vertical component of the station coordinates, are assumed to be correlated and mutually influence each other, in particular if the stochastic model of the observations is not complete. Consequently, the ZWD estimates do not reflect meteorological and physical conditions in a plausible way in many cases.

Another issue reveals severe deficits since only long-periodic effects in the range of years to hours are considered routinely in the data analysis of space-geodetic observations. In contrast, small-scale refractivity fluctuations of minutes to sub-seconds due to turbulent swirls are largely ignored.

The refractivity variations induce phase fluctuations of wave fronts passing through the atmosphere, which lead to a serious error source for electromagnetic wave propagation (THOMPSON et al. 2001). Additionally, turbulence-induced processes in the troposphere induce spatial and temporal correlations between the observations, which are also not accounted for in the routine data analysis of the IVS and the IGS (International GNSS Service, DOW et al. 2009).

Actually, to go even further, atmospheric refraction is the limiting factor of any further improvements of the accuracy of Earth orientation parameters or telescope positions (PETRACHENKO et al. 2008; PANY et al. 2011). Consequently, the current tropospheric model is not sufficient to fulfill future requirements, for instance, 1 mm accuracy of station positions on a global scale (e.g., PETRACHENKO et al. 2008) as defined within the framework of the Global Geodetic Observing System (GGOS, GROSS et al. 2009) established by the International Association of Geodesy (IAG, DREWES et al. 2016). To meet the high demands of the GGOS requirements, the next generation VLBI system, referred to as VLBI Global Observing System (VGOS, NIELL et al. 2013), has been designed by the IVS. In this context, faster and more precise VLBI telescopes lead to a clearly increased observation density and a better sampling of the atmosphere. However, this also requires an enhancement of the current data analysis and modeling strategy. In particular, an improved and proper modeling of the stochastic properties of atmospheric refraction remains a crucial issue and is the main objective of this thesis.

In addition, also the commissioning phase of so-called twin radio telescopes, two more or less identically constructed adjacent antennas, offers new opportunities. The potential and importance of the twin telescopes is substantial to analyze atmospheric refraction effects. However, the behavior of atmospheric refraction cannot be analyzed before the stability of the VLBI observing system is understood sufficiently, since the estimation of atmospheric parameters and the interpretation of the post-fit residuals in VLBI data analysis are closely linked to these stability issues. Consequently, for an improved characterization of atmospheric refraction, it is indispensable to separate the influence of different system stability effects and to assess their order of magnitude. Particular attention should be paid to the hydrogen maser clocks feeding the local oscillators and other necessary electronics, the uncertainties emerging from the correlation process, and the effect of phase calibration which is necessary to compensate for dispersive instrumental phase shifts. An optimal experimental setup for both, investigations in atmospheric refraction and system stability issues, can however only be provided by close-range geodetic VLBI observations between two adjacent radio telescopes, which have not been realized so far.

1.3 Scientific Context

The quality of space-geodetic observations for the determination of precise telescope and radio source positions and monitoring Earth rotation is known to be hampered by insufficient knowledge of the temporal and spatial variability of atmospheric refraction already for some time. However, variability issues have been widely ignored. At the same time, the demand for high rate space-geodetic products is steadily increasing in interdisciplinary fields, e.g., climatology or meteorology, and atmospheric parameters derived by space-geodetic techniques in the radio frequency domain become more and more important to understand dynamic processes in the Earth's atmosphere. For instance, atmospheric parameters derived from near real time Global Positioning System (GPS) observations are used for data assimilation procedures in numerical weather models (e.g., CREWELL et al. 2008; DENG et al. 2011; DOUSA and BENNITT 2013). Currently, VLBI observations are not

yet used for such purposes, because the observations are not continuous and the global distribution and spatial coverage lags behind GPS observations. However, the VLBI Global Observing System leads to an increasing number of observations per unit of time as well as to a better sky coverage. With a better sampling of the atmosphere a more valuable contribution to atmospheric sciences will be possible. One conceivable option could be a multi-technique combination of atmospheric parameters, or the VLBI observations could be particularly used for calibration purposes. Further, an important advantage of VLBI over GPS is the very long time series of atmospheric parameters of almost 40 years, which is particularly relevant for climate studies (e.g., HEINKELMANN et al. 2007).

Currently, the total refraction effect is modeled by a tropospheric propagation delay which is divided into a hydrostatic and a wet component (DAVIS et al. 1985). Both parts are represented as the product of a zenith delay correction and a corresponding mapping function to relate an observation from zenith to an arbitrary elevation angle. The order of magnitude of the hydrostatic component in zenith direction is about 2.3 m extra path length, while the additional zenith wet delay ranges from a few millimeters in dry regions up to 50 cm in the wet tropics. The hydrostatic component depends only on the air pressure with only little variation proportional to the pressure variations and can be modeled with sufficient precision (see, e.g., SAASTAMOINEN 1972; SAASTAMOINEN 1973; DAVIS et al. 1985). The pressure can either be quantified using in-situ measurements at the antenna site, numerical weather models or empirical so-called blind models (e.g., the Global Temperature and Pressure model, GPT, BÖHM et al. 2007B; GPT2, LAGLER et al. 2013; GPT3, LANDSKRON and BÖHM 2017). The mapping functions are also considered to be modeled accurately enough and several models have been proposed by different authors (e.g., CHAO 1971; DAVIS et al. 1985; HERRING 1992; NIELL 1996; BÖHM et al. 2006A; BÖHM et al. 2006B). In contrast, the variations of the wet component are unpredictable due to the high temporal and spatial variability of water vapor in the atmosphere and cannot be modeled sufficiently (ELGERED 1993). Generally, the long-periodic variations of the water vapor content can either be directly measured by water vapor radiometers, which however, do not meet the accuracy requirements of today, or estimated as zenith wet delay. In the data analysis of the IVS, the long-periodic components of the zenith wet delays are generally treated as pseudo-stochastic continuous piece-wise linear functions in a least squares adjustment (e.g., KOCH 1999), or alternatively, as a stochastic process in a filter estimation (e.g., HERRING et al. 1990; NILSSON et al. 2015) or by a least squares collocation approach (e.g., TITOV 2000). Additionally, atmospheric gradients due to horizontal refractivity variations are estimated, which are necessary to consider the azimuthal asymmetry of the neutral atmosphere around the station (DAVIS et al. 1993; MACMILLAN 1995; CHEN and HERRING 1997).

Micro-scale meteorological phenomena are still completely neglected, although they form a serious error source for electromagnetic wave propagation. Further, dynamic processes in the troposphere, particularly in the atmospheric boundary layer (the lowest part of the atmosphere; 0-2 km altitude) and the free atmosphere (at heights greater than 1 km), induce spatial and temporal correlations between the observations, which are also largely ignored so far. Since the stochastic model in the routine VLBI data analysis of the IVS and IGS does not include any correlations, the derived target parameters are not as accurate as indicated by the corresponding variance-covariance matrix, and said to be too optimistic (SCHÖN and KERMARREC 2015). This was confirmed in HALSIG et al. (2016A) by comparing the standard deviations to the average noise level of dedicated IVS sessions in terms of weighted root mean squared error of single-session position estimates, computed by BÖCKMANN et al. (2010) after removing offset, rate and annual signal.

In order to fulfill the future GGOS requirements, and with regard to the high potential due to new VGOS radio telescopes and high rate GNSS data of 1 Hz sampling and below, the situation has to

be improved by proper modeling strategies. Consequently, both small-scale refractivity fluctuations due to turbulent motions in the neutral part of the atmosphere and temporal and spatial correlations between the observations have to be taken into account sufficiently.

To overcome the model deficiencies in the stochastic description, the standard deviations derived from the VLBI cross-correlation process are mostly inflated artificially in the traditional VLBI data analysis, for instance, by adding either a constant noise term to the variances of the observations or performing a station- or baseline-dependent iterative re-weighting of the observations (e.g, GIPSON et al. 2008).

Over the last decades, more sophisticated concepts have been proposed to improve the stochastic model of space-geodetic observations. SCHÖN and KUTTERER (2005) investigated the modeling of uncertainties due to remaining systematic errors of GPS data processing. Refining the standard stochastic model of VLBI observations by estimating variance and covariance components was investigated by LUCAS and DILLINGER (1998), TESMER (2004) and ZUBKO et al. (2012). Other authors suggested empirical models, which are either based on elevation-dependent weighting methods (EULER and GOAD 1991; GIPSON 2006; GIPSON 2007; GIPSON et al. 2008) or signal-to-noise models (LUO et al. 2011), generally resulting in an easy-to-implement diagonal variance-covariance structure. For instance, GIPSON et al. (2008) include station-depended delay noise to the stochastic model to obtain more realistic standard deviations. Two different types of delay noise are distinguished: a constant additional component to deal with the clock behavior and an elevation-dependent noise term to consider atmospheric characteristics.

While the models presented above are generally of theoretical or mathematical nature not considering actual physical conditions, EL-RABBANY (1994) suggested an empirical approach by analyzing auto-correlation functions of phase residuals and proposed a simple exponential function with empirically determined correlation time. This study was restricted to short GPS baselines (10-40 km) but adapted for longer baselines up to 500 km by HOWIND et al. (1999).

Empirically derived models can however only describe the stochastic character of the atmosphere, particularly the dominant contribution of tropospheric refraction, to a limited extent. In order to go even further and to allow for a physically more reliable modeling of the stochastic properties correlations due to high-frequency refractivity fluctuations have to be introduced, which can be best described stochastically following the widely accepted Kolmogorov turbulence theory (KOLMOGOROV 1941a; KOLMOGOROV 1941b). Since fluctuations in the signal phase are assessed to be non-stationary (see Sec. 4.2 for more details), the stochastic behavior of refractivity variations is generally described in terms of so-called structure functions or power spectral densities. KOLMOGOROV (1941a) showed, that these structure functions, in general, follow specific power-law processes. The prevailing turbulent regime is then characterized by the shape of the structure function, which leads to typical slopes in a log-log-plot of $5/3$, $2/3$ and 0, referring to 3D, 2D, and no turbulence, respectively (e.g., TREUHAFT and LANYI 1987; SCHÖN and KERMARREC 2015). In the past, some authors analyzed the power law exponents and compared them with their theoretical values (e.g., ARMSTRONG and SRAMEK 1982; STOTSKII et al. 1998; SCHÖN and BRUNNER 2006; NILSSON et al. 2009; VENNEBUSCH et al. 2011).

Over the last decades, a few turbulence models have been developed, which make either use of the structure function or a power spectrum representation (see Ch. 4 for more details). TREUHAFT and LANYI (1987) have pioneered turbulence modeling for space-geodetic techniques. They determined a turbulence-based variance-covariance matrix for tropospheric delays of VLBI observations based

on refractivity structure functions. The model follows the Kolmogorov turbulence theory and describes the stochastic variations of the refractivity around its mean value. Many other authors used the TREUHAFT and LANYI (1987) model for further investigations. For instance, DAVIS (1992) studied the impact of turbulence on atmospheric gradients, and ROMERO-WOLF et al. (2012) presented a simplified modification of this model applied to observations of the VLBA (Very Long Baseline Array) network. PANY et al. (2011) also used the turbulence model for extended simulation studies to assess the impact of the most important stochastic error sources in VLBI, such as uncertainties of the clocks or refractivity variations in the atmosphere. The impact of this model on continuous VLBI campaigns (CONT) was investigated by NILSSON and HAAS (2010) and particular consideration was given to the parametrization of specific station-dependent turbulence parameters, e.g., the structure constant or the effective tropospheric height (see Sec. 4.2 for more details).

Turbulence investigations have also been carried out for GNSS observations. SCHÖN and BRUNNER (2008a;b) developed the so-called SIGMA-C model for GPS carrier phases, a variance-covariance model following the turbulence theory of Kolmogorov and based on the time-dependent distance separating the ray paths of two signals. In contrast to other applications, where the turbulent medium is generally assumed to be homogeneous and isotropic (WHEELON 2004, pp. 47ff), the model has been generalized to allow for inhomogeneity and anisotropy. One main challenge of introducing physical correlations is evident: due to the necessary volume of integrations, which can only be solved numerically, turbulence models are mathematically difficult to handle and require high computational effort. Using the so-called Matérn covariance family (MATÉRN 1960), KERMARREC and SCHÖN (2014) proposed an extension of the SIGMA-C model to overcome this issue.

1.4   Main Objectives and Challenges of this Thesis

Temporal and spatial correlations between the observations and small-scale refractivity fluctuations due to turbulent motions in the neutral atmosphere are widely ignored in the routine data analysis of the IVS and the IGS. In order to allow for a physically more reliable modeling of the stochastic properties of VLBI observations it is necessary to expand the tropospheric model to high-frequency refractivity variations and physically induced correlations between the observations. Both can be best described stochastically following the widely accepted Kolmogorov turbulence theory. In order to overcome these severe deficiencies and to develop an operationally efficient method for turbulent modeling in routine mass analysis of VLBI observing sessions, a VLBI-specific and modified version of the KERMARREC and SCHÖN (2014) model is developed in this thesis.

The main challenge is the development of a turbulence model, which can be applied in a meaningful and appropriate sense and to both, traditional long baselines on global networks as well as short baselines on a local or regional scale. The resulting variance-covariance matrix of observations must comply with the requirements of providing realistic standard deviations of the derived target parameters within the parameter model and estimation process. Consequently, the stochastic model becomes far more complicated compared to the standard case of the IVS. The derived variance-covariance matrix is always fully populated, since spatial and temporal correlations between the observations due to the highly variable behavior of turbulent motions in the atmosphere are taken into account. Despite the high requirements in the modeling domain it is of great importance to still provide an approach for operational and not just for experimental purposes. Thus, one of the key objectives of this thesis is to develop a suitable strategy to consider atmosphere-based correlations

between VLBI observations in an operational way. In this context, it must be guaranteed that the model is mathematically easy to handle and the use of a fully populated variance-covariance matrix is feasible without excessive computational effort. In this context, the determination of certain turbulence parameters, particularly the structure constant and the effective tropospheric height, which behave as scaling parameters, but also the wind velocity and the so-called stretching parameters describing the flattening of the turbulent eddies to consider anisotropy, can be very time consuming, especially, if the turbulence parameters are aimed to be simultaneously estimated within the parameter estimation process. Consequently, it is of utmost importance to validate the influence of the different turbulence parameters on different modeling approaches to describe atmospheric turbulence. Concluding, one major challenge of this thesis is the development of a turbulence model providing reliable results for all fields of applications distinguishing between traditional and global baselines on the one hand side and more local network geometries on the other hand, and at the same time, allowing the turbulence parameters to be determined based on experience-related values.

Another key challenge occurs due to the missing "ground truth" (e.g., empirical evidence provided by direct measurements) for the prevailing small-scale atmospheric conditions and turbulent behavior, and the corresponding validation of the devised turbulence model. Turbulent motions are highly variable, unpredictable and of stochastic nature, and, therefore, it is difficult to generate a "reference solution". Consequently, the turbulence model is applied to numerous VLBI experiments of different temporal and spatial dimensions. The turbulence-based solutions including the modified stochastic model are validated against other strategies refining the stochastic model and the standard case of the IVS. This is achieved by diverse validation criteria, such as baseline length repeatabilities, the weighted root mean square (WRMS) error of post-fit residuals for the whole experiment or individual baselines, statistical tests, and, of course, the standard deviations of the derived parameters.

Characterizing the behavior of the atmosphere is a crucial and extremely challenging task, not only due to the highly variable properties of the neutral atmosphere, but also since the estimation of atmospheric parameters and the interpretation of the post-fit residuals in VLBI data analysis are closely linked to the stability of the observing system. Geodetic VLBI observations of radio telescopes, which are located in an immediate neighborhood, provide an optimal experimental setup for investigations in atmospheric refraction and system stability issues, but have never been realized so far. Up to now, the impact of atmospheric refraction effects in geodetic and astrometric VLBI applications has always been characterized through baselines of at least a few hundreds of kilometers, while local refraction effects in space-geodetic techniques have generally not been investigated by VLBI observations but by small scale GNSS networks (e.g., BEVIS et al. 1992; ELÓSEGUI et al. 1999; SCHÖN and BRUNNER 2008a; SCHÖN and BRUNNER 2008b; NILSSON et al. 2009; VENNEBUSCH et al. 2011), which are affected by the same refraction phenomena.

In this work, it is demonstrated, that geodetic close-range VLBI observations provide an optimal experimental setup for both, investigations in atmospheric refraction and system stability issues. Although observations on short baselines up to several hundred meters have been carried out at several occasions beforehand, generally as part of standard network observations (HASE and PETROV 1999; HERRERA-PINZON et al. 2017), the numbers of observations on the short baseline were limited by the network observing schedules which always balance between radio telescopes of different slew speeds. However, the commissioning phase of the worldwide first twin radio telescope at the Geodetic Observatory Wettzell in the Bavarian Forest in Germany (SCHÜLER et al. 2015) allows investigations of atmospheric refraction and system stability in the context of geodetic

VLBI observations with radio telescopes on a local scale. The completion of the first of the two new telescopes at the Wettzell Geodetic Observatory already provides an ample opportunity to carry out VLBI test observations on a baseline with a length of only about 120 m. This new opportunity is exploited within this thesis work through dedicated observing sessions, which are referred to as WHISP (Wettzell HIgh SPeed) experiments. The influence and the order of magnitude of individual system stability effects is quantified. Special consideration is given to the hydrogen maser clocks feeding the local oscillators and other necessary electronics, the uncertainties emerged from the correlation process, and the effect of phase calibration which is necessary to compensate for dispersive instrumental phase shifts. In order to evaluate the stability of the observing system, the so-called Two Way Optical Time Transfer (TWOTT, KODET et al. 2016a) method is applied. New findings about the temporal and spatial behavior of refraction effects will emerge by a reliable interpretation of (differential) zenith wet delay estimates and post-fit residuals.

Although the long-periodic tropospheric effects in the range of years to hours are routinely taken into account by the current tropospheric model of VLBI observations, the implementation is not optimal and reveals severe deficiencies. In order to allow for an improved characterization of atmospheric refraction and for an optimal estimation of atmospheric parameters, the state-of-the-art approach determining tropospheric delays has been modified in this thesis with alternative modeling and adjustment strategies. First, an inequality constrained least squares approach of the field of convex optimization has been used to overcome the deficiency, that occasionally zenith wet delay estimates become negative. The zenith wet delays can be directly related to the water vapor content in the atmosphere, and, from a meteorological point of view, negative values do not correspond to actual meteorological conditions and physical properties. According to the Clausius-Clapeyron equation, (see, e.g., KRAUS 2004), there is very little water vapor content at temperatures below $0°C$, and there is nothing like negative water vapor which could produce a negative delay contribution. Deficiencies in the hydrostatic delays are generally compensated by the zenith wet delay estimates. Since a constraining of specific atmospheric parameters would directly influence the result of the least squares adjustment, the hydrostatic a priori calibrations have to be modeled sufficiently. A strategy to homogenize the hydrostatic delays is presented in this thesis, and the influence of the inequality constraints on other parameters is investigated in detail.

Alternatively to the application of inequality constraints, the parametrization of the tropospheric propagation delays as piece-wise linear functions with a typical temporal resolution of 60 minutes is critically examined. The pseudo-stochastic character of the piece-wise linear representation is generally not optimal to model the highly dynamic nature of the atmosphere, and additional soft constraints are often needed to stabilize the solution due to missing observations in some piece-wise linear segments. The piece-wise linear model does not represent more than an auxiliary construction to approximate the stochastic behavior of the neutral atmosphere. In order to replace the piece-wise linear representation by a fully stochastic description of the atmospheric behavior, a least squares collocation method is applied in this thesis. The stochastic properties of the neutral atmosphere are reflected by suitable covariance functions. A covariance model which has been already applied to VLBI observations was transferred to a second order Gauss Markov process and appropriately modified. Several other covariance models are used for validation purposes. A case study is performed to compare the least squares collocation approach fed by different covariance functions to the classical least squares adjustment using piece-wise linear interval lengths of 30 and 60 minutes, respectively.

In summary, the main objective of this thesis is to characterize and model turbulence-based refractivity fluctuations and propose new modeling and adjustment strategies for space-geodetic observing techniques at radio frequency bands. In particular, this includes the following three key issues:

Objective 1: Modeling atmospheric turbulence.
  Special emphasis is given to the development of an operationally efficient atmospheric turbulence model describing small-scale refractivity fluctuations in a meaningful and appropriate sense. From the model, a fully populated variance-covariance matrix will be derived resulting in an enhanced stochastic model of VLBI observations now considering physical correlations in space and time due to turbulent motions in the neutral atmosphere.

Objective 2: Improved characterization of atmospheric refraction.
  Atmospheric refraction effects are closely linked to the stability issues of the VLBI observing system. The individual components of the observing system will be quantified and assessed in order to allow for an improved characterization of atmospheric refraction effects, particularly on a local scale using a short baseline at Wettzell, Germany.

Objective 3: Enhanced modeling and adjustment strategies to determine atmospheric parameters.
  The current tropospheric model reveals severe deficiencies with respect to the estimation of atmospheric parameters. Enhanced modeling and adjustment strategies will be introduced to better describe the behavior of the neutral atmosphere and to allow for the estimation of zenith wet delays in a more meaningful and appropriate sense.

The contents of this thesis have been partly published in the following articles, ordered in chronological sequence of progress.

Halsig, S., Artz, T., Leek, J., Nothnagel, A. (2014) *VLBI analyses using covariance information from turbulence models.* In: Behrend, D., K.D. Baver (eds) IVS 2014 General Meeting Proceedings "VGOS: The New VLBI Network", 2–7 March 2014, Shanghai, China, Science Press (Beijing), 2014, 272 - 276, 2014

Halsig, S., Artz, T., Iddink, A., Nothnagel, A. (2015a) *Augmenting the stochastic model in VLBI data analysis by correlations from atmospheric turbulence models.* In: Haas, R., Colomer, F. (eds) Proceedings of the 22th European VLBI Group for Geodesy and Astrometry Working Meeting, 18–21 May 2015, Ponta Delgada, pp 167 - 171.

Halsig, S., Roese-Koerner. L., Artz, T., Nothnagel, A., Schuh, W.-D. (2015b) *Improved Parameter Estimation of Zenith Wet Delays Using an Inequality Constrained Least Squares Method.* In: International Association of Geodesy Symposia, Vol. 143, 69 - 74, Springer International Publishing Berlin.

Halsig, S., Artz, T., Iddink, A., Nothnagel, A. (2016a) *Using an atmospheric turbulence model for the stochastic model of geodetic VLBI data analysis.* Earth, Planets and Space, 68:106, doi:10.1186/s40623-016-0482-5.

Halsig, S., Artz, T., Iddink, A., Nothnagel, A. (2016b) *An Inequality Constrained Least-Squares approach as an alternative estimation procedure for atmospheric parameters from VLBI observations.* In: Behrend, D., Baver, K.D., Armstrong, K. (eds) IVS 2016 General Meeting Proceedings "New Horizons with VGOS", Johannesburg, South Africa, March 13-19 2016, pp 326 - 330.

1.5 Outline

The general structure of this thesis is as follows. The first part of the thesis consists of three chapters and provides an introduction on the fundamentals necessary for a better understanding of the objectives and achievements of this thesis, which are presented in the second part of the thesis again including three chapters.

Chapter 2 ("Very Long Baseline Interferometry") provides a short overview on the VLBI principle with the focus on data analysis including the modeling component and the geodetic parameter estimation procedure. Both the state-of-the-art functional and stochastic model of the International VLBI Service for Geodesy and Astrometry are described.

Chapter 3 ("Modeling the Atmosphere") provides the theoretical fundamentals on the neutral part of the atmosphere. The propagation of electromagnetic waves is described and the propagation delay of space-geodetic observations due to the troposphere is defined. In Chapter 4 ("Atmospheric Turbulence") the widely accepted Kolmogorov turbulence theory (Sec. 4.1) is represented. Since turbulence can be best described stochastically, Sec. 4.2 provides an overview on statistical strategies to characterize high-frequency refractivity fluctuations in a random medium. Finally, three turbulence models relevant for this thesis are introduced in Sec. 4.3.

After providing fundamental insights relevant for this thesis, the main objectives and achievements of this thesis are presented in the following three chapters. The general focus always lies on atmospheric refraction and turbulence modeling.

In Chapter 5 ("Turbulence Modeling in VLBI"), the focus lies on improving the stochastic modeling of space-geodetic observations, since physical correlations induced by refractivity fluctuations have been largely ignored in the routine data analysis of the IVS and IGS. Therefore, an atmospheric turbulence model describing small-scale refractivity variations is devised and presented in Sec. 5.1. It is demonstrated that the turbulence model leads to improved results and is well suitable for routine mass VLBI data analysis. This related to objective 1 of this thesis.

In Chapter 6 ("Case Study: The WHISP Project"), special emphasis is given to sophisticated investigations and an enhanced characterization of refraction effects in the neutral atmosphere, which is part of objective 2 of this thesis. For this purpose, specially dedicated VLBI sessions providing close-range observations are used in the framework of the WHISP project to quantify both system stability issues and local refraction effects with VLBI.

In Chapter 7 ("Alternative Strategies for Modeling Atmospheric Refraction"), new modeling and adjustment methods have been applied to VLBI observations, which are related to objective 3 of this thesis. First, an inequality constrained least squares approach is used to overcome the deficiency, that sometimes zenith wet delay estimates become negative, which, of course, does not reflect meteorological conditions in a plausible way (Sec. 7.1). Second, the pseudo-stochastic behavior of the piece-wise linear representation for the atmospheric parameters, which only models the stochastic character of the atmosphere to a limited extent, is replaced by a least squares collocation method (Sec. 7.2).

Chapter 8 ("Conclusion and Outlook") concludes the thesis and gives an outlook on possible further research.

2. Very Long Baseline Interferometry

The basic ideas of Very Long Baseline Interferometry (VLBI) were first introduced in the mid-1960s (MATVEENKO et al. 1965, BROTEN et al. 1967, MORAN et al. 1967; for more details, see, e.g., SOVERS et al. 1998), although, the general principle is based on a classical interferometer in the visible spectrum as already invented by MICHELSON (1890). However, long baseline interferometry was only possible since atomic clocks were introduced in the 1970s providing a stable time mark for the different receiving units and overcoming the issue of connecting the different devices (TAKAHASHI et al. 2000). According to NOTHNAGEL et al. (2016), high-precision geodetic and astrometric VLBI with precision in the centimeter or even few millimeter level started in 1979.

VLBI is a space-geodetic technique based on radio interferometry. The geodetic VLBI concept consists of two or more VLBI radio telescopes and numerous extragalactic radio sources, preferably compact radio galaxies or quasi-stellar radio sources (quasars) without proper motions. The radio telescopes observe a radio signal at 8.4 GHz (X-band) and 2.3 GHz (S-band), which is emitted as noise by the extragalactic sources. At each VLBI antenna, the received signal is recorded and, along with highly precise time marks provided by a hydrogen maser, sent to particular correlation centers for cross-correlation purpose to create so-called fringes and obtain the group delay and the delay rate as the fundamental observables (SCHUH and BÖHM 2013). In this context, the correlation process generally includes two steps. First, a cross-correlation of two signals is performed and a Fourier transform is applied to the cross-correlation function resulting in the power spectrum (or cross-spectral density). Second, in a process commonly known as fringe-fitting, the maximum correlation amplitude is searched in the power spectrum to obtain the group delay. For a more detailed description on the correlation and fringe-fitting process the reader is referred to, e.g., WHITNEY (2000).

VLBI contributes considerably to the International Terrestrial Reference Frame (ITRF), which is realized by combining the results of different space-geodetic techniques, and is unique for the realization and maintenance of the International Celestial Reference Frame (ICRF). A further key objective is the determination of highly precise Earth orientation parameters (EOP) describing the non-uniform rotational motion of the Earth (PETIT and LUZUM 2010). According to SCHUH and BÖHM (2011), variations of the instantaneous position of the rotation axis with respect to an Earth-fixed reference system, e.g, a terrestrial reference frame (TRF), are called polar motion, while precession and nutation are the long-term and periodic variations of the position of the instantaneous rotation axis with respect to a celestial reference frame (CRF). Finally, the rotational phase is expressed as the difference between the Universal Time (UT1) and the uniform atomic time (Universal Time Coordinated, UTC). VLBI is the only space-geodetic technique allowing the measurement of the full set of EOP parameters without hypothesis (ARTZ 2011). A subset of the EOP only including polar motion and UT1 is generally referred to as Earth rotation parameters (ERP). For more details on Earth rotation, the reader is referred to SCHUH and BÖHM (2011).

The International VLBI Service for Geodesy and Astrometry (IVS, NOTHNAGEL et al. 2016) is an international collaboration of organizations which operate or support VLBI and has been accepted as an official service of the International Association of Geodesy (IAG) in 1999. According to NOTHNAGEL et al. (2016), today an active global network of about 45-50 radio telescopes observing 4920 radio sources exists within the IVS. Depending on different target parameters, the network configuration varies as well as the session duration. On the one hand, a standard 24 h VLBI

experiment is usually performed two or three times a week and consists of 3 to 15 VLBI stations. On the other hand, so-called Intensive sessions, that means single-baseline sessions of 1 h duration, are almost observed daily for continued UT1 determinations.

In Sec. 2.1, the general VLBI principle and the delay model will be described. The geodetic data analysis including the functional and stochastic model of VLBI observations as well as the parameter estimation process are presented in Sec. 2.2.

2.1 The Basic Principle of VLBI

Although two or more VLBI radio telescopes and numerous extragalactic sources are used for a VLBI session, the delay model can be formulated for a single baseline configuration without loss of generality, since the correlator generates the observations independently (SOVERS et al. 1998).
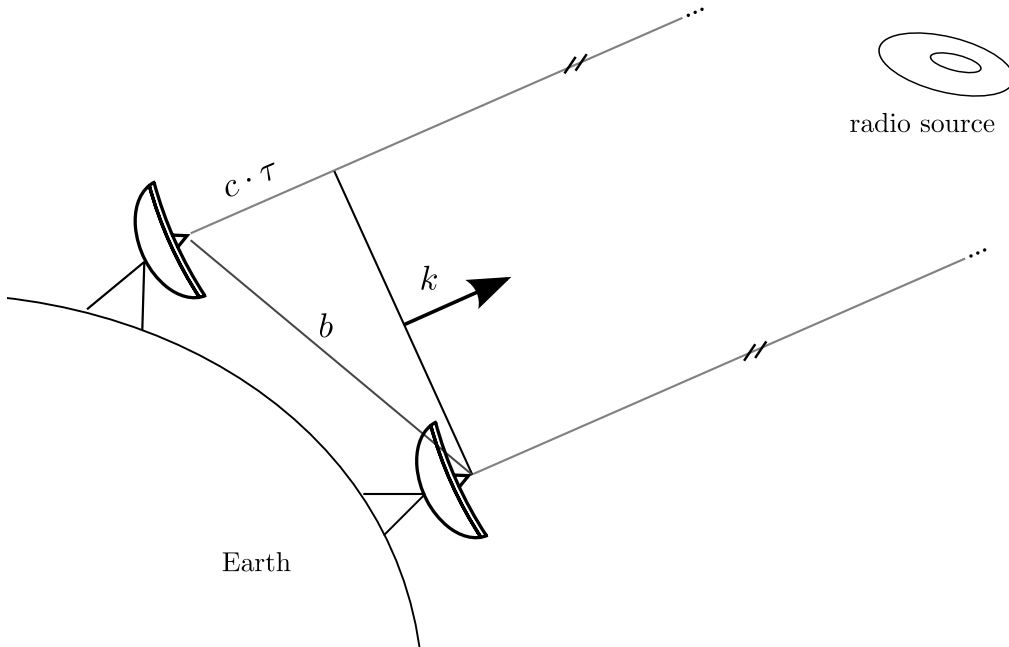
Figure 2.1: The VLBI basis principle.

The general configuration of a single VLBI observation consists of two stations separated by the baseline $\boldsymbol{b}$, which are simultaneously pointed at the same extragalactic source (see Fig. 2.1). From this source radio waves are emitted as noise and travel along the unit vector $\boldsymbol{k}$. Since the radio signals originate from sources completely outside our galaxy, which are located 2-12 billion light years from the Earth, a planar wave front can be assumed without any loss of generality (TAKAHASHI et al. 2000). One wave front will reach both antennas at different times and, thus, the time of arrival defines the so-called group delay, the fundamental VLBI observable. As depicted in Fig. 2.1, the geometrical delay τ_{geom} is obtained in a rectangular triangle as the scalar product between the baseline $\boldsymbol{b}$ and source unit vector $\boldsymbol{k}$,

$$\tau_{geom} = t_B - t_A = -\frac{1}{c}\boldsymbol{b} \cdot \boldsymbol{k}, \tag{2.1}$$

where c represents the velocity of light and $t_{i=A,B}$ defines the time of arrival for station A and B, respectively. In the celestial reference frame the source unit vector $\boldsymbol{k}$ is defined by

$$\boldsymbol{k} = \begin{bmatrix} \cos\alpha \cdot \cos\delta \\ \sin\alpha \cdot \cos\delta \\ \sin\delta \end{bmatrix}, \tag{2.2}$$

with the source coordinates given in right ascension α and declination δ. The baseline vector $\boldsymbol{b}$ can be computed from the position vectors of two VLBI antennas A and B,

$$\boldsymbol{b} = \begin{bmatrix} x_B - x_A \\ y_B - y_A \\ z_B - z_A \end{bmatrix}, \tag{2.3}$$

and is referred to the time of arrival t_A. The time-dependency of the baseline length is represented by $\Delta\boldsymbol{b}$ which includes corrections due to tectonic motions as well as periodic and non-periodic deformations of the Earth's crust, such as, e.g, Earth tides or loading effects. A more detailed description on Earth deformation effects can be found in, e.g, HAAS (1996) or SOVERS et al. (1998).

Equation (2.1) requires that the baseline and unit source vectors are given in the same reference frame, which, in general, is not the case: the antenna positions are given in an Earth-fixed reference frame, a TRF, while the radio sources are defined in a geocentric celestial reference frame (GCRF). Thus, the station locations have to be transformed into the GCRF and Eq. (2.1) becomes

$$\tau_{geom} = t_B - t_A = -\frac{1}{c}\,(\boldsymbol{b} + \Delta\boldsymbol{b}) \cdot \boldsymbol{W} \cdot \boldsymbol{R} \cdot \boldsymbol{Q} \cdot \boldsymbol{k}, \tag{2.4}$$

where $\boldsymbol{W}$ denotes the transformation matrix due to polar motion, $\boldsymbol{R}$ describes the rotation of the Earth around the axis associated with the pole, and $\boldsymbol{Q}$ represents precession and nutation (PETIT and LUZUM 2010). For a more detailed overview on the Earth orientation parameters including an explicit form of the matrices described above, the reader is referred to, e.g., SOVERS et al. (1998), SCHUH and BÖHM (2011) or SCHINDELEGGER et al. (2013). Further, a Lorentz transformation from the geocentric celestial system to the solar system barycentric (SSB), a frame at rest relative to the center of mass of the solar system and rotationally aligned with the GCRF, is necessary to account for relativistic effects, primarily caused by gravitational forces of the Sun and the planets of the solar system (TAKAHASHI et al. 2000, pp 134f). A more detailed explanation of the specific transformations necessary to express the group delay in the barycentric system is given in, e.g., SCHUH (1987), SOVERS et al. (1998), or TAKAHASHI et al. (2000).

Per definition, the (geometric) delay is the difference in arrival time of a radio signal received at two telescopes, that would be measured using an ideal instrumentation, perfectly synchronized, and assuming a vacuum between the extragalactic source and the radio telescopes. In reality, however, several additional correction terms are required due to effects occurring on the way through the solar system and the Earth's atmosphere. In addition, geophysical phenomena and instrumental effects have to be accounted for. Finally, the observational delay τ_{obs} for high accuracy VLBI measurements is given by

$$\tau_{obs} = \tau_{geom} + \tau_{instr} + \tau_{clock} + \tau_{iono} + \tau_{tropo} + \ldots. \tag{2.5}$$

In Eq. (2.5), the term τ_{instr} denotes the propagation delays due to on-site cable runs and other instruments (SCHUH and BEHREND 2012) and τ_{clock} represents the correction term due to local

oscillator instabilities and mis-synchronization of the reference clocks used for each radio telescope (CAMPBELL 1987). The correction terms τ_{iono} and τ_{tropo} correspond to the propagation delays due to the ionosphere and the neutral atmosphere, respectively.

The ionosphere is a dispersive (frequency-independent) medium in the radio frequency domain. Thus, the ionosphere delay correction can be corrected to first order by observing at two different frequencies in X- and S-band. The model for the ionospheric contribution in X-band is given as the ionosphere free linear combination:

$$\tau_{iono} = \frac{f_S^2}{(f_X^2 - f_S^2)}\left(\tau_X - \tau_S\right), \tag{2.6}$$

where $f_X = 8.4$ GHz (X-band) and $f_S = 2.3$ GHz (S-band) are the observing frequencies, and τ_X and τ_S denote the group delay observable in X- and S-band, respectively. Currently, the maximum effect of the second order ionosphere delay correction is in the sub-millimeter level and can therefore be neglected (HAWAREY et al. 2005).

The model for the propagation delay due the neutral atmosphere can be expressed by (cf. Eq. (3.65) in Sec. 3.3)

$$\tau_{tropo} = mf_h(\varepsilon)\Delta L_h^z + mf_w(\varepsilon)\Delta L_w^z + mf_h(\varepsilon)\left[G_n\cos(\alpha) + G_e\sin(\alpha)\right], \tag{2.7}$$

where both the hydrostatic (index h) and the wet (index w) components consist of a propagation delay in zenith direction (ΔL_h^z and ΔL_w^z) and the corresponding mapping functions ($mf_h(\varepsilon)$ and $mf_w(\varepsilon)$) relating the zenith delay to an arbitrary elevation angle ε. The second term, $mf_h(\varepsilon)\left[G_n\cos(\alpha) + G_e\sin(\alpha)\right]$, is due to horizontal refractivity variations and necessary to consider the azimuthal asymmetry (α denotes the azimuth angle) of the neutral atmosphere around the station. The gradients in north and east direction are denoted by G_n and G_e, respectively, and $mf_h(\varepsilon)$ describes the mapping function used for the delay due to atmospheric gradients. Equation (2.7) is derived in Sect. 3.3 of this thesis and further details on the individual variables are provided.

A more detailed description of the atmospheric modeling and the definition of the propagation delay in the neutral atmosphere are given in Ch. 3.

2.2   Geodetic Data Analysis and Parameter Estimation Process

The progressing of geodetic VLBI data analysis can be generally divided into two main components (see flow diagram in Fig. 2.2): on the one hand, the group delays as the actual observables are corrected by instrumental and environmental effects leading to the reduced observed delays $\boldsymbol{o}$ (red fields in Fig. 2.2); on the other hand, theoretical delays $\boldsymbol{c}$ (green fields in Fig. 2.2) are computed on the basis of a priori parameters.

The reduced observation vector, in the following referred to as the "observed minus computed" vector

$$\boldsymbol{l} = \boldsymbol{o} - \boldsymbol{c}, \tag{2.8}$$

is formed and entered in the parameter estimation process. The target parameters can either be estimated in a classic least squares adjustment (e.g., KOCH 1999), a Kalman Filter (KALMAN 1960),
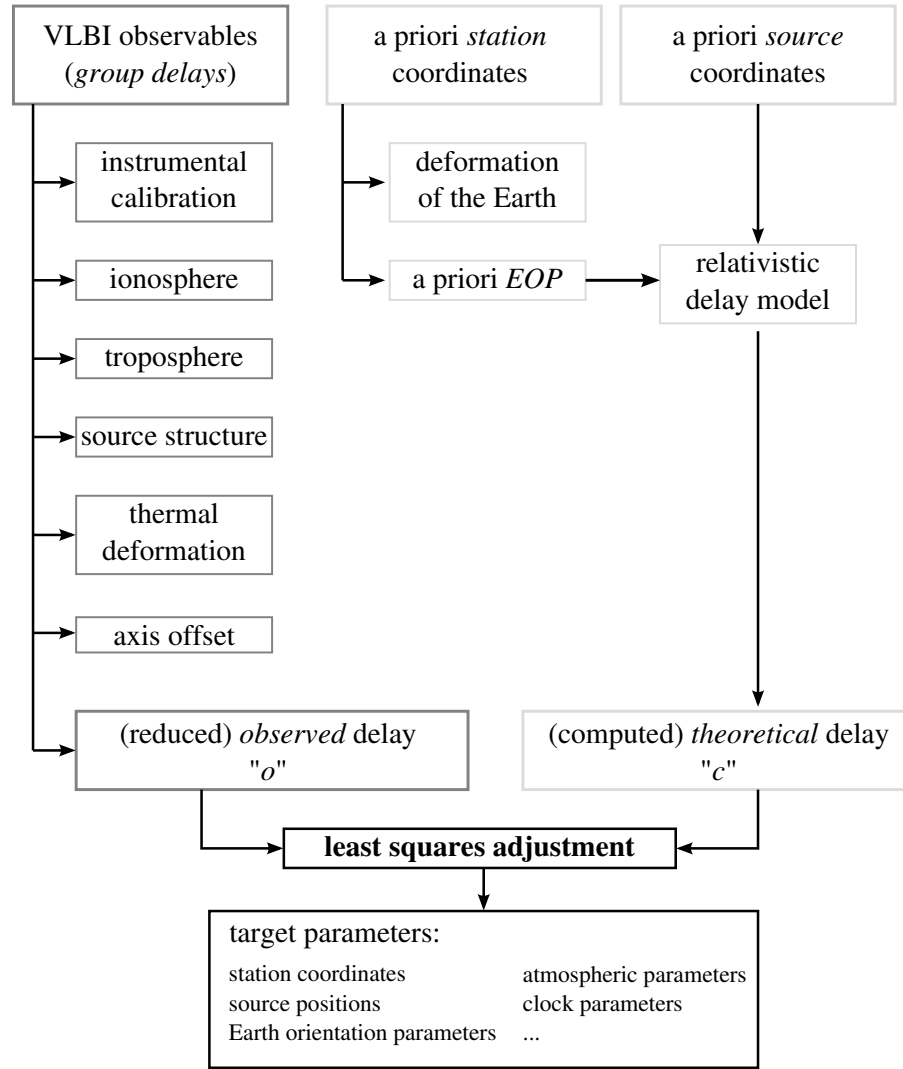
Figure 2.2: Geodetic VLBI data analysis - flow diagram; modified according to SCHUH and BÖHM (2013).

least squares collocation methods (e.g., KRARUP 1969; MORITZ 1972) or a square root information filter (e.g., BIERMAN 1977). The following description of both the functional and the stochastic model always refers to the classical least squares adjustment, which is currently the standard processing method in the data analysis of the IVS.

2.2.1   Functional Model

A more explicit form of the observational delay in Eq. (2.5) for a standard parameter setting in an independent single session of 24 hour duration ignoring the detailed Lorentz transformation can be expressed by

$$
\begin{aligned}
\tau_{obs}(t) = -\frac{1}{c}(\boldsymbol{b} + \Delta\boldsymbol{b}(t)) \cdot \boldsymbol{W}(t) \cdot \boldsymbol{R}(t) \cdot \boldsymbol{Q}(t) \cdot \boldsymbol{k} \\
\cdot \left\{ 1 - \frac{(v_i + v_i^B) \cdot k_i}{c} + \frac{(v_i \cdot k_i)^2 + 2(v_i \cdot k_i)(v_i^B \cdot k_i)}{c^2} + \frac{(b_i \cdot v_i)(v_i^B \cdot k_i)}{c^3} + \frac{(b_i \cdot v_i)(v_i \cdot k_i)}{2c^3} \right\} \\
- (\mathcal{T}_0^A + \mathcal{T}_1^A \cdot (t - t_0) + \mathcal{T}_2^A \cdot (t - t_0)^2) \\
+ (\mathcal{T}_0^B + \mathcal{T}_1^B \cdot (t - t_0) + \mathcal{T}_2^B \cdot (t - t_0)^2) \\
- \left(T^A(t_0) + \frac{T^A(t_1) - T^A(t_0)}{t_1 - t_0}(t - t_0) + ... + \frac{T^A(t_i) - T^A(t_{i-1})}{t_i - t_{i-1}}(t - t_i) \right) \\
+ \left(T^B(t_0) + \frac{T^B(t_1) - T^B(t_0)}{t_1 - t_0}(t - t_0) + ... + \frac{T^B(t_i) - T^B(t_{i-1})}{t_i - t_{i-1}}(t - t_i) \right) \\
+ \mathcal{MF}_w^a \cdot \left[\mathcal{AT}^A(t_0) + \frac{\mathcal{AT}^A(t_1) - \mathcal{AT}^A(t_0)}{t_1 - t_0}(t - t_0) + ... + \frac{\mathcal{AT}^A(t_i) - \mathcal{AT}^A(t_{i-1})}{t_i - t_{i-1}}(t - t_i) \right] \\
+ \mathcal{MF}_w^B \cdot \left[\mathcal{AT}^B(t_0) + \frac{\mathcal{AT}^B(t_1) - \mathcal{AT}^B(t_0)}{t_1 - t_0}(t - t_0) + ... + \frac{\mathcal{AT}^B(t_i) - \mathcal{AT}^B(t_{i-1})}{t_i - t_{i-1}}(t - t_i) \right] \\
+ \mathcal{MF}_w^A(\varepsilon^A) \cdot \cot\varepsilon^A \cdot [\mathcal{G}_n^B \cos\alpha^A + \mathcal{G}_e^A \sin\alpha^A] \\
+ \mathcal{MF}_w^B(\varepsilon^B) \cdot \cot\varepsilon^B \cdot [\mathcal{G}_n^B \cos\alpha^B + \mathcal{G}_e^B \sin\alpha^B] \\
+ \tau_{other} + \boldsymbol{\epsilon}
\end{aligned}
$$

$$(2.9)$$

with

$\boldsymbol{k}$	source unit vector (see Eq. 2.2) with its three components k_i
$\boldsymbol{b}$	baseline vector (see Eq. 2.3) with its three components b_i
$\Delta\boldsymbol{b}(t)$	baseline vector corrections at epoch t for tectonic motions and geophysical effects
v_i	x-, y- or z-velocity component of the geocenter
v_i^B	x-, y- or z-velocity of station B w.r.t. the geocenter
c	velocity of light
$\boldsymbol{W}(t)$	transformation matrix due to polar motion (Petit and Luzum 2010, Ch. 5)
$\boldsymbol{R}(t)$	transformation matrix due to the rotation of the Earth (Petit and Luzum 2010, Ch. 5)
$\boldsymbol{Q}(t)$	transformation matrix due to precession and nutation (Petit and Luzum 2010, Ch. 5)
$\mathcal{T}_j^*$	parameters of the clock polynomial at station A or B
$T^*(t_i)$	additional clock parameters at station A or B for a specific epoch t_i parametrized as continuous piece-wise linear functions (CPWLF), i.e., linear splines (e.g., De Boor 1978)
$\mathcal{MF}_w^*$	mapping function of the wet part of the atmosphere at station A or B
$\mathcal{AT}^*(t_i)$	zenith wet delays parametrized as CPWLF at station A or B for a specific epoch t_i
$\mathcal{G}_{n/e}^*$	atmospheric gradients in north or east direction at station A or B
$\boldsymbol{\tau}_{other}$	remaining effects of Eq. (2.5)
$\boldsymbol{\epsilon}$	measurement noise

The VLBI target parameters, such as Earth orientation parameters and telescope or radio source positions, are generally estimated in a classical least squares adjustment following the Gauss Markov model of the form (e.g., KOCH 1999)

$$
\begin{aligned}
\boldsymbol{l} &= \boldsymbol{A}\boldsymbol{x} + \boldsymbol{v}, \\
\boldsymbol{\Sigma}_{ll} &= \sigma_0 \boldsymbol{Q}_{ll}
\end{aligned}
\tag{2.10}
$$

where $\boldsymbol{l}$ describes the $n \times 1$ vector of observations, $\boldsymbol{x}$ is the $m \times 1$ vector of unknown parameters to be estimated (the vector of estimated parameters is denoted by $\widetilde{\boldsymbol{x}}$), and vector

$$
\boldsymbol{v} = \boldsymbol{A}\widetilde{\boldsymbol{x}} - \boldsymbol{l}
\tag{2.11}
$$

contains the post-fit residuals. In addition to the target parameters, $\boldsymbol{x}$ further contains clock and tropospheric model parameter corrections. The matrix $\boldsymbol{A}$ is the $n \times m$ Jacobian matrix which contains the partial derivatives of the observation equations with respect to the parameters. The partial derivatives for the specific VLBI parameters are explicitly stated in, e.g., SCHUH (1987), NOTHNAGEL (1991) and HAAS (1996). The matrix $\boldsymbol{\Sigma}_{ll}$ represents the variance covariance matrix of the observations as the product of the a priori variance factor σ_0 and the cofactor matrix $\boldsymbol{Q}_{ll}$, which is derived from the VLBI correlation process and an additional noise term to consider quasi-random deficiencies in the stochastic model (see Sec. 2.2.2). Minimizing the sum of squared residuals

$$
\boldsymbol{v}^T \boldsymbol{P} \boldsymbol{v} \dots min
\tag{2.12}
$$

yields the vector of estimated parameters

$$
\widetilde{\boldsymbol{x}} = \left(\boldsymbol{A}^T \boldsymbol{\Sigma}_{ll}^{-1} \boldsymbol{A} \right)^{-1} \boldsymbol{A}^T \boldsymbol{\Sigma}_{ll}^{-1} \boldsymbol{l},
\tag{2.13}
$$

or, described in form of the normal equation system

$$
\widetilde{\boldsymbol{x}} = \boldsymbol{N}^{-1}\boldsymbol{n},
\tag{2.14}
$$

with

$$
\boldsymbol{N} = \boldsymbol{A}^T \boldsymbol{\Sigma}_{ll}^{-1} \boldsymbol{A}
\tag{2.15}
$$

representing the normal equation matrix and

$$
\boldsymbol{n} = \boldsymbol{A}^T \boldsymbol{\Sigma}_{ll}^{-1} \boldsymbol{l}
\tag{2.16}
$$

being the corresponding right-hand side. The matrix $\boldsymbol{P}$ in Eq (2.12) denotes the weight matrix as the inverse of the variance-covariance matrix of the observations, that means $\boldsymbol{P} = \boldsymbol{\Sigma}_{ll}^{-1}$.

In the following, the solution given in Eq. (2.13) is referred to as the classical or ordinary least squares (OLS) adjustment, which is used in Chs. 5 and 6, and forms the basis for different alternative modeling and adjustment strategies presented in Ch. 7 in order to overcome specific deficiencies in the current tropospheric model of the IVS (see Sec. 3.3.6) and to estimate atmospheric parameters in a more meaningful and appropriate way. In this context, an inequality constrained least squares approach is developed to overcome the deficiency, that occasionally zenith wet delay estimates become negative, which, of course, does not reflect meteorological conditions in a plausible way. Additionally, the pseudo-stochastic behavior of the piece-wise linear representation (cf., Eq. 2.9) for the zenith wet delays, which only describes the stochastic character of the atmosphere to a limited extent, is replaced by a least squares collocation method and suitable covariance functions to represent the stochastic properties of the neutral atmosphere.

2.2.2 Stochastic Model

The stochastic model of VLBI observations is described by the variance-covariance matrix of the observations $\mathbf{\Sigma}_{ll}$. In the traditional data analysis of the IVS, the variance-covariance matrix has a diagonal structure and, thus, correlations between the observations are neglected. The variances are directly obtained during the correlation process (CLARK et al. 1985). According to CAMPBELL (1987), the standard deviations of the group delay can be determined by

$$\sigma_\tau = \frac{1}{2\pi \cdot SNR \cdot B_{eff}}. \tag{2.17}$$

The effective bandwidth B_{eff} is defined as the root mean square (RMS) of the n individual channel frequencies ν_i about their mean value $\bar{\nu}$,

$$B_{eff} = \sqrt{\frac{\sum\limits_{i=1}^{n}(\nu_i - \bar{\nu})^2}{n}}, \tag{2.18}$$

and is therefore also called the RMS spanned bandwidth (e.g., ROGERS 1970 or WHITNEY 2000). The signal to noise ratio (SNR) is defined by

$$SNR = \mu\sqrt{2B \cdot T_{int}}\ \frac{S}{2k}\ \sqrt{\frac{A_1 \cdot A_2}{T_{n_1} \cdot T_{n_2}}}, \tag{2.19}$$

and, thus, proportional to the flux density S, the area of both antennas A_1 and A_2, the recorded total bandwidth B as well as the so-called coherent integration time T_{int} and inversely proportional to the system noise temperature of the recording systems T_{n_1} and T_{n_2}, respectively. Finally, $k = 1.38 \times 10^{-23} \frac{J}{K}$ defines the Boltzmann constant and μ represents the so-called digital loss factor, which describes the quality of the digitization and filtering of the signals.

Since the variances of the observations only depend on the correlation process and correlations between observations are completely neglected, the standard deviations of the VLBI target parameters are generally too optimistic (e.g., SCHÖN and KERMARREC 2015, HALSIG et al. 2016a). To overcome this deficiency, in traditional VLBI data analysis the standard deviations derived from the VLBI cross correlation process are inflated artificially. For instance, this is achieved by adding either a constant term to the variances of the observations, as done in the Vienna VLBI Software (VieVS, BÖHM et al. 2012), or doing an interactive baseline-dependent re-weighting (PETROV 1998), as done in Calc/Solve (MA et al. 1990).

Several investigations have been performed by different authors to improve the stochastic model of space-geodetic observations, although neither of these approaches has become part of the operational data analysis so far. In general, the strategies to optimize the stochastic model of VLBI observations can be divided into four categories. The first concept depends on analyzing the post-fit residuals, including, for instance, the work of QIAN (1985) and SCHUH and WILKIN (1989) who obtained correlation coefficients from several VLBI sessions. Second, the general concept of estimating variance and covariance components was used to refine the stochastic model of VLBI observations (e.g., LUCAS and DILLINGER 1998; TESMER 2004; TESMER and KUTTERER 2004; ZUBKO et al. 2012). The third category includes empirical models predominately incorporating station- or baseline-dependent noise components to the stochastic model of the observations. For

instance, GIPSON (2006), GIPSON (2007) and GIPSON et al. (2008) proposed a strategy to account for unmodeled variances and covariances by adding station-dependent delay noise to the standard deviations of the observations. For this purpose, they have distinguished two different types of delay noise: a constant additional component to deal with the clock-like behavior and an elevation-dependent noise term to consider atmospheric characteristics. Finally, the stochastic properties of the observations are derived by atmospheric turbulence models (TREUHAFT and LANYI 1987; TREUHAFT and LOWE 1991; NILSSON et al. 2010; ROMERO-WOLF et al. 2012) following the widely accepted Kolmogorov turbulence theory (KOLMOGOROV 1941a, KOLMOGOROV 1941b). Similar investigations have been performed for GPS (e.g., EULER and GOAD 1991; WANG et al. 2002; BISCHOFF et al. 2006; TIBERIUS and KENSELAAR 2003; HOWIND et al. 1999; HOWIND 2005; SCHÖN and BRUNNER 2008a; SCHÖN and BRUNNER 2008b; LUO et al. 2011; KERMARREC and SCHÖN 2014).

The concept of modeling atmospheric turbulence is, however, the only approach which allows for a physically more reliable modeling of the stochastic properties, while most other strategies depend on empirical findings or are based on iterative re-weighting procedures forcing certain statistic criteria to specific numbers. Further, the turbulence description is the only method that enables the modeling of physical correlations between the observations instead of only mathematical correlations, if at all.

An improved and proper modeling of the stochastic properties, however, still remains a major challenge and is the main objective in this thesis. Special consideration is given to the neutral atmosphere as the dominant error source of VLBI observations (cf. PETRACHENKO et al. 2008; PANY et al. 2011). Chapter 3 provides the theoretical fundamentals on the neutral part of the atmosphere including the tropospheric propagation delay of space-geodetic observations. A description of Kolmogorov's turbulence theory (Sec. 4.1) and the turbulence models (Sec. 4.3) developed by different authors in the last decades is given in Ch. 4. In particular, the model of the KERMARREC and SCHÖN (2014) has been chosen in this thesis to be further developed in order to provide an enhanced stochastic model of VLBI observations considering small-scale refractivity fluctuations in an operational mass production, since no numerical integration is necessary, which reduces the computational effort compared to most other turbulence models. A detailed description of the turbulence model developed in this thesis is given in Sec. 5.1.

3. Modeling the Atmosphere

Electromagnetic waves emitted by natural or artificial sources, such as extragalactic radio sources or satellites, pass through the atmosphere to an antenna on the Earth's surface and are affected by atmospheric conditions leading to attenuation, scintillation and delay of the signal. The atmosphere generally consists of several layers, and the most relevant compartments for space-geodetic techniques in the radio frequency domain are the neutral atmosphere up to 100 km altitude and the ionosphere extending from about 60 to more than 1.000 km altitude (e.g., Böhm et al. 2013).

The iononization by solar radiation leads to ionospheric refraction. The ionosphere is a dispersive (frequency-dependent) medium, and the effects of ionospheric refraction can be accounted for, to first order, by observing at more than one frequency. In case of Very Long Baseline Interferometry (VLBI), ionospheric effects are determined and eliminated by observing at two frequencies in X- and S-band (frequencies at 8.4 GHz and 2.3 GHz, respectively). Since this strategy is deemed to be sufficient in the current geodetic data analysis of VLBI observations, ionospheric refraction is not discussed in this thesis. For a detailed overview on ionospheric effects the reader is referred to, e.g., Alizadeh et al. (2013).

In contrast, the neutral atmosphere is a non-dispersive medium and sophisticated strategies are necessary to model atmospheric refraction. In the following chapter, theoretical fundamentals on the neutral atmosphere are presented. In Sec 3.1, the propagation delay for electromagnetic waves is described. The terms refractivity and refractive index are introduced in Sec. 3.2, followed by Sec. 3.3 on the propagation delay of space-geodetic observations due to the troposphere.

In addition, the diurnal heating of the atmosphere causes a time-varying atmospheric pressure distribution, which can lead to displacements at the Earth's surface (Sovers et al. 1998, pp 1413f). The corresponding effect is referred to as atmospheric pressure loading and several models have been proposed to correct displacements at the observation level (e.g., Van Dam and Wahr 1987; Petrov and Boy 2004). The effect of atmospheric pressure loading is also not subject to this thesis. A more detailed overview can be found in, e.g., Wijaya et al. (2013).

3.1 Propagation Delay for Electromagnetic Waves

Generally, the propagation of electromagnetic waves is described by Maxwell's equations (Jackson 1998, pp 2f)

$$\nabla \cdot \mathbf{D} = \rho, \tag{3.1}$$

$$\nabla \cdot \mathbf{B} = 0, \tag{3.2}$$

$$\nabla \times \mathbf{E} = -\frac{\partial \mathbf{B}}{\partial t}, \tag{3.3}$$

$$\nabla \times \mathbf{H} = \mathbf{J} + \frac{\partial \mathbf{D}}{\partial t}, \tag{3.4}$$

where $\mathbf{E}$ and $\mathbf{B}$ denote the electric and magnetic field vectors, respectively, $\mathbf{D}$ is the electric displacement vector, $\mathbf{H}$ describes the magnetic field intensity, and ρ and $\mathbf{J}$ are the volume charge density

and the current density, respectively. Since the troposphere is assumed to be a non-conducting ($\mathbf{J} = 0$), neutral ($\rho = 0$) and non-dispersive medium, Maxwell's equations can be simplified to

$$\nabla \cdot (\epsilon \mathbf{E}) = 0, \tag{3.5}$$

$$\nabla \cdot \mathbf{B} = 0, \tag{3.6}$$

$$\nabla \times \mathbf{E} = -\frac{\partial \mathbf{B}}{\partial t}, \tag{3.7}$$

$$\nabla \times \mathbf{B} = \epsilon \mu \frac{\partial \mathbf{E}}{\partial t}, \tag{3.8}$$

with $\mathbf{D} = \epsilon \mathbf{E}$ and $\mathbf{B} = \mu \mathbf{H}$, where ϵ and μ represent the (relative) permittivity (or dielectric constant) and the permeability (WHEELON 2004, pp 6ff). Assuming that the temporal and spatial variations of ϵ and μ are small and combining Maxwell's equations yields the so-called wave equation for the electric field (NILSSON et al. 2013)

$$\nabla^2 \mathbf{E} = \mu \epsilon \frac{\partial^2 \mathbf{E}}{\partial^2 t} = \frac{n^2}{c^2} \frac{\partial^2 \mathbf{E}}{\partial^2 t}, \tag{3.9}$$

where c is the velocity of light in vacuum and n represents the refractive index. From the wave equation it is evident, that the propagation of electromagnetic waves depends on the refractivity (NILSSON et al. 2013). The term refractivity is discussed in more detail in Sec. 3.2.

3.2   Refractivity for Microwaves

Refractivity causes a bending effect as well as a propagation delay of an electromagnetic signal. The relationship between the refractivity N and the refractive index n is defined by

$$N = 10^6(n - 1), \tag{3.10}$$

and it is common practice to use N, because n is very close to one in the neutral atmosphere ($n \approx 1.0003$). As a complex number, the refractivity can generally be divided into an imaginary part $iN''(\nu)$ and a real part, consisting of a dispersive (frequency-dependent; ν denotes the frequency) term $N'(\nu)$ as well as a non-dispersive term N_0 (e.g., NILSSON et al. 2013):

$$N = N_0 + N'(\nu) - iN''(\nu). \tag{3.11}$$

While the real part of the refractivity is responsible for propagation delay and refraction, the imaginary part quantifies the absorption (LIEBE et al. 1993).

In the data analysis of space-geodetic techniques the absorption effect can be typically neglected, since space-geodetic observations are measurements of the travel time of electromagnetic waves and the propagation delay is not directly affected by absorption (NILSSON et al. 2013). Further, using suitable models developed for the calculation of the refractivity (e.g, the Millimeter-wave Propagation Model; LIEBE 1985, LIEBE 1989, and LIEBE et al. 1993), it was shown, that the influence of the dispersive term $N'(\nu)$ in Eq. (3.11) is smaller than about 3 ps for frequencies up to 40 GHz (LIEBE 1985). For space-geodetic techniques, such as GPS (L-band; frequencies of 1.2 GHz and 1.5 GHz, respectively) and VLBI (X-band and S-band; frequencies at 2.3 GHz and 8.4 GHz, respectively), the effect is even smaller (for more details, see, e.g., LIEBE 1985 and BÖHM 2004, p. 28).

Based on these assumptions, the refractivity can be expressed as a function of meteorological parameters, particularly temperature, pressure and humidity (THAYER 1974)

$$N \approx N_0 = \underbrace{k_1 \frac{p_d}{T} Z_d^{-1}}_{N_h} + \underbrace{k_2 \frac{e}{T} Z_w^{-1} + k_3 \frac{e}{T^2} Z_w^{-1}}_{N_w}, \tag{3.12}$$

and is generally divided into the hydrostatic and wet refractivity N_h and N_w, respectively. In Eq. (3.12), k_1, k_2, k_3 are constants (for more details, see, e.g., BEVIS et al. 1994), p_d and e represent the partial pressure of dry air and water vapor, respectively, and T describes the temperature. The inverse compression factors of dry air and water vapor, Z_d^{-1} and Z_w^{-1}, represent the deviating behavior from an ideal gas, which, according to the ideal gas law, satisfies the condition

$$Z = \frac{PV}{mRT} = 1, \tag{3.13}$$

where P, V and T are the pressure, the volume and the temperature of the gas, respectively. R represents the universal gas constant and m is the amount of substance of gas. OWENS (1967) found the following expressions for the inverse compression factors:

$$Z_d^{-1} = 1 + p_d \left[57.97 \times 10^{-8} \left(1 + \frac{0.52}{T_{[K]}} \right) - 9.4611 \times 10^{-4} \frac{T_{[°C]}}{T_{[K]}^2} \right], \tag{3.14}$$

$$Z_w^{-1} = 1 + 1650 \frac{e}{T_{[K]}^3} \left[1 - 0.01317 T_{[°C]} + 1.75 \times 10^{-4} T_{[°C]}^2 + 1.44 \times 10^{-6} T_{[°C]}^3 \right]. \tag{3.15}$$

The refractivity depends on the permanent and induced dipole moments of the individual molecular constituents in the atmosphere. These dipole moments contribute on the refractivity as $\propto \frac{p}{T}$ in case of the induced dipole moment and $\propto \frac{p}{T^2}$ in case of the permanent dipole moment (BÖHM 2004, p. 28). The first and second term in Eq. (3.12) represent the effect of the induced dipole moment for the dry constituents and the water vapor, respectively, while the third term expresses the permanent dipole moments of the water molecules (NOTHNAGEL 2000). While none of the principal constituents of dry air, nitrogen and oxygen, have a permanent dipole moment, and only contribute due to their induced dipole moments, water vapor has a substantial dipole moment (DAVIS et al. 1985).

3.3   Definition of the Propagation Delay in the Neutral Atmosphere

Space-geodetic observations are generally based on a measurement of the travel time between a natural or artificial source and the receiving antenna. However, the Earth's atmosphere directly affects the propagation path of the electromagnetic way (see Eq. 3.9) and consequently the travel time measurement, because the propagation velocity in the atmosphere c_0 differs from the speed of light in vacuum c. To define the propagation delay in the neutral part of the atmosphere, the geometric optics approximation is used, which allows to describe the electromagnetic wave as a ray (NILSSON et al. 2013).
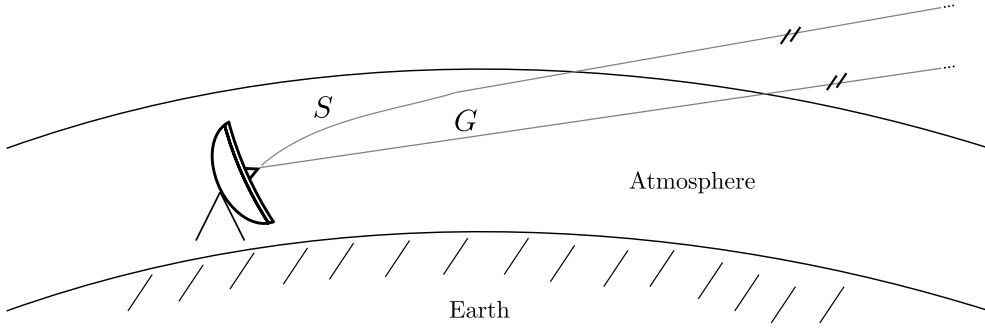
Figure 3.1: Signal path through the atmosphere; modified according to ELGERED (1993)
.

According to Fermat's principle on wave propagation in geometrical optics, the signal follows the path S through the atmosphere that minimizes the electric path length L (see Fig. 3.1)

$$L = \int_S n(S)ds. \tag{3.16}$$

However, the electric path is longer than the geometric length G, the straight line the ray would take if the atmosphere would be replaced by vacuum (DAVIS et al. 1985). Thus, the excess path length ΔL due to the neutral atmosphere, in the following referred to as atmospheric delay (ignoring the scale factor $\frac{1}{c}$), can be described by

$$\Delta L = L - G \tag{3.17}$$

or, reformulated to

$$\Delta L = \int_S n(s)ds - G = \int_S (n(s) - 1)ds + \int_S ds - G = \underbrace{[\int_S (n(s) - 1)ds]}_{\Delta L_n} + \underbrace{[S - G]}_{\Delta L_s} \tag{3.18}$$

to separate the excess path delay caused by troposphere relative to a vacuum ΔL_n and ΔL_s describing the geometrical signal delay caused by bending effects. According to NOTHNAGEL (2000), the latter can be ignored, because assuming a horizontal layered atmosphere the path lengths S and G are identical in zenith direction and the differences in path length at low elevations would be modeled within the so-called mapping functions (see Sec. 3.3.4). Thus, the bending term is neglected in the following, yielding

$$\Delta L = \int_S (n(s) - 1)ds = 10^{-6} \int_S N(s)ds, \tag{3.19}$$

and using Eq. (3.12) to solve the integral in Eq. (3.19) leads to

$$\Delta L = 10^{-6} \left[\int_S k_1 \frac{p_d}{T} Z_d^{-1} ds + \int_S \left(k_2 \frac{e}{T} Z_d^{-1} + k_3 \frac{e}{T^2} Z_d^{-1} \right) ds \right]. \tag{3.20}$$

The integration of the refractivity in Eq. (3.20) requires the knowledge of the mixing ratio of the wet and hydrostatic constituents, which is not subject to a physical law and highly variable (DAVIS

et al. 1985). In contrast, the overall pressure is in hydrostatic equilibrium and, following DAVIS et al. (1985), it is possible to obtain a term nearly independent of the mixing ratio. The first two terms in Eq. (3.12) can be expressed with the equation of state as

$$
\begin{aligned}
k_1 \frac{p_d}{T} Z_d^{-1} + k_2 \frac{e}{T} Z_w^{-1} &= k_1 \frac{R}{M_d} \rho_d + k_2 \frac{R}{M_w} \rho_w \\
&= k_1 \frac{R}{M_d} \rho + k_2' \frac{e}{T} Z_w^{-1},
\end{aligned}
\tag{3.21}
$$

with the total mass density $\rho = \rho_d + \rho_w$ and

$$
k_2' = \left(k_2 - k_1 \frac{M_w}{M_d} \right),
\tag{3.22}
$$

where M_w and M_d denote the molar weights of the hydrostatic and wet constituents (BÖHM 2004, pp 33ff). Rewriting Eq. (3.12) leads to

$$
N = \underbrace{k_1 \frac{R}{M_d} \rho}_{N_h} + \underbrace{k_2' \frac{e}{T} Z_w^{-1} + k_3 \frac{e}{T^2} Z_w^{-1}}_{N_w} .
\tag{3.23}
$$

Thus, the expression for the propagation delay in Eq. (3.20) becomes

$$
\begin{aligned}
\Delta L &= 10^{-6} \left[\int_S N_h(s) ds + \int_S N_w(s) ds \right] \\
&= 10^{-6} \left[\int_S k_1 \frac{R}{M_d} \rho ds + \int_S \left(k_2' \frac{e}{T} Z_w^{-1} + k_3 \frac{e}{T^2} Z_w^{-1} ds \right) \right] \\
&= \Delta L_h + \Delta L_w.
\end{aligned}
\tag{3.24}
$$

The first term of Eqs. (3.23) and (3.24), respectively, which is referred to as the hydrostatic refractivity N_h, only depends on the total density of and not on the mixing ratio of the wet and hydrostatic constituents. In contrast, the so-called wet refractivity N_w depends on the temperature and the partial pressure of water vapor (DAVIS et al. 1985).

In space-geodesy, it is common practice to describe the propagation delay of both, the hydrostatic and wet component, as a delay correction term in zenith direction, ΔL_h^z and ΔL_w^z, respectively, and a corresponding mapping function, $mf_h(\varepsilon)$ and $mf_w(\varepsilon)$, relating the zenith delay to an arbitrary elevation angle ε in vacuum (DAVIS et al. 1985):

$$
\begin{aligned}
\Delta L &= \Delta L_h + \Delta L_w \\
&= mf_h(\varepsilon) \Delta L_h^z + mf_w(\varepsilon) \Delta L_w^z,
\end{aligned}
\tag{3.25}
$$

with

$$
\Delta L_h^z = 10^{-6} \int_{h_0}^{\infty} N_h(h) dh,
\tag{3.26}
$$

$$
\Delta L_w^z = 10^{-6} \int_{h_0}^{\infty} N_w(h) dh,
\tag{3.27}
$$

where h_0 represents the reference height, either defined as the height above ground or the intersection of the rotation axes of the radio telescope. In the following, both the hydrostatic (Sec. 3.3.1) and wet (Sec. 3.3.2) part of the propagation delay as well as the mapping functions (Sec. 3.3.4) are discussed in more detail.

3.3.1 Hydrostatic Delay

According to DAVIS et al. (1985), the propagation delay due to the hydrostatic refractivity, from here on referred to as zenith hydrostatic delay (ZHD), can be integrated if the condition of hydrostatic equilibrium

$$\frac{dp}{dh} = -\rho(h)g(h), \tag{3.28}$$

is satisfied, where $g(h)$ denotes the gravitational acceleration and $p(h)$ is the total pressure. Integrating Eq. (3.28) yields the reference pressure p_0 at height h_0 (e.g., the height above ground or the intersection of the rotation axes of the radio telescope)

$$p_0 = \int_{h_0}^{\infty} \rho(h)g(h)dh, \tag{3.29}$$

or,

$$p_0 = g_m \int_{h_0}^{\infty} \rho(h)dh, \tag{3.30}$$

replacing the height-dependent gravitational acceleration by the mean gravitational acceleration g_m, which can be formulated as

$$g_m = \frac{\int_{h_0}^{\infty} \rho(h)g(h)dh}{\int_{h_0}^{\infty} \rho(h)dh}. \tag{3.31}$$

SAASTAMOINEN (1972) proposed the following expression for the mean gravitational acceleration,

$$g_m = 9.8062(1 - 0.00265\cos(2\phi) - 0.00031h_c), \tag{3.32}$$

where ϕ represents the geocentric latitude and h_c is the height of the center of mass of the atmosphere above the site, which can be strictly formulated as

$$h_c = \frac{\int_{h_0}^{\infty} \rho(h)hdh}{\int_{h_0}^{\infty} \rho(h)dh}. \tag{3.33}$$

However, for practical application, SAASTAMOINEN (1972) suggested an approximation for the effective height h_c valid for all latitudes and seasons,

$$h_c = (0.9h_0 + 7300) \pm 400, \tag{3.34}$$

and g_m is simplified to

$$g_m = 9.784(1 - 0.00266\cos(2\phi) - 0.00028h_0) \pm 0.001. \tag{3.35}$$

Using this approximation, the integral for the hydrostatic component in Eq. (3.24) can be solved, and the hydrostatic delay becomes (BÖHM 2004, p. 37)

$$\Delta L_h^z = 10^{-6}k_1 \frac{R}{M_d \, g_m} \frac{p_0}{1 - 0.00266\cos(2\phi) - 0.00028h_0}. \tag{3.36}$$

Using all simplifications, the zenith hydrostatic delay can be defined by

$$\Delta L_h^z = 0.0022768 \frac{p_0}{1 - 0.00266 \cos(2\phi) - 0.00028 h_0},\tag{3.37}$$

which is referred to as the modified Saastamoinen model proposed by DAVIS et al. (1985). Given a standard air pressure of $p_0 = 1000$ hPa the magnitude of the zenith hydrostatic delay according to Eq. (3.37) is 2.28 m (NOTHNAGEL 2000). The accuracy of the zenith hydrostatic delay using this approach is estimated to be < 3 mm (HERRING et al. 1990) or even 0.5 mm, assuming that the pressure can be observed with a sufficient accuracy (MACMILLAN and MA 1998).

The initial equation of SAASTAMOINEN (1972) was formulated as

$$\Delta L_h^z = \frac{1}{\sin(\varepsilon)} 0.002277 \left[p_0 + \left(\frac{1255}{T} + 0.05 \right) - B \cot^2(\varepsilon) \right] + \delta_R,\tag{3.38}$$

already including a simple mapping function $\frac{1}{\sin(\varepsilon)}$. The parameters B and δ_R are correction quantities obtained from tables provided in SAASTAMOINEN (1972). Later, SAASTAMOINEN (1973) suggested a further correction factor

$$1 + 0.0026 \cos(2\phi) - 0.28 \cdot 10^{-6} h_0,\tag{3.39}$$

which is very similar to the denominator of the modified model in Eq. (3.37). Both models are used frequently, but in the traditional VLBI data analysis it is common practice to use the modified Saastamoinen model proposed by DAVIS et al. (1985).

3.3.2 Wet Delay

The propagation delay due to the wet refractivity, in the following referred to as zenith wet delay (ZWD), consists of the remaining two terms in Eq. (3.23):

$$\Delta L_w^z = \int_{h_0}^{\infty} \left(k_2' \frac{e}{T} Z_w^{-1} + k_3 \frac{e}{T^2} Z_w^{-1} \right) ds.\tag{3.40}$$

Compared to the hydrostatic delay, modeling the wet delay is by far more challenging since the amount and the distribution of water vapor in the atmosphere underlies huge variations in both spatial and temporal scales and is therefore unpredictable (ELGERED 1982). Further, the partial pressure e measured at the Earth's surface is not representative for the overlying atmosphere.

Nonetheless, several models have been developed for the wet delay (e.g., HOPFIELD 1969, SAASTAMOINEN 1972, MENDES 1999 or THOMPSON et al. 2001). Most of these models, however, require information about the water vapor distribution in the atmosphere in any form, and consequently, are not suitable for high accuracy applications. Thus, in general VLBI analysis, the wet delays are estimated within the parameter estimation process (see Sec. 2.2).

Wet Delay and Water Vapor Content

The description of the zenith wet delay can be directly related to the water vapor content in the neutral part of the atmosphere. In order to quantify the water vapor content in the atmosphere, the total amount of the water vapor in a vertical water column over a given unit of area (for instance, one square meter) is used, which is referred to as integrated water vapor (IWV) in the following,

$$IWV = \int \rho_{wv} dh, \tag{3.41}$$

where ρ_{wv} is the density of the water vapor. Scaling the IWV by the density of liquid water ρ_{lw} leads to the so-called precipitable water (PW),

$$PW = \frac{IWV}{\rho_{lw}}. \tag{3.42}$$

Since $\rho_{lw} \approx 1 \frac{g}{mm^3}$ the integrated water vapor and the precipitable water are almost identical. Using the ideal gas law the precipitable water can be directly related to the zenith wet delay by

$$PW = \kappa \Delta L_w^z, \tag{3.43}$$

with $\kappa = \frac{\Pi}{\rho_{lw}} \approx 0.16$. The proportionality factor Π is given by

$$\Pi = \frac{10^6 M_w}{\left(k_2' + \frac{k_3}{T_m}\right) R}, \tag{3.44}$$

with k_2' and k_3 being constants. R is the general gas constant and T_m describes the weighted mean temperature of the atmosphere. Although T_m is not known exactly, Bevis et al. (1992) proposed a linear relation between the weighted mean temperature and the surface temperature T_s,

$$T_m = 70.2 + 0.72 T_s, \tag{3.45}$$

empirically derived from radiosonde profiles from 13 stations in the United States. The error introduced by using this empirical formula is expected by the authors to be about 2%. A more detailed description on the relation between the zenith wet delay and the water vapor content, including the corresponding constants used in this section can be found in Bevis et al. (1992), Bevis et al. (1994) and Böhm (2004, pp 41f).

3.3.3   Impact of Meteorological Data on the Zenith Delay Determination

As described in Sec. 3.3.1, the zenith hydrostatic can be modeled sufficiently using adequate models mainly depending on the air pressure with only little variation proportional to the pressure variations. As a consequence, the quality of meteorological data is very important, because erroneous values directly impact the quality of the geodetic VLBI data analysis. Deficiencies in the hydrostatic calibrations are absorbed by the zenith wet delay estimates to almost 100 %, which, in turn influences the parameter estimation process in the data analysis.

Janes et al. (1991) investigated the influence of the uncertainty of meteorological data measurements on the tropospheric delay model of GPS, which is identical to the VLBI case. Based on a

ray-tracing algorithm they found that under nominal conditions (relative humidity of 75 %, temperature of 0-30 $°C$) the zenith delay sensitivity to surface pressure is about 1 mm per 0.5 hPa. According to ELGERED (1992), a variation of 1 hPa in the surface pressure corresponds to a change in the tropospheric propagation delay of VLBI observations of about 2.3 mm, which follows directly from the hydrostatic delay model of DAVIS et al. (1985) and fits very well the results obtained for GPS. SCHÜLER et al. (2000) indicate the accuracy of a barometer sensor to be of the order of magnitude of about 0.5 hPa or less, which would conversely corresponds to 1 mm in the hydrostatic calibrations.

Consequently, the on-site meteorological data recorded in the vgosDB data files (the new data format to store data obtained from VLBI observations; BOLOTIN et al. 2016) or the former Mark III database format (see, e.g., GIPSON 2012) needs to be homogeneous, which, however, is hardly true in reality since outliers and data gaps may occur due to sensor failures during the in-situ measurements at the VLBI sites. Comparing the pressure data found in the Mark III database format with pressure values from a numerical weather model of the European Centre for Medium-Range Weather Forecast (ECMWF) during the continuous VLBI campaign 2008 (CONT08), LE BAIL and GIPSON (2011) found a maximum offset of about 10 hPa for the VLBI station in Svetloe, Russia, over this period. Thus, an homogenization of the observed meteorological data is of utmost importance in order to not distort the VLBI target parameters (cf., HEINKELMANN et al. 2007). This includes the detection of outliers using statistical tests and the identification of inhomogeneities compared to other meteorological data sets on the one hand, and the correction of the affected measurements by more appropriate data sources on the other hand.

In this context, it is also worth mentioning, that the so-called tropospheric ties between either the VLBI or GNSS reference point and the barometer or two adjacent VLBI or GNSS antennas have to be introduced to correct for the height differences between two co-located antennas (see, Sec. 6.4.1 or TEKE et al. 2013). An incorrect height difference would directly influence the surface pressure according to Eq. (6.2) and, consequently, lead to a change in the tropospheric propagation delay, as discussed above.

3.3.4 Mapping Functions

As mentioned above, the total signal propagation delay is divided into a hydrostatic and a wet delay, and both components consist of a zenith delay correction and a corresponding elevation-dependent mapping function. This model is described by Eq. (3.25) under the assumption of azimuthal symmetry of the neutral atmosphere around a station. In other words, this means that for a constant elevation angle the propagation delay is independent from the azimuth angle of the observation. Since the bending effect in Eq. (3.18) is accounted for by the hydrostatic mapping function, the (geometric) elevation angle in vacuum has to be used as input for the mapping functions instead of the refracted elevation angle.

According to NIELL (2000), the mapping functions are defined as the ratio between the electrical path length L through the atmosphere at elevation ε and the electrical path length in zenith direction. Comparing the mapping functions for the hydrostatic and wet component, respectively, the hydrostatic mapping function is smaller than the wet mapping function, except for observations at very low elevation angles, where the geometric bending effect attributed to the hydrostatic mapping function is increasing considerably (BÖHM 2004). The reason is the smaller scale height H for the wet part of the atmosphere ($H \approx 2\ km$) compared to the hydrostatic component ($H \approx 8\ km$).

Thus, the mapping functions can be interpreted as a measure for the thickness of the Earth's atmosphere compared to the Earth's radius (NIELL 2000). If the thickness of the atmosphere decreases, the atmosphere appears to be flatter. Assuming the atmosphere to be planar and evenly stratified, the mapping function can be formulated as

$$mf(\varepsilon) = \frac{1}{\sin(\varepsilon)}. \tag{3.46}$$

This simple approach was used by SAASTAMOINEN (1972), which, however, is only sufficient for observations with high elevation ($\varepsilon > 20°$). MARINI (1972) found that the continued fraction form

$$mf(\varepsilon) = \frac{1}{\sin(\varepsilon) + \dfrac{a}{\sin(\varepsilon) + \frac{b}{\sin(\varepsilon) + c}}} \tag{3.47}$$

could be used to consider corrections accounting for the Earth's curvature, where a, b and c are constants. During the last decades, many approaches were developed, which are generally slightly modified versions of the continued fraction form using constants from analytic fits to ray-tracing either for a defined standard atmosphere, for observed atmospheric profiles based on radiosonde measurements, or numerical weather models. In the following, a short overview of the different mapping function is given.

The first mapping function for space-geodetic applications with different coefficients for both mapping functions was published by CHAO (1971) who truncated the continued fraction form to a representation with two coefficients a and b and replaced the second $\sin(\varepsilon)$ by $\tan(\varepsilon)$ in order to force $mf(\varepsilon) = 1$ at the zenith. DAVIS et al. (1985) developed the mapping function CfA-2.2 for the hydrostatic delay down to 5° elevation. The three constants a, b, and c of the continued fraction form were derived from a ray-tracing analysis through idealized model atmospheres. HERRING (1992) introduced the mapping function MTT, for which radiosonde data were used instead of standard atmospheres to fit the coefficients of the slightly modified continued fraction form

$$mf(\varepsilon) = \frac{1 + \dfrac{a}{1 + \frac{b}{1 + c}}}{\sin(\varepsilon) + \dfrac{a}{\sin(\varepsilon) + \frac{b}{\sin(\varepsilon) + c}}}. \tag{3.48}$$

The coefficients in the mapping functions depend on the latitude and height of the site and the surface temperature, and were determined by a least squares fitting performed separately for the hydrostatic and wet component. The new mapping functions developed by NIELL (1996) (often called Niell mapping functions, NMF) are unique in that global weather variations are represented analytically as a function of station latitude and height as well as the day of year instead of meteorological parameters at the sites. The coefficients in the mapping functions were derived from profiles of standard atmosphere data down to 3° elevation angle using the continued fraction form in Eq. (3.48). Further, sine functions are introduced to describe the temporal variation of the coefficients, and a height correction describing the increase of the mapping function with increasing height was used for the hydrostatic mapping function. The first mapping functions based on numerical weather models were the isobaric mapping functions (IMF) developed by NIELL (2000). For the coefficients b and c empirical functions are used, whereas the coefficient a is determined from re-analysis data of the Data Assimilation Office (DAO) of the Goddard Space Flight Center. At present the most accurate mapping functions that are available globally are the Vienna mapping functions 1 (VMF1, BÖHM et al. 2006B) which are based on a direct ray-tracing through the numerical weather model to make use of the entire model information provided instead of calculating

intermediate parameters as necessary in the IMF. The coefficients a and b for both the hydrostatic and wet VMF1 are determined from empirical equations depending on the day of year and station latitude, whereas the a coefficients for both components are obtained based on different pressure level data sets from the ECMWF. The VMF1 is realized as discrete time series with 6 h resolution either on a global grid or for specific VLBI sites. Further, Böhm et al. (2006b) introduced the alternative approach of the so-called total Vienna Mapping Function 1 (VMF1-T) for a mapping of the total delays instead of separating the delays into a hydrostatic and a wet component. The principle idea was to introduce a mapping function which is not affected by poor a priori hydrostatic delays, because errors in the a priori model would not be fully compensated by the estimated wet part (cf. discussion in Sec. 3.3.3). However, this concept is not recommended since variations in the wet delay are faster than they could be described by the coefficients with a 6 h resolution (Nilsson et al. 2013). Böhm et al. (2006a) proposed the Global Mapping Function (GMF) to create, on the one hand, an easy-to-handle mapping function depending only on the day of year and station latitude, longitude and height, which, on the other hand, is consistent with VMF1 (Tesmer et al. 2007). The GMF is based on monthly mean profiles of meteorological data from the ECMWF 40-years reanalysis data (ERA-40).

For a more detailed description on mapping functions, the reader is referred to Mendes (1999), Nothnagel (2000), Böhm (2004), Tesmer et al. (2007), Böhm et al. (2007a) or Nilsson et al. (2013).

3.3.5 Atmospheric Gradients

In this chapter, the atmosphere has been assumed to satisfy the condition of azimuthal symmetry around a station so far, which, however, is limited. On the one hand, this can be due to different local weather phenomena and climatic conditions. On the other hand, the vertical thickness of the neutral atmosphere is larger above the equator compared to the poles. Thus, it is recommended to take azimuthal asymmetry into account (Davis et al. 1993; MacMillan 1995; MacMillan and Ma 1997).

The gradient model described in the following was first proposed by Davis et al. (1993) and later modified by MacMillan (1995). To model the azimuthal asymmetry of the neutral atmosphere around a station, horizontal refractivity variations (i.e., the derivation of linear horizontal gradients) are described. The first degree Taylor series approximation of the refractivity at a station is

$$N(\boldsymbol{x}, z) = N_0(z) + \boldsymbol{\xi}(z)\boldsymbol{x}, \tag{3.49}$$

where $N_0(z)$ describes the refractivity above the station, $\boldsymbol{x}$ is the horizontal position vector and the horizontal linear gradient of the refractivity can be expressed as

$$\xi_i(z) = \left.\frac{\partial N(\boldsymbol{x}, z)}{\partial x_{i=n,e}}\right|_{\boldsymbol{x}=0} \tag{3.50}$$

with $x_{i=n,e}$ being the north and east component of the position vector, respectively. Integrating Eq. (3.49) along the path s yields the propagation delay in an arbitrary direction, which can be described by elevation ε and azimuth angle α:

$$
\begin{aligned}
\Delta L(\alpha, \varepsilon) &= 10^{-6} \int_0^\infty N(s) ds \\
&= 10^{-6} \left[\int_0^\infty N_0(z) ds + \int_0^\infty \boldsymbol{\xi}(z) \boldsymbol{x} ds \right] \\
&= \Delta L(\varepsilon) + 10^{-6} \int_0^\infty \boldsymbol{\xi}(z) \boldsymbol{x} ds,
\end{aligned}
\tag{3.51}
$$

where $\Delta L(\varepsilon)$ is the propagation delay for azimuthal symmetry of the atmosphere as defined in Eq. (3.25). It should be noted that the difference in the integration paths for the gradient and no-gradient cases is neglected in Eq. (3.51). For a more detailed discussion about the influence of this assumption, the reader is referred to DAVIS et al. (1993).

Similar to Eq. (3.25), the concept of a mapping function is introduced, and the path delay $\Delta L(\alpha, \varepsilon)$ can be again expressed as a combination of the zenith propagation delay ΔL^z and a corresponding elevation- and azimuth-dependent mapping function $mf(\alpha, \varepsilon)$,

$$
\Delta L(\alpha, \varepsilon) = \Delta L^z mf(\alpha, \varepsilon),
\tag{3.52}
$$

with

$$
\begin{aligned}
mf(\alpha, \varepsilon) &= mf_0(\alpha, \varepsilon) + \delta mf(\alpha, \varepsilon) \\
&= mf_0(\alpha, \varepsilon) + 10^{-6} \int_0^\infty \boldsymbol{\zeta}(z) \boldsymbol{x} ds
\end{aligned}
\tag{3.53}
$$

and

$$
\boldsymbol{\zeta}(z) = \frac{\boldsymbol{\xi}(z)}{\Delta L^z}.
\tag{3.54}
$$

Consequently, the gradients lead to a modification of the mapping function described in the additional term $\delta mf(\alpha, \varepsilon)$, which can be determined using the following relations (DAVIS et al. 1993)

$$
\begin{aligned}
x(\alpha, \varepsilon) &\approx z \cot(\hat{\varepsilon}) \left[\cos(\alpha) \hat{\boldsymbol{n}} + \sin(\alpha) \hat{\boldsymbol{e}} \right], \tag{3.55} \\
\boldsymbol{\zeta}(z) &= \zeta_n \hat{\boldsymbol{n}} + \zeta_e \hat{\boldsymbol{e}}, \tag{3.56} \\
ds &\approx dz \; mf_0(\varepsilon), \tag{3.57}
\end{aligned}
$$

where $\hat{\varepsilon}$, $\hat{\boldsymbol{n}}$ and $\hat{\boldsymbol{e}}$ denote the refracted elevation angle, the unit vectors in north and east direction, respectively:

$$
\begin{aligned}
\delta mf(\alpha, \varepsilon) &\approx 10^{-6} mf_0(\varepsilon) \cot(\hat{\varepsilon}) \left[\cos(\alpha) \int_0^\infty z \zeta_n(z) dz + \sin(\alpha) \int_0^\infty z \zeta_e(z) dz \right] \\
&= mf_0(\varepsilon) \cot(\hat{\varepsilon}) \left[Z_n \cos(\alpha) + Z_e \sin(\alpha) \right]
\end{aligned}
\tag{3.58}
$$

with

$$
\boldsymbol{Z} = 10^{-6} \int_0^\infty z \boldsymbol{\zeta}(z) dz.
\tag{3.59}
$$

As already discussed in Sec. 3.3.4, the general concept of mapping functions is related to the elevation angle in vacuum. In the gradient case, the mapping function $\delta mf(\alpha, \varepsilon)$ also includes

another term $\cot(\hat{\varepsilon})$ which depends on the refracted elevation angle $\hat{\varepsilon}$. A general relation between both elevation angles is defined by

$$\hat{\varepsilon} = \varepsilon + \delta\varepsilon, \tag{3.60}$$

and DAVIS et al. (1993) suggested the approximation

$$\delta\varepsilon \approx \varepsilon 10^{-6} N_{es} \cot(\varepsilon), \tag{3.61}$$

where N_{es} defines the total refractivity at the Earth's surface. Assuming $\delta\varepsilon$ to be small ($\delta\varepsilon \approx 0.2°$ for $N_{es} \approx 300$ and $\varepsilon = 5°$; according to DAVIS et al. 1993), the term $\cot(\hat{\varepsilon})$ can be expanded into a series, leading to

$$\delta mf(\alpha, \varepsilon) \approx mf_0(\varepsilon) \cot(\varepsilon) \left(1 - 10^{-6} N_{es} \csc^2(\varepsilon)\right) [Z_n \cos(\alpha) + Z_e \sin(\alpha)]. \tag{3.62}$$

Finally, Eq. (3.51) becomes

$$\Delta L(\alpha, \varepsilon) = \Delta L(\varepsilon) + mf_0(\varepsilon) \cot(\varepsilon) \left(1 - 10^{-6} N_{es} \csc^2(\varepsilon)\right) [G_n \cos(\alpha) + G_e \sin(\alpha)], \tag{3.63}$$

where the gradients for the north and east direction, G_n and G_e, respectively, are given by

$$\boldsymbol{G} = \boldsymbol{Z}\Delta L^z. \tag{3.64}$$

MACMILLAN (1995) uses the model of DAVIS et al. (1993) as in Eq. (3.63), but neglected the difference between the geometrical elevation in vacuum ε and the refracted elevation angle $\hat{\varepsilon}$ and published the modified model for the propagation delay through an azimuthal asymmetric atmosphere as

$$\begin{aligned} \Delta L(\alpha, \varepsilon) &= \Delta L(\varepsilon) + mf_h(\varepsilon) \cot(\varepsilon) [G_n \cos(\alpha) + G_e \sin(\alpha)], \\ &= mf_h(\varepsilon)\Delta L_h^z + mf_w(\varepsilon)\Delta L_w^z + mf_h(\varepsilon) \cot(\varepsilon) [G_n \cos(\alpha) + G_e \sin(\alpha)], \end{aligned} \tag{3.65}$$

which is currently the standard in the data analysis of the International VLBI Service for Geodesy and Astrometry (IVS).

As an alternative concept to describe atmospheric gradients, CHEN and HERRING (1997) proposed the model

$$\Delta L(\alpha, \varepsilon) = \Delta L(\varepsilon) + mf_G(\varepsilon)G_n \cos(a) + mf_G(\varepsilon)G_e \sin(a), \tag{3.66}$$

where

$$mf_G = \frac{1}{\sin(\varepsilon)\tan(\varepsilon) + C}, \tag{3.67}$$

$$C = \frac{3 \int \xi h^2 dh}{2 \int \xi h(h + R_e)dh}, \tag{3.68}$$

and R_e is the radius of the Earth. The coefficient C can be determined to 0.0031 and 0.0007 for the hydrostatic and wet part, respectively (CHEN and HERRING 1997). When applying this model, the IVS community agreed to use $C = 0.0032$ as recommended by HERRING (1992) for the estimation of total gradients.
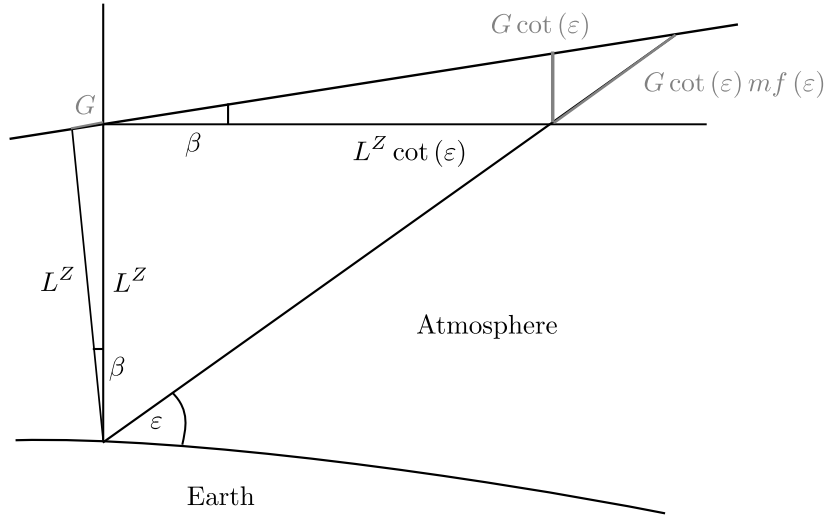
Figure 3.2: Gradients interpreted by a tilting of the mapping function by the angle β, according to Nilsson et al. (2013)

.

According to Rothacher et al. (1998), atmospheric gradients can be interpreted as a tilting of the mapping function if the atmosphere is assumed to be evenly stratified, which yields to a simple mapping function ($\frac{1}{\sin(\varepsilon)}$, cf. Eq. 3.46), and the zenith propagation delay is independent of the tilting of the mapping function. If G defines the deflection of the path delay caused by the tilting angle β (see Fig. 3.2), it can be shown that the additional path delay at elevation ε due to the gradient equals $\cot(\varepsilon)\, mf(\varepsilon)\, G$, which leads to the relationship

$$\Delta L(\varepsilon - \beta) = \Delta L^z mf(\varepsilon) + \cot(\varepsilon)mf(\varepsilon)G. \tag{3.69}$$

In general, it is recommended to estimate gradients within the VLBI parameter estimation process, particularly when observing at low elevation angles (Nilsson et al. 2013). On local VLBI networks consisting of baseline lengths of a few hundred meters, as is the case for the WHISP (Wettzell HIgh SPeed) experiments (see Ch. 6), this is, however, not true since short baselines are not sensitive to atmospheric gradients.

3.3.6   Discussion of the Current Atmosphere Model

In the current data analysis of the IVS, the model in Eq. (3.65) is used to consider the additional propagation delay due to the neutral atmosphere. The hydrostatic component can be taken into account with sufficient precision using suitable models and measured pressure values at the VLBI sites as described in Sec. 3.3.1, while the wet component is more challenging due to the highly variable water vapor content in the atmosphere. As already described in Sec. 3.3.2, the zenith wet delays are routinely estimated as continuous piece-wise linear functions (CPWLF) in the geodetic VLBI data analysis (see Sec. 2.2).

The tropospheric model, however, reveals some deficiencies. The mapping functions are not optimal since the numerical weather models are rather coarse with a temporal resolution of only six hours

(BÖHM et al. 2006A). Of course, it would be desirable to obtain atmospheric delays directly in slant direction, which would completely eliminate the mapping function as additional uncertainty source, which, however, is only possible with a clearly increased number of observations. The piece-wise linear representation is generally not optimal, since the highly dynamic nature of the atmosphere can only be modeled to a limited extent. Further, constraints are often needed to stabilize the solution due to missing observations in some piece-wise linear segments. A similar situation applies to the atmospheric gradients, since the estimation of the model coefficients heavily depends on observations at low elevation angles and constraints are often necessary to stabilize the solution. Additionally, the results of the parameter estimation procedure are very sensitive to a priori gradients and may lead to a tilt of the terrestrial reference frame estimates by up to a few millimeters (TESMER et al. 2006).

In the current atmospheric propagation delay model only long-periodic variations are taken into account, although micro-scale phenomena also play a very crucial role. Since turbulence-induced variations in the refractivity induce phase fluctuations, they form a serious error source for electromagnetic wave propagation and represent a major deficiency in the current atmospheric model. At the same time, physically-induced correlations in space and time occur between the observations, which are generally neglected. Both issues will be addressed in more detail in Ch. 4 on atmospheric turbulence.

4. Atmospheric Turbulence

The propagation delay for electromagnetic waves in the neutral atmosphere is described in Sec. 3.1 and the tropospheric model for space-geodetic observations is defined by Eq. (3.65) in Sec. 3.3. Here, only long-periodic from annual to hourly variations are taken into account, while short-periodic fluctuations due to variations in the refractive index are largely ignored. However, with respect to the steadily increasing requirements to the target parameters of space-geodetic techniques, such as Earth orientation parameters and coordinates of telescopes or radio sources, it is not sufficient to neglect refractivity fluctuations since they induce phase fluctuations and form a serious error source for electromagnetic wave propagation. Refractivity variations are primarily induced by turbulent motions or swirls in the neutral atmosphere and can be best described stochastically following the widely accepted turbulence theory of Kolmogorov.
An introduction to Kolmogorov's theory on atmospheric turbulence is given in Sec. 4.1, followed by Sec. 4.2 providing an overview on statistical strategies to characterize high-frequency fluctuations in a random medium. Finally, atmospheric turbulence models are outlined in Sec. 4.3, which stochastically describe refractivity fluctuations and introduce physical correlations between the observations due to turbulent irregularities.

4.1 Turbulence Theory

Short-periodic refractivity fluctuations are induced by dynamic processes in the neutral atmosphere and can be represented as the interaction or superposition of turbulent swirls, so-called eddies, of different length scales ranging between millimeters and kilometers depending on the altitude (Wheelon 2004; Kermarrec and Schön 2014). Since atmospheric turbulence has different scales, which occur simultaneously, it is not possible to describe the behavior of each eddy individually. Consequently, turbulence-induced refractivity irregularities are generally regarded as randomly varying in space and time and, thus, have to be described stochastically (Ishimaru 1991).

In order to receive a mathematical description of a random medium, such as the refractive index n, it is separated into two components $n = \bar{n} + \Delta n$ ("Reynolds decomposition", Tatarskii 1971). On the one hand, $\bar{n}$ defines a deterministic part and describes a slowly varying, mean component, while, on the other hand, Δn is characterized by rapid fluctuations assigned to turbulence. The phenomena described by Δn can be defined as an arbitrary flow pattern characterized by its size (Batchelor 1950) and are, therefore, of stochastic nature. According to Wheelon (2004, p. 83), the shape and size of the turbulent eddies depend on the altitude. While the eddies are assumed to be small and almost symmetrical in the atmospheric boundary layer, the lowest part of the atmosphere at heights between 0 and 2 km, they become more flattened in horizontal direction in the free atmosphere at altitudes greater than 1 km, and thus, are highly anisotropic (see Fig. 4.1). The isotropic microscale structures correspond to 3D turbulence. In contrast, the larger scales in the free atmosphere are referred to as 2D turbulence (Schön and Kermarrec 2015, pp 1301ff), which is more relevant in the context of this thesis, particularly in creating correlations between VLBI observations.

Turbulent processes are often illustrated by the energy cascade theory (Kolmogorov 1941a), depicted in Fig. 4.2, which describes the variability of the eddies and provides information on the
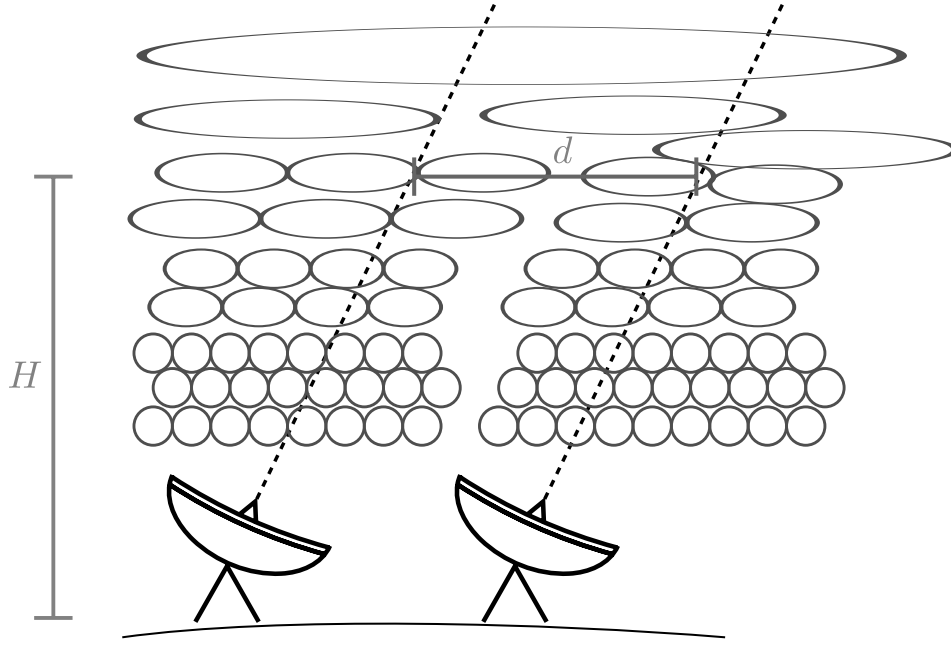
Figure 4.1: Eddy size and flattening with height. The distance d denotes the separation of the ray paths of the radio signal at height H, referred to as the effective tropospheric height. Both are introduced the following sections (HALSIG et al. 2016A).

amount of turbulent energy with respect to the eddy scale l and the size of the wavenumber κ, respectively. Small eddies correspond to large wavenumbers and, consequently, large eddies are represented by small wavenumbers, or mathematically,

$$\kappa = \frac{2\pi}{l}. \tag{4.1}$$

The model consists of three regimes: the energy injection region, the inertial subrange and the energy dissipation region. At large scales, atmospheric turbulence occurs when a small fraction of the kinetic energy in the ambient wind field is converted into turbulent energy producing initial inhomogeneities (energy injection). Large eddies with highly elongated shape and a considerable amount of kinetic energy are created. The initial size of the eddies is called the outer scale length L_0. These eddies are not stable and immediately begin to break up and subsequently transfer their energy to turbulent elements of smaller and smaller scale (energy cascade), although energy is neither created nor dissipated. The size of the eddies reduces and their shape becomes more and more symmetrical (inertial subrange). The redistribution during the decay cascade continues until the eddy size is approximately equal to the inner length scale l_0, at which their remaining energy is dissipated into heat (energy dissipation). For more details, the reader is referred to WHEELON (2004, pp 27ff) and SCHÖN and KERMARREC (2015, pp 1306ff).
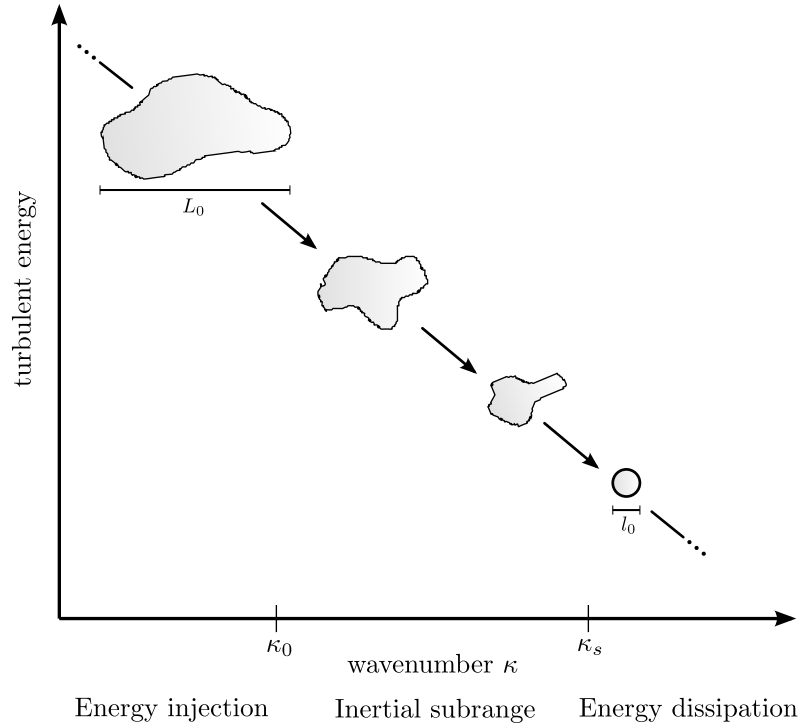
Figure 4.2: The energy cascade model of Kolmogorov describes the process of turbulent decay. As soon as the turbulent eddies are created with an initial size called the outer scale length L_0, they break up into smaller and more symmetric eddies until the eddy size is approximately equal to the inner length scale l_0 and their energy is dissipated into heat. The corresponding wavenumbers to the outer and inner scale length L_0 and l_0 are represented by κ_0 and κ_s, respectively (HALSIG et al. 2016A).

4.2 Turbulence Description

Since high-frequency refractivity variations due to turbulence can be best described stochastically, statistical approaches are necessary to characterize fluctuations in a random medium. First, the temporal behavior of the random process is discussed. Generally, time series of quantities to describe atmospheric turbulence, such as the refractive index n, are not stationary. A process is defined to be stationary (SCHÖN and KERMARREC 2015, p. 1311), if its properties do not vary with time. Therefore, such a random process is separated into two components $n = \bar{n} + \Delta n$, where Δn defines a turbulent or fluctuating component and $\bar{n}$ represents a slowly varying mean component. Although $\bar{n}(t)$ is time dependent (with t denoting the time), the difference $\bar{n}(t+\tau) - \bar{n}(t)$ satisfies the conditions for a stationary process over a large range of time increments τ. Such a process is referred to as a process with stationary increment (SCHÖN and KERMARREC 2015, pp. 1311f), and leads to the definition of the so-called structure function

$$\mathcal{D}_n(\tau) = \langle [\Delta n(t+\tau) - \Delta n(t)]^2 \rangle, \tag{4.2}$$

where $\langle \ldots \rangle$ denotes the ensemble average. In this context, an ensemble is defined as all possible configurations of the random medium. Alternatively, the structure function can also be written by a time-shifted phase covariance expression

$$\mathcal{C}_n\left(t, t+\tau\right) = \langle \Delta n(t) \Delta n(t+\tau) \rangle. \tag{4.3}$$

Similar to the time domain, a random process can also be characterized in a spatial sense. Given two antennas operating at two (adjacent) positions $\boldsymbol{r}_1$ and $\boldsymbol{r}_2$, which are separated by distance $\boldsymbol{d}$ in a random medium, the similarity of a random process in a spatial sense can be described by the spatial covariance function:

$$\mathcal{C}_n\left(\boldsymbol{r}_1, \boldsymbol{r}_2\right) = \langle \Delta n(\boldsymbol{r}_1, t) \Delta n(\boldsymbol{r}_2, t) \rangle. \tag{4.4}$$

In general, the atmosphere is assumed to be homogeneous and isotropic. A stochastic process is defined to be homogeneous if the covariance function does not depend on the positions $\boldsymbol{r}_1$ and $\boldsymbol{r}_2$ but solely on the baseline $\boldsymbol{d}$ separating these positions (WHEELON 2004, pp 15ff). Consequently, homogeneity can be interpreted as the spatial analogy of the stationarity in the time domain. Further, a medium is also defined as isotropic, if the vertical scale is the same as both horizontal scales, i.e., the covariance function only depends on the magnitude of the baseline, not on its orientation (WHEELON 2004, p. 15ff). Including both assumptions, Eq. (4.4) becomes

$$\mathcal{C}_n\left(\boldsymbol{d}\right) = \langle \Delta n(\boldsymbol{r}, t) \Delta n(\boldsymbol{r} + \boldsymbol{d}, t) \rangle. \tag{4.5}$$

Equivalent to the time domain, TATARSKII (1971) defines the atmosphere to be a "locally homogeneous random medium with smoothly varying characteristics" leading again to a separation of the random medium into a varying mean and a rapidly changing fluctuating component. Thus, the slowly varying term is canceled out by taking the difference and assuming a sufficient similarity for both positions $\boldsymbol{r}_1$ and $\boldsymbol{r}_2$, yielding the structure function description:

$$\mathcal{D}_n\left(\boldsymbol{d}\right) = \langle [\Delta n(\boldsymbol{r}, t) - \Delta n(\boldsymbol{r} + \boldsymbol{d}, t)]^2 \rangle. \tag{4.6}$$

By dimensional analysis, KOLMOGOROV (1941A) found a power law dependency for the structure function

$$\mathcal{D}_n\left(\boldsymbol{d}\right) = C_n^2 \boldsymbol{d}^{\frac{2}{3}}, \tag{4.7}$$

where C_n^2 represents the so-called structure constant as a general measure for the strength of turbulence. The widely-spread two-third power law is successfully experimentally applicable to a surprisingly wide range of conditions, and sometimes even works for cases in which the turbulent medium cannot be expected to either be isotropic nor homogeneous (WHEELON 2004, p. 31). Here, the power law process is used to describe spatial correlations, however, the same power law dependency holds for the temporal case.

In Fig. 4.3, the general behavior of a temporal structure functions is illustrated as a typical log-log-plot. Here, the structure functions can be represented as straight lines with different slopes, which are equal to the specific exponents of the power law processes (SCHÖN and BRUNNER 2006). The general behavior of the structure function can be divided into three components. The curve is flat with a corresponding power law exponent close to zero for very short time differences of a few seconds (A). For slightly larger time differences turbulent fluctuations become the dominant
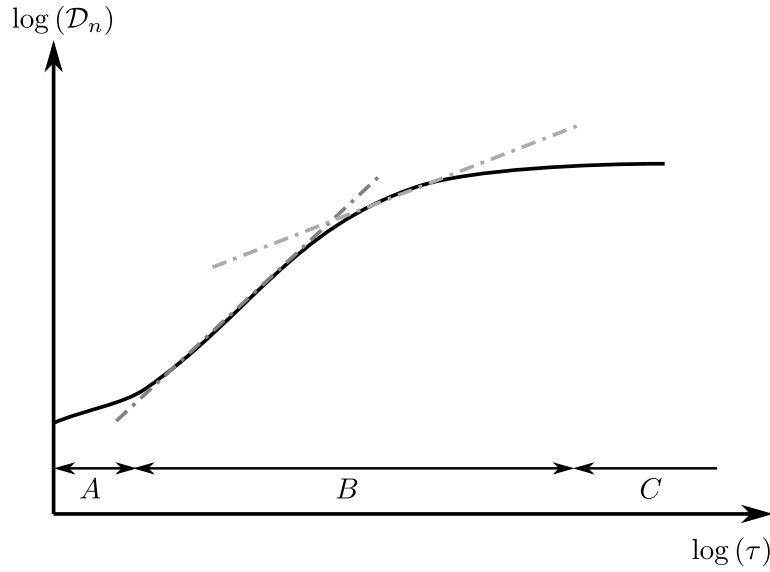
Figure 4.3: General behavior of a (temporal) structure function illustrated as a typical log-log-plot. The green and red dotted line correspond to the typical 2/3 and 5/3 power law exponents; modified according to SCHÖN and BRUNNER (2006).

effect (B). In the log-log-plot, the characteristic exponents of 2/3 (2D turbulence; green dotted line) and 5/3 (3D turbulence; red dotted line) occur. Finally, the structure functions becomes flat again with a power law exponent close of zero (C), indicating that the quantities describing atmospheric turbulence, such as the refractive index n, are uncorrelated (SCHÖN and BRUNNER 2006). For a more detailed description on the power law relations for atmospheric turbulence, the reader is referred to, e.g., THOMPSON et al. (2001).

Up to now, the structure and covariance function representation have been used in this section to either describe temporal or spatial variations in the refractive index. Another possibility to describe temporal variations in a random medium is given by the widely known frozen flow hypothesis of TAYLOR (1938). It postulates that the entirety of turbulent air mass is frozen during the observing period and transported horizontally at a constant wind velocity v without any deformation. As a consequence, the motion of the entire turbulence mass is equivalent to a parallel shifting of the ray path (see Fig. 4.4). Mathematically, it is assumed that

$$\Delta n(\boldsymbol{r}, t + \tau) = \Delta n(\boldsymbol{r} - \boldsymbol{v}\tau, t). \tag{4.8}$$

Thus, the temporal structure function at time t and $t + \tau$ can be interpreted as a spatial structure function between these rays separated by $\boldsymbol{d} = \boldsymbol{v}\tau$ (WHEELON 2004, pp 242ff).

The covariance function of refractivity fluctuations in a random medium can also be formulated as a Fourier wavenumber integral of the turbulence spectrum (WHEELON 2004, p 21),

$$\mathcal{C}_n(\boldsymbol{r}_1, \boldsymbol{r}_2) = \int_0^\infty \int_0^\infty \int_0^\infty \Phi_n(\boldsymbol{\kappa}) \left\{ e^{i\boldsymbol{\kappa}(\boldsymbol{r}_1 - \boldsymbol{r}_2)} \right\} d^3\kappa. \tag{4.9}$$
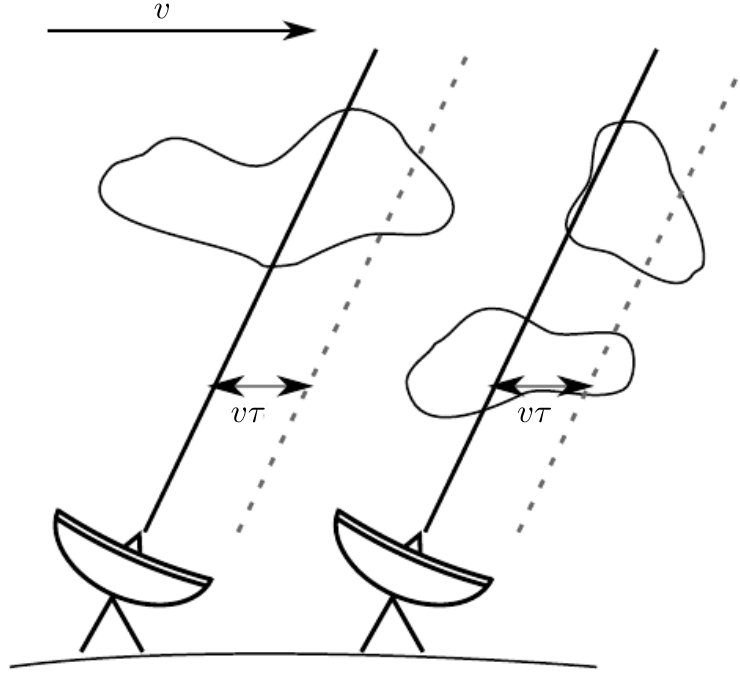
Figure 4.4: Taylor's frozen flow hypothesis assumes the entirety of turbulent medium to be frozen during the observing period τ and traveling in the direction, in which the wind blows with a constant velocity $\boldsymbol{v}$. The motion of the entire turbulence mass is equivalent to a parallel shifting of the ray path (HALSIG et al. 2016A).

Using a three-dimensional Fourier transform, a similar expression can be found for the structure function of refractivity fluctuations (WHEELON 2004, p 25f),

$$
\mathcal{D}_n\left(\boldsymbol{r}_1, \boldsymbol{r}_2\right) = 2 \int\limits_0^\infty \int\limits_0^\infty \int\limits_0^\infty \Phi_n(\boldsymbol{\kappa}) \left\{1 - e^{i\boldsymbol{\kappa}(\boldsymbol{r}_1 - \boldsymbol{r}_2)}\right\} d^3\kappa. \tag{4.10}
$$

In the wavenumber-spectrum representation the random medium is completely described by the turbulence spectrum $\Phi_n(\boldsymbol{\kappa})$ and the wavenumber vector $\boldsymbol{\kappa} = [\kappa_x, \kappa_y, \kappa_z]$. Assuming the random medium again to be homogeneous and isotropic, the structure function in Eq. (4.10) can be simplified to

$$
D_n(\boldsymbol{d}) = 8\pi \int_0^\infty \kappa^2 \Phi_n(\boldsymbol{\kappa}) \left(1 - \frac{\sin(\kappa d)}{\kappa d}\right) d\kappa. \tag{4.11}
$$

Since the energy spectrum should also follow a power law process, KOLMOGOROV (1941A) proposed the following turbulence spectrum

$$
\Phi_n(\kappa) = \frac{0.033 C_n^2}{\kappa^{\frac{11}{3}}}, \tag{4.12}
$$

which he found to be equivalent to his two-third power law (see Eq. 4.7) by solving the following integral equation (WHEELON 2004, p. 26f):

$$
C_n^2 \boldsymbol{d}^{\frac{2}{3}} = 8\pi \int_0^\infty \kappa^2 \Phi_n(\boldsymbol{\kappa}) \left(1 - \frac{\sin(\kappa d)}{\kappa d}\right) d\kappa. \tag{4.13}
$$

However, the Kolmogorov model leads to infinite values for some quantities like the mean square variations of the refractive index. To overcome this issue, the von Kármán spectrum (VON KÁRMÁN 1948)

$$\Phi_n(\boldsymbol{\kappa}) = \frac{0.033 C_n^2}{\left(\kappa_x^2 + \kappa_y^2 + \kappa_z^2 + \kappa_0^2\right)^{\frac{11}{6}}}, \tag{4.14}$$

can be applied. Both models are valid for the inertial subrange (indicated by (B) in Fig. 4.5) and the energy input region, $0 < \kappa < \kappa_s$ (where κ_0 and κ_s denote the corresponding wavenumber to the outer and inner scale length L_0 and l_0, respectively) and for a medium where isotropy and homogeneity are justified. The general power law behavior of the power spectra of refractivity fluctuations as proposed by Kolmogorov (black solid line) and von Kármán (dashed gray line) is shown in Fig. 4.5. The green dotted line refers to the typical $-11/3$ power law exponent which is equivalent to the two-third power law exponent for 2D turbulence in the structure function representation.
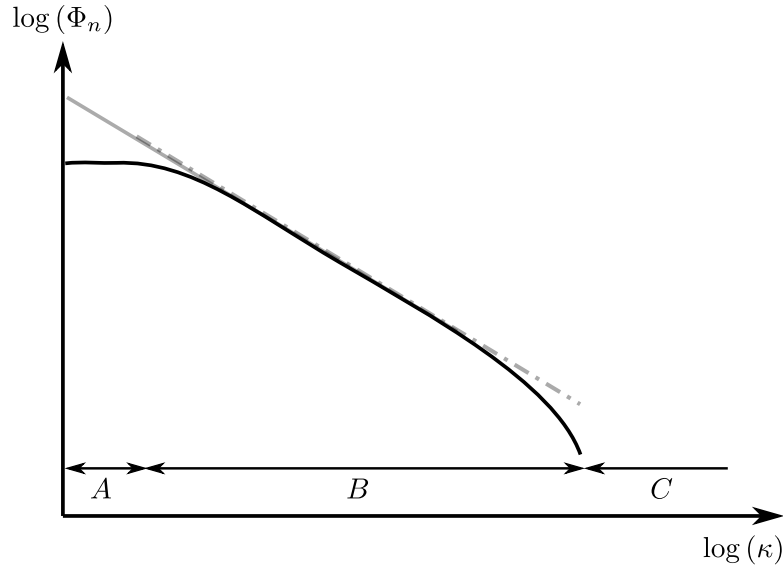
Figure 4.5: General power law behavior of the turbulent power spectrum of refractivity fluctuations. It is distinguished between the spectra proposed by Kolmogorov (black solid line) and von Kármán (dashed gray line). The green dotted line corresponds to the typical $-11/3$ power law exponent; modified according to (WHEELON 2004, pp. 32f).

For a general case of an inhomogeneous medium, the von Kármán model has to be extended. Since TATARSKII (1971) defined the atmosphere as a "locally homogeneous random medium with smoothly varying characteristics", we can again subdivide $\Phi_n(\boldsymbol{\kappa}, \frac{\boldsymbol{r}_1 + \boldsymbol{r}_2}{2})$ into a slowly varying component $\overline{\Phi}_n(\boldsymbol{\kappa})$ and a rapidly fluctuating term $C_n^2(\frac{\boldsymbol{r}_1 + \boldsymbol{r}_2}{2})$ (KERMARREC and SCHÖN 2014), yielding

$$\Phi_n(\boldsymbol{\kappa}, \frac{\boldsymbol{r}_1 + \boldsymbol{r}_2}{2}) = C_n^2(\frac{\boldsymbol{r}_1 + \boldsymbol{r}_2}{2})\overline{\Phi}_n(\boldsymbol{\kappa}). \tag{4.15}$$

To also take anisotropy into account, the so-called stretched wavenumber coordinates are introduced according to Wheelon (2004, pp. 42ff). The anisotropic scaling factors a, b and c describe the flattening of the eddies in both horizontal and the vertical direction, leading to

$$\Phi_n(\boldsymbol{\kappa}) = \frac{0.033C_n^2 abc}{\left(a^2\kappa_x^2 + b^2\kappa_y^2 + c^2\kappa_z^2 + \kappa_0^2\right)^{\frac{11}{6}}}. \tag{4.16}$$

Up to now, only fluctuations in the refractive index, particularly large horizontal flattened eddies in the free atmosphere, have been taken into account, which distort the arriving plane wave front of VLBI observations. Integrating these refractivity fluctuations along the line of sight leads to the signal phase variations. According to Wheelon (2004, p. 206), the corresponding phase covariance function can be formulated as

$$\mathcal{C}_\varphi = k^2 \int\limits_0^\infty ds_1 \int\limits_0^\infty ds_2 \int\limits_{-\infty}^\infty \int\limits_{-\infty}^\infty \int\limits_{-\infty}^\infty \kappa \Phi_n(\boldsymbol{\kappa}, \frac{\boldsymbol{r}_1 + \boldsymbol{r}_2}{2}) e^{i\boldsymbol{\kappa}(\boldsymbol{r}_1 + \boldsymbol{r}_2 - \boldsymbol{d})} d^3\kappa. \tag{4.17}$$

Based on Kolmogorov's turbulence theory described above, a few covariance models have been developed to model atmospheric turbulence, which will be briefly outlined in the following section.

4.3 Modeling Atmospheric Turbulence

Different modeling strategies have been developed following Kolmogorov's turbulence theory to either investigate and describe turbulent behavior of the neutral atmosphere or to simulate the variations in the refractive index to assess the quantity of turbulent motion in the atmosphere. In the following, three turbulent models are shortly described: first, the model of Treuhaft and Lanyi (1987), which has been the basis for several other studies on turbulence theory; second, the SIGMA-C approach (Schön and Brunner 2008a; Schön and Brunner 2008b) and, third, the turbulence model of Kermarrec and Schön (2014), which forms the basis for the turbulence model developed in the framework of this thesis (see Ch. 5).

4.3.1 The Treuhaft and Lanyi Model (1987)

The Treuhaft and Lanyi (1987) turbulence model was originally developed for VLBI observations and follows the general structure function description given in Eq. (4.6). The model is subject to a few principal assumptions. First, a homogeneous and isotropic medium and the frozen flow hypothesis of Taylor (1938) are required. Further, a "slab model" is assumed, which postulates the turbulent behavior to be constant up to an effective height H and vanishing above. Treuhaft and Lanyi (1987) formulated the spatial structure function of phase signals arriving at two antennas separated by the distance $\boldsymbol{d}$, and looking along a ray with an elevation ε and azimuth angle α, as

$$\mathcal{D}_\varphi(\boldsymbol{d}) = \frac{1}{\sin^2(\varepsilon)} \int_0^H \int_0^H$$
$$\left\{ \mathcal{D}_n\left[\boldsymbol{d}^2 + 2(s_1 - s_2)\,\boldsymbol{d}\cot(\varepsilon)\cos(\alpha) + \left(\frac{|s_1 - s_2|}{\sin(\varepsilon)}\right)^2\right]^{\frac{1}{2}} - \mathcal{D}_n\left(\frac{|s_1 - s_2|}{\sin(\varepsilon)}\right) \right\} ds_1 ds_2, \tag{4.18}$$

where $\mathcal{D}_n$ is the structure function of the refractive index, which is directly integrated along the line of sight, s_1 and s_2, respectively. Temporal correlations can be taken into account with the frozen flow model of TAYLOR (1938) as described in Eq. (4.8). Further, the authors showed that the structure function behaves as a $\frac{5}{3}$ power law at small distances or 3D turbulence, and $\frac{2}{3}$ for larger separation distances or 2D turbulence.

Additionally, TREUHAFT and LANYI (1987) determined an expression for the covariance between two tropospheric slant delays τ_i,

$$\mathcal{C}_\varphi(\tau_1, \tau_2) = \frac{1}{\sin(\varepsilon_1)\sin(\varepsilon_2)}\left(H^2\sigma_{wr}^2 - \frac{1}{2}\int_0^H\int_0^H \mathcal{D}_n\left(\frac{|s_1(z) - s_2(z') - v\Delta t|}{\sin(\varepsilon)}\right)dzdz'\right), \quad (4.19)$$

where v denotes the wind velocity and $s_1(z)$ and $s_2(z')$ represent the points on the lines of sight at heights z and z', respectively. The variance of the wet refractivity fluctuations σ_{wr} is defined by

$$\sigma_{wr} = \frac{1}{2}\mathcal{D}_n(\infty), \qquad (4.20)$$

assuming the troposphere to be completely uncorrelated at distances $\boldsymbol{d} \to \infty$. Since Kolmogorov's two-third law in Eq. (4.7) does not converge at infinity, TREUHAFT and LANYI (1987) proposed the modified expression

$$\mathcal{D}_n\left(\boldsymbol{d}\right) = C_n^2 \frac{\boldsymbol{d}^{\frac{2}{3}}}{1 + \left(\frac{R}{L}\right)^{\frac{2}{3}}} \qquad (4.21)$$

with $L = 3000$ km being the saturation scale length. In their study, TREUHAFT and LANYI (1987) assumed the tropospheric effective height to be $H \approx 1000$ m and used a mean value at average mid-latitude for the structure constant $C_n^2 = 5.8 \cdot 10^{-14} \mathrm{m}^{-\frac{2}{3}}$ and the geostrophic wind velocity of $v = 8 \frac{\mathrm{m}}{\mathrm{s}}$.

4.3.2 The SIGMA-C Model of Schön and Brunner (2008A;B)

In contrast to the structure function representation in the TREUHAFT and LANYI (1987) model, the model of SCHÖN and BRUNNER (2008A) makes use of a three-dimensional power spectrum expression to describe the covariance between observations induced by refractivity variations in the atmosphere. The model was originally developed for GPS carrier phase data and allows to introduce inhomogeneity and anisotropy.

The spatial covariance function of refractivity fluctuations can be formulated as a power spectral density by using a three-dimensional Fourier transform (WHEELON 2004, p. 21)

$$\langle[\Delta n(\boldsymbol{r}, t) - \Delta n(\boldsymbol{r} + \boldsymbol{d}, t)]^2\rangle = \int_{-\infty}^{\infty}\int_{-\infty}^{\infty}\int_{-\infty}^{\infty} \Phi_n(\boldsymbol{\kappa}, \boldsymbol{x})e^{i\boldsymbol{\kappa}^T\boldsymbol{d}}\, d^3\kappa, \qquad (4.22)$$

where $\Phi_n(\boldsymbol{\kappa}, \boldsymbol{x})$ represents the power spectrum and $\boldsymbol{\kappa}$ is the vector of wavenumbers. Again, the frozen flow hypothesis of TAYLOR (1938) in Eq. (4.8) can be used to link spatial and temporal correlations.

Integrating the refractivity variations along the line-of-sight leads to the most general case describing the covariance between two phase observations from station A to satellite i at epoch t_i and from station B to satellite j at epoch t_j,

$$\langle \Delta\varphi_A^i(t_A), \Delta\varphi_B^j(t_B) \rangle = \int_0^\infty \int_0^\infty \int_{-\infty}^\infty \int_{-\infty}^\infty \int_{-\infty}^\infty \Phi_n \left(\boldsymbol{\kappa}, \frac{\boldsymbol{r_1} + \boldsymbol{r_2}}{2} \right) e^{i\boldsymbol{\kappa}^T \boldsymbol{d}} \; d^3\kappa \; ds_1 \; ds_2. \qquad (4.23)$$

In order to represent the power spectrum, SCHÖN and BRUNNER (2008A) chose the von Kármán spectrum described in Eq. (4.14), which, in contrast to the initial formulation by Kolmogorov in Eq. (4.12) has no singularity for $\kappa = 0$. The von Kármán model is extended for a general case of inhomogeneity and anisotropy according to Eqs. (4.15) and (4.16).

Finally, SCHÖN and BRUNNER (2008A) give the covariance of the GNSS carrier phase observations as

$$\langle \Delta\varphi_A^i(t_A), \Delta\varphi_B^j(t_B) \rangle = \frac{12}{5} \frac{0.033}{\Gamma\left(\frac{5}{6}\right)} \frac{\sqrt{\pi^3}\kappa_0^{-\frac{2}{3}} 2^{-\frac{1}{3}}}{\sin\varepsilon_i \sin\varepsilon_j} C_n^2 \int_0^H \int_0^H (\kappa_0 \boldsymbol{d})^{\frac{1}{3}} \, \boldsymbol{K}_{-\frac{1}{3}} (\kappa_0 \boldsymbol{d}) \, dz_1 dz_2, \qquad (4.24)$$

where $\Gamma(\nu)$ denotes the gamma function (ABRAMOWITZ and STEGUN 1964, pp. 253ff) and $\boldsymbol{K}$ the modified Bessel function of second kind, also known as MacDonald function (ABRAMOWITZ and STEGUN 1964, pp. 355ff). It is worth noting that for the determination of the separation distance $\boldsymbol{d}$ not only the wind velocity, but also the wind orientation, both parametrized as a wind vector, is taken into account (see SCHÖN and BRUNNER 2008A for more details), which is generally not the case for most other turbulence models. Similarly, an expression for the variances is given as

$$\langle \Delta\varphi(t)^2 \rangle = \frac{12}{5} \frac{0.033}{\Gamma\left(\frac{5}{6}\right)} \frac{\sqrt{\pi^3}\kappa_0^{-\frac{2}{3}} 2^{-\frac{1}{3}}}{(\sin\varepsilon)^2} C_n^2 H^2$$
$$\left\langle \frac{\pi 2^{\frac{1}{3}}}{\sqrt{3}\Gamma\left(\frac{2}{3}\right)} \boldsymbol{F}_3^2 \left(\left[\frac{1}{2}, 1\right], \left[\frac{2}{3}, \frac{3}{2}, 1\right], \frac{z^2}{4} \right) - \frac{27}{80} 2^{\frac{2}{3}} \Gamma\left(\frac{2}{3}\right) z^{\frac{2}{3}} \boldsymbol{F}_2^1 \left(\left[\frac{5}{6}\right], \left[\frac{11}{6}, \frac{7}{3}\right], \frac{z^2}{4} \right) \right\rangle,$$
$$(4.25)$$

where $\boldsymbol{F}$ describes the hypergeometric function (ABRAMOWITZ and STEGUN 1964, pp. 556ff),

$$\boldsymbol{F}(a, b, c, z) = \frac{\Gamma(c)}{\Gamma(a)\Gamma(b)} \sum_{n=0}^\infty \frac{\Gamma(a+n)\Gamma(b+n)}{\Gamma(c+n)} \frac{z^n}{n!}. \qquad (4.26)$$

For the dimensionless argument z the expression $z = \frac{p\kappa_0 H}{\sin\varepsilon}$ can be used, where p gives the impact of anisotropy on the variance. For instance, $p = 1$ describes an isotropic medium.

SCHÖN and BRUNNER (2008B) extended this model by a receiver-antenna dependent white noise component. Although the term SIGMA-C model initially refers to the combination of the variance-covariance matrix due to refractivity fluctuations and the white noise component, it is equally used to describe only the variance-covariance model due to atmospheric conditions in this thesis.

Although the turbulence model has been formulated for GNSS observations, it is appropriately modified for the application of VLBI observations in Sec. 5.2. It should be pointed out here already, that in this context any additional noise component is added to the variances of the observations.

4.3.3 The Kermarrec and Schön Model (2014)

The turbulence model of KERMARREC and SCHÖN (2014) is an extension of the SIGMA-C model described in Sec. 4.3.2 and is, therefore, also based on the power spectrum representation.

Generally, the power spectrum $\mathcal{W}_\varphi(\omega)$ and the covariance function of the phase fluctuations are intimately connected by the Wiener-Khinchine-theorem (WHEELON 2004, p. 257),

$$\mathcal{W}_\varphi(\omega) = \int\limits_{-\infty}^{\infty} d\tau e^{i\omega\tau} \langle \varphi(t)\varphi(t+\tau) \rangle \, d\tau. \tag{4.27}$$

A simplified expression for the spectrum of phase measurements can be formulated according to WHEELON (2004, Sec. 6.5), as well as KERMARREC and SCHÖN (2014),

$$\mathcal{W}_\varphi(\omega) = \frac{2.192 H k^2 C_n^2 c a^{-\frac{5}{3}} v^{\frac{5}{3}}}{\sin^2(\varepsilon) \left[\omega^2 + \left(\frac{\kappa_0 v}{a} \right)^2 \right]^{\frac{4}{3}}}, \tag{4.28}$$

which is valid for a so-called "slab model" using a few assumptions and the von Kármán spectrum. The "slab model" postulates the wind velocity v and the structure constant C_n^2 to be non-varying up to the tropospheric effective height H and no atmospheric turbulence above. However, it is worth mentioning that anisotropy and inhomogeneity are taken into account in this model. KERMARREC and SCHÖN (2014) found, that the corresponding covariance,

$$\mathbf{C}(t, t+\tau) = 0.7772 \frac{k^2 H C_n^2 c}{\sin(\varepsilon_i(t)) \sin(\varepsilon_j(t+\tau))} \times \kappa_0^{-\frac{5}{3}} \left(\frac{\kappa_0 v\tau}{a} \right)^{\frac{5}{6}} K_{\frac{5}{6}} \left(\frac{\kappa_0 v\tau}{a} \right), \tag{4.29}$$

is a so-called Matérn covariance function (MATÉRN 1960) with a smoothness parameter $\nu = \frac{5}{6}$ and a Matérn correlation time $\mathcal{T} = \frac{1}{\alpha}$ with $\alpha = \frac{\kappa_0 v}{a}$ and $\kappa_0 = \frac{2\pi}{L_0}$. Here, $K_{\frac{5}{6}}$ represents the modified Bessel function of second kind (ABRAMOWITZ and STEGUN 1964, pp. 355f). The corresponding variance expression reads

$$\mathbf{C}(t, t) = 0.782 \frac{k^2 H C_n^2 c \kappa_0^{-\frac{3}{5}}}{\sin^2(\varepsilon_i(t))}. \tag{4.30}$$

A major and very important advantage of the KERMARREC and SCHÖN (2014) model over most other turbulence models is the fact, that no numerical integration is necessary, which reduces the computational effort.

This is one reason why the model has been chosen in this thesis to be further developed in order to achieve an enhanced stochastic model of VLBI observations considering small-scale refractivity fluctuations in an operational mass production. A detailed description and an extensive validation of the modified and VLBI-specific version of the turbulence model developed in this thesis is given in Sec. 5.1.

5. Turbulence Modeling in VLBI

Although atmospheric refractivity fluctuations restrict the attainable accuracy of VLBI target parameters, variability issues have been largely ignored. To allow for a physically more reliable modeling of the stochastic properties of VLBI observations it is necessary to expand the current tropospheric model to high-frequency refractivity variations and physically induced correlations between the observations. Both can be best described stochastically following the widely accepted Kolmogorov turbulence theory. In the last decades, some authors proposed empirically derived power law descriptions or turbulence-based covariance models (see Sec. 1.3 for more details), however, these models are either based on general assumptions, which are hardly true in reality, or are not suitable in operational data analysis due to a very high computational effort.

In order to overcome these severe deficiencies and to develop an operationally efficient method for turbulent modeling in routine mass analysis of VLBI observing sessions, a new atmospheric turbulence model is devised in this thesis (Sec. 5.1). With the objective of developing a turbulence model which is practicable for traditional long baselines as well as local VLBI networks, the model is evaluated for specially designed short baseline observations in the framework of the WHISP (Wettzell HIgh SPeed) project (see Ch. 6), and routinely processed VLBI sessions provided by the International VLBI Service for Geodesy and Astrometry (IVS, NOTHNAGEL et al. 2015; NOTHNAGEL et al. 2016). The turbulence model is validated against different strategies to refine the stochastic model of VLBI observations, which are common practice in current VLBI analysis software packages.

As an alternative strategy, the SIGMA-C model of SCHÖN and BRUNNER (2008A;B, see Sec. 4.3), which was originally developed for GNSS carrier phases, is modified for VLBI observations (see Sec. 5.2). One focus is on the selection of appropriate turbulence parameters, particularly, the structure constant C_n^2 and the effective tropospheric height H. The turbulence model is applied to the continuous VLBI campaign 2002 and the results are again validated against standard analysis strategies of the IVS community.

5.1   A VLBI-specific Turbulence Model

In the endeavor to develop an operationally efficient strategy to realize an appropriate stochastic model in routine mass analysis of VLBI observing sessions, a VLBI-specific and modified version of the KERMARREC and SCHÖN (2014) model has been developed (see also HALSIG et al. 2015A; HALSIG et al. 2016A). The turbulence model has to meet the requirements of generating a fully populated variance-covariance matrix of the observations considering small-scale refractivity fluctuations in the neutral atmosphere as well as physically induced spatial and temporal correlations between the observations. As a consequence, the standard deviations of the derived target parameters are expected to become higher and therefore more realistic. One of the key objectives of this thesis is to develop an appropriate strategy to describe refractivity variations in an operational way, which ensures a model that can be mathematically easy handled, and allows for a fully populated variance-covariance matrix without too much computational effort.

5.1.1 Turbulence Description

Atmospheric turbulence is usually described stochastically by either structure or covariance functions or a power spectrum representation. In general, the temporal covariance function of the phase measurements $\mathcal{C}_\varphi (t, t + \tau) = \langle \varphi(t)\varphi(t+\tau) \rangle$ is intimately connected to the power spectrum $\mathcal{W}_\varphi(\omega)$ by the Wiener-Khinchine-theorem (WHEELON 2004, p. 257)

$$\mathcal{W}_\varphi(\omega) = \int\limits_{-\infty}^{\infty} d\tau e^{i\omega\tau} \langle \varphi(t)\varphi(t+\tau) \rangle \, \mathrm{d}\tau, \tag{5.1}$$

where φ describes the phase fluctuation, t and τ denote the time and time increment, and ω is the corresponding frequency. For a detailed explanation on how to describe atmospheric turbulence the reader is referred to Sec. 4.2.

Following WHEELON (2004, Sec. 6.5), the expression

$$\mathcal{W}_\varphi(\omega) = \frac{2.192 H k^2 C_n^2 c a^{-\frac{5}{3}} v^{\frac{5}{3}}}{\sin^2(\varepsilon) \left[\omega^2 + \left(\frac{\kappa_0 v}{a}\right)^2 \right]^{\frac{4}{3}}} \tag{5.2}$$

can be used to formulate the spectrum of phase measurements in a slab model of the atmosphere. In Eq. (5.2), a and c are the anisotropic scaling parameters in the horizontal and vertical direction, $k = \frac{2\pi}{\lambda}$ denotes the electromagnetic wavenumber with the wavelength of electromagnetic radiation λ, and $\kappa_0 = \frac{2\pi}{L_0}$ represents the outer scale wavenumber to the corresponding outer scale length L_0 (see Fig. 4.2 and Sec. 4.1 for more details). The term $\sin(\varepsilon)$ describes a simple mapping function to relate the measurement from zenith to an arbitrary elevation angle ε (see Sec. 3.3.4). The approximation in a slab model assumes the level of turbulent activity to be consistent up to a certain effective tropospheric height H and zero above. This includes both, a non-varying structure constant C_n^2 within the defined interval and a constant wind velocity v. The turbulence spectrum is described by the von Kármán spectrum (VON KÁRMÁN 1948), and the general validity describing the turbulence as an anisotropic and inhomogeneous medium is maintained. One advantage of representing the atmosphere as a slab model is the fact that certain integrations can be expressed in terms of hypergeometric functions (ABRAMOWITZ and STEGUN 1964, pp. 556ff), and the model can more easily be evaluated numerically (WHEELON 2004, Sec. 5.2), as demonstrated explicitly in case of the SIGMA-C model (see Eqs. (4.23) - (4.25) in Sec. 4.3.2).

The covariance function and the power spectrum provide equivalent descriptions of the phase fluctuations. If the phase spectrum is known, the covariance can be determined by the inverse Fourier integral

$$\langle \varphi(t)\varphi(t+\tau) \rangle = \frac{1}{2\pi} \int\limits_{-\infty}^{\infty} d\omega e^{-i\omega\tau} \mathcal{W}_\varphi(\omega). \tag{5.3}$$

Applied to Eq. (5.2), and following KERMARREC and SCHÖN (2014), leads to the following expression for the covariance of phase measurements

$$\mathcal{C}_\varphi (t, t + \tau) = 0.7772 \frac{k^2 H C_n^2 c}{\sin(\varepsilon_i(t)) \sin(\varepsilon_j(t+\tau))} \kappa_0^{-\frac{5}{3}} \left(\frac{\kappa_0 v\tau}{a} \right)^{\frac{5}{6}} K_{\frac{5}{6}} \left(\frac{\kappa_0 v\tau}{a} \right), \tag{5.4}$$

where $K_{\frac{5}{6}}$ represents the modified Bessel function of second kind (ABRAMOWITZ and STEGUN 1964, pp. 355ff).

KERMARREC and SCHÖN (2014) found that the covariance description in Eq. (5.4) is a so-called Matérn covariance function (MATÉRN 1960) of the general form

$$\boldsymbol{\mathcal{C}}\left(r\right) = \phi\left(\alpha r\right)^{\nu} K_{\nu}\left(\alpha r\right), \tag{5.5}$$

with a smoothness parameter $\nu = \frac{5}{6}$ and a Matérn correlation time $\mathcal{T} = \frac{1}{\alpha}$, where $\alpha = \frac{\kappa_0 v}{a}$ and $\kappa_0 = \frac{2\pi}{L_0}$.

The covariance model in Eq. (5.4) can be expressed alternatively with respect to the distance separating the paths of two satellites observed by two antennas (KERMARREC and SCHÖN 2014). More details on the separation distance for GNSS observations to satellites can be found in SCHÖN and BRUNNER (2008a) and KERMARREC and SCHÖN (2014).

This concept is also used for VLBI observations, where the separation distance between the ray paths of radio signals emitted by extragalactic sources to the two radio telescopes A and B of a VLBI observation $d_H(t)$ is determined as follows. First, the local source vector $\boldsymbol{k}'$ is determined in terms of homogeneous coordinates

$$\boldsymbol{k}' = \begin{bmatrix} \cos(\varepsilon_A) \cdot \cos(\alpha_A) \\ \cos(\varepsilon_A) \cdot \sin(\alpha_A) \\ \sin(\varepsilon_A) \\ 1 \end{bmatrix}, \tag{5.6}$$

where α_A and ε_A denote the azimuth and elevation angle of station A, and needs to be transformed in a global system in order to derive the unit source vector

$$\boldsymbol{k} = \boldsymbol{R}_2^{-1} \boldsymbol{R}_1^{-1} \boldsymbol{k}'. \tag{5.7}$$

The rotation matrices $\boldsymbol{R}_1$ and $\boldsymbol{R}_2$ are given by

$$\boldsymbol{R}_1 = \begin{bmatrix} \cos(\beta) & 0 & \sin(\beta) & 0 \\ 0 & 1 & 0 & 0 \\ -\sin(\beta) & 0 & \cos(\beta) & 0 \\ 0 & 0 & 0 & 1 \end{bmatrix} \tag{5.8}$$

and

$$\boldsymbol{R}_2 = \begin{bmatrix} \cos(\delta) & -\sin(\delta) & 0 & 0 \\ \sin(\delta) & \cos(\delta) & 0 & 0 \\ 0 & 0 & 1 & 0 \\ 0 & 0 & 0 & 1 \end{bmatrix}, \tag{5.9}$$

respectively, with the rotation angles

$$\beta = \arccos\left(\begin{bmatrix} 0 & 0 & 1 \end{bmatrix} \frac{\boldsymbol{r}_A}{\|(\boldsymbol{r}_A)\|}\right) \tag{5.10}$$

and

$$\delta = \pi - \arccos\left(\begin{bmatrix} 1 & 0 & 0 \end{bmatrix} \frac{\begin{bmatrix} r_A^x & r_A^y & 0 \end{bmatrix}^T}{\|(\begin{bmatrix} r_A^x & r_A^y & 0 \end{bmatrix})\|}\right), \tag{5.11}$$

where $\boldsymbol{r}_A$ denotes the position vector for station A and $r_A^{j=X,Y}$ the components therein. Second, the baseline vector $\boldsymbol{b}$ can be generally computed from the position vectors of two VLBI antennas $\boldsymbol{r}_A$ and $\boldsymbol{r}_B$ according to Eq. (2.3). In order to calculate the separation distance at a specific height H, the positions vectors are modified by an additional term corresponding to the selected height,

$$\widehat{\boldsymbol{r}}_A = \boldsymbol{r}_A \cdot \left(1 + \frac{H}{\|\boldsymbol{r}_A\|}\right), \tag{5.12}$$

$$\widehat{\boldsymbol{r}}_B = \boldsymbol{r}_B \cdot \left(1 + \frac{H}{\|\boldsymbol{r}_B\|}\right), \tag{5.13}$$

and the corresponding modified baseline vector becomes

$$\widehat{\boldsymbol{b}} = \widehat{\boldsymbol{r}}_A - \widehat{\boldsymbol{r}}_B. \tag{5.14}$$

Finally, the separation distance is determined according to the Pythagorean theorem (see Fig. 2.1),

$$d_H = \sqrt{\widehat{\boldsymbol{b}}^2 - (\tau c)^2}, \tag{5.15}$$

where τc is related to the unit source vector $\boldsymbol{k}$ and the modified baseline vector $\widehat{\boldsymbol{b}}$ by Eq. (2.4).

The covariance model in Eq. (5.4) is modified in a way that the outer scale length L_0 in $\kappa_0 = \frac{2\pi}{L_0}$ is replaced by the separation distance $d_H(t)$, leading to

$$\boldsymbol{C}\left(t, t+\tau\right) = 0.7772 \frac{k^2 H C_n^2 c}{mf\left(\varepsilon_i(t)\right) mf\left(\varepsilon_j(t+\tau)\right)} \left(\frac{2\pi}{d_H(t)}\right)^{-\frac{5}{3}} \left(\frac{2\pi v\tau}{d_H(t)a}\right)^{\frac{5}{6}} K_{\frac{5}{6}}\left(\frac{2\pi v\tau}{d_H(t)a}\right). \tag{5.16}$$

The corresponding variance expression to Eq. (5.16) reads

$$\boldsymbol{C}_\varphi\left(t, t\right) = 0.782 \frac{k^2 H C_n^2 c \kappa_0^{-\frac{3}{5}}}{\left[mf\left(\varepsilon_i(t)\right)\right]^2}. \tag{5.17}$$

The wavelength of the radio signals λ, which is used for the determination of the electromagnetic wavenumber

$$k = \frac{2\pi}{\lambda} \tag{5.18}$$

in Eqs. (5.16) and (5.17), is 8.4 GHz (X-band) in case of VLBI. Please remember, that the radio telescopes generally observe at two frequencies at 8.4 GHz (X-band) and 2.3 GHz (S-band), however, the S-band data is only used to eliminate the effects of ionospheric refraction (see Chs. 2 and 3).

In case of VLBI observations, the very simple elevation-dependent scaling factor $\frac{1}{\sin(\varepsilon)}$ in Eq. (5.4) is also replaced by a more sophisticated model in Eqs. (5.16) and (5.17), such as the Vienna mapping functions 1 (VMF1, BÖHM et al. 2006b), $mf\left(\varepsilon_i(t)\right)$. This is necessary, since the cutoff angle of VLBI observations (up to 3 degrees) is lower than for GNSS observations (about 10 degrees), and the simplified sine model becomes very inaccurate for observations with small elevation angles, which are, however, needed to separate different parameter groups, particularly the zenith wet delays (cf. SCHUH and BÖHM 2013).

Equations (5.16) and (5.17) are used to generate a variance-covariance matrix based on high-frequency refractivity fluctuations in the neutral atmosphere, which is then, in a next step,

incorporated in the VLBI estimation procedure. The turbulence-based variance-covariance matrix is therefore added to the routine variance-covariance matrix of the Gauss Markov model, which is currently a pure diagonal matrix and includes, almost exclusively, the uncertainties from the VLBI correlation process.

One crucial aspect in turbulence modeling is the determination of the turbulence parameters, particularly the "scaling parameters" C_n^2, H and a, b, c as well as the wind parametrization. Although the structure constant decreases with height from $C_n^2 = 10^{-14}$ m$^{-\frac{2}{3}}$ at 1 km height to $C_n^2 = 10^{-18}$ m$^{-\frac{2}{3}}$ at 10 km height (WHEELON 2004, pp 62ff), C_n^2 can generally be assumed to be constant up to the tropospheric height $H \approx 2000$ m and zero above (cf., e.g., TREUHAFT and LANYI 1987; SCHÖN and BRUNNER 2008a). In principle, however, the height dependency could be taken into account following TATARSKII (1971) or NILSSON et al. (2010). Generally, there are different methods to estimate the structure constant at the specific VLBI site, e.g., from water vapor radiometer, radiosonde or GPS data (NILSSON and HAAS 2010). However, for a suitable description of the turbulent behavior over a VLBI station, such sensors have to be available near to these radio telescopes, which is usually only the case for GPS sensors, if at all. However, particularly with regard to the VLBI Global Observing System, which leads to a clear increase of observations and a better sky coverage, the estimation of C_n^2 parameters using VLBI observations may be possible in future. Here, especially short baselines in local networks, for instance, by using so-called twin telescopes, should be used to determine turbulent motions in the atmosphere assuming that other disturbing effects can be sufficiently quantified by observations on short baselines. A detailed case study concerning close-range VLBI observation in a local network is presented in Ch. 6. The parameters a, b and c describing the flattening of the turbulent medium are chosen to $a = b > c$ due to the increasing horizontal flattening with height up to $a = b = 100\,c$ (WHEELON 2004). The wind is parametrized as a constant horizontal wind velocity and a wind direction, which is defined by the separation distance $d_H(t)$ between the two radio signals at height H. Assuming the so-called free atmosphere from 1000 m to 3000 m to be crucial inducing physical correlations between the observations, a wind velocity $v \approx 8 \frac{\text{m}}{\text{s}}$, which approximately corresponds to the geostropic wind at that height, seems to be sufficient (cf. KERMARREC and SCHÖN 2014). Mostly, the same structure constants are applied for both stations of a baseline, although, of course, for global VLBI networks, which are the standard case in VLBI, the meteorological conditions may not be the same at the two VLBI stations. Ideally, the structure constant is chosen or even estimated with respect to the current weather conditions, which, however, conflicts the requirement of an operationally efficient modeling approach increasing the computational effort as little as necessary. For this reason, it will be demonstrated that the turbulence model performs very well, also only based on experience-based values.

Only when additionally considering 3D turbulence (see Sec. 4.1 for more details) in the atmospheric boundary layer below 1000 m, which is easily possible with this model, the parametrization described above must be specified accordingly. For instance, the anisotropic scaling parameters in the horizontal and vertical direction are identical, $a = b = c = 1$, since the eddies become almost symmetrical in the boundary layer. Of course, the tropospheric height reduces, $H < 1000\ m$, and the structure constant is assumed to be smaller (cf. WHEELON 2004, pp 62ff). The approximation of using the geostropic wind velocity is also not sufficient any more, and the wind velocity v has to be specified accordingly, e.g., by numerical weather models.

5.1.2   Data Analysis Setup and Turbulence Parametrization

The model evaluation is performed on a basis of about 2700 traditional VLBI sessions between 1993 and 2014, provided by the IVS (Nothnagel et al. 2015), as well as a series of specially designed experiments on a local scale. These so-called WHISP (Wettzell HIgh SPeed) sessions only consist of one short baseline of about 120 m between the 20 m diameter radio telescope and the north antenna of the twin telescope at the Wettzell Geodetic Observatory, and allow close-range VLBI observations to characterize local refraction effects. For comparison purposes, another short baseline between two adjacent VLBI stations located in Hobart, Tasmania (Australia) has been analyzed for the period of the continuous VLBI campaign 2014. With only a few exceptions, all sessions are generally intended to last 24 hours. The results of both the global and local scale are presented in Sec. 5.1.3 and 5.1.4, respectively.

The data analysis setup for both the traditional baselines and local VLBI networks is performed using the VLBI software package ivg::ASCOT (Artz et al. 2016; Halsig et al. 2017), developed at the Institute of Geodesy and Geoinformation of the University of Bonn, and following the conventions (2010) of the International Earth Rotation and Reference Systems Service (IERS, Petit and Luzum 2010). The VLBI target parameters, such as telescope positions or Earth orientation parameters (EOP), are estimated in a least squares adjustment using a Gauss Markov model (e.g., Koch 1999) as described in Sec. 2.2. The parametrization setup for single-session VLBI data analysis has been chosen with respect to the routine data analysis strategies of the IVS. The coordinates of the radio telescopes are estimated with respect to the current version of the International Terrestrial Reference Frame (ITRF2014, Altamimi et al. 2016). In order to eliminate the datum defect, i.e., to remove the natural VLBI rank deficiency, additional no-net-rotation (NNR) and no-net-translation (NNT) conditions (e.g., Angermann et al. 2004) have been applied. Polar motion and UT1-UTC are parametrized with offsets and rates while radio source coordinates are not estimated, but fixed to their positions in the current version of the International Celestial Reference Frame (ICRF2, Fey et al. 2015).

In addition to the target parameters, further auxiliary quantities including clock and atmospheric model correction parameters are estimated as well. The clock parameters are modeled by a second order polynomial and additional continuous piece-wise linear functions (CPWLF), i.e., linear splines (De Boor 1978), with a temporal resolution of 60 min. Finally, the wet component of the atmospheric delay is estimated in zenith direction and parametrized as CPWLFs with a resolution of 60 min. In order to map the tropospheric wet delay from zenith to the slant direction (i.e., the line-of-sight) the mapping functions VMF1 are used, which are derived from a numerical weather model of the European Centre for Medium-Range Weather Forecast (ECMWF). Further, azimuthal gradients are estimated with a resolution of 6 hours. In order to stabilize the equation system, the clock, zenith wet delay and gradient parameters are supplemented by additional constraints which affect the equation system as weighted pseudo observations.

Concerning the stochastic model of the observations, in the current standard case, the weight matrix of the Gauss Markov model is a pure diagonal matrix. The same applies for all concepts refining the stochastic model of VLBI observations, which are introduced in the following sections, except for the turbulence model. Here, a fully populated variance-covariance matrix is provided describing the refractivity fluctuations due to turbulent motions in the atmosphere

The model parameters describing the state of the turbulent atmosphere have been kept very simple and have been chosen to be the same for all stations. A constant structure constant $C_n^2 = 1 \cdot$

10^{-14} m$^{-\frac{2}{3}}$ is used, the effective tropospheric height is set to $H = 2000$ m and a constant wind velocity $v = 8$ $\frac{m}{s}$ in horizontal direction is assumed. The stretching factors describing the flattening of the turbulent eddies have been chosen to $a, b = 1$ and $c = 0.01$ to consider for anisotropy in the free atmosphere.

5.1.3 Model Validation with Traditional VLBI Baselines

As already described in Sec. 2.2.2, the standard VLBI stochastic model includes, almost exclusively, the uncertainties from the VLBI correlation process while correlations between the observations are, in general, completely ignored. The derived target parameters are not as accurate as indicated by the corresponding variance-covariance matrix, which is said to be too optimistic (SCHÖN and KERMARREC 2015).

An indicator to validate the quality of the observation model is given by the χ^2 value, which is defined as the quotient of the a posteriori $\tilde{\sigma}^2$ and the a priori variance factor σ_0^2,

$$\chi^2 = \frac{\tilde{\sigma}^2}{\sigma_0^2}, \tag{5.19}$$

and gives an information whether the global test for an adjustment is fulfilled or not. Assuming $\chi^2 \approx 1$ indicates that the global test is fulfilled, whereas $\chi^2 \neq 1$ indicates an under- ($\chi^2 > 1$) or overestimation ($\chi^2 < 1$) of the variances of the observations $\sigma_{obs}^2(t)$ or an incorrect modeling of the system, or a combination of both. The term overestimation is referred to the fact, that the a priori model is too idealistic in the sense of too enthusiastic initial weights, which is compensated for in the estimation procedure. Conversely, underestimation would imply a too pessimistic a priori modeling and too unpromising initial weights. For single VLBI experiments, typical values of $\chi^2 \approx 3-4$ occur (e.g., GIPSON et al. 2008), indicating an underestimation and too optimistic variances. Expressed in other words, the stochastic model of VLBI observations is not complete.

In the routine data analysis of the IVS, the derived variances are inflated artificially to satisfy $\chi^2 \approx 1$, leading to more realistic variances of the observations

$$\sigma_{obs}^2(t) = \sigma_{init}^2(t) + \sigma_{wgt}^2(t), \tag{5.20}$$

where $\sigma_{init}^2(t)$ and $\sigma_{wgt}^2(t)$ describe the initial variances from the correlation process and the additional re-weighting term, respectively. Generally, $\sigma_{wgt}^2(t)$ could be chosen independently for each observation (GIPSON et al. 2008), however, in practice, either the same constant term is added to the variances of the observations, or a station- or baseline-dependent re-weighting procedure is applied. In the last decade, a few strategies have been developed for the re-weighting of the observations. For instance, the most widely spread VLBI software package Calc/Solve (MA et al. 1990) uses a baseline-dependent approach iteratively re-weighting the observations until $\chi^2 \approx 1$ is fulfilled. A detailed description of the re-weighting algorithm used in Calc/Solve can be found in PETROV (1998).

In order to evaluate the turbulence model, the derived standard deviations are quantified with respect to some of the most widely applied concepts in the VLBI community, which are shortly described in the following (see Tab. 5.1). First, a simple approach without using any kind of additional noise term, referred to as reference solution (A) in the following, was defined. The most simple approach (B) of re-weighting the observations is to add the same constant noise term for

Table 5.1: Different solution setups including the reference solution and different strategies to refine the stochastic model of VLBI observations. The mean χ^2 and WRMS values over about 2700 VLBI sessions between 1993 and 2014 are illustrated for all solution setups (HALSIG et al. 2016a).

	Solution type	χ^2 [-]	**WRMS** [ps]
A	reference solution	2.32	34.53
B	constant additional noise: 1 cm	0.86	42.46
C	Gipson et al. (2006-2008) constant and elevation-dependent noise	1.13	36.24
D	turbulence-based correlations	1.18	34.93

all observations and sessions, which is chosen to approximately 30 ps, or about 1 cm in metric dimensions. In this case, the re-weighting term $\sigma_{wgt}^2(t)$ in Eq. (5.20) can be written as

$$\sigma_{wgt}^2(t) = \sigma_{const.}^2(t) \qquad\qquad (5.21)$$

However, this simple strategy is applied here not only for validation purposes, it is common practice in some widely spread VLBI software packages, as for instance, the Vienna VLBI Software (VieVS, BÖHM et al. 2012). The third strategy (C) distinguishes between different sources of observational noise: a constant and an elevation-dependent noise term are added to the standard deviations, which correspond to the clock and troposphere model parameter, respectively (GIPSON 2007; GIPSON et al. 2008). Mathematically, this yields

$$\sigma_{wgt}^2(t) = \sigma_{clo}^2(t) + \sigma_{atm}^2(t) \cdot mf\left(\varepsilon\right), \qquad\qquad (5.22)$$

where $mf\left(\varepsilon\right)$ defines a mapping function, which, in this context, is simplified to $1/\sin\varepsilon$. The order of magnitude of both components is related to the results presented by GIPSON (2007) and GIPSON et al. (2008). There are two reasons why the baseline-dependent re-weighting method of PETROV (1998) was turned off for all solutions. First, the observations are re-weighted iteratively until $\chi^2 \approx 1$, which, however, is supposed to serve as a suitability criteria for the stochastic model of the corresponding refinement strategy. Second, GIPSON et al. (2008) demonstrated that applying the re-weighting option in addition to the elevation-dependent noise term degrades the solution. Finally, the turbulence model developed in this thesis (D) is used according to Eqs. (5.16) and (5.17) to modify the stochastic model of VLBI observations. In contrast to all the other strategies, the observations are not weighted by any additional noise terms in case of the turbulence model.

In the following figures, the reference solution is always illustrated as black crosses, and purple triangles are referred to the simple approach adding 1 cm constant noise terms for all observations. The results corresponding to GIPSON et al. (2008) are marked as green circles, and, finally, the turbulence-based solution is represented by brown stars.

As already described, the derived target parameters are not as accurate as indicated by the corresponding variance-covariance matrix. Refining the stochastic model should lead to larger standard deviations, which are, however, more realistic. The traditional stochastic model is augmented by the variance-covariance matrix based on the turbulence model describing high frequency refractivity fluctuations in the atmosphere. Through this approach, the standard deviations of the estimated

parameters become more realistic, as depicted exemplarily in Fig. 5.1 for the 15-day continuous VLBI campaign in October 2002 (CONT02). Here, the standard deviations of the vertical component of the station coordinates are illustrated as differences between the solutions refining the stochastic model described above, including the routine data analysis strategy of the IVS. The situation looks very similar for both horizontal components (not shown here). According to Böckmann et al. (2010), the average noise level of about 115 IVS sessions in terms of the weighted root mean square (WRMS) error of single session position estimates, computed after removing the offset, rate and annual signal is about 4.5 mm for the horizontal and about 6.5 mm for the vertical component. Using a modified stochastic model, i.e., either the turbulence-based model or the Gipson et al. (2008) model, the level of uncertainty is getting closer to these values with very few exceptions, assuming that the noise level becomes more realistic (Halsig et al. 2016a).
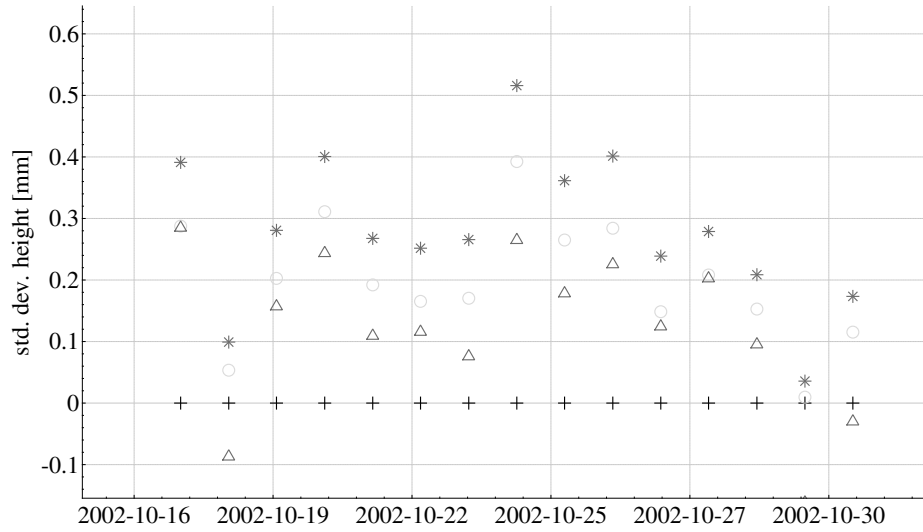
Figure 5.1: Differences in standard deviations of the vertical component of the station coordinates between a simple solution with a constant additional noise term (purple triangles), the Gipson et al. (2008) approach (green circles) and the turbulence-based solution (brown stars) with respect to the reference solution (black crosses).

The atmospheric turbulence model is first evaluated for VLBI experiments on traditional baselines between a few thousand kilometers. For this purpose, about 2700 VLBI sessions between 1993 and 2014, provided by the IVS, are used, which include several observation campaigns consisting of different network geometries. For all available VLBI sessions, the different strategies have been processed in order to evaluate the fully populated turbulence-based variance-covariance matrix.

The quality of the different solution setups is quantified by two statistical criteria. First, the χ^2 value defined in Eq. (5.19) gives an information whether the stochastic properties of VLBI observations are modeled sufficiently, with $\chi^2 \approx 1$ indicating that the deterministic and stochastic model assumptions are valid. Second, the WRMS of post-fit residuals r_i (where $r_i = -v_i$ with the v_i defined in Eq. 2.11) can be formulated as

$$WRMS = \sqrt{\frac{\sum_i r_i^2 \frac{1}{\sigma_i^2}}{\sum_i \frac{1}{\sigma_i^2}}}. \tag{5.23}$$

The χ^2 values and WRMS of post-fit residuals are depicted in Fig. 5.2(a) and Fig. 5.2(b), respectively. In addition, Tab. 5.1 shows the WRMS of post-fit residuals of the delay observables as well as the χ^2 values as mean values per solution setup over the 2700 VLBI sessions. Compared to the reference solution (black, $\chi^2 \approx$ 2-5), the χ^2 values are generally reduced as soon as an arbitrary refinement strategy is used. Although only a very simple model is used in case of the easiest approach (purple), the χ^2 values are quite close to one. However, considering the mean values in Tab. 5.1, it becomes evident that here $\chi^2 < 1$, still indicating an overestimation in the data analysis. Positive results can be obtained by the turbulence-based solution (brown) and the Gipson et al. (2008) approach (green), where the χ^2 values are approximately one indicating a realistic adjustment, but they are still slightly too high. However, in case of the turbulence model, this is not surprising when recalling the fact that only atmospheric effects are considered in the stochastic model, which are the dominant but not sole error source in VLBI data analysis. For instance, the uncertainties of clock behavior are neglected in the stochastic model. Additionally, the parameters describing the atmospheric turbulence, C_n^2, H, a, b, c, and v depend on a experience-based parametrization and are not taken into account as station-dependent estimates (see the more detailed discussion in Sec. 5.1.5).

(a)

(b)
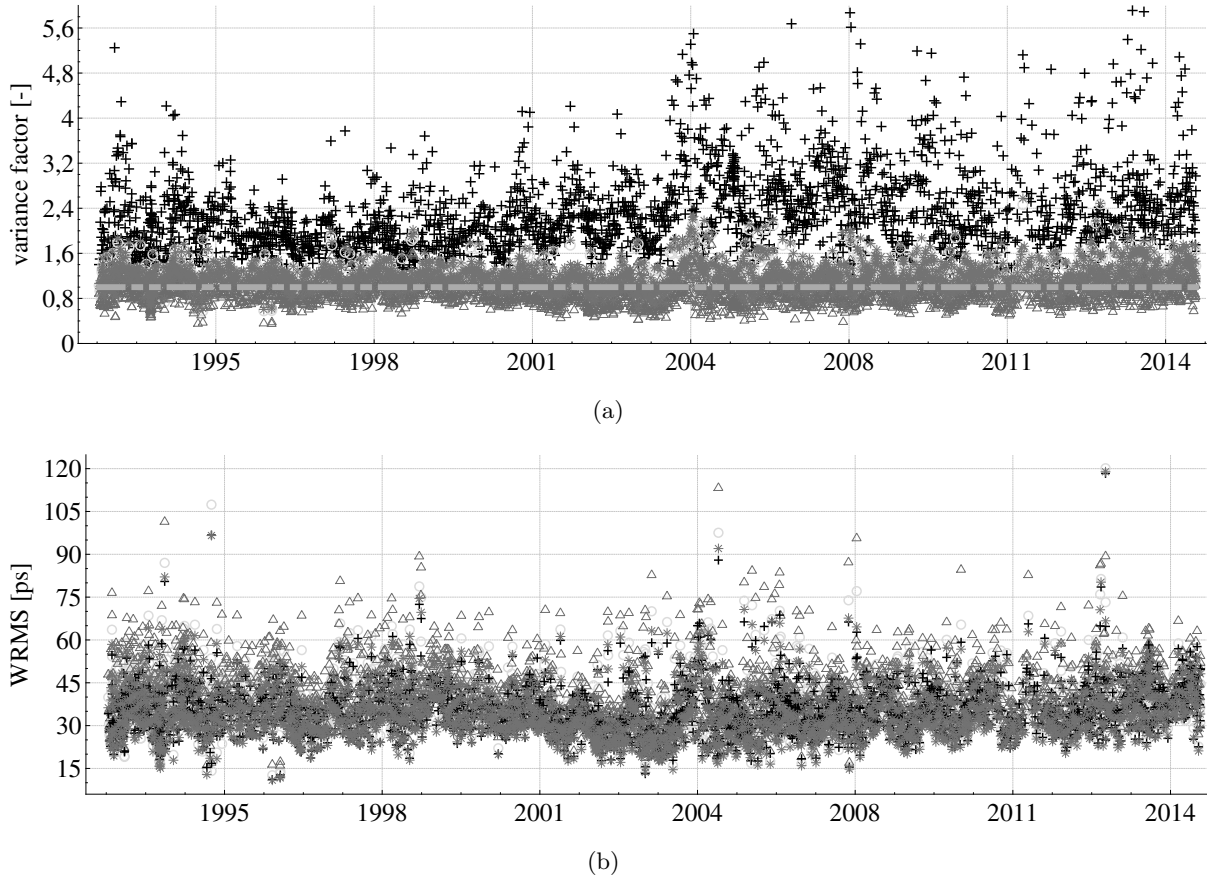
Figure 5.2: (a) χ^2 values and (b) WRMS of post-fit residuals for about 2700 VLBI sessions between 1993 and 2014 and different solution setups including a reference solution (black crosses), a simple solution with a constant additional noise term (purple triangles), the Gipson et al. (2008) approach (green circles) and the turbulence-based solution (brown stars). The grey dashed line in (a) represents $\chi^2 = 1$ (Halsig et al. 2016a).

Considering the WRMS of post-fit residuals, it is apparent that, compared to the other refinement strategies, the use of the new turbulent variance-covariance matrix produces the lowest WRMS of post-fit residuals. Expressed in numbers and, for instance compared to the GIPSON et al. (2008) approach, the turbulence-based solution improves by 9.5 ps in quadrature. Nevertheless, both solutions are much better than the solution adding constant noise terms only, where the mean WRMS value is degraded by about 24 ps and 22 ps in quadrature with respect to the turbulence-based and GIPSON et al. (2008) approach, respectively. Surprisingly perhaps, the WRMS of post-fit residuals for the reference solution are on the same level as for the turbulence-based solution. However, keeping in mind that the χ^2 values are too high by the factor of two or even more, it should be discouraged to use the different validation criteria separately.

(a)

(b)
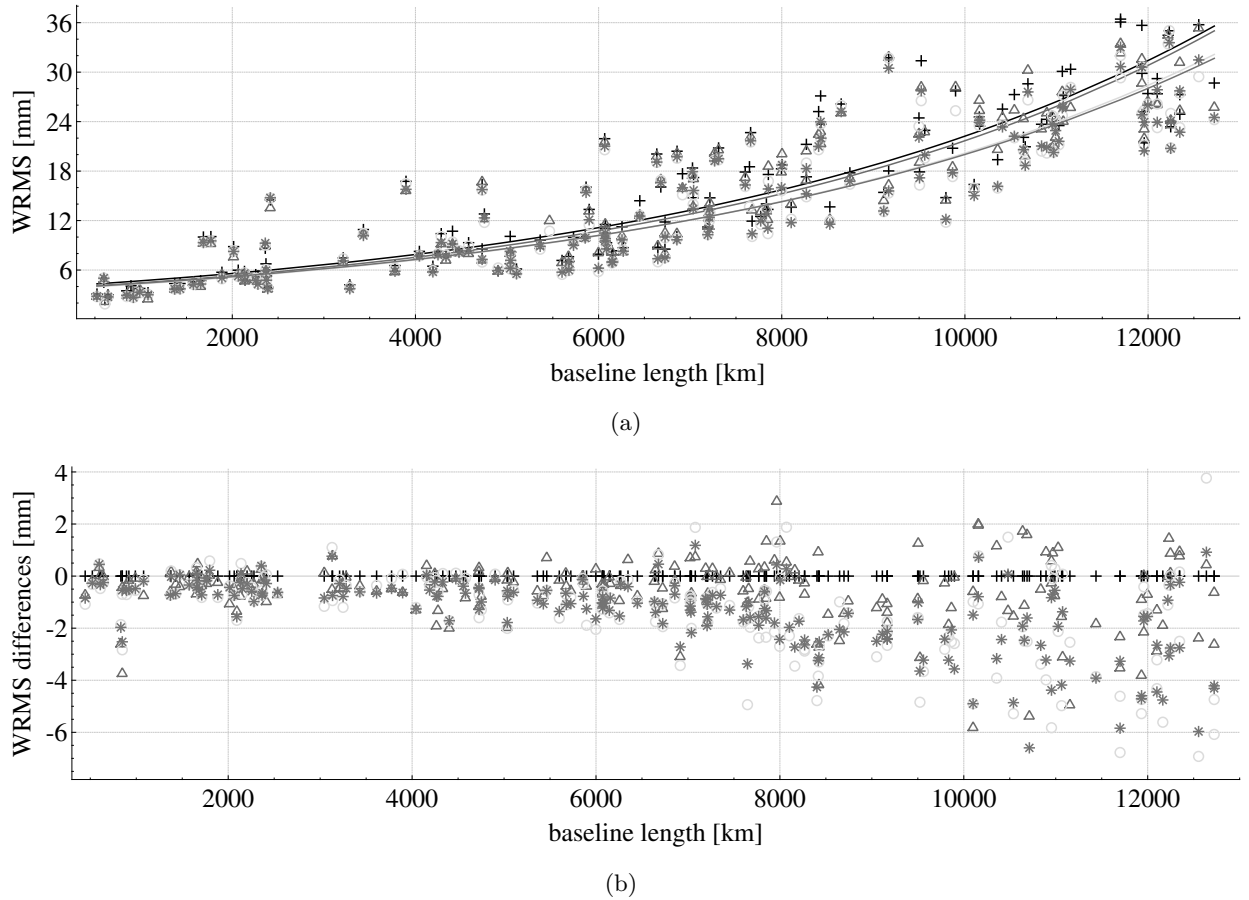
Figure 5.3: Baseline length repeatabilities for about 2700 VLBI sessions between 1993 and 2014 and different solution setups including a reference solution (black crosses), a simple solution with a constant additional noise term (purple triangles), the GIPSON et al. (2008) approach (green circles) and the turbulence-based solution (brown stars) (HALSIG et al. 2016A).

Finally, the baseline length repeatabilities are introduced, which can be regarded as the standard deviation for an individual baseline after removing a linear trend from a time series of baseline lengths (e.g., SCHUH and BÖHM 2013), and which is common practice in order to measure the accuracy of baseline length determinations. Fig. 5.3(a) shows the baseline length repeatabilities for all baselines, which occur in at least 30 sessions, for the same 2700 VLBI sessions and solution

setups as used before. An exponential trend is fitted to the data, which is included as solid lines in Fig. 5.3(a). Again, the turbulence-based solution and the approach by GIPSON et al. (2008) lead to the best results. For a better visualization, the baseline length repeatabilities shown in Fig. 5.3(a) are calculated as differences with respect to the reference solution. The result is illustrated in Fig. 5.3(b), where negative WRMS differences indicate an improvement, whereas positive values show a degradation in baseline length repeatabilities. It is evident, that including only a constant noise term to the variances of the observations, the results are getting better or worse to the same extent. Contrary, using the turbulence-based model as well as the GIPSON et al. 2008 model leads to a clear improvement in (almost) all cases. Expressed in numbers: compared to the reference solution, the baseline length repeatabilities improve for 50.3% of all baselines by at least 1 mm when using a turbulence-based stochastic model, whereas no baselines lead to a degradation by at least 1 mm. 49.7% of the baselines remain unchanged. A quite similar result is obtained when comparing the turbulence-based solution to the solution at constant noise level (improvement of 35.6% of the baselines versus degradation of 3.4% of the baselines by at least 1 mm; 61% of the baselines remain unchanged), which, as already stated, is not unusual in practice.

It was demonstrated, that incorporating refractivity fluctuations due to turbulent motions into the stochastic model of VLBI observations, the solution improves substantially. The quality of the estimated parameters increases sharply with respect to the baseline length repeatabilities. When using the turbulence-based solution in contrast to the routine IVS solution or a solution based on an empirical model, up to 50 % of all baselines are improved by at least 1 mm, whereas only a few baselines are degraded. Concerning the WRMS of post-fit residuals, the turbulence-based solution improves on average by 9.5 ps in quadrature compared to the empirical model, and even 24 ps in quadrature compared to the reference solution (cf. Tab. 5.1). Finally, the χ^2 values are almost always close to one indicating a realistic adjustment or, more precisely, an almost complete stochastic model of the observations. Only in a few cases and individual experiments $\chi^2 \approx 1$ is not satisfied. This issue has to be investigated in more detail in the future, but nevertheless, possible reasons will be briefly discussed in Sec. 5.3.

5.1.4   Model Validation in a Local VLBI Network

In addition to the traditional VLBI networks, the turbulence model was applied to two short baselines in Hobart, Australia, and Wettzell, Germany. Since the initial turbulence model of KER-MARREC and SCHÖN (2014) was originally developed for small-scale GNSS networks, these sessions provide an opportunity to validate the VLBI-specific turbulence model for local VLBI networks as well.

The first two out of a total of seven specially designed WHISP sessions (WHISP1 and WHISP2; see Ch. 6) observed on 27 August 2014 and 23 October 2014, respectively, were analyzed. Both sessions only consist of one short baseline between the 20 m radio telescope and the north antenna of the twin telescope at the Wettzell Geodetic Observatory. Tab. 5.2 lists the χ^2 values and WRMS of post-fit residuals for both sessions. The results vary from the findings of the global baselines. The χ^2 values derived from the reference solution are approximately 1.3 and 1.8, and, therefore, much smaller than in the traditional case. Introducing a constant term to the variances of the observations or following GIPSON et al. (2008), the χ^2 values are clearly too small, particularly in case of the WHISP1 session ($\chi^2 < 0.5$), leading to an overestimation of the variances of the observations in these solutions. In contrast, the turbulence model always leads to results with $\chi^2 \approx 1$. Regarding the WRMS of post-fit residuals, the situation appears similar to the global

Table 5.2: Different solution setups including the reference solution and different strategies to refine the stochastic model of VLBI observations. The χ^2 and WRMS values for two specially designed WHISP sessions on 27 August (WHISP1) and 23 October 2015 (WHISP2) are illustrated for all solution setups (Halsig et al. 2016a).

	Solution type	χ^2 [-]		WRMS [ps]	
		WHISP1	WHISP2	WHISP1	WHISP2
A	reference solution	1.27	1.76	14.23	22.26
B	constant additional noise: 1 cm	0.32	0.48	15.01	23.29
C	Gipson et al. (2006-2008) constant and elevation-dependent noise	0.47	0.79	13.61	23.51
D	turbulence-based correlations	0.96	1.02	11.55	22.53

case, at least for WHISP2. In contrast, the WRMS of post-fit residuals for WHISP1 are sharply improved using the turbulence-based solution in comparison with all other approaches including the reference solution. The turbulence model will also be used for a more detailed evaluation of the WHISP sessions in Ch. 6.

The results obtained for the two WHISP sessions have been confirmed by analyzing a second short baseline between the two adjacent VLBI stations in Hobart, Tasmania (Australia) observed during the continuous VLBI campaign 2014 (CONT14). The χ^2 values for the same set of solutions is shown in Fig. 5.4(a). Concerning the global test, the results look similar to the findings obtained for the WHISP sessions in case of the simple solution with a constant additional noise term (purple triangles), where the solution leads to an overestimation of the variances of the observations, and the turbulence model (brown stars), where $\chi^2 \approx 1$ is satisfied. In contrast, the approach by Gipson et al. (2008) acts different for the Hobart experiment, because the solution leads, in contrast to the WHISP baseline, to an underestimation of the variances of the observations. The WRMS of post-fit residuals, on the other hand, confirm the previous findings (see Fig. 5.4(b)).

It has been demonstrated that the turbulence-based stochastic information introduced in this thesis leads to a clear improvement of the solution. For all short baselines, $\chi^2 \approx 1$ is fulfilled indicating a realistic adjustment and an almost complete stochastic model. In contrast, most of the other refinement strategies either lead to an overestimation or underestimation, which is not even identical for a certain strategy applied to different baselines. Concerning the WRMS of post-fit residuals, the turbulence-based solution provides the best results for almost all cases. While in the global case the Gipson et al. (2008) method and the turbulence based method show a similar performance, here the application of the latter is clearly advantageous.

(a)

(b)
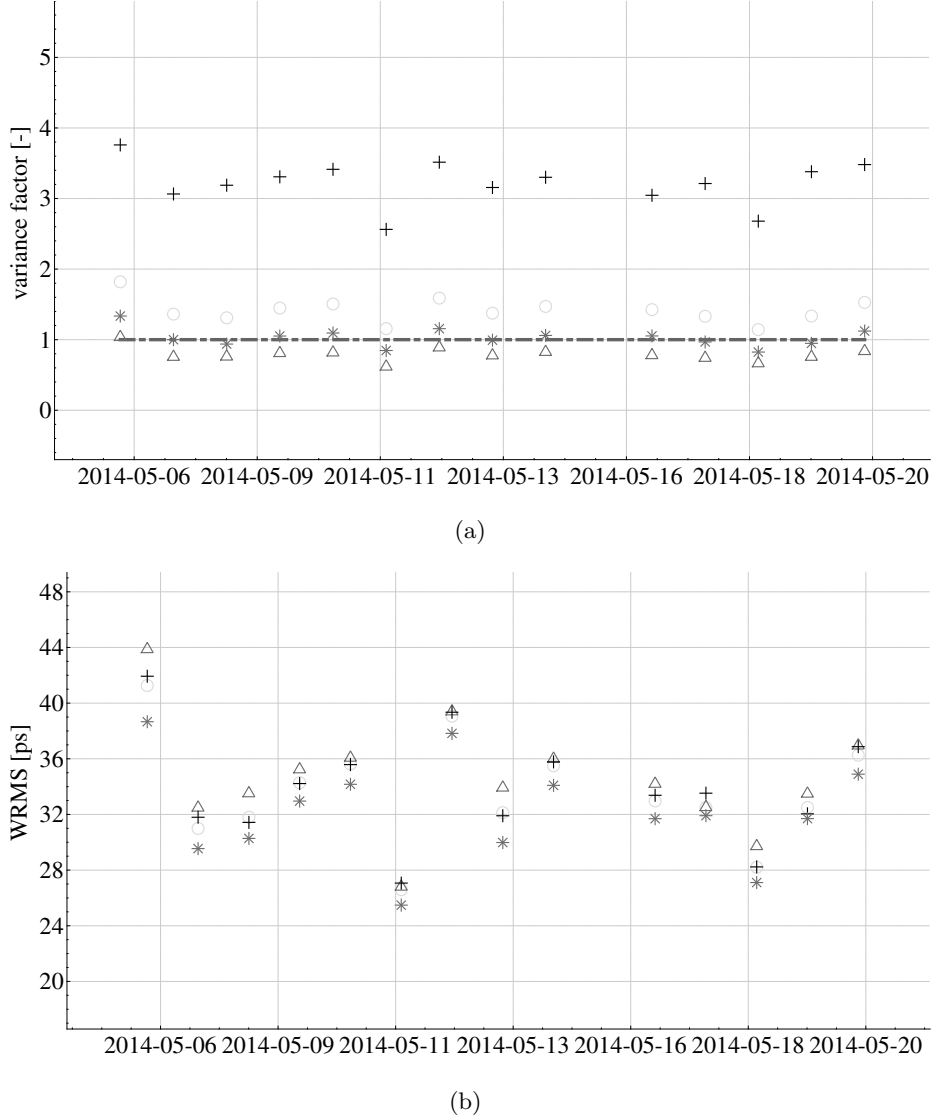
Figure 5.4: (a) χ^2 values and (b) WRMS of post-fit residuals for the short baseline in Hobart, Australia, observed during the CONT14 campaign in May 2014 and different solution setups including a reference solution (black crosses), a simple solution with a constant additional noise term (purple triangles), the GIPSON et al. (2008) approach (green circles) and the turbulence-based solution (brown stars). The grey dashed line in (a) represents $\chi^2 = 1$ (HALSIG et al. 2016A).

5.1.5 Influence of the Turbulence Parametrization

As already stated in Sec. 5.1.2, the determination of the input parameters for the turbulence model is challenging. Although it has been demonstrated that the turbulence model performs very well only based on experience-based values for C_n^2, H, v and a, b, c, the influence of the turbulence parameters on the VLBI solution is briefly discussed in this section.

For this purpose, the experiments of the two-week continuous VLBI campaign 2002 (CONT02) have been analyzed seven times with respect to the data analysis setup described in Sec. 5.1.2, only differing in the determination of the turbulence parameters. The different data analysis settings are summarized in Tab. 5.3. The experience-based parametrization used in the previous sections is described by setup 1, which is referred to as the reference solution in the following. The other parameter settings are chosen in a way that in each case one turbulence parameter is modified with respect to the reference parametrization (highlighted in Tab. 5.3). In this context, setup 2 leads to a modification of the structure constant, while a change of the effective tropospheric height is covered by setup 3 and 4, respectively. The anisotropic scaling factors are changed in setup 5 and 6, and finally, a change in the wind velocity is performed in setup 7. Additionally, a solution without using the turbulence model (denoted by solution (A) in the previous sections) is provided as a general reference (setup 0).

Table 5.3: Different data analysis settings with respect to the turbulence parameters: the structure constant C_n^2, the effective tropospheric height H, the anisotropic scaling factors a, b, c, and the wind velocity v.

Setup:	C_n^2 $[\mathrm{m}^{\frac{2}{3}}]$	H [m]	a, b $[-]$	c $[-]$	v $[\frac{\mathrm{m}}{\mathrm{s}}]$
0	-	-	-	-	-
1 (reference)	$1 \cdot 10^{-14}$	2000	1	0.01	8
2	$\mathbf{2 \cdot 10^{-14}}$	2000	1	0.01	8
3	$1 \cdot 10^{-14}$	**1000**	1	0.01	8
4	$1 \cdot 10^{-14}$	**3000**	1	0.01	8
5	$1 \cdot 10^{-14}$	2000	1	**1**	8
6	$1 \cdot 10^{-14}$	2000	1	**0.1**	8
7	$1 \cdot 10^{-14}$	2000	1	0.01	**4**

In order to investigate the influence of the turbulence parameters on the individual VLBI session, the χ^2 values are determined for all experiments and parametrization settings and illustrated in Fig. 5.5(a). The turbulence-based reference solution (setup 1) is depicted as red dots, while the reference solution without using a turbulence model (setup 0) is represented in black. The solution with respect to a modified structure constant (setup 2) is given by green dots, and a change of the effective tropospheric height is visualized by light (setup 3) and dark blue (setup 4) dots. Assuming more symmetric eddies as represented by the relation of the anisotropic scaling factors is represented by purple (setup 5) and magenta (setup 6) dots. Finally, a reduction in the wind velocity is visualized by orange dots.

(a)

(b)
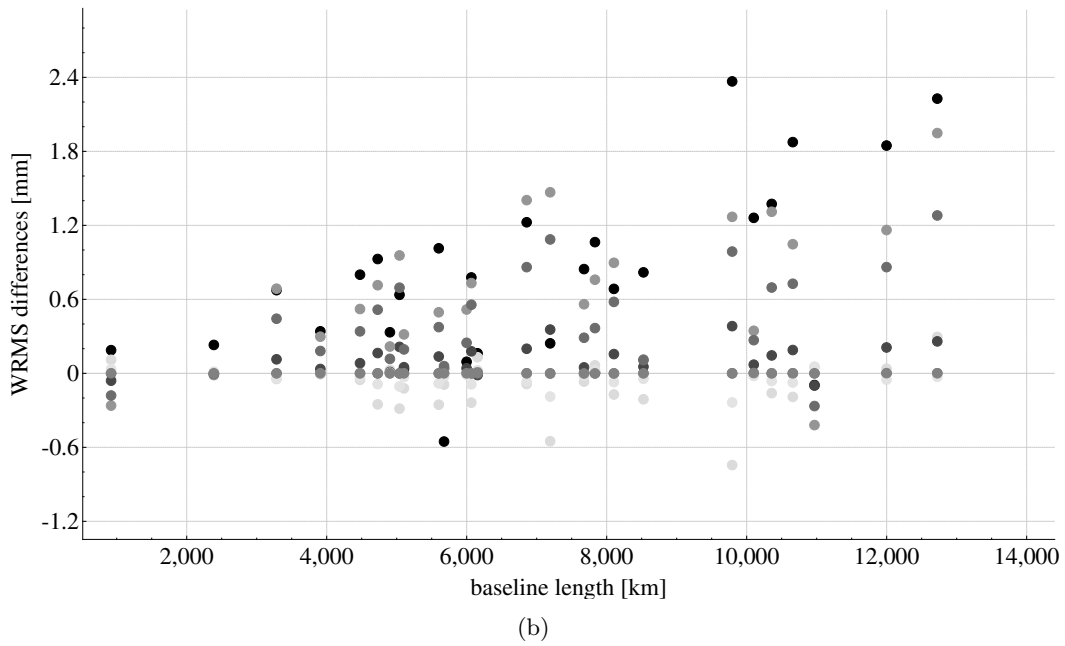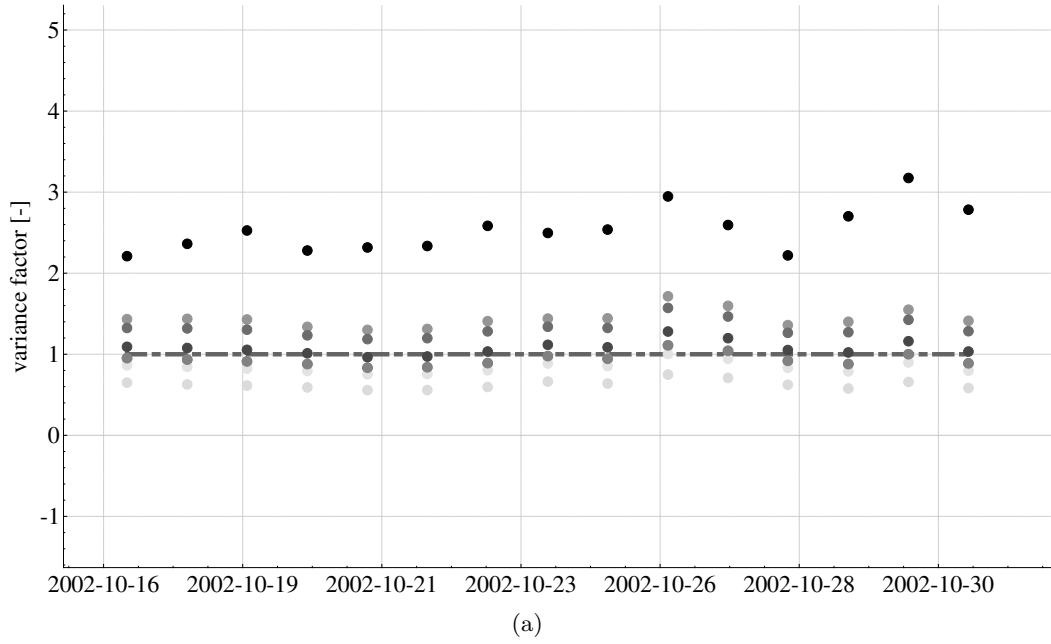
Figure 5.5: The influence of different turbulence parametrizations on the χ^2 values and the VLBI target parameters in terms of the baseline length repeatabilities, plotted as difference with respect to the turbulence-based reference solution (setup 1; red). The black dots (setup 0) denote a solution without using a turbulence model. The solution with a modified structure constant (setup 2) is given by green dots, and a change of the effective tropospheric height is visualized by light (setup 3) and dark blue (setup 4) dots. A modification of the anisotropic scaling factors is represented by purple (setup 5) and magenta (setup 6) dots. Finally, a reduction in the wind velocity is visualized by orange dots (almost fully covered by the red dots).

The reference turbulence solution generally satisfies the condition $\chi^2 \approx 1$, while the solution without applying the turbulence model leads to $\chi^2 \approx 2 - 3$, which fits very well the findings summarized in Tab. 5.1. Increasing the structure constant ($2 \cdot 10^{-14}$ instead of $1 \cdot 10^{-14}$; green), the χ^2 values become smaller, indicating an underestimation of the variances of the observations. A change in the effective tropospheric height results in a minor increase or decrease in the derived χ^2 values, depending on whether reduce (1000 m instead of 2000 m; dark blue) or increase the tropospheric height (3000 m instead of 2000 m; light blue). Considering the turbulent eddies to be more symmetric, and therefore, ignoring the requirement of anisotropy, leads to a degradation of the solution: the smaller the ratio between the vertical anisotropic scaling parameters c to the horizontal ones a and b, the larger the increase of the χ^2 value. Finally, reducing the wind velocity from 8 to 4 $\frac{\mathrm{m}}{\mathrm{s}}$ has hardly any effect on the χ^2 values (the orange dots are almost fully covered by the red dots). It is evident, that the modification of the turbulence parameters seems to behave as a scaling effect in the χ^2 values of the individual VLBI sessions.

The influence of the turbulence parameters is also evaluated with respect to the VLBI target parameters in terms of the differences in baseline length repeatabilities with respect to the turbulence-based reference solution (setup 1; red). Using the same color codes as defined above, the result is illustrated in Fig. 5.5(b), where positive values denote a degradation while negative values represent an improvement. It is evident, that the different parametrization settings show a more random behavior in contrast to the scaling effect observed in case of the χ^2 values. Compared to the turbulence-based reference solution, the baseline length repeatabilities decrease for the adjustment without applying the turbulence model (black), which however could have been expected based on the findings of the previous sections, but also for both solutions increasing the anisotropic scaling factor c (purple and magenta). Again, this is clear proof that the turbulence medium can not be assumed as an isotropic medium. In contrast, the modification of the structure constant leads to an improvement in terms of baseline length repeatabilities. However, keeping in mind, that the solution showed an underestimation of the variances of the observations, this parameter setting seems not be optimal. The influence of the effective tropospheric height is comparatively small, and, finally, the reduction of the wind velocity has again no considerable effect on the results.

In general, the order of magnitude in the differences of baseline length repeatabilities is comparably small in all cases, expect for the modification of the anisotropic scaling factors, which leads to a clear degradation, and the structure constants, which lead to an improvement in terms of baseline length repeatabilities, but shows a worse behavior concerning the χ^2 values. In conclusion, this analysis confirms the assumption, that, first, the turbulence parameter is considerably less sensitive to the turbulence parameters than other turbulence models, as for instance, the SIGMA-C model, which is applied to VLBI observations in Sec. 5.2, and second, the experience-based model parametrization is sufficient in case of VLBI observations.

5.1.6 Performance and Computational Costs

Usually, the use of a fully populated variance-covariance matrix in the stochastic model represents the restrictive factor keeping the computational costs small. In this regard, several VLBI sessions of different network volumes and, therefore, with different quantity of data are used to validate the initial performance of the turbulence model.

For the single-baseline VLBI Intensive sessions of 1 hour duration, which are almost observed daily for continued UT1 determinations, the computational effort is practically identical to the standard

case of the IVS. This relates as well to small networks consisting of three stations and about 400 observations. Regarding for instance the WHISP sessions with over 1000 observations on one baseline (e.g., WHISP1-3), there is hardly no difference between the solutions with and without turbulent correlations. For the WHISP sessions observing in a triangular network (e.g., WHISP5-7), the computational costs are already slightly increasing by a factor of approximately 1.5 to 2, if the full parameter set (station positions, EOPs, atmosphere and clock correction parameters with piece-wise linear intervals of 30 to 60 minutes, and atmospheric gradients) is estimated. When increasing the number of observation (i.e., 5.000 and more), the additional computational time increases up to the factor 5. In this case, the turbulence-based solution also requires a little more time than the other strategies taken for validation purposes (i.e., the Gipson et al. (2008) model and the approach with constant additional noise), which is of course due to the correlations only taken into account by the turbulence-based model. However, the maximum computational effort is still not higher than 60 seconds in these cases. Thus, the turbulence model is feasible for common VLBI sessions without introducing too much additional computational effort.

However, for future applications, particularly in case of the new VGOS (VLBI Global Observing System, Niell et al. 2013) networks providing tenfold increased number of observations, and there-fore, a dramatically increased data volume, the performance of the initial strategy is not sufficient anymore. VGOS-like experiments are given by, for instance, the continuous VLBI campaign in 2014 (CONT14), providing up to 20.000 observations and more per session. For such applications, further optimization strategies have to be found to adapt the model to the new challenges. One very simple possibility would be the use of finite variance-covariance matrices, when assuming that the spatial and temporal correlations are restricted to certain distances and time periods, respectively. This leads to a block diagonal structure instead of a fully populated variance covariance matrix. This could be achieved without loss of generality, since the covariances of observations with very large temporal or spatial distances are numerically zero anyway. This concept is already implemented in ivg::ASCOT within this thesis allowing for a first reduction of the computational effort.
Further potential savings of computational costs could be achieved by introducing a parallel com-puting system. For instance, the covariance matrices for the individual stations could be calculated separately and subsequently merged into an overall variance covariance matrix for all observa-tions. For this purpose, different functionalities for the structure of the turbulence model have been already implemented in ivg::ASCOT in the context of this thesis. The turbulence-based variance-covariance matrix can either be created together for all stations, or calculated separately for each individual station in a first step and combined to one overall variance covariance matrix in a second step. Both approaches deliver the same results. Although the computational effort is, of course, increasing for the alternative implementation in a stand-alone-mode, the functionality already lays the foundation for parallel computing, which is generally already possible with ivg::ASCOT.

5.2 An Alternative Model Describing Turbulence in VLBI

As a first step towards the development of the turbulence model presented in Sec. 5.1, also an alternative approach describing atmospheric turbulence in VLBI data analysis has been implemented and evaluated. The SIGMA-C model (SCHÖN and BRUNNER 2008A; SCHÖN and BRUNNER 2008B, see Sec. 4.3) initially developed for GNSS carrier phases was modified for VLBI observations to describe atmospheric turbulence in a physically reliable sense and to include spatial and temporal correlations between the observations, which are induced by turbulent motions in the neutral atmosphere. The turbulence model is also based on the Kolmogorov turbulence theory and the distance separating the two signal rays, and is formulated in a power spectrum representation. Similar to the turbulence model presented in Sec. 5.1, the atmosphere can be described as an inhomogeneous and anisotropic medium, which is not the case for most other approaches modeling atmospheric turbulence.

5.2.1 Model Validation with Continuous VLBI Observations

In order to perform a first evaluation of the VLBI-specific SIGMA-C model, the turbulence model is applied to the continuous VLBI campaign 2011 (CONT11), which provides continuous VLBI observations over two weeks with an almost identical network over the whole period. CONT sessions benefit from the high number of observations compared to the routine 24 h sessions and are supposed to represent the next generation of VLBI observations (VGOS). For validation purposes, two reference solutions are generated only differing in the application of the baseline-dependent re-weighting procedure (PETROV 1998, see Sec. 5.1.1). The VLBI parameters are determined in a classical least squares adjustment with standard modeling and parameter estimation settings following the IERS 2010 conventions (PETIT and LUZUM 2010). While the source positions are fixed to their positions in the current version of the International Celestial Reference Frame (ICRF2, FEY et al. 2015), telescope coordinates are estimated. A no-net-translation (NNT) and a no-net-rotation (NNR) condition with three equations each are formulated as constraints to remove the natural VLBI rank deficiency and to prevent the system of equations from singularities (e.g., ANGERMANN et al. 2004). The clock behavior is modeled by a quadratic polynomial and additional continuous piece-wise linear functions (CPWLF) with a temporal resolution of 60 minutes, and the zenith wet delays and troposphere gradients are parametrized as CPWLF with a temporal resolution of 60 minutes and 6 h, respectively. In order to stabilize the equation system, the clock and tropospheric parameters are supplemented by further constraints in the form of pseudo observations. The mapping functions VMF1 are used to relate the atmospheric parameters from zenith to the line of sight.

While the two reference solutions have to be supplemented by an arbitrary re-weighting procedure, in case of turbulence modeling the re-weighting option is completely turned off, and the stochastic model is purely derived from the initial correlator weights and the turbulence model, leading to a fully populated variance-covariance matrix.

All solutions are compared in terms of baseline length repeatabilities measuring the accuracy of baseline length determinations. The baseline length repeatabilities are calculated for the solution re-weighting the observations (setup 1, black diamonds), the solution turning off the re-weighting option (setup 2, dark gray points), and the turbulence-based adjustment (setup 3, dark gray squares). The results are depicted in Fig. 5.6(a). Both solutions using strategies to refine the stochastic model

(a)

(b)
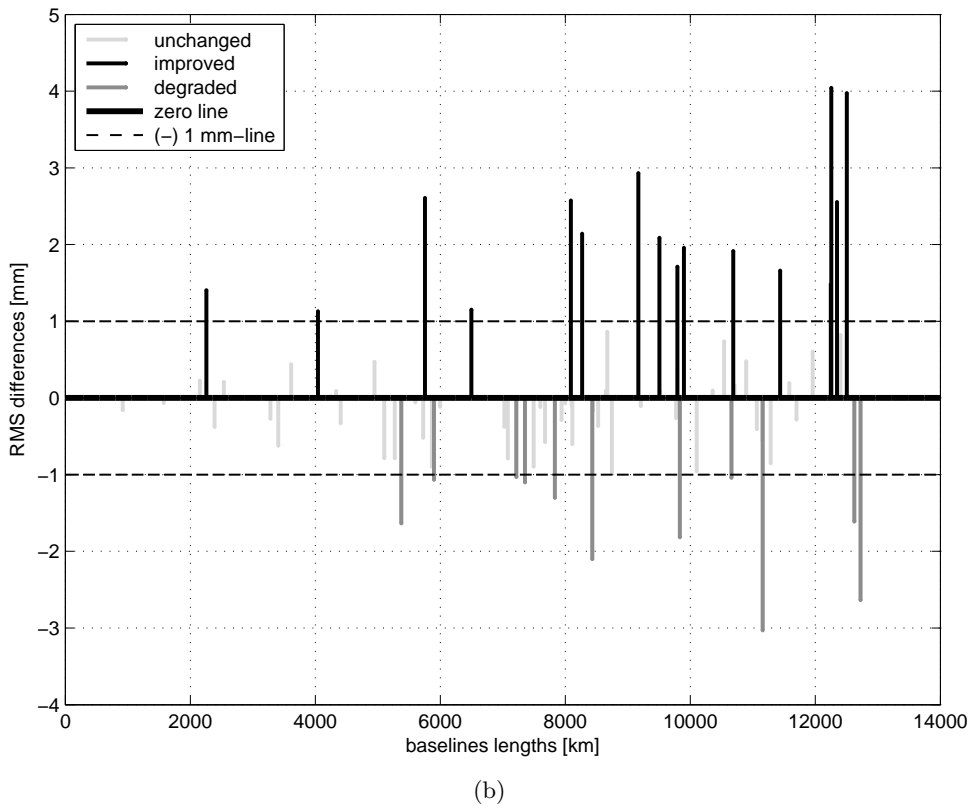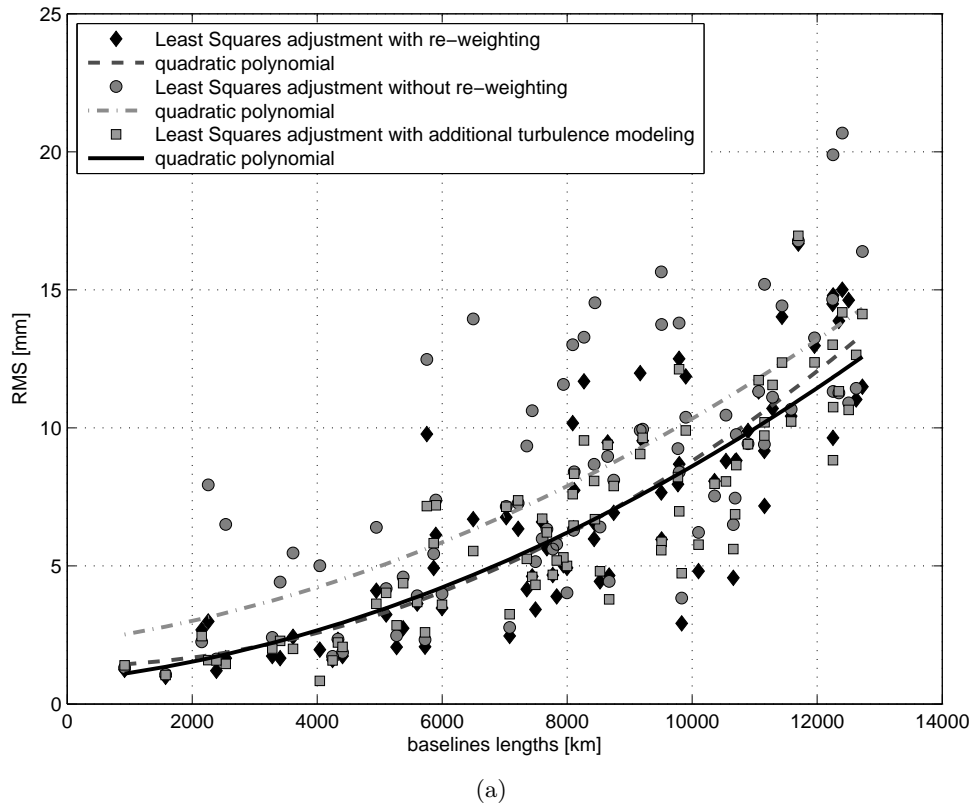
Figure 5.6: (a) Baseline length repeatabilities for a least squares adjustment with (setup 1, black diamonds) and without (setup 2, dark gray points) re-weighting the observations as well as for a least squares adjustment with turbulence modeling (setup 3, dark gray squares). (b) RMS differences between setup 1 and 3, where black bars show an improvement, dark gray bars denote a degradation and light gray bars indicate unchanged baseline lengths (HALSIG et al. 2014).

are quite similar and the root mean squared (RMS) error for the baseline length repeatabilities decreases sharply compared to the solution without additional weights in any form.

In order to go into more detail, the RMS differences between the solution re-weighting the observations and the solution modeling turbulent conditions are presented in Fig. 5.6(b), where black bars indicate an improvement, light gray bars denote a degradation and light gray bars indicate unchanged baseline lengths. Expressed in figures, about 25% of the baselines are improved by at least 1 mm, whereas 12% get worse by at least 1 mm and 63% remain unchained.

5.2.2 The Influence of Different Turbulence Parameters

In a second validation step, the configuration options of the turbulence model are analyzed in more detail. Special consideration is given to the input turbulence parameters necessary for the model, particularly the structure constant C_n^2 as a general measure for the strength of turbulence and the effective tropospheric height H. Different solution setups have been processed with the same analysis settings described above but a different turbulence parametrization, and are summarized in Tab. 5.4. The structure constant is either assumed to be equal for each station (setups 3 and 4) or estimated from radar measurements, radiosonde data or GNSS data (setups 5, 6 and 7) as described by NILSSON et al. (2010). The station-dependent C_n^2 values used in this study (cf., HALSIG et al. 2014) are taken from NILSSON et al. (2010) or NILSSON et al. (2014).

Table 5.4: Solution setups w.r.t. the Calc/Solve re-weighting option (PETROV 1998) and the parametrization of the structure constant (equal for all stations or station-dependent estimates) and the tropospheric effective height (equal for all stations or station-dependent estimates). The mean χ^2 value and WRMS of post-fit residuals for the delay observables are given for the CONT11 interval (HALSIG et al. 2014).

Setup	re-weighted	C_n^2	H	χ^2 [-]	WRMS [mm]
1	YES	-	-	0.93	25.07
2	NO	-	-	3.68	26.32
3	NO	$C_n^2 = 1 \cdot 10^{-14}\ m^{-\frac{2}{3}}$	1 km	3.25	17.22
4	NO	$C_n^2 = 1 \cdot 10^{-14}\ m^{-\frac{2}{3}}$	2 km	2.99	16.50
5	NO	NILSSON et al. (2014)	2 km	2.32	14.55
6	NO	NILSSON et al. (2010)	NILSSON et al. (2010)	2.27	14.39
7	NO	NILSSON et al. (2014)	2.5 km	2.17	14.01

The quality of the different solution setups is again quantified by the χ^2 value and the WRMS of post-fit residuals. The χ^2 value and the WRMS of post-fit residuals of the delay observables are

depicted in Fig. 5.7(a) and Fig. 5.7(b), respectively, and the mean values over the period of the CONT11 campaign are given in Tab. 5.4.

Since additional noise is iteratively added to the observations during the re-weighting strategy (black diamonds), the χ^2 are close to one, while turning off the re-weighting option (setup 2, dark gray points) leads to typical values of $\chi^2 \approx 3 - 4$ as also reported by Gipson et al. (2008). Compared to this reference value, the solutions with constant atmospheric parameters (setup 3, dark gray squares and setup 4, light gray triangles, respectively) lead only to a little decrease in the χ^2 value. Using estimated structure constants (setup 5, black circles; setup 6, black triangles, setup 7, light gray diamonds) sharply reduces the χ^2 value. However, for all cases the χ^2 values are still slightly too high, concluding that the deterministic or stochastical model assumptions are not optimal. For the same solution setup, Fig. 5.7(b) shows the weighted root mean squared scatter per solution based on the post-fit residuals. It is obvious that for some solutions, particularly using the more realistic C_n^2 values (setup 5, black circles; setup 6, black triangles; setup 7, light gray diamonds), the WRMS of post-fit residuals decrease sharply compared to the reference solution defined above. There are only small differences in the three solution types using estimated C_n^2 values.
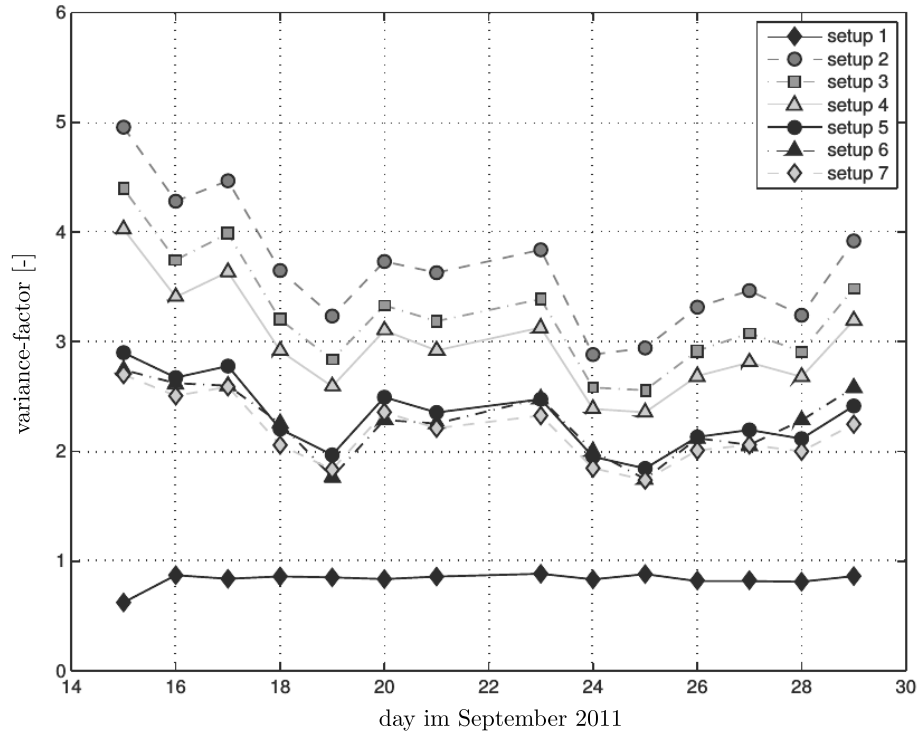
(a)
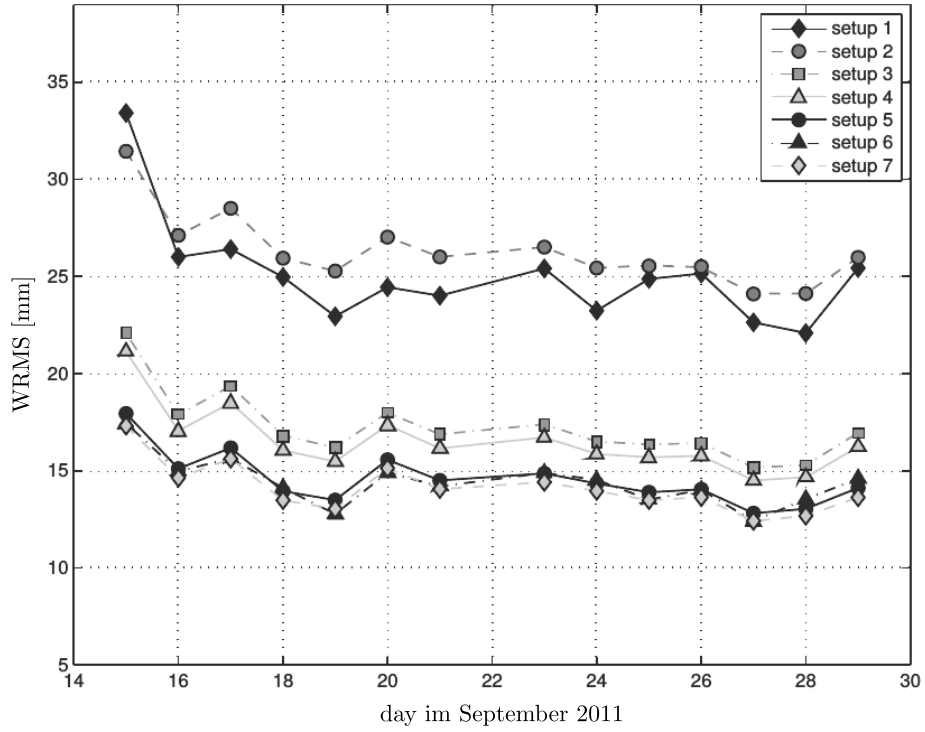
(b)

Figure 5.7: Validation of the different solution parametrizations for the CONT11 campaign: (a) χ^2 values and (b) WRMS of post-fit residuals of the delay observables (HALSIG et al. 2014).

5.3   Discussion

One main objective of this thesis is to ensure an operationally sufficient method to deal with correlations between the observations due to high-frequency refractivity variations in the neutral atmosphere as the dominant source of uncertainty in the VLBI data analysis (objective 1). In order to reconcile both objectives, an atmospheric turbulence model has been developed in this thesis.

As a first step towards the development of the final turbulence model presented in Sec. 5.1, the SIGMA-C model has been implemented and evaluated as an alternative approach describing atmospheric turbulence in VLBI data analysis.
It has been demonstrated that the WRMS of post-fit residuals have been reduced sharply compared to two reference solutions with and without applying a method (PETROV 1998) to re-weight the observations. This applies in particular when using appropriate estimates for the structure constant and the effective tropospheric height, which can be determined, e.g., from GPS data. But even in case of only using model or experience-based parameters for C_n^2 and H, the WRMS of post-fit residuals still decreases compared to the reference solutions. In terms of baseline length repeatabilities, the turbulence-derived solutions improve sharply compared to the least squares adjustment without re-weighting the observations, but only minor improvements are observed with respect to the solution turning on the re-weighting option. Although the χ^2 values decrease for the new approach, they are still little too high ($\chi^2 \approx 2-3$ compared to $\chi^2 \approx 3-4$ for the case without any re-weighting) indicating that the variances of the observations are still underestimated or there are still some other terms that are not adequately modeled. Concluding, the SIGMA-C model might not work as well as expected for VLBI data analysis, at least with respect to the statistical tests. Due to the necessary volume of integrations the SIGMA-C model is also mathematically difficult to handle and leads to large computational costs.

The two shortcomings have been already addressed by the preferred turbulence model introduced in Sec. 5.1. Applied to VLBI observations, this model leads to a better overall performance in VLBI data analysis.

It has been demonstrated that the turbulence-based model is generally suitable for different network geometries and can be used for traditional long baselines as well as for local approaches. The quality of the estimated parameters increases sharply with respect to the baseline length repeatabilities, evaluated for over 2700 VLBI sessions provided by the IVS. When using the turbulence-based solution in contrast to the routine IVS solution or a solution based on an empirical model, up to 50 % of all baselines are improved by at least 1 mm, whereas only a few baselines are degraded. A clear solution improvement with respect to additional statistical validation criteria has been demonstrated. The WRMS of post-fit residuals generally decreases for the majority of VLBI experiments, in particular for observations on short baselines. The mean χ^2 values are approximately between 1 and 1.2 in all cases, indicating a complete or almost complete stochastic model of VLBI observations.

This does not apply to the other approaches evaluated here, independent of using only a constant additional noise term or empirical models as, for instance, provided by GIPSON et al. (2008). It is worth mentioning that, of course, the amount of re-weighting the observations in these models could be varied individually to always guarantee $\chi^2 \approx 1$. A similar approach was suggested by PETROV (1998), who proposed a baseline-dependent procedure for an iterative re-weighting of the observations until $\chi^2 \approx 1$. However, it needs to be clearly pointed out that there is no general validity on the amount of additional noise which needs to be added for the individual session,

baseline, or station. Generally, the different models either lead to an over- or underestimation of the variances of the observations. The behavior is not necessarily identical, or even similar for a specific strategy applied to different VLBI experiments. Solely the turbulence-based solution is able to generally allow $\chi^2 \approx 1$ in global and local networks.

It is worthwhile to note that also for the turbulence case the results on local baselines are even better than those for global applications. Keeping in mind, that of all strategies refining the stochastic model of VLBI observations, only the turbulence model considers correlations between the observations in a proper way. Consequently, it becomes obvious that the differences between the results of the solution setups are larger in local VLBI applications where high spatial and temporal correlations are found. Contrary, traditional VLBI baselines between two stations are very large ranging up to several hundreds of kilometers, and the spatial correlations disappear almost completely and only temporal correlations between successive observations are present. Due to the fact that the same turbulence parametrization is used at both stations of a baseline, it could be expected that this assumption is valid in local but not in global applications. For instance, it is well known that the weather conditions for the VLBI station Tsukuba, Japan, are quite severe (e.g., PANY et al. 2011), and a larger structure constant might be assumed. The consequence would however be, that the structure constant has to be chosen or even estimated with respect to the current weather conditions, which conflicts the requirement of an operationally efficient modeling approach. Although the stochastic model might be further improved, it may be doubted that only modifying the turbulence parametrization could completely explain this issue. Instead, it is presumed, that refractivity fluctuations in the neutral atmosphere are known to be the dominant but not only uncertainty sources in VLBI data analysis. Please note that, at this stage, the stochastic model of VLBI observations now consists of uncertainties derived from the VLBI correlation process and the atmospheric turbulence model. It might be worth to investigate the influence of other uncertainty sources such as the stability of the VLBI system. This includes, first of all, the clock behavior, but also addresses certain issues occurring during the signal recording and correlation process. Since, however, stability issues can be better quantified by close-range VLBI observations, this topic will be further discussed within the framework of the WHISP project in Ch. 6. Additionally, the influence of the atmospheric gradients, for which the short baselines are not sensitive, on the turbulence model needs to be further investigated.

One major achievement is the fact that the application of the turbulence model is operationally efficient and appropriate for routine mass analysis of VLBI sessions. The computational costs are kept to a limited extent for common VLBI sessions, which is a not inconsiderable factor in the data analysis. For future applications, such as the upcoming VGOS networks, further optimization strategies have to be found to adapt the model to the new challenges. First measures have already been initiated in ivg::ASCOT to address the identified issues in the context of this thesis..

In conclusion, incorporating the atmospheric turbulence model into the stochastic model of geodetic VLBI data analysis leads to an improvement of the solution with regard to the baseline length repeatabilities, statistical tests, the WRMS of post-fit residuals, and more realistic standard deviations of the target parameters. The turbulence model is operationally efficient, particular for current VLBI networks, and appropriate for routine mass analysis of VLBI sessions (objective 1). The approach is now a standard component of ivg::ASCOT.

6. Case Study: The WHISP Project

Geodetic VLBI observations with radio telescopes, which are located in an immediate neighborhood, provide an optimal experimental setup for investigations on atmospheric refraction and system stability issues, but have never been realized so far. Up to now, the stability of observing systems and the impact of atmospheric refraction effects in geodetic and astrometric VLBI applications has always been characterized through baselines with lengths of at least a few hundreds of kilometers.

The commissioning phase of the worldwide first twin radio telescope at the Geodetic Observatory Wettzell in the Bavarian Forest in Germany (SCHÜLER et al. 2015) now allows investigations of atmospheric refraction and system stability issues in the context of geodetic VLBI observations with radio telescopes on a local scale. Together with the 20 m diameter radio telescope, two identical radio telescopes of 13.2 m diameter will form the first geodetic cluster of this type providing the basis for such close-range VLBI observations. In particular, the extremely high slewing rates of 12 degrees per second in azimuth and 6 degrees per second in elevation of the twin telescope will allow for a much improved sampling of the atmosphere. The completion of the first of the two new telescopes at the Wettzell Geodetic Observatory already provides an ample opportunity to carry out VLBI test observations on a baseline with a length of only about 120 m. This new opportunity is exploited within this thesis work through dedicated observing sessions.

Before refraction studies can be approached, some investigations are necessary to characterize the influence of the stability of the VLBI system. First of all, the estimation of zenith wet delay (ZWD) parameters and the interpretation of the residuals in the VLBI data analysis are closely linked to the stability of the hydrogen maser clocks feeding the local oscillators and other necessary electronics. While the telescopes are generally separated too far from each other so that a direct clock comparison is impossible, the favorable situation of co-located antennas now occurs at Wettzell to overcome this limitation.

A series of dedicated local and European VLBI sessions, referred to as WHISP (Wettzell HIgh SPeed) sessions, have been designed for quite different purposes (see Sec. 6.1 for more details). At first, sessions employing only the short baseline between the two radio telescopes at Wettzell have been observed. Those allow investigations on differential atmospheric parameters and, therefore, on refractivity variations in the neutral atmosphere. Then, the scenario was augmented by another VLBI station in Onsala, Sweden. The resulting European triangle is, on the one hand, used to compare atmospheric time series derived by two adjacent baselines. On the other hand, the stability of the observing system, in particular the clock system stability, is investigated in more detail. This allows a separation and classification of the different uncertainty contributions.

6.1 Close-range VLBI Observations

Geodetic short baseline observations, i.e., of up to several hundred meters, have been carried out at several occasions beforehand as part of standard network observations in the late 1990ies (HASE and PETROV 1999) or more recently (HERRERA-PINZON et al. 2017). In these cases, the number of observations on the short baseline was limited to not more than about 70-200 observations (IVS MASTER FILES 2017), depending on the network observing schedules which always balance between radio telescopes of different slew speeds.

In an observing schedule, the slowest telescope defines the overall speed for changing from one radio source to the next. On the baseline between the Wettzell 20 m telescope (Wz) and the new 13.2 m telescope (Wn), the Wz antenna is, thus, the limiting instrument with 3 and 1.5 degrees per second in azimuth and elevation, respectively (Tab. 6.1).

Table 6.1: Slewing rates of the three radio telescopes in the WHISP triangle, including the 20 m antenna (Wz) and the north tower of the twin telescope (Wn) at Wettzell, Germany, and the Onsala (On) radio telescope, Sweden).

Telescope	azimuth	elevation
	[degrees per second]	[degrees per second]
Wz	3	1.5
Wn	12	6
On	2.4	1

At a later stage when the south tower of the twin telescopes (Ws) will be operating, local high speed observations can be exploited with a triple of radio telescopes, and the potential of the new generation VLBI telescopes can be fully exhausted. The high potential of the VGOS (VLBI Global Observing System, NIELL et al. 2013) telescopes has already been demonstrated for the pair of prototype VGOS radio telescopes at the Goddard Geophysical and Astronomical Observatory (GGAO) of the Goddard Space Flight Center, Maryland, USA, and the Westford antenna at Haystack Observatory, Massachusetts, USA, which are separated by approximately 600 km. The slewing rates in azimuth and elevation are 5 and 1.1 degrees per second for the GGAO telescope and 3.3 and 2 degrees per second for the Westford antenna. An observing rate of approximately 45 observations per hour was obtained, which corresponds to about 1080 observations per 24 hour experiment (NIELL et al. 2014; NIELL 2015; NIELL et al. 2016).

In contrast to these tests, the emphasis of the WHISP project is the performance on a very short baseline of less than 200 m rather than on a 600 km baseline or even longer. Further, the limiting slewing rate of the 20 m diameter radio telescope is still comparatively high compared to other IVS telescopes in operation today. This applies particularly on other sites with co-located VLBI antennas as, for instance, Hobart, Australia, with a slewing rate of only 0.65 degrees per second in both azimuth and elevation. In addition, the number of observations, even including Onsala (On) in the schedule, is larger than most of the current routine data sets of the IVS, and twice to four times larger than any existing VLBI data set on a local scale.

Another interesting fact of these short baseline observations is that the sky above the Wettzell Geodetic Observatory is fully covered with observations in the short baseline case (Fig. 6.1(a)) and with only a small obstruction on the baselines to Onsala (Fig. 6.1(b)). This is a very big advantage compared to other network sessions where the horizon limits of distant telescopes produce rather asymmetric sky coverage features. It is, therefore and due to the large number of observations per unit of time, expected that the troposphere estimates are more reliable than in any other network session.

In this project, the aim is to investigate atmospheric refraction and system stability effects in geodetic and astrometic VLBI applications. A series of dedicated sessions has been designed and

(a) (b)
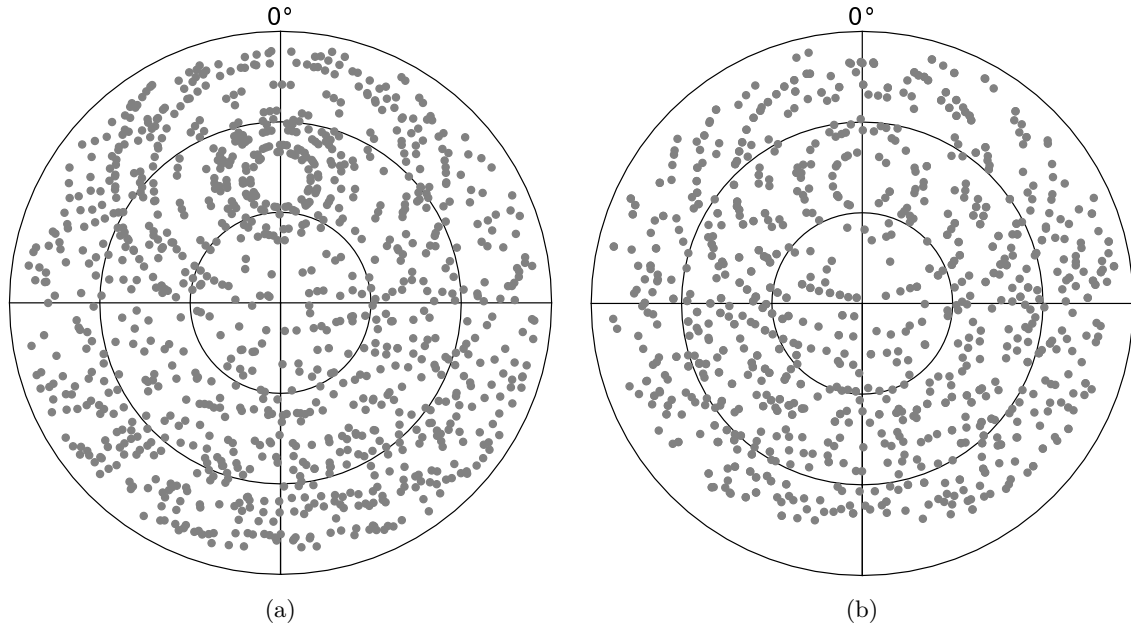
Figure 6.1: Sky plots of the 20 m radio telescope at Wettzell for the short baseline observations (here, WHISP3, a) and on the baseline to Onsala (here, WHISP5, b).

observed for quite different purposes. Three WHISP sessions were performed only using the 20 m diameter radio telescope and the north antenna of the twin telescopes, and therefore, consists of only one short baseline. Since the two stations are only separated by about 123 m and both telescopes always point in the same direction, it can be assumed that most systematic effects not stemming from the atmosphere and from the frequency distribution system are canceled out in the differential mode. These sessions are aimed to investigate local refractivity effects in a differential mode.

Table 6.2: Specially designed WHISP (Wettzell HIgh SPeed) sessions used in this study.

Name	observation time	# successful observations	baselines	comment
WHISP1	27 August 2014	658	Wn-Wz	
WHISP2	23 October 2014	1015	Wn-Wz	
WHISP3	18 February 2015	801	Wn-Wz	
WHISP4	3 August 2016	-	Wn-Wz-On	failed
WHISP5	9 November 2016	1958	Wn-Wz-On	
WHISP6	22 February 2017	1724	Wn-Wz-On	
WHISP7	5 July 2017	1852	Wn-Wz-On	

For three further WHISP sessions, also another VLBI radio telescope in Onsala (Sweden) is used in order to obtain two different European baselines between Onsala and the two antennas in Wettzell.

In the first place, these sessions are designed to estimate absolute atmospheric parameter series for both European baselines and compare them to each other. Second, these sessions are also used to investigate system stability effects. Unfortunately, one of these sessions (WHISP4) failed due to technical reasons and could not be used in this case study. An overview of the observed WHISP sessions is given in Tab. 6.2.

Generally, all WHISP sessions last 22 hours, and not, as is usually the case, 24 hours, since Wettzell joins the daily routine Intensive sessions of the IVS of one-hour duration. One of the main advantages of the WHISP sessions is the considerably increased number of observations compared to traditional 24h-sessions (Tab. 6.2).

6.2   Data Analysis

The geodetic data analysis is performed using the VLBI software package ivg::ASCOT (Artz et al. 2016; Halsig et al. 2017) following the Conventions (2010) of the International Earth Rotation and Reference Systems Service (IERS, Petit and Luzum 2010). The modeling settings are chosen with respect to the routine single-session data analysis strategies of the IVS. The VLBI target parameters are estimated in a least squares method using a Gauss Markov model (e.g., Koch 1999).

In case of the differential application, only atmospheric and clock parameters are estimated. The clock model parameter corrections are estimated as a second order polynomial and additional continuous piece-wise linear functions (CPWLF), i.e., linear splines (De Boor 1978), with a different resolution (see Sec. 6.4.2). The tropospheric model is described by Eq. (3.65) in Sec. 3.3, and the zenith wet delays are parametrized as CPWLF with a resolution of 15 to 60 minutes. Only differential zenith wet delays are estimated for well known reasons. In the least squares adjustment, the partial derivatives of the zenith wet delays are equal to the mapping functions with respect to the elevation angle of the respective observation. Under the assumption of estimating atmospheric parameters in an absolute sense, the elevation angles would be very similar for both stations only separated by about 120 m from each other. As a consequence, the partial derivatives are approximately the same for both parameters leading to highly correlated columns in the Jacobian matrix, which is, of course, not advisable. The Vienna mapping functions 1 (VMF1, Böhm et al. 2006a) are used to relate the atmospheric parameters from zenith to the line of sight. Azimuthal gradients are not estimated, because the short baseline is not sensitive to them. On the short baseline, the ionospheric correction term (see Sec. 2.1 for more details) has to be turned off, since the S-band data would harm the solution due to a radio frequency interference (RFI) issue on the Wettzell premises. The radio telescope coordinates are fixed with respect to an ivg::ASCOT multi-session solution, while source positions from the International Celestial Reference Frame (ICRF2, Fey et al. 2015) are used. Finally, the Earth orientation parameters are fixed to a priori values of the IERS C04 series.

Performing the data analysis of the triangle observations, zenith wet delays are parametrized as CPWLFs of different resolution (see Sec. 6.4.2), but now in absolute terms and not relative to another VLBI radio telescope. In this case, azimuthal gradients are estimated with a temporal resolution of 6 hours and the ionospheric correction was applied for the two baselines to Onsala, but not for the short baseline in Wettzell.

For the stochastic model, two approaches are distinguished. First, only a diagonal variance-covariance matrix is used, which consists of observation uncertainties based on the observed signal-to-noise ratio. In order to ensure $\chi^2 \approx 1$, the variances are inflated artificially by a constant and an elevation-dependent noise term according to GIPSON (2007) and GIPSON et al. (2008). Second, the stochastic model is augmented by the atmospheric turbulence model devised in this thesis and presented in Sec. 5.1, which automatically leads to $\chi^2 \approx 1$ without any further re-weighting. With the application of the turbulence model it is possible to routinely consider correlations due to turbulence-induced processes in the atmosphere in a physical and meteorologically meaningful sense, and stochastically describe small-scale refractivity variations in the neutral atmosphere. This leads to a fully populated variance-covariance matrix and to more realistic estimates and standard deviations. The successful application of the turbulence model has already been demonstrated in Sec. 5.1, where it has been shown, that the turbulence model leads to an improvement of the solution, in particular for local scale networks as used in this project.

6.3   System Stability

6.3.1   Behavior of Atomic Clocks

The estimation of zenith wet delay parameters and the interpretation of the residuals in the VLBI data analysis are closely linked to the stability of the hydrogen maser clocks feeding the local oscillators and other necessary electronics. In the case of the parameter estimation, the general assumption is that there are non-negligible correlations between the estimates of the atmosphere and the clock parameters. However, when studying the correlation matrix of the estimated parameters the correlations are only around 0.3 (NOTHNAGEL et al. 2002) which is still in the range of weak correlations.

The relative clock behavior is generally estimated in the form of a clock polynomial plus continuous piece-wise linear (CPWL) offsets while for the zenith path delays it is only the CPWL offsets. Both have a time resolution of 60 minutes, normally. Clocks and atmosphere are not resolved any further to keep the significance of the residuals. It should be emphasized that no soft constraints in the form of pseudo observations are used for the clocks, which usually are necessary to stabilize the equation system due to missing observations in some piece-wise linear segments. However, due to the clearly increased number of observations in case of the WHISP sessions, these constraints are omitted here. Consequently, we do not expect any adverse effects from that side on the estimates of the zenith wet delays because any clock variations on a time scale beyond 1 hour are covered by the CPWL estimates. Individual observations and the respective residuals within the one hour periods are considered to be more affected by variations in the clock behavior at shorter time scales.

Usually, the telescopes are separated too far from each other so that a direct clock comparison is impossible. However, at Wettzell we are in the favorable situation that the two telescopes are close enough together that a two-way time transfer with a fiber-optics link (TWOTT) can be realized (KODET et al. 2016B). In the last years, a very precise two-way time transfer (TWTT) using a coaxial cable as the transmission link (PÁNEK et al. 2013) was developed and implemented with high effort in order to identify unaccounted system delays at the Geodetic Observatory Wettzell. The general principle of the TWTT approach is depicted in Fig. 6.2. The system is divided into two units, A and B, which are connected by a transmission link. Both units consist of a timing signal generator (TSG) and an event timer (ET) measuring the arrival times of timing signals. The output
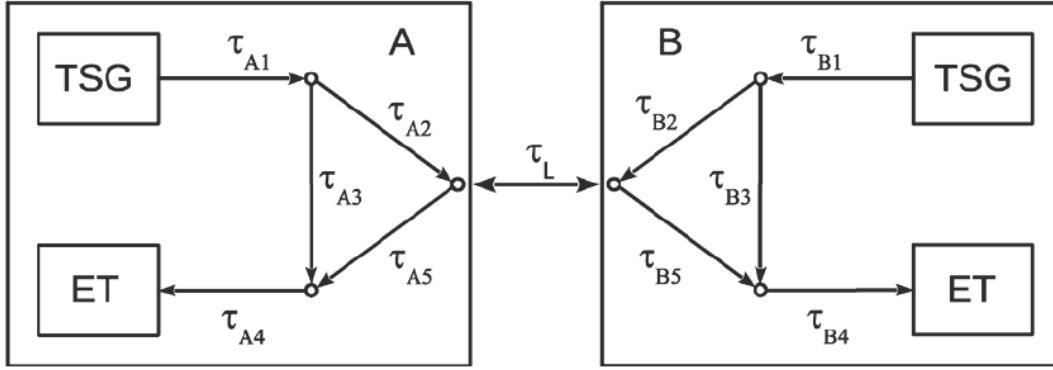
Figure 6.2: The general setup of the Two-Way Time Transfer system, which is divided into two units A und B connected by a transmission link, each consisting of a timing signal generator (TSG) and an event timer (ET) measuring the arrival times of timing signals. The output of the TSG and the input of the ET are connected to the transmission link by a network of five branches and three splitters and couplers, providing feedback of the transmitted signals back to the ET and the bidirectional use of the transmission line. The delays of the branches and the transmission link are denoted by $\tau_{A_{i=1\ldots5}}$, $\tau_{B_{i=1\ldots5}}$ and τ_L (KODET et al. 2016A).

of the TSG and the input of the ET in both units are connected to the transmission link. Therefore, a network of five branches connected with three splitters and couplers, is used, which provides feedback of the transmitted signals back to the ET and the bidirectional use of the transmission line. All branches and the transmission link have delays, which are referred to as $\tau_{A_{i=1\ldots5}}$, $\tau_{B_{i=1\ldots5}}$ and τ_L, respectively (see Fig. 6.2). Analyzing the TWTT process provides the opportunity to investigate the influence of the partial delays within the TWTT units on the resulting uncertainty of the time transfer (KODET et al. 2016A). The main disadvantage of this method results from the substantial increase of the uncertainty of the time transfer with the length of the transmission link due to the propagation loss at high frequencies (KODET et al. 2016A). To overcome this issue, the TWTT system was redesigned by using optical telecommunications technology. This results in the two-way optical time transfer (TWOTT) system implementing standard small form-factor pluggable optical transceivers, which leads to an increased area where the time transfer can be guaranteed with picosecond accuracy (KODET et al. 2016B).

Due to the rather involved evaluation process, this link had only been active during the WHISP7 experiment, but not for the other WHISP sessions. For this reason, the following arguments have to be discussed on the basis of WHISP7 and two further routine IVS sessions (on 26 October and 21 December 2015, NOTHNAGEL et al. 2015) where the 20 m (Wz) and the 13.2 m (Wn) telescopes observed simultaneously.

The TWOTT provides clock offsets with sampling rates of 1 s between the two hydrogen masers involved in the experiments, which supply the radio telescopes with a reference frequency. In Fig. 6.3, the stability of the two involved H-Masers is compared, which is expressed as Allan deviation (ADEV) during the two IVS sessions mentioned above. Concluding, the H-Masers have the same stability of $8.3^{-13}/\tau$ for averaging times up to 300 s with dominant white phase modulation, and for averaging times longer than 300 s the white frequency modulation is the dominant noise floor.

Since the frequency offset between the two H-Masers is $\frac{\Delta f}{f_0} = 2.1^{-13}$ (Jan Kodet, pers. comm.), the linear trend was subtracted to allow for a better recognition of the small-scale variations (e.g.,
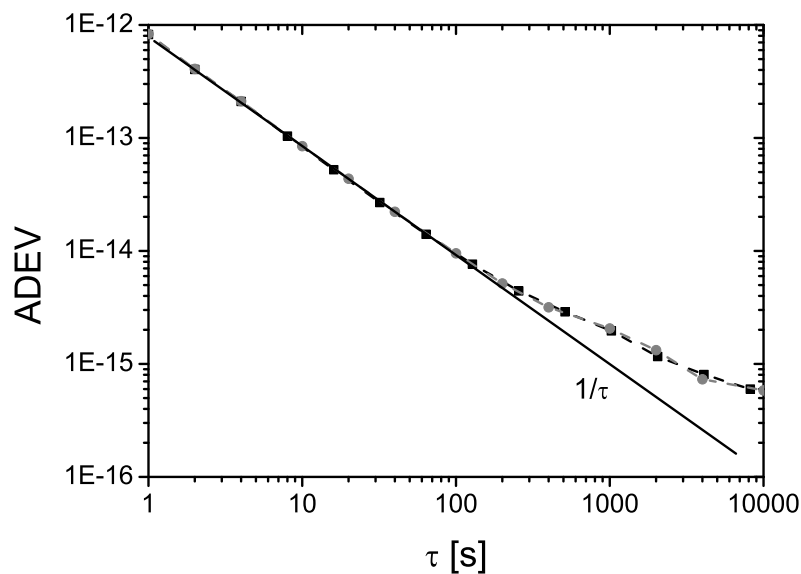
Figure 6.3: The stability of the two H-Masers used in Wz and Wn expressed by Allan deviation (ADEV) for 26 October 2015 (red) and 21 December 2015 (black); by courtesy of Jan Kodet (Technical University of Munich, Geodetic Observatory Wettzell, Germany).

Fig. 6.4, red). Two phenomena can be identified, the one is a short-scale fluctuation of about 8 ps within a few tenths of seconds and the other one are smooth variations of an hourly time-scale. While the first group is essential for the characterization of the observation by observation variability, the latter one is rather well behaved and should easily be compensated for by the hourly CPWL offsets. At least, this is the expectation.

However, when plotting the estimates for the same periods (see also Fig. 6.4, black), these only coincide very roughly with the TWOTT values (red). The differences at the level of 20-30 ps in the better case (e.g., for the VLBI session on 21 December 2015; see Fig. 6.4(a)) or up to 60 ps in the other extreme case (e.g., for the experiment on 26 October 2015; see Fig. 6.4(b)) cannot be explained by additional effects caused by the cable links between the hydrogen maser clocks and the VLBI electronics because these variations are expected to be rather smooth, mostly following the daily temperature cycle.

Fortunately, the TWOTT system could be activated simultaneously to the last WHISP experiment. The corresponding measurement (red) and the clock correction parameters derived from the VLBI estimation process (brown) for the same period are depicted in Fig. 6.5. At first glance, the differences perform similar to the better case of the routine IVS sessions. Concerning the modeling of the clock behavior, different parametrization settings have been used to allow for a better understanding of the level of difference to the TWOTT measurements. First, the clocks are parametrized as a quadratic polynomial and additional piece-wise linear functions with interval lengths of 60 minutes. As already mentioned, the clock parameters are supplemented by soft constraints in the form of pseudo observations. In the standard data analysis, these pseudo observations are less heavily weighted, e.g., by $\sigma_{clo} = 2 \cdot 10^{-14} \frac{s}{s}$. The clock parameters referring to the standard case are represented by dark brown dots in Fig. 6.5. A second adjustment is performed turning off the additional soft constraints, which leads to the clock parameters in light brown. Similarly, this procedure is repeated for piece-wise linear segments of 30 and 20 minutes, respectively. The solution using a
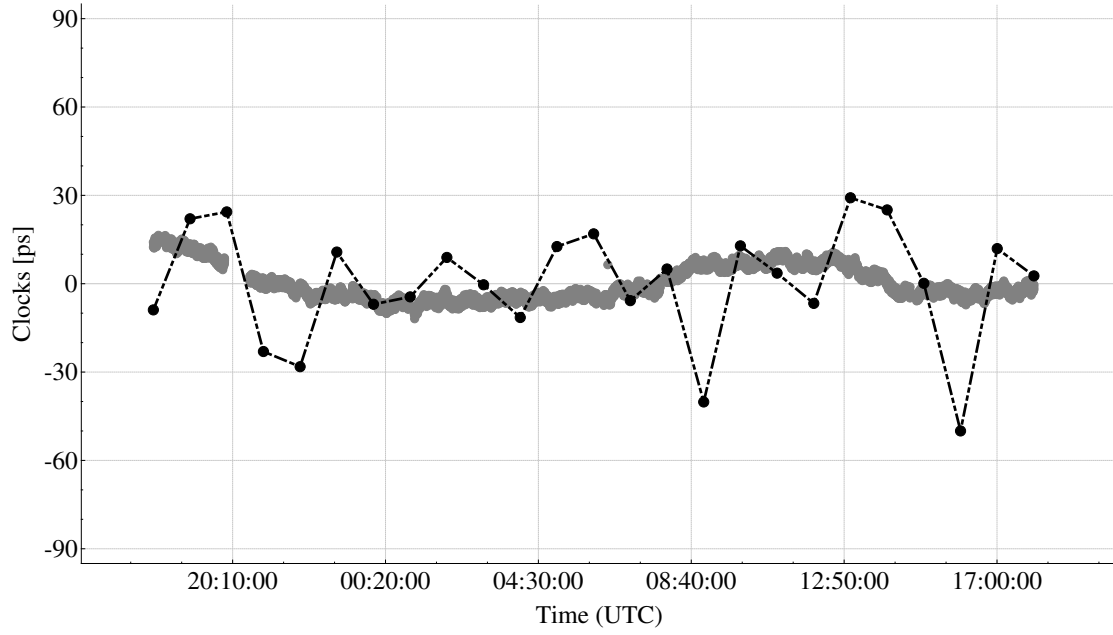
(a)
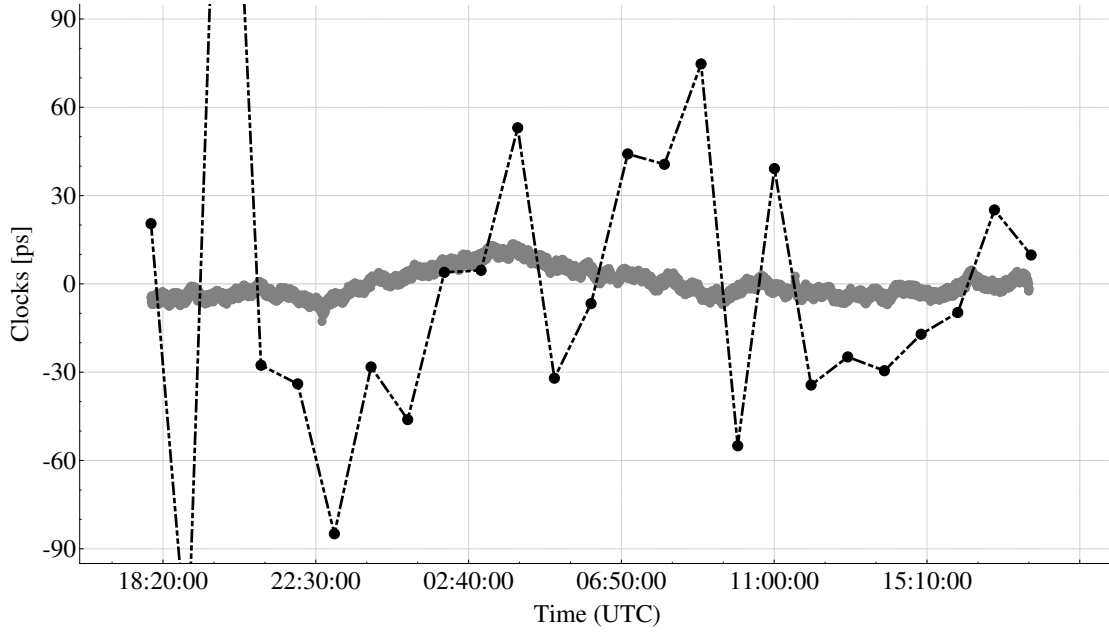
(b)

Figure 6.4: Two-way time transfer measurements (red) and VLBI estimates (CPWLF and quadratic polynomial, black) for two VLBI sessions on 21 December 2015 (a) and 26 October 2015 (b).
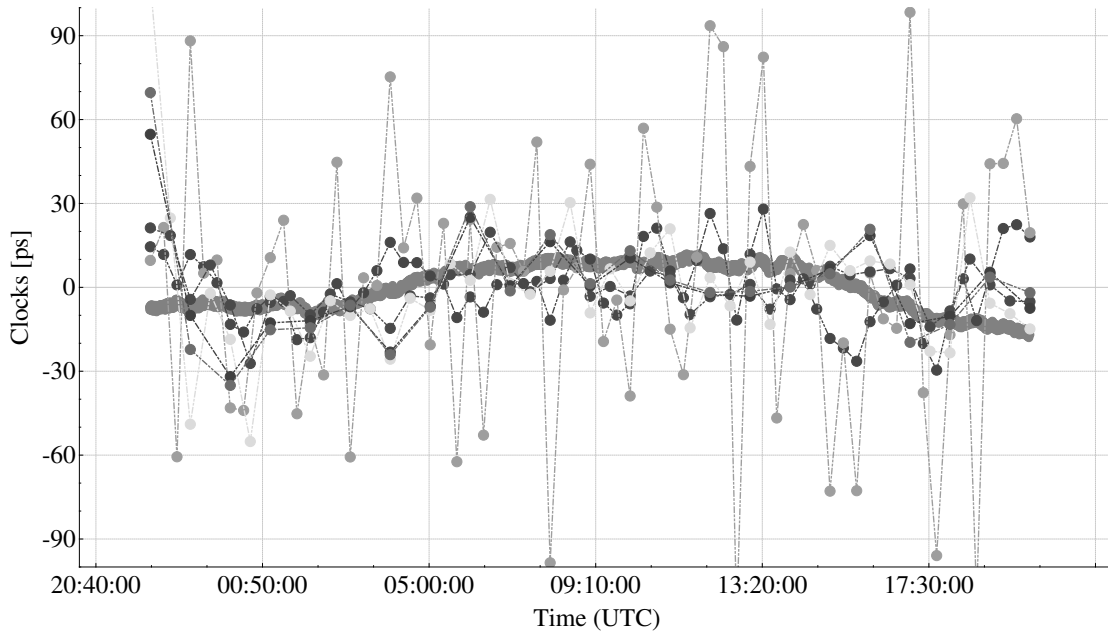
Figure 6.5: Two-way time transfer measurements (red) and VLBI estimates (CPWLF and quadratic polynomial) for different parametrization settings for the clocks and WHISP7: CPWLF 60 min. with (dark brown) and without (light brown) constraints; CPWLF 30 min. with (dark green) and without (light green) constraints; CPWLF 20 min. with (dark blue) and without (light blue) constraints.

30 minute interval with and without constraints are depicted in dark and light green, while the results of the adjustment with even shorter piece-wise linear intervals of 20 minutes are represented in dark and light blue for the two settings applying and turning off the constraints.

First, it is noteworthy, that for solution intervals of 30 or 60 minutes, the effect of the pseudo observations seems to be negligible, except for the first CPWL segment, and, therefore, the pseudo observations could in principle be neglected. However, the situation looks worse when reducing the piece-wise linear interval to 20 minutes. As soon as the soft constraints are turned off, the scatter of the clock estimates is clearly increasing, while the performance of the solution applying constraints is similar to the adjustment with CPWLF of 30 minutes. Most likely, the number of observations in the respective intervals is sufficient in a segment of 30 to 60 minutes, but not for shorter interval lengths below 30 minutes. However, also for the solutions showing a better clock behavior, the VLBI estimates coincide only very roughly with the TWOTT values, and the differences for the WHISP7 experiment are assessed to be in the order of magnitude of 20-30 ps.

The unexpected differences between the clock parameter estimates and the TWOTT measurements are in fact confirmed by the findings of KODET et al. (2016A). They can only be explained by the assumption that the clock estimates compensate for more than the clock effect but rather anything else with an unmodeled clock-like behavior. With the CPWL estimates of one-hour long intervals we should have caught all the clock-like variations within the one-hour periods. Taking this into account, the 8 ps variations measured with the TWOTT is considered as the value to be taken for characterizing the noise component induced by the relative clock behavior in the post-fit residuals in Sec. 6.4.

6.3.2   Contribution of the Correlation Process

A further component in the error budget is the contribution of the correlation process for determining the group delay observables. This is an independent process for each baseline (see, e.g., Sovers et al. 1998) and, thus, produces three independent delay observables in a triangle. In order to assess the group delay uncertainties, a so-called triangle or delay closure test is performed. It is postulated that the sum of the so-called geocentric group delays for the three individual baselines $\tau_{AB}\left(t_{geoc}\right)$, $\tau_{BC}\left(t_{geoc}\right)$ and $\tau_{CA}\left(t_{geoc}\right)$ is always zero in an ideal case (see Fig. 6.6),

$$\tau_{AB}\left(t_{geoc}\right) + \tau_{BC}\left(t_{geoc}\right) + \tau_{CA}\left(t_{geoc}\right) \overset{!}{=} 0. \tag{6.1}$$

In this context, the geocentric group delay is defined as the group delay, that would be obtained if the station A would be located in the geocenter. In the triangle, Wn, Wz, On, the weighted root
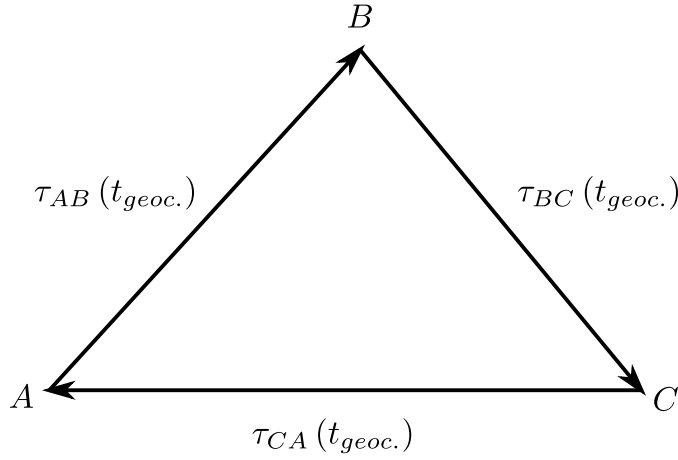
Figure 6.6: Delay closure with respect to the geocenter.

mean square (WRMS) closure error is 7.2 ps. Assuming uncorrelated observations, the correlation error level for each baseline is 4.2 ps (7.2 ps/$\sqrt{3}$). These results could already be confirmed by Ray and Corey (1991). Together with the clock variations of 8 ps, it can be concluded that the noise contribution within a few tens of seconds is not more than 10 ps while, except of the unaccounted measurement noise, the rest of the observation to observation variations are purely atmosphere-driven.

Finally, the effect of phase calibration in the framework of the VLBI correlation process is briefly discussed. Generally, phase calibration is necessary to compensate for instrumental phase shifts. A signal of known phase is generated, which is injected into the front end of the VLBI signal path. After the signal has traversed the instrumentation, the phase of the signal is examined (Sovers et al. 1998, pp 1395ff). This is important since such phase errors can corrupt the estimated phase and hence the group delay of the incoming signal (Sovers et al. 1998). Sometimes this technique can not be used and, instead, a procedure commonly known as "manual" phase calibration is applied (see, e.g., Martí-Vidal et al. 2012 for further details). However, this method is restricted by the assumption that the instrumental effects do not considerably change during the duration of the VLBI session, which may not be the case in reality.

However, on a short baseline the phase calibration signals of two closely-spaced VLBI antennas produce spurious group delay determinations in the correlation process. As a consequence, the phase calibration of one telescope has to be turned off, as was the case for the north tower of the twin telescope in all sessions.

6.4 Local Refractivity Effects

6.4.1 Atmospheric Tie Consideration

The zenith wet delay estimates are directly influenced by the a priori hydrostatic calibrations, which mainly depend on the pressure data observed at the VLBI site or derived from numerical weather models (see Sec. 3.3.3). It is necessary that the data derived from meteorological sensors are always related to the reference point, which is generally defined by the intersection of the rotation axes of the VLBI telescope.

In order to determine the pressure p at the intersection of axes of a telescope at height H, the following approximation can be used (see, e.g., TEKE et al. 2013),

$$p = p_0 \left(1 - \frac{\gamma \left(H - H_0 \right)}{T_0} \right)^{\frac{g}{\gamma R_L}} , \qquad (6.2)$$

with H_0 referring to the reference height. The meteorological data, particularly the pressure p_0 but also the temperature T_0, is measured initially. Finally, $\gamma = -0.0065 \ Km^{-1}$ represents the average temperature lapse rate, g denotes the gravity at the site, and $R_L \approx 287.058 m^2 s^{-2} K^{-1}$ is the specific gas constant. Based on p and using the modified Saastamoinen model in Eq. (3.37), the zenith hydrostatic delays are computed and incorporated in the VLBI parameter estimation process to determine zenith wet delay parameters with respect to the corresponding reference height.

In order to analyze the difference between two sets of ZWD estimates (as done, e.g., for WHISP5, WHISP6 and WHISP7) so-called tropospheric ties have to be introduced to correct for the height differences between two co-located antennas. Tropospheric tie corrections are derived by the sum of a wet $\delta_{\Delta L_w^z}$ and a hydrostatic component $\delta_{\Delta L_h^z}$. First, the hydrostatic tie follows directly from the modified Saastamoinen equation (DAVIS et al. 1985) in Eq. (3.37)

$$\delta_{\Delta L_h^z} = \Delta L_h^z \left(p \right) - \Delta L_h^z \left(p_0 \right) = \frac{0.0022768 \left(p - p_0 \right)}{1 - 0.00266 \cos \left(2\Phi_0 \right) - 0.00028 H_0}, \qquad (6.3)$$

where ΔL_h^z denotes the zenith hydrostatic delay according to Eq. (3.37) for a specific pressure value p and p_0, respectively. Second, the expression for the wet tie can be formulated according to BRUNNER and RÜEGER (1992) as

$$\delta_{\Delta L_w^z} = \frac{-2.789 e_0}{T_0^2} \left(\frac{5.383}{T_0^2} - 0.7803 \right) \gamma \left(H - H_0 \right) . \qquad (6.4)$$

Here, H_0 and Φ_0 denote the reference height and the latitude of one telescope, and p_0, T_0 and e_0 are the meteorological data at this height, while H and p represent the reference height and pressure of the co-located site. In case of differential zenith wet delays estimated for Wz relative to Wn, the tropospheric ties, at least for the hydrostatic calibrations, have to be taken into account accordingly prior to the parameter estimation process.

6.4.2 Parametrization of Zenith Wet Delays

The modeling and estimation settings for the WHISP experiments have been described in Sec. 6.2. In the case, which is currently standard in the IVS data analysis, the resolution of the piece-wise linear intervals is generally chosen to be 60 minutes. Due to the increased number of observations compared to traditional 24h-sessions and the resulting shorter time intervals between the observations, it might be worth to also reduce the solution interval of the piece-wise linear segments of the atmospheric parameters. This is realized for all available WHISP experiments, and the interval lengths are reduced to half (30 minutes) or even a forth (15 minutes) of the initial 60 minute time segments. In Tab. 6.3, the session-dependent WRMS of post-fit residuals (see Eq. 5.23) are shown with respect to the different CPWL interval lengths. In order to ensure $\chi^2 \approx 1$, either a constant additional noise term of approximately 15 ps is added to the standard deviations derived from the correlator output, or the turbulence model without any re-weighting option is used. The results of both strategies are also represented by Tab. 6.3.

Table 6.3: Session-dependent WRMS of post-fit residuals [ps] based on different data analysis settings varying the interval lengths of the continuous piece-wise linear functions (CPWLF). In order to ensure $\chi^2 \approx 1$, either a constant additional noise term is added to the standard deviations from the correlator process (Std. IVS data analysis) or the turbulence model is used. The overall best solution for the individual sessions are highlighted in yellow, and the most promising results for the standard IVS data analysis re-weighting the standard deviations of the observations are emphasized by slightly highlighted areas.

Session	Std. IVS data analysis			Turbulence model		
CPWLF interval length	60 min.	30 min.	15 min.	60 min.	30 min.	15 min.
WHISP1	13.95	13.33	13.61	11.50	10.98	10.96
WHISP2	26.04	25.67	25.90	23.18	22.85	22.92
WHISP3	22.16	21.91	22.07	19.54	19.18	19.31
WHISP5	28.63	27.18	27.65	27.23	26.21	26.63
WHISP6	-	-	-	-	-	-
WHISP7	27.04	25.74	27.53	20.60	19.68	20.77

Please remember, that the first three WHISP sessions (first block) consist of only a single local baseline, while in the other three experiments (second block) the two radio telescopes in Wettzell observe in a triangle network together with Onsala. The numbers given in Tab. 6.3 are always related to the overall WRMS of post-fit residuals for all baselines, which is, of course, only relevant for the WHISP sessions including Onsala and not for the single baseline observations. The impact of the interval lengths on the VLBI solution with respect to individual baselines will be further discussed in Sec. 6.4.4 for WHISP5 and WHISP7.

Immediately, it is evident, that for all WHISP sessions and both strategies refining the stochastic model the best results are generally obtained with CPWL interval lengths of 30 minutes. Only in

case of WHISP1 the smallest WRMS is obtained when using a resolution of 15 minutes, although the difference to the solution based on the 30 minute time segment is negligible anyway. Further, applying the turbulence model in the data analysis, the solution improves in all cases and independent of the respective interval length, as already demonstrated in Sec. 5.1.4. The fact, that the results generally improve when applying piece-wise linear segments of 30 minute interval lengths compared to the standard case of the IVS with a resolution of the CPWLF of one hour, but in turn, decrease with an even better temporal resolution of only 15 minutes, can be explained by the balance between pseudo observations and actual measurements within the individual time segments. The impact of the pseudo observations, which are necessary to stabilize the solution due to missing observations in some piece-wise linear segments, increases for the interval lengths of 15 minutes, whereas the number of observations within the 30 minute segments are high enough to minimize the influence of the constraints.

6.4.3 Single Baseline Studies

In order to investigate refractivity variations on a local scale, three WHISP sessions (WHISP1-3, see Tab. 6.2) consisting of only a single baseline between the 20 m diameter radio telescope (Wz) and the north antenna of the twin telescopes (Wn) are used. In a first solution, differential zenith wet delay parameters are estimated for Wz relative to Wn. The results for the zenith wet delays vary mostly between ± 2 mm (red dots in Fig. 6.7). In a second independent least squares adjustment, an offset parameter valid for the whole 22h session (red line) is estimated to identify remaining systematics. Please note, that these are only relative changes of the zenith wet delays. The behavior of the hydrostatic calibrations reduced by a constant term (about 2.15 m, blue dots) gives some indication of the overall weather fluctuations within the sessions which is quite severe in the last one (see Fig. 6.7(c)).

The temporal variations of the estimated relative atmospheric parameters over each 22h period with only a few millimeters appear to be realistic estimates. This is supported by the fact that they are not (anti-) correlated with the hydrostatic calibrations. Since the two stations are only separated by about 120 m and both telescopes always point in the same direction, it can be assumed that any systematic effect not stemming from the atmosphere is canceled out in the differential mode. Tests with variations in the clock parametrization support this assumption (not shown here). The non-zero estimates of the average ZWD offsets are presumably caused by differential paraboloid deformation effects which have invariant sin (elevation) characteristics (NOTHNAGEL et al. 2017). As a consequence of these interpretations, the majority of the fluctuations within each hourly segment are then attributed to the stochastic character of the neutral part of the atmosphere.

In order to validate this assumption, the effect of refractivity fluctuations due to turbulent motions in the atmosphere are investigated. Here, the atmospheric turbulence model presented in Sec. 5.1 is applied to describe the stochastic behavior of the small-scale refractivity variations and introduce physical correlations between the observations. Again, differential zenith wet delays are estimated for Wz relative to Wn (see red dots in Fig. 6.8), which, compared to the results in Fig. 6.7, only differ in the application of the turbulence model. The 22h session offset parameter (red line) and the reduced hydrostatic calibrations (blue dots) are plotted as well. Comparing these results to the standard case of VLBI data analysis (Fig. 6.7), it is apparent, that, the scatter of the differential zenith wet delay estimates are considerably smoother, particularly for WHISP1 and WHISP3 (Fig. 6.8, (a) and (c)). Additionally, the standard deviations of the ZWD estimates become clearly larger and more realistic, remembering the fact that the standard deviations of space-geodetic

(a)

(b)

(c)
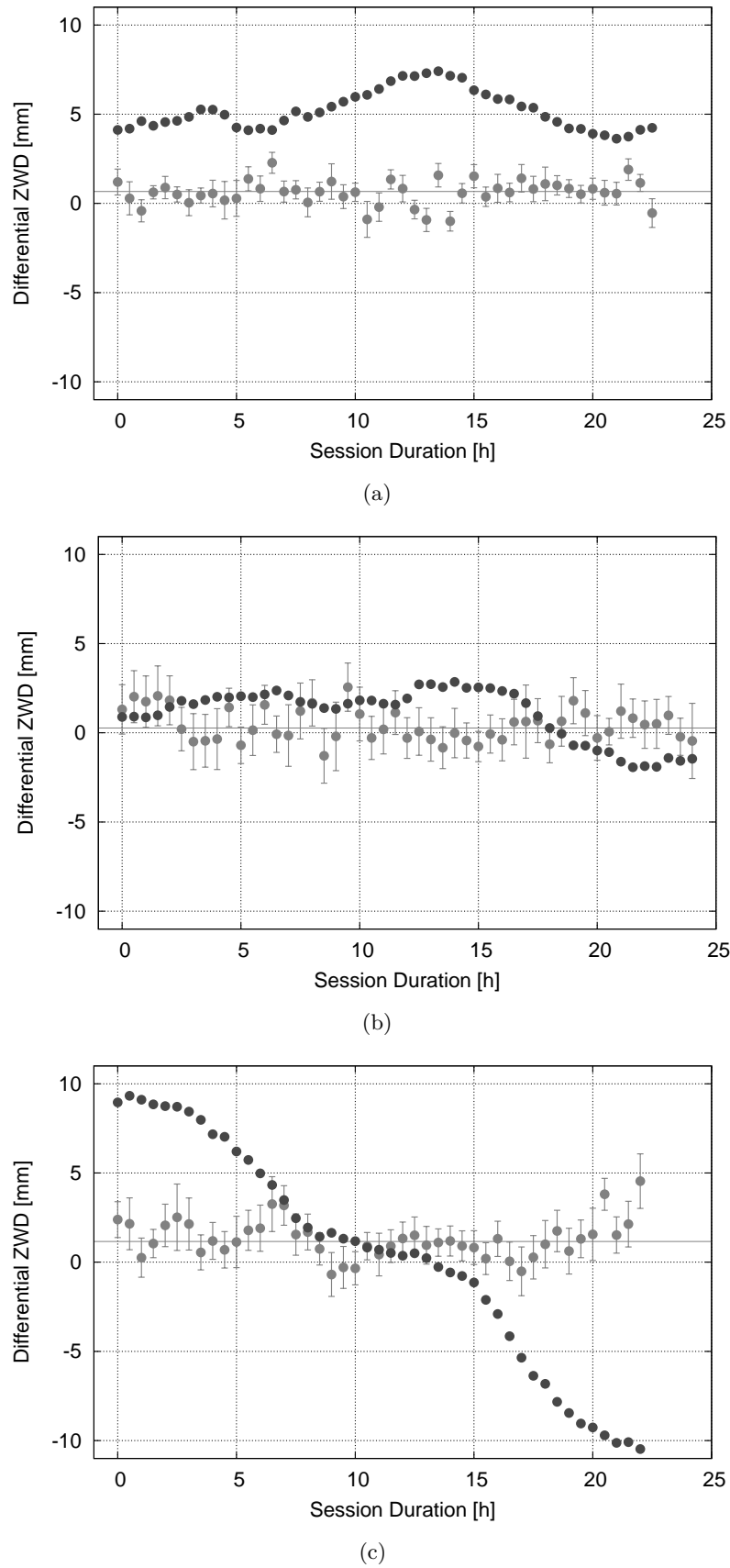
Figure 6.7: Differential zenith wet delay estimates (CPWFL, red) between the VLBI stations Wz and Wn for WHISP1-3 (a-c). An offset parameter estimated over the 22h session length is plotted as red line. The modeled zenith hydrostatic delays are represented in blue (reduced by a constant offset).

(a)

(b)

(c)
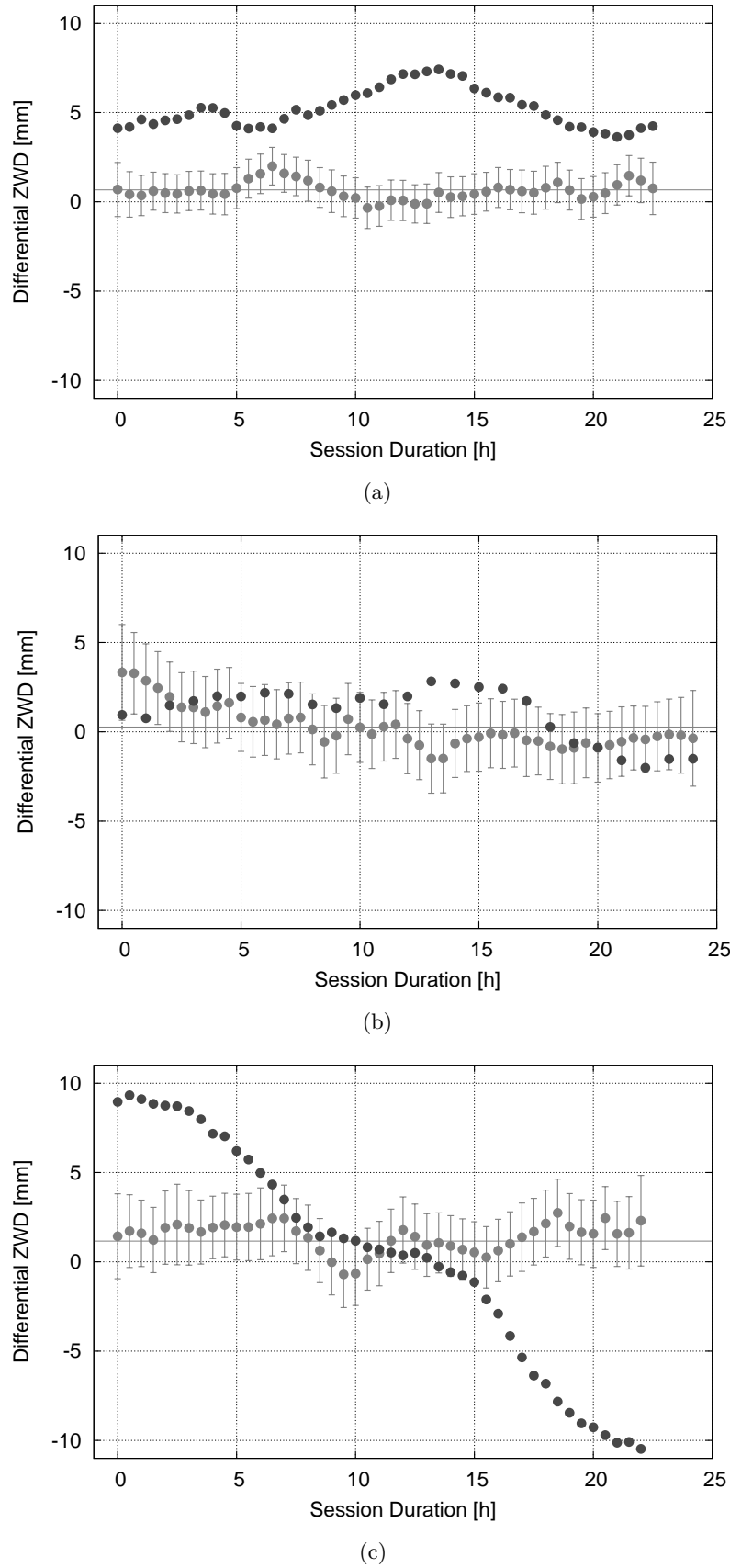
Figure 6.8: Differential zenith wet delay estimates (CPWFL, red) between the VLBI stations Wz and Wn for WHISP1-3 (a-c) using the atmospheric turbulence model described in Sec. 5.1. An offset parameter estimated over the 22h session length is plotted as red line. The modeled zenith hydrostatic delays are represented in blue (reduced by a constant offset).

techniques are generally too optimistic (see, e.g., HALSIG et al. 2016A). Except for two to three data points, the estimates for all differential zenith wet delays are not different from zero considering their 1σ standard deviations. In the standard analysis, many more data points exceed this criterion. Consequently, the atmospheric turbulence model is able to improve the solution and the assumption that the majority of the variations from hour to hour can be assigned to the stochastic character of the atmosphere is hereby confirmed.

Second, the results of the three WHISP sessions are examined whether there exists a dependency on the observation geometry. It is generally known, that the extra signal path length through the neutral atmosphere with respect to a theoretical path in vacuum depends on the elevation angle ε of the observation: the lower the elevation angle, the larger the path length. Generally, mapping functions are used to map an observation from an arbitrary elevation to the zenith direction (cf. Sec. 3.3.4).
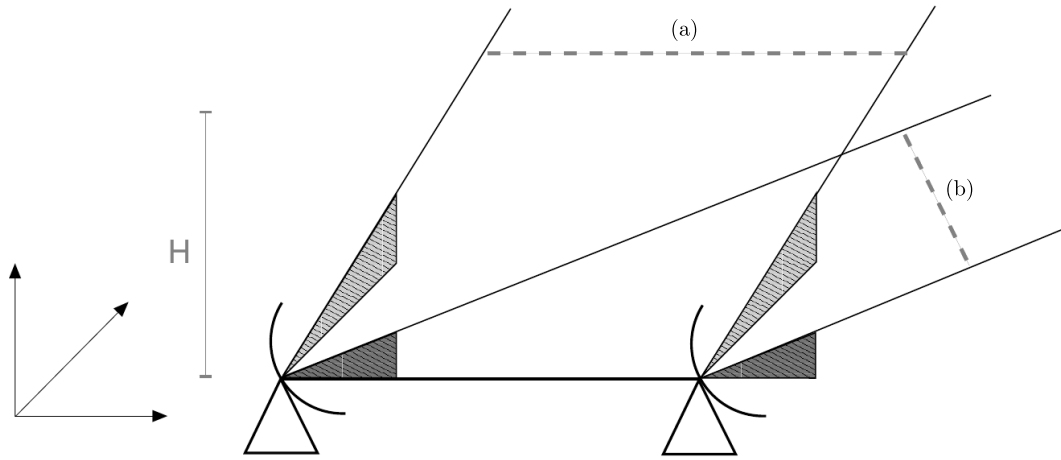
Figure 6.9: Separation distance (dashed red line) of the signal rays of two radio telescopes for (a) an observation perpendicular to the baseline, and for (b) an observation in the direction of the baseline.

For very short baselines such as the one used here, the separation distance of the two ray paths of the radio signal (dashed red line, Fig. 6.9), referred to as ray distance in the following, also depends on the azimuth and elevation angle of the observation. Assuming both radio telescopes pointing into zenith direction, the separation distance would be maximal and equal to the baseline length separating the telescopes, which is about 123 m in the Wettzell case. When moving to a radio source with an arbitrary azimuth and elevation angle, the separation distance becomes smaller: the lower the elevation angle, the lower the distance between the two rays. Fig. 6.9 shows two different pointing directions and the corresponding separation distances illustrated as dashed red lines. The colored triangles are supposed to emphasize, that for the determination of the separation distance a two-dimensional problem (in azimuth and elevation) is taken into account instead of a one-dimensional one only relating to the elevation angle. Mathematically, the ray distance can be calculated following Eqs. (5.6) to (5.11) in Sec. 5.1. The separation distance is evaluated at a certain height $H = 2000$ m representing the effective tropospheric height, which, however, results from implementing the turbulence model and is not important for the determination of the separation distance at this point. The ray distances are determined for each observation and a residual analysis is performed with respect to the separation distance.
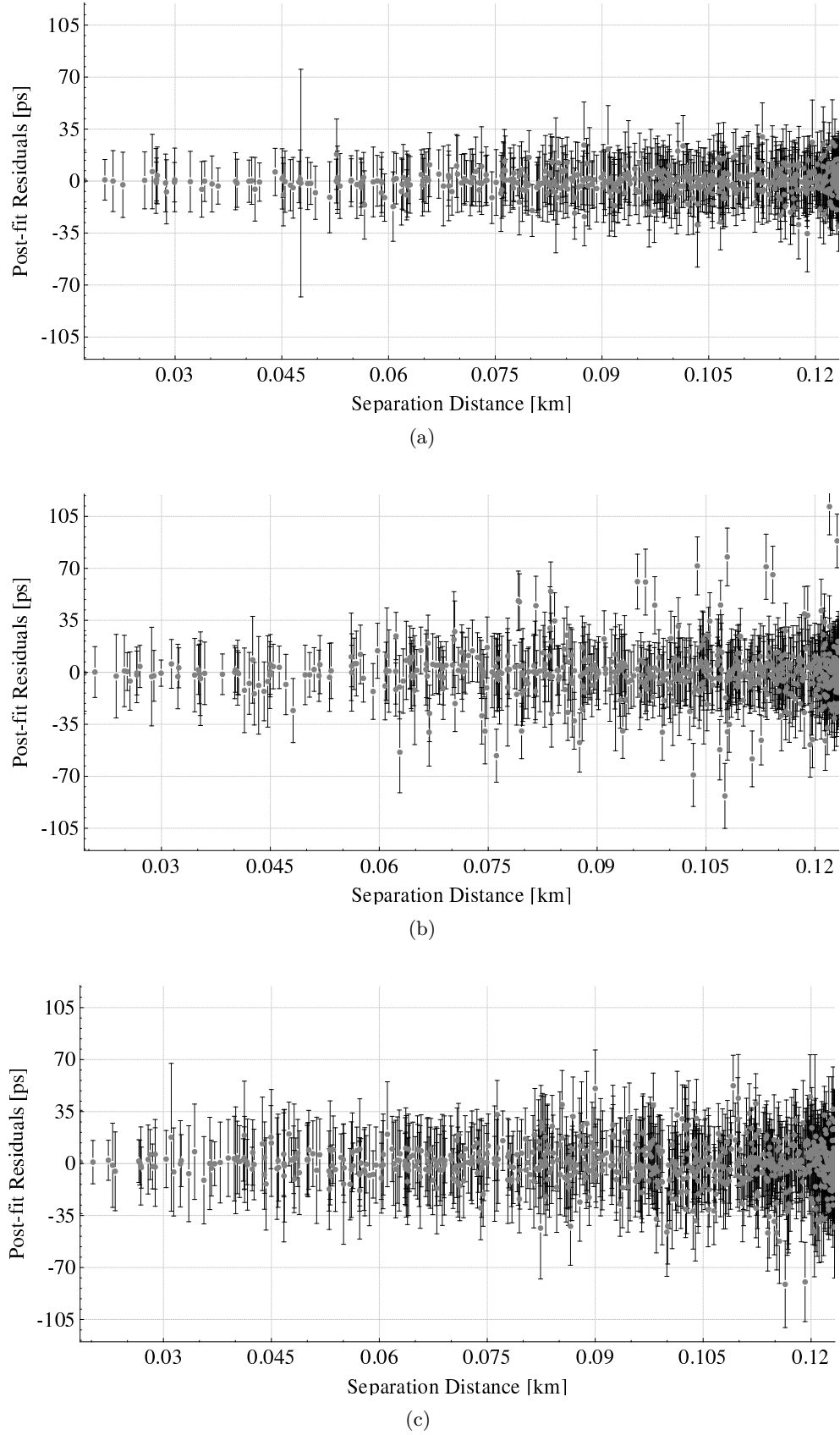
Figure 6.10: Post-fit residuals of the WHISP1 (a), WHISP2 (b) and WHISP3 (c) experiment as a function of the distance separating the ray path of the radio signals.

Under the conditions set above that any remaining variations can be attributed to the wet atmosphere, it is assumed that there should be a dependency of scatter of the post-fit residuals on the ray distances. In Fig. 6.10, the post-fit residuals of the three WHISP-sessions are shown as a function of the separation distance of the ray path of the radio signals. To eliminate the elevation-dependent multiplication of the refraction errors implemented as mapping functions, the post-fit residuals have to be scaled by an inverse mapping function, simply approximated by $\sin(\varepsilon)$. This ensures that only the spatial dependency of the residuals due to the separation distance is analyzed, and not blended by other effects necessary for the data analysis.

The assumption, that the post-fit residuals become larger for an increasing separation is doubtlessly verified, particularly for WHISP2 and WHISP3 (Fig. 6.10, (b) and (c)). It may be assumed that this is due to the fact that the turbulent refractivity variations lose their spatial correlations with increasing ray separation. In order to see whether the turbulence model had any effect, two solutions with and without applying the turbulence model are compared, but there is no a clear evidence, that the post-fit residuals would become more randomly when introducing spatial correlations into the data analysis.
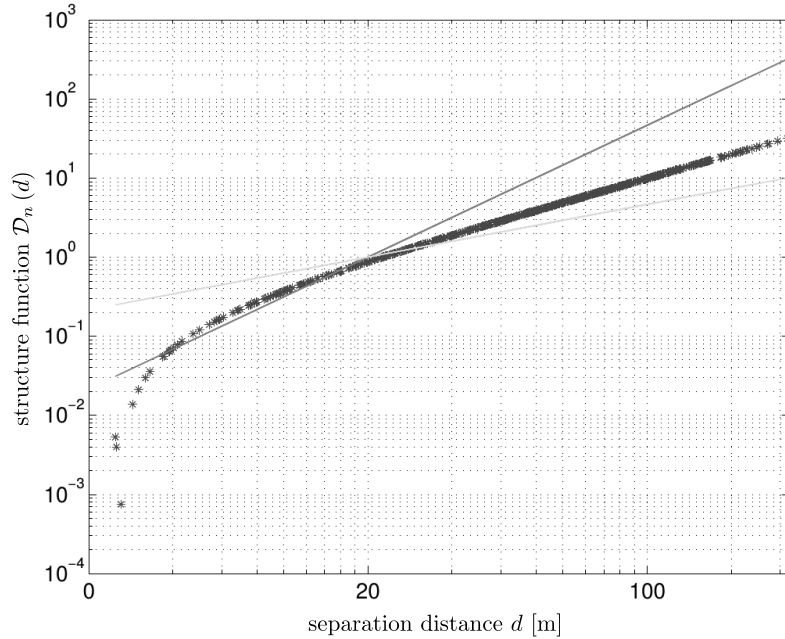
Figure 6.11: The spatial structure function of the post-fit residuals $\mathcal{D}_r(\boldsymbol{d})$, illustrated as a typical log-log-plot with respect to the separation distance $\boldsymbol{d}$ (the x-axis label is given in linear scale). The green and red dotted line correspond to the typical $2/3$ and $5/3$ power law exponents according to turbulence theory.

This issue is further investigated by calculating the spatial structure function of the post-fit residuals $\mathcal{D}_r(\boldsymbol{d})$, which is plotted with respect to the separation distance $\boldsymbol{d}$. As an example, the result for WHISP1 is shown in Fig. 6.11. The findings for WHISP1 are consistent with the results of WHISP2 and WHISP3 (not shown here). As already described in Sec. 4.2, the structure functions can generally be represented as straight lines with different slopes, which are equal to the specific exponents of the power law processes. According to turbulence theory, power law processes with

two characteristic exponents of ²/₃ (2D turbulence; green line) and ⁵/₃ (3D turbulence; red line) are predicted. A more detailed description on the power law relations for atmospheric turbulence can be found in Sec. 4.2 or, e.g., THOMPSON et al. (2001). Compared to Fig. 4.3 in Sec. 4.2, which describes the idealized general behavior of a structure function, the computed slopes from the post-fit residuals do not clearly reflect the theoretical ²/₃ and ⁵/₃ power law exponents, but are still close to the expected values. The initial slopes for short distances of 15 to 20 m follows approximately the power law exponent of ⁵/₃ and quickly decreases to a value close to, but slightly higher than the expected ²/₃. One explanation for the difference between the computed and the theoretical slopes might the be fact, that the post-fit residuals are superimposed by other unmodeled effects. It is also conceivable that the calculated slope would become even closer to the theoretical one when further increasing the separation distance, at least up to a certain distance, where the structure functions becomes flat again (with a power law exponent close of zero) and the post-fit residuals are uncorrelated. Nonetheless, the separation distance is limited by the baseline length between the two telescopes, and therefore the maximum distance is about 123 m when looking in the zenith direction.

Finally, the solutions with shorter piece-wise linear segments of 15 or 30 minutes show only minor effects in the dependency of the post-fit residuals on the separation distance, although in both cases the solution itself improves (compare Tables 6.3 and 6.4).

6.4.4 Studies in a Triangle Network

As described in Sec. 6.1, three further WHISP sessions (WHISP5 to WHISP7) have been observed successfully in a network consisting of the two VLBI antennas at Wettzell and a third radio telescope at Onsala (Sweden), separated by 920 km. The two independent baselines between Onsala and the two telescopes at Wettzell are now employed to also estimate absolute atmospheric parameters. Again, the derived ZWD estimates are corrected for tropospheric ties to account for the height difference between the two VLBI antennas as described in Sec. 6.4.1.

As already stated in Sec. 6.4.2, the impact of the piece-wise linear interval lengths on the two baselines to Onsala (On-Wn and On-Wz) and the local short baseline in Wettzell (Wn-Wz) has been investigated for WHISP5 and WHISP7. It should be already noted, that the WHISP6 experiment will be declared as a special case and has, therefore, to be discussed separately. The baseline-dependent WRMS of post-fit residuals are represented in Tab. 6.4. Again, two different strategies have been used for the stochastic model in order to ensure $\chi^2 \approx 1$: the standard IVS data analysis re-weighting the observations (here, a constant additional noise term of 15 ps is used) and the turbulence-based solution developed in this thesis.

Regarding Tab. 6.4, it is evident that the WRMS of post-fit residuals for the European baselines are, as expected, always higher than for the local baselines (On-Wz and On-Wn: about 28-31 ps; Wn-Wz: about 7-12 ps). In general, similar conclusions can be found compared to the session-based analysis in Tab. 6.3. First, the solution always improves when reducing the solution time intervals of the piece-wise linear segments from 60 to 30 minutes, except for the short baseline Wn-Wz analyzing WHISP5 and the standard case of the IVS.

Second, for all baselines the WRMS of post-fit residuals decreases sharply when introducing stochastical information due to turbulence modeling, and the overall best results are obtained for the

Table 6.4: Baseline-dependent WRMS of post-fit residuals [ps] based on different data analysis settings varying the interval lengths of the continuous piece-wise linear functions (CPWLF). In order to ensure $\chi^2 \approx 1$, either a constant additional noise term is added to the standard deviations from the correlator process (Std. IVS data analysis) or the turbulence model is used. The overall best solutions are highlighted in yellow, and the most promising results for the standard IVS data analysis re-weighting the standard deviations of the observations are emphasized by slightly highlighted areas.

WHISP5						
Baseline	**Std. IVS data analysis**			**Turbulence model**		
CPWLF interval length	60 min.	30 min.	15 min.	60 min.	30 min.	15 min.
On-Wn	30.70	29.16	29.68	29.50	28.30	28.75
On-Wz	30.76	29.12	29.64	29.88	28.71	29.21
Wn-Wz	11.31	11.28	11.20	10.22	9.95	10.00
WHISP7						
On-Wn	32.02	30.52	32.72	25.19	24.34	25.66
On-Wz	30.10	28.62	30.65	22.96	21.76	23.07
Wn-Wz	8.45	7.99	8.01	7.84	7.28	7.33

turbulence-based solution applying CPWL interval lengths of 30 minutes for the atmospheric parameters. It is conspicuous, that the level of improvement, when considering atmospheric turbulence compared to the standard case, is considerably higher for WHISP7, particularly for the longer baselines. It is recalled that, most likely, the impact of the pseudo observations is responsible for the fact, that the solution cannot be further improved by even shorter interval lengths of 15 minutes.

Table 6.5: (Pearson) correlation coefficient between the ZWD estimates of Wz and Wn for WHISP5, WHISP6 and WHISP7.

	WHISP5	**WHISP6**	**WHISP7**
Std. IVS data analysis	0.97	0.94	0.99
Turbulence model	0.98	0.97	0.99

The zenith wet delay estimates for both Wettzell telescopes, represented as CPWLF with interval lengths of 30 minutes, are shown in Fig. 6.12, where black and green dots represent the estimates for Wz and Wn, respectively. Since the two antennas are only separated by about 120 m, the resulting zenith wet delay parameter sets for both stations are expected to be almost identical. This assumption may be affirmed by calculating the (Pearson) correlation coefficients between the ZWD estimates of both stations (first row of Tab. 6.5), which varies between 0.94 and 0.99 for the
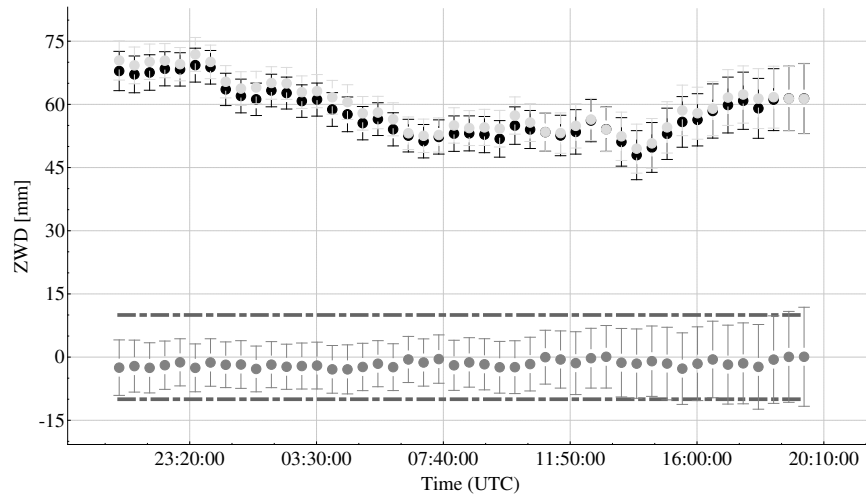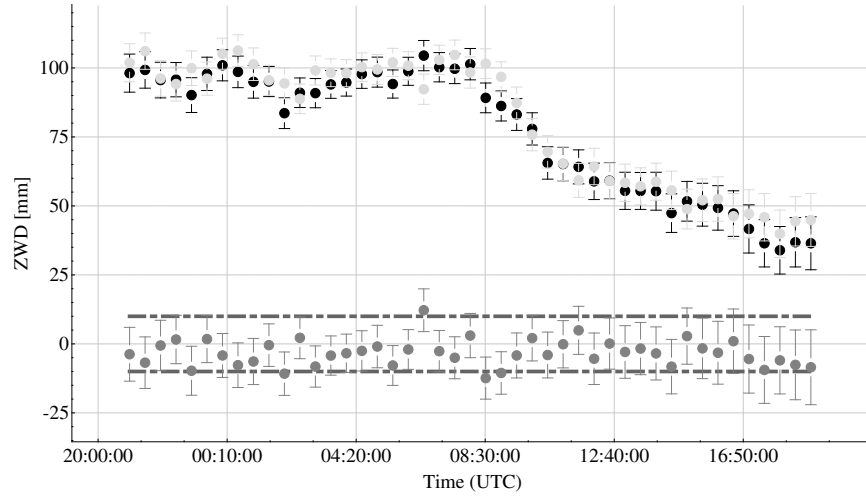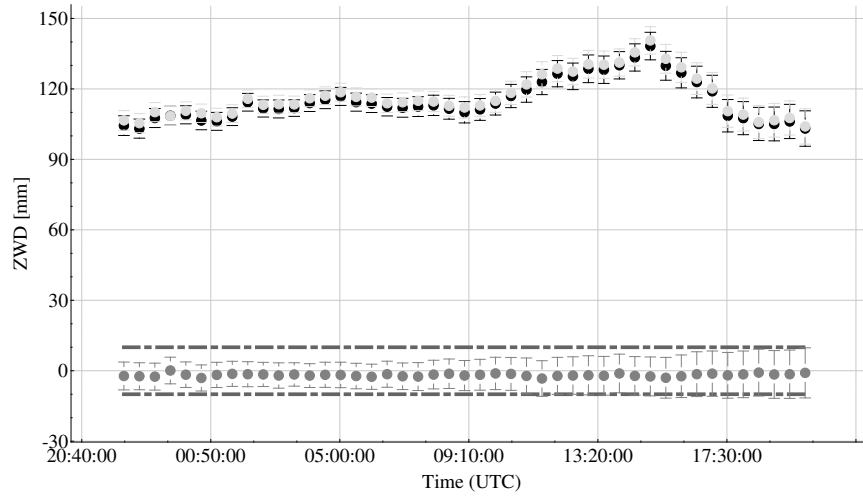
Figure 6.12: Zenith wet delay estimates (CPWFL, 30 min.) for the VLBI stations Wz (black dots) and Wn (green dots) for WHISP5 (a), WHISP6 (b) and WHISP7 (c). The difference between both parameter sets is depicted as red dots. The gray dotted lines indicate the centimeter level.

three experiments. The correlation even becomes marginally higher when using the atmospheric turbulence model (correlation coefficients between 0.97 and 0.99, second row of Tab. 6.5).

Fig. 6.12 also depicts the differences between the ZWD estimates of both VLBI stations (red dots), which are generally in the order of a few millimeters. Going further into detail, the differences do not exceed ±3 mm in case of WHISP5 (Fig. 6.12(a)), which fits very well the analysis of the differential zenith wet delays for WHISP1-3. Similar results have been found for the WHISP7 experiment (Fig. 6.12(c)), while the results of WHISP6 have to be discussed separately (see Fig. 6.12(b)). Here, the differences between the ZWD estimates of both VLBI stations generally vary in the range of 3-5 mm, but occasionally reach maximal differences of about one centimeter (indicated by gray dotted lines in Fig. 6.12).

Initially this was surprising, since the correlation coefficient is only slightly lower for WHISP6 compared to WHISP5 or WHISP7. However, manual phase calibration had to be applied to the Wz data instead of the routinely applied scan-by-scan system calibration (see Sec. 6.3.2) leading to an increased noise level in the atmosphere estimates. Furthermore, when analyzing the post-fit residuals of the baseline between Onsala and the 20 m antenna in Wettzell (Fig. 6.13), a clear signal can be found, which is clearly due to the fact of only applying manual phase calibration for the 20 m telescope.
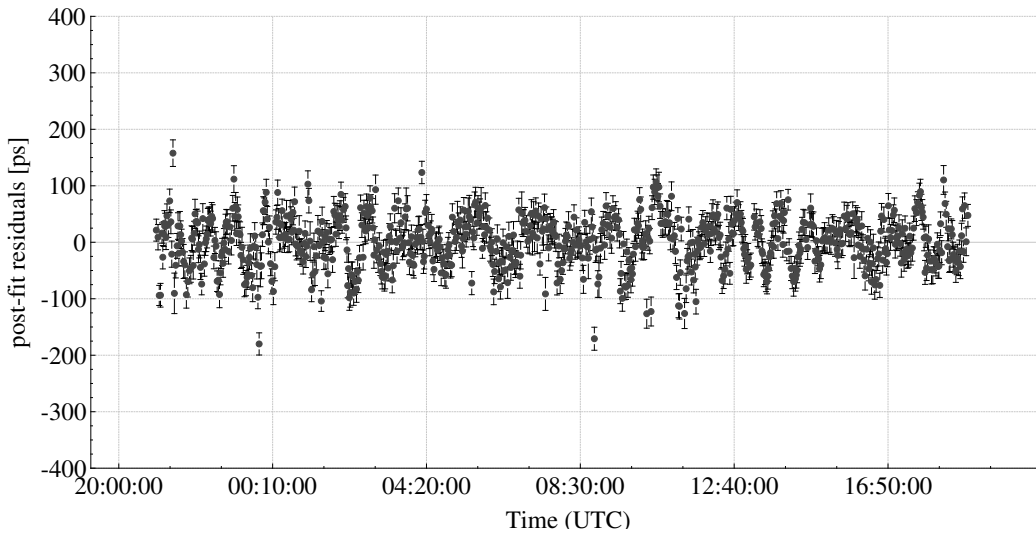
Figure 6.13: Systematic effect in the post-fit residuals of the baseline On-Wz for WHISP6.

In order to quantify this effect, the fringe fitting process (i.e., searching the maximum correlation amplitude in the power spectrum; see Sec. 2 or WHITNEY (2000) for more details) of the WHISP5 session is repeated analogous to the initial one, except for applying manual phase calibration for both radio telescopes. In the following, this experiment is referred to as WHISP5-M. Recalling the discussion in Sec. 6.3.2, the situation remains unchanged for Wn, where manual phase calibration was applied anyway, while the regular scan-wise phase calibration for Wz was now turned off. Regarding the post-fit residuals of the baseline between Onsala and the 20 m antenna in Wettzell obtained by analyzing WHISP5-M, again a clear signal can be found (Fig. 6.14(a)). In order to quantify the phase calibration effect, the WRMS of post-fit residuals for both experiments, WHISP5 and WHISP5-M, are calculated, which are 27.5 ps and 34.7 ps, respectively. The obtained WRMS

(a)

(b)
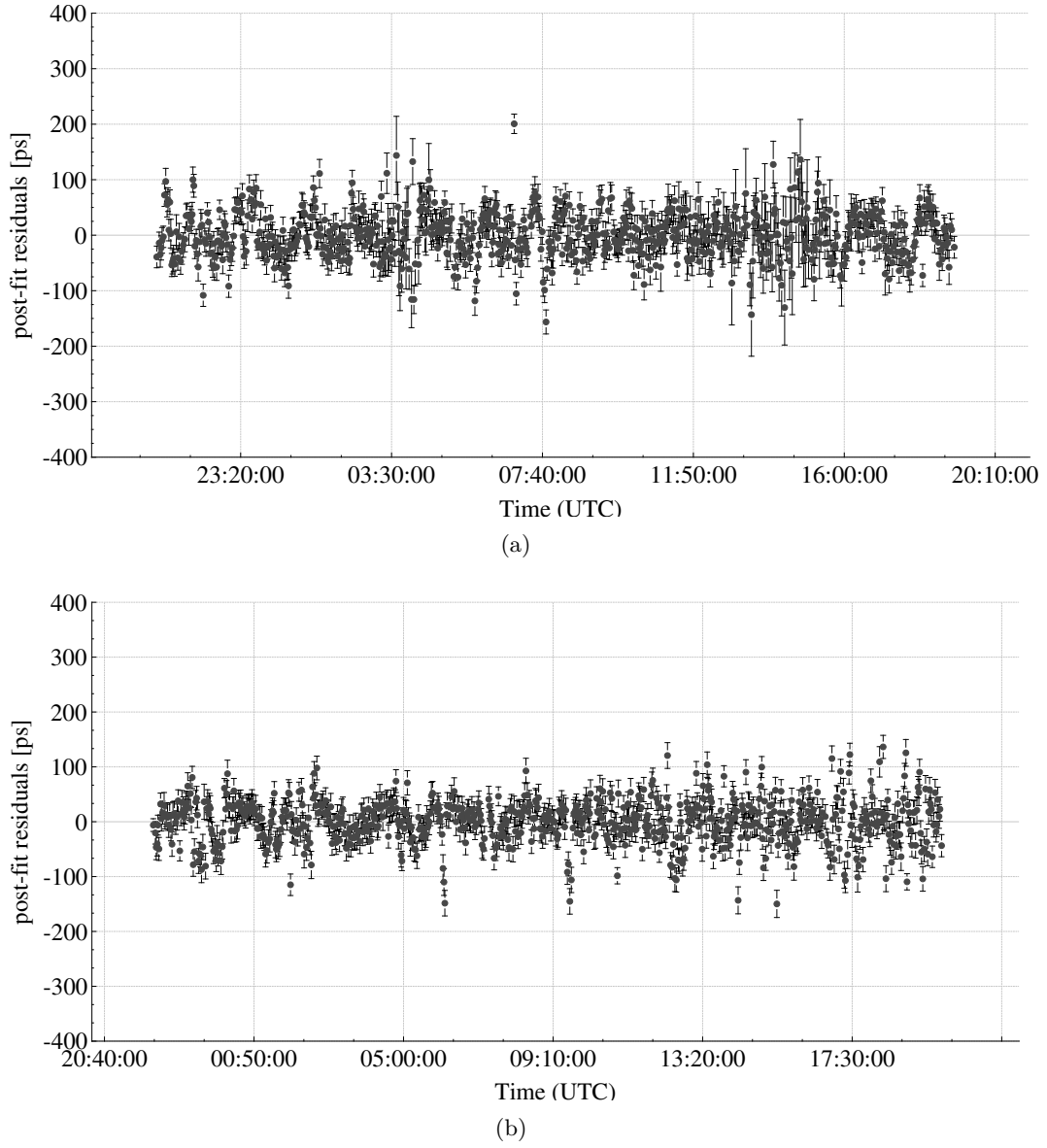
Figure 6.14: Systematic effect in the post-fit residuals of the baseline On-Wz for WHISP5-M and WHISP7-M when applying manual phase calibration for both radio telescopes.

is reduced by 10 ps in quadrature, which has been found to be the approximate noise contribution mainly including the clock variations and the correlation error (Sec. 6.3). Finally, the effect of using manual phase calibration instead of scan-by-scan system calibration is calculated as the difference between WHISP5 and WHISP5-M, yielding a net difference of

$$\sqrt{\left[(34.7\ ps)^2 - (10.0\ ps)^2\right] - \left[(27.5\ ps)^2 - (10.0\ ps)^2\right]} \approx 21.2\ ps. \tag{6.5}$$

The same investigation was repeated for WHISP7: the initial experiment was re-fringed (WHISP7-M in the following), and again manual phase calibration was applied to both radio telescopes. From the data analysis WRMS of post-fit residuals of 27.0 ps and 34.2 ps are obtained for WHISP7

and WHISP7-M, respectively. The effect of using manual phase calibration instead of scan-by-scan system calibration is again computed as the net difference between WHISP7 and WHISP7-M,

$$\sqrt{\left[(34.2\ ps)^2 - (10.0\ ps)^2\right] - \left[(27.0\ ps)^2 - (10.0\ ps)^2\right]} \approx 21.0\ ps, \tag{6.6}$$

which is, compared to the WHISP5 experiment, almost identical. Further, a similar signal as found for WHISP5-M is again visible in the post-fit residuals of WHISP7-M (see Fig. 6.14(b)).

For a further insight into this issue, a comparative residual analysis is performed based on the two baselines to Onsala. In Fig. 6.15(a), the post-fit residuals of the baseline On-Wz are plotted against the respective post-fit residuals of the baseline On-Wn for WHISP5. The resulting point cloud shows the typical behavior of well correlated data sets with a slope close to one and a reasonable noise belt reflecting the random errors. The correlation coefficient between both residual series can be calculated to about 0.73 supporting the indication of a high correlation. As expected, the results look worse when analyzing WHISP5-M and plotting the post-fit residuals of the baselines On-Wz and On-Wn against each other (see Fig. 6.15(b)). It is apparent, that the pattern becomes more randomly when applying manual phase calibration for both telescopes. The corresponding correlation coefficient is about 0.48 indicating weak to medium correlation, which is still clearly lower than for the experiment using the standard scan-by-scan system phase calibration. Again this is very good evidence for the influence of the missing phase calibration of the Wz data in case of WHISP6.

A similar situation occurs for WHISP7 which, in fact, leads to the best results. The resulting point cloud after plotting the post-fit residuals of the baseline On-Wz is plotted against the respective post-fit residuals of the baseline On-Wn shows again the typical behavior of well correlated data sets. The corresponding correlation coefficient between both data sets is 0.84 which indicates a high correlation. Analyzing WHISP7-M and plotting the post-fit residuals of the baselines On-Wz and On-Wn against each other (see Fig. 6.16(b)), the results are clearly degraded as expected, since the pattern again becomes more randomly when applying manual phase calibration for both telescopes. However, the corresponding correlation coefficient of 0.69 is unexpectedly high compared to the findings of the WHISP5(-M) session.

For WHISP6 manual phase calibration had to be applied for both telescopes. Plotting again the post-fit residuals of the baselines On-Wz and On-Wn against each other (Fig. 6.17), the pattern looks more random and the expected slope can be discerned only vaguely. This can also be confirmed in the correlation coefficient of approximately 0.31, which is only in the range of weak correlations. Based on these findings, and hypothetically speaking, appropriate results and more realistic ZWD estimates would be expected if the fringe fitting process could be repeated using the regular scan-wise phase calibration, which, unfortunately, cannot be realized since the phase calibration signal has not been registered.
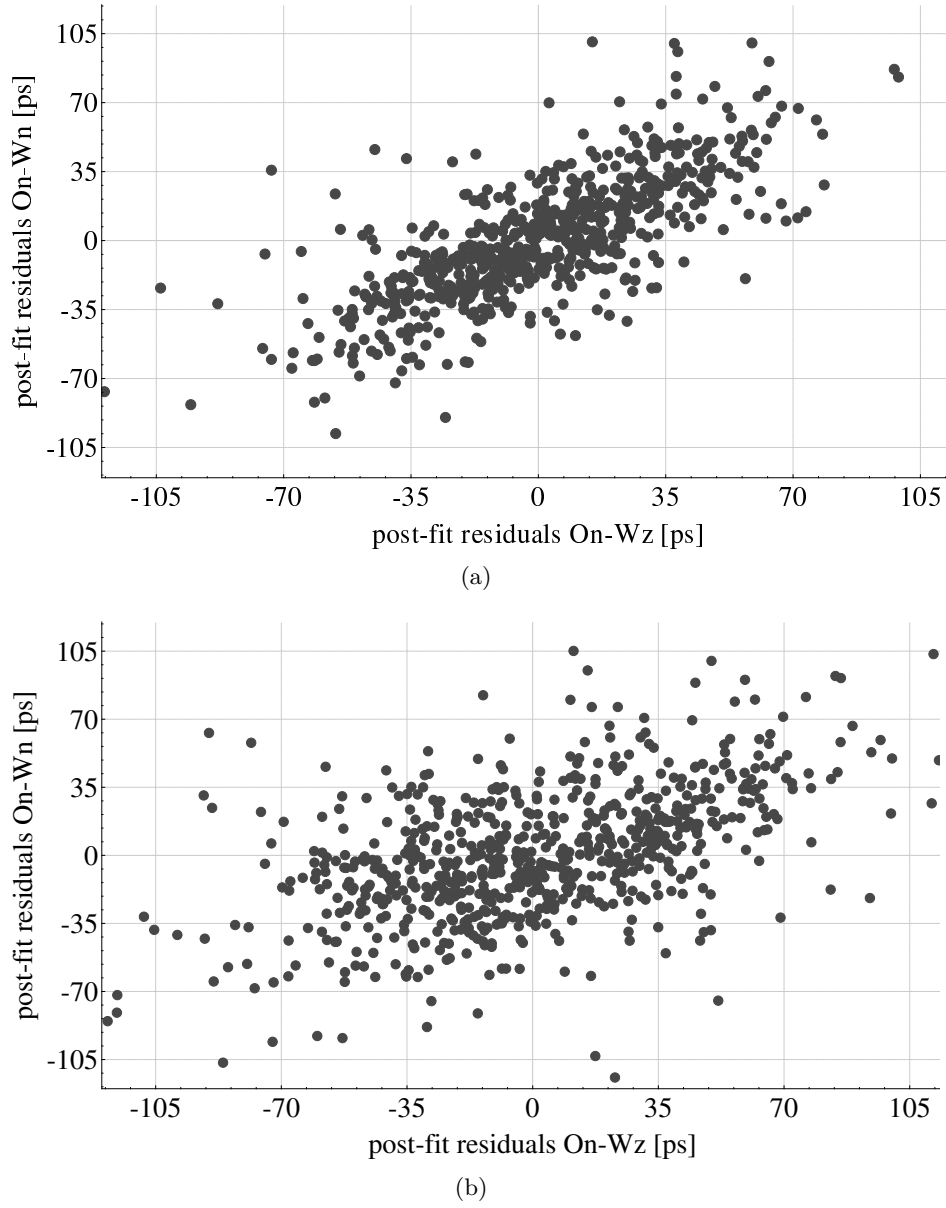
Figure 6.15: Post-fit residuals of the baseline On-Wz versus post-fit residuals of the baseline On-Wn for WHISP5 (a) and WHISP5-M (b).
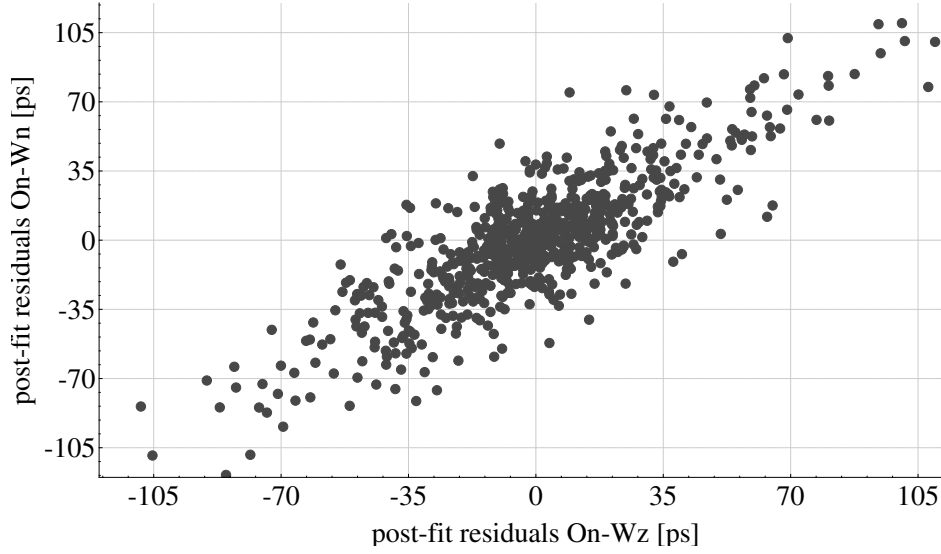
(a)
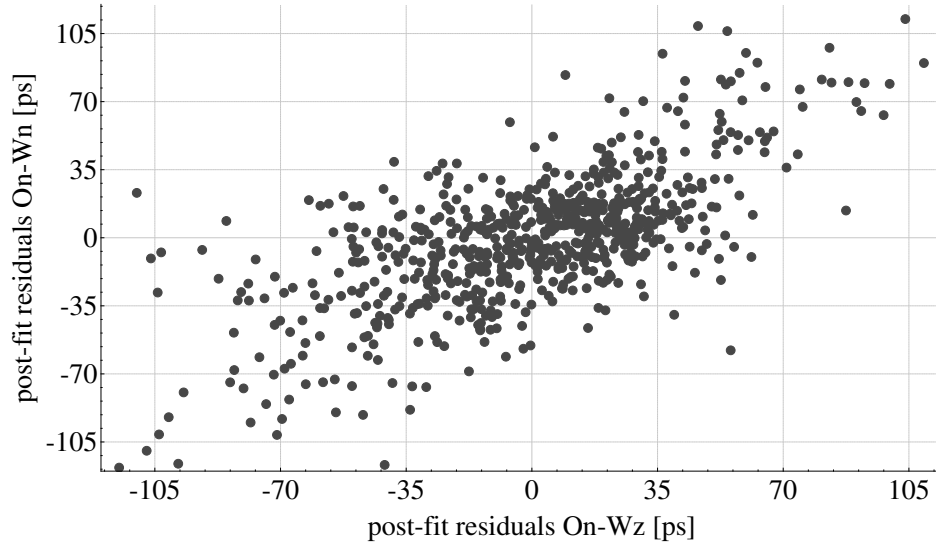
(b)

Figure 6.16: Post-fit residuals of the baseline On-Wz versus post-fit residuals of the baseline On-Wn for WHISP7 (a) and WHISP7-M (b).
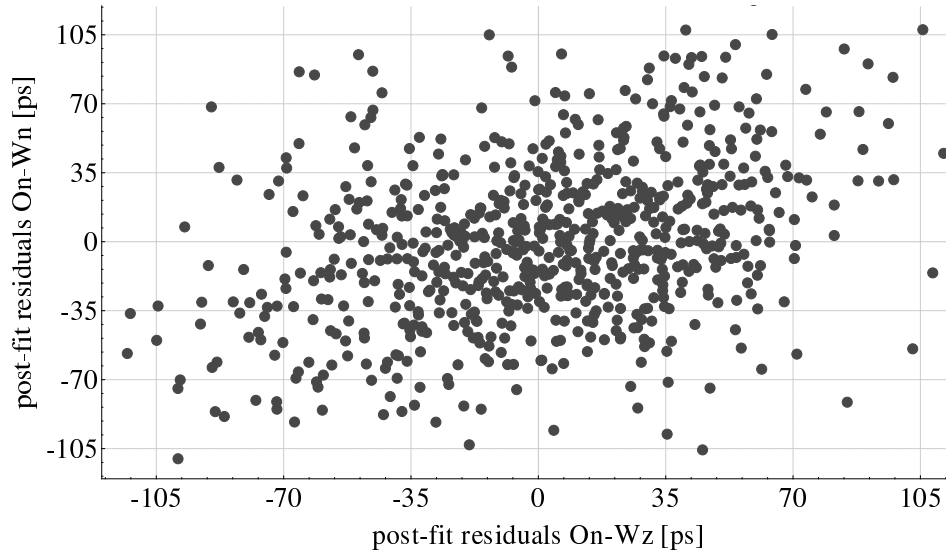
Figure 6.17: Post-fit residuals of the baseline On-Wz versus post-fit residuals of the baseline On-Wn for WHISP6.

Finally, the effect of applying scan-by-scan system calibration and manual phase calibration, respectively, is also investigated with respect to the piece-wise linear segments. According to the findings above, only interval lengths of 30 and 60 minutes are investigated, and the baseline-dependent WRMS of post-fit residuals is shown in Tab. 6.6.

Table 6.6: Baseline-dependent WRMS of post-fit residuals [ps] with respect to different interval lengths of the continuous piece-wise linear functions (CPWLF) for the zenith wet delays and applying scan-by-scan system calibration or manual phase calibration. The best solution is highlighted in yellow.

WHISP5(-M)				
Baseline	**Scan-by-Scan phase cal.**		**manual phase cal.**	
CPWLF interval length	60 min.	30 min.	60 min.	30 min.
On-Wn	30.70	29.16	31.32	29.42
On-Wz	30.76	29.12	39.91	37.19
Wn-Wz	11.31	11.28	27.38	22.84
WHISP7(-M)				
On-Wn	32.02	30.52	35.43	33.32
On-Wz	30.10	28.62	39.30	37.44
Wn-Wz	8.45	7.99	20.82	18.46

Using piece-wise linear segments of 30 minutes instead of 60 minutes leads to an improvement, but the effect due to the different phase calibration methods is even more relevant in this analysis. As expected, the WRMS of post-fit residuals increases sharply when applying manual phase calibration instead of scan-by-scan phase calibration. However, it is striking that particularly the short baseline gets considerably worse: in case of manual phase calibration the WRMS of post-fit residuals is more than twice as high as for the normal scan-by-scan system calibration. But also the degradation for the longer baselines is still considerable. When only considering the solutions with 30 minute piece-wise linear intervals, the solution degrades at least for about 4 ps up to almost 25 ps in quadrature (degradation of about 4 and 13 ps in quadrature for baseline On-Wn, and about 23 and 24 ps in quadrature for baseline On-Wz, in each case for WHISP5 and WHISP7, respectively). Somehow surprising, the effect of degradation is always higher for the baseline On-Wz compared to On-Wn, but, of course, still much lower compared to the short baseline in Wettzell.

6.5   Discussion

In the experiments described in this chapter, local refraction phenomena and system stability issues have been investigated and characterized using two adjacent VLBI radio telescopes at the Wettzell Geodetic Observatory (objective 2). For this purpose, specially designed WHISP sessions with a large number of observations per baseline (600-1000) were performed. A number of noteworthy conclusions has been drawn which would not have been possible without the novel observing approach.

First, differential zenith wet delays were estimated for one station relative to the other station. The relative variations are of the order of only 1-3 millimeters. While a non-zero offset is assumed to be the result of relative paraboloid deformation effects, the remaining variations are assigned to unmodeled random effects in the stochastic model of the observations, particularly refractivity fluctuations in the neutral atmosphere. This has been confirmed by introducing the atmospheric turbulence model developed in Sec. 5.1, since the scatter of differential ZWDs reduces and the standard deviations become more realistic.

Additionally, a residual analysis has been performed taking into account the observation geometry, in particular the separation distance of the signal paths. The post-fit residuals have been found to become larger with increasing ray distance. One reason is the loss of spatial correlations between observations of larger separations.

In order to assess the stability of the observing system, the two way optical time transfer method was used and compared to the VLBI estimates for the clock correction parameters. We found that the agreement is only at the tens of picosecond level (20-30 ps in the better case and up to 60 ps in the worst case), and assume that the clock estimates compensate for more than the clock effect. Since, however, it can be well assumed that all clock-like variations within the one-hour periods are caught by the 60 minute CPWL estimates, the 8 ps variations measured with the TWOTT are assigned to the value to be taken for characterizing the noise component induced by the relative clock behavior. Based on a delay closure test, the correlation error level for each baseline are found to be 4.2 ps, which fits very well the results obtained by RAY and COREY (1991). Together with the clock variations, the noise contribution within a few tens of seconds is not more than 10 ps while, except of the unaccounted measurement noise, the rest of the observation to observation variations are purely atmosphere-driven.

Second, two independent baselines between the two Wettzell antennas and a telescope in Onsala have been observed to estimate (absolute) zenith wet delays for the two Wettzell stations. The correlation between the zenith wet delay parameters of the two adjacent telescopes has been found to be in the order of 0.94 to 0.99, e.g., when modeling small scale refractivity fluctuations with the turbulence model. Although this should have been expected, it is the first proof that the VLBI systems are capable to measure these effects reliably.

For WHISP5 and WHISP7, the differences between the ZWDs of both stations generally vary only in the range of 1-3 millimeters, which fits very well the conclusions obtained for the single baseline WHISP sessions. The situation looks worse for WHISP6, where the ZWD differences almost reach the centimeter level. It can be assumed that the reason is due to the fact that "manual" phase calibration had to be applied for both radio telescopes in Wettzell. This assumption could be unequivocally established by analyzing the post-fit residuals of two further experiments, WHISP5-M and WHISP7-M, where the fringe fitting process was repeated, but manual phase calibration was applied for both Wettzell stations. For the first time, the effect of applying manual phase calibration instead of scan-by-scan system calibration has been identified and quantified, which is in the order of about 20 ps.

In all these investigations the large number of observations is necessary to guarantee a very stable estimation of the parameters and warrants a reliable interpretation of the residuals.

Concluding, the individual components of the observing system, particularly the hydrogen maser clocks feeding the local oscillators and other necessary electronics, the uncertainties emerging from the VLBI correlation process, and the effect of phase calibration, have been quantified, in part for the first time. Additionally, atmospheric refraction effects have been found to be in the range of 1-3 millimeters, which has been validated with two different observing strategies pursued by specially designed experiments. The investigations have also benefit from the turbulence model developed in this thesis to characterize refractivity fluctuations in the neutral atmosphere. Finally, the WHISP project has laid the basis for an improved characterization of atmospheric refraction effects, particularly on a local scale (objective 2).

7. Alternative Strategies for Modeling Atmospheric Refraction

As has been explained in Sec. 3.3.6, certain deficiencies exist in treating the atmosphere in the current tropospheric model of VLBI observations defined in Eq. (3.65). For instance, the pseudo-stochastic character of the piece-wise linear representation, which is used to parametrize the zenith wet delay parameters, is generally not optimal to model the highly dynamic nature of the atmosphere. Additionally, soft constraints in the form of pseudo observations are often needed to stabilize the solution due to missing observations in some piece-wise linear segments. A similar situation applies to the atmospheric gradients modeling azimuthal asymmetries of the neutral atmosphere. Since the estimation of the model coefficients heavily depends on observations at low elevation angles, soft constraints are again necessary to stabilize the solution. Also the mapping functions, which are used to map the zenith delays to an arbitrary elevation angle, are also not optimal, even in case of the Vienna mapping functions 1 as the currently most accurate mapping function. Here, numerical weather models are necessary which are rather coarse with a temporal resolution of only six hours (Böhm et al. 2006b). In order to avoid the mapping function as additional uncertainty source, it would also be desirable to obtain atmospheric delays directly in slant direction, which, however, is only possible, if the number of observations is large enough. Finally, several parameter groups, such as atmospheric and clock parameters as well as the vertical component of the station coordinates, are assumed to be correlated and mutually influence each other, in particular if the stochastic model of the observations is not complete. Consequently, the ZWD estimates do not reflect meteorological and physical conditions in a plausible way in many cases.

In this chapter, two of these issues will be addressed in more detail, leading to two alternative modeling and adjustment strategies which help to estimate atmospheric parameters in a more reliable way. First, an inequality constrained least squares approach (ICLS) has been developed to overcome the deficiency, that occasionally zenith wet delay (ZWD) estimates become negative, which, of course, does not reflect meteorological conditions in a plausible way (Sec. 7.1). Second, the pseudo-stochastic behavior of the piece-wise linear representation for the zenith wet delays, which only models the stochastic character of the atmosphere to a limited extent, was replaced by a least squares collocation method and suitable covariance functions to describe the stochastic properties of the troposphere (Sec. 7.2).

7.1 Constraining Tropospheric Delays in the VLBI Data Analysis

In the standard data analysis of the International VLBI Service for Geodesy and Astrometry (IVS, Nothnagel et al. 2016), a classical or ordinary least squares (OLS) adjustment is used to determine terrestrial coordinates, source positions, Earth orientation parameters as well as clock and atmospheric model correction parameters. The tropospheric propagation delay is generally taken into account by applying an adequate model (hydrostatic component) and by additionally estimating parameter corrections (wet component) in the parameter estimation process (see Chs. 2.1 and 3 for more details). Sometimes, the classical least squares adjustment may lead to negative zenith wet delay estimates.

However, from a meteorological point of view, negative values do not correspond to actual meteorological conditions and physical properties. As already described in Sec. 3.3.2, the zenith wet delays can be directly related to the water vapor content in the atmosphere by a (positive) proportionality factor. The amount of water vapor in the atmosphere is generally described by the partial pressure of water vapor, which can increase up to the so-called saturated vapor pressure per unit of volume. The saturated vapor pressure depends on the temperature as defined by the Clausius-Clapeyron-equation for water vapor (see, e.g., Kraus (2004) for more details). From that equation, it follows that the amount of water vapor in the atmosphere is smaller in locations where the temperature is comparably low. Concluding, there is very little water vapor content at temperatures below $0°C$, but there is nothing like negative water vapor which could produce a negative delay contribution. Negative zenith wet delay estimates occur more frequently for stations located in cold regions, where the wet component of the atmospheric delay is assumed to be comparably small. Assuming a correct hydrostatic modeling, it seems reasonable that unmodeled non-tropospheric effects are absorbed by the ZWD estimates. Of course, it is absolutely essential to avoid this absorption effect as long as the zenith wet delay estimates are a parameter of interest - as is increasingly the case - and allow for a reliable interpretation of the atmospheric estimates.

As a new method, an inequality constrained least squares adjustment from the field of convex optimization (Boyd and Vandenberghe 2004) is introduced as an alternative adjustment strategy for the determination of tropospheric parameters from VLBI observations in this thesis (see also Halsig et al. 2015b; Halsig et al. 2016b). The introduction of inequality constraints, which restrict quantities to a fixed interval instead of a fixed value, i.e. in this case, positive ZWD estimates, allows for a more reliable modeling of physical properties and meteorological conditions.

However, deficiencies in the hydrostatic calibrations, for example due to missing or incomplete pressure data (Heinkelmann et al. 2011), are absorbed by the ZWD estimates. According to the hydrostatic delay model of Davis et al. (1985, Eq. 3.37), a wrong surface pressure of +1 hPa corresponds to an overestimated hydrostatic delay of about 2.3 mm (see also Sec. 3.3.3). Since the ZWDs compensate mis-modeling effects in the hydrostatic calibrations to almost 100%, the corresponding estimated ZWD would be about -2 mm in this case. Constraining now a single ZWD parameter to a positive value in the ICLS adjustment, mis-modeling effects in hydrostatic delays are not compensated for any more. Consequently, not only the remaining ZWD estimates are affected due to the piece-wise linear representation, but also correlated parameters, such as the vertical component of the station coordinates or clock model corrections may be influenced directly. Thus, homogeneous time series of meteorological data are of utmost importance in order to not distort the VLBI target parameters. In addition to bad a priori information, wrong mapping functions could also be compensated for by the ZWD estimates, although, the compensation of this effect is negligible (Halsig et al. 2015b).

To guarantee adequately modeled a priori information, the hydrostatic calibrations are derived from numerical weather models (e.g., of the European Centre for Medium-Range Weather Forecasts, ECMWF). Although the differences to meteorological in-situ observations could reach a few millimeters (Snajdrova et al. 2006), homogeneous time series of meteorological data could be guaranteed. However, numerical weather models are not optimal, since the time resolution of six hours is still rather coarse and actual variability is not taken into account. To overcome this issue, a new strategy is proposed in this thesis (cf. Halsig et al. 2016b), where the ECMWF model is used to define the level of the meteorological data, while their variability is taken from in-situ observations derived at the VLBI sites after removing outliers and filling data gaps.

7.1.1 Inequality Constrained Least Squares Method

The classical or ordinary least squares model is described in Eq. (2.10). The optimal solution $\widetilde{\boldsymbol{x}}$ is obtained by minimizing the objective function, defined as the (possibly weighted) sum of squared residuals,

$$\boldsymbol{v}^T \boldsymbol{\Sigma}_{ll}^{-1} \boldsymbol{v} \ldots \ \min, \tag{7.1}$$

where $\boldsymbol{\Sigma}_{ll}$ denotes the variance covariance matrix of the observations (see Sec. 2.2 for more details).

In case of the inequality constrained least squares method, this concept is extended by p linear inequality constraints of the form

$$\boldsymbol{B}^T \boldsymbol{x} \leq \boldsymbol{b}, \tag{7.2}$$

which have to be fulfilled strictly. $\boldsymbol{B}$ is the $m \times p$ matrix of constraints and $\boldsymbol{b}$ the corresponding $p \times 1$ right-hand side. In the context of VLBI observations, the ICLS method can be used to restrict the tropospheric parameters to positive and, therefore, more reliable estimates in a meteorological and physical sense. Finally, the optimal solution $\widetilde{\boldsymbol{x}}_{ICLS}$ is now obtained by minimizing the objective function in Eq. (7.1) under the constraint in Eq. (7.2).

In Fig. 7.1, the contour lines of the objective function of an example problem as well as the estimates derived by the classical and inequality constrained least squares solution are illustrated. The inequality constraints ($x_1 \leq 3, x_2 \geq 2, x_1 + x_2 \geq 2$, red lines) limit the feasible region (yellow area). In addition to the classical least squares solution $\widetilde{\boldsymbol{x}}'$ (blue cross), which lies in the infeasible region of the ICLS problem, the initial solution $\boldsymbol{x}^{(0)}$ (black dot), the interim solution $\boldsymbol{x}^{(1)}$ (black dot) and the final solution $\widetilde{\boldsymbol{x}}_{ICLS}$ (green cross) of the ICLS problem are depicted.

	(a) OLS	(b) ICLS
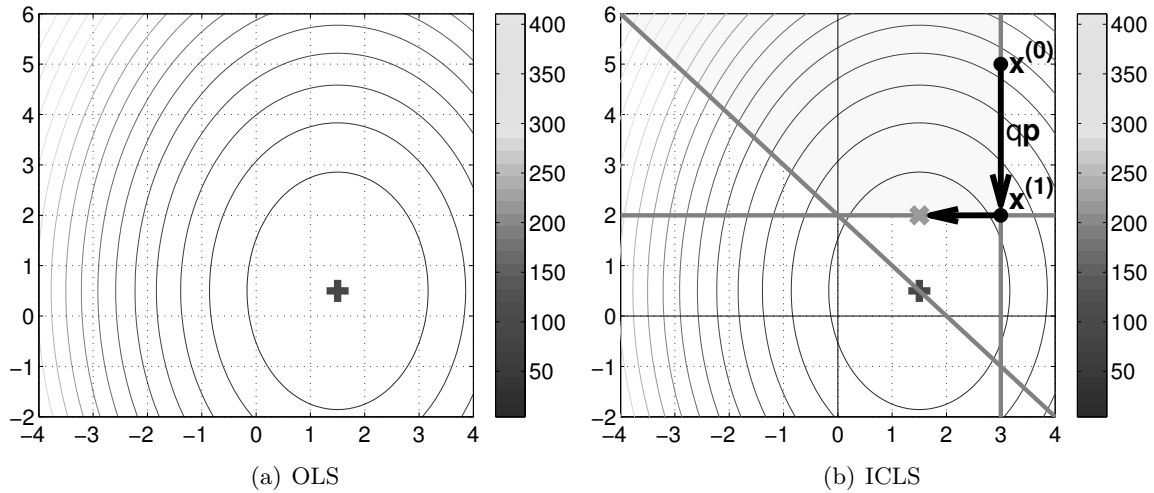
Figure 7.1: Contour lines of the objective function and OLS and ICLS estimates for an example problem. The inequality constraints ($x_1 \leq 3, x_2 \geq 2, x_1 + x_2 \geq 2$, red lines) limit the feasible region (yellow area). The initial solution $\boldsymbol{x}^{(0)}$, interim solution $\boldsymbol{x}^{(1)}$ (black dots) and final solution (green cross) of the Active Set method are shown as black dots. The OLS solution (blue cross) in the infeasible region of the ICLS problem is shown for comparison (HALSIG et al. 2015B).

Since it is not known in the beginning, which inequality constraints will influence the result, the ICLS problem can only be solved iteratively. In the following, one of these iterative methods, the so-called Active Set method, will be explained in some detail.

Active Set Method

The Active Set method (GILL et al. 1981, pp. 167-173) is a simplex-type algorithm designed to solve ICLS problems. The principle idea is to follow the boundary (red lines in Fig. 7.1(b)) of the feasible set (yellow region), where all inequality constraints are fulfilled, until the optimal solution $\widetilde{\boldsymbol{x}}$ (green cross) is reached. Following ROESE-KOERNER et al. (2012A), who introduced the Active Set method to geodetic problems, the algorithm can be subdivided into four main steps which are described briefly below.

Step 1. Choose an initial point and find active constraints: First, an initial point $\boldsymbol{x}^{(0)}$ is chosen, which fulfills all constraints. Subsequently, the set of constraints is subdivided into active constraints, which hold as equality constraints $\boldsymbol{W}^T \boldsymbol{x}^{(i)} = \boldsymbol{w}$, and inactive constraints, which hold as strict inequalities $\boldsymbol{V}^T \boldsymbol{x}^{(i)} < \boldsymbol{v}$. In more detail, the jth inequality constraint $x_j \leq 0$ is called active at point $\boldsymbol{x}$ if $x_j = 0$. In contrast, the constraint $x_j \leq 0$ is assigned to be inactive if $x_j < 0$. Otherwise, if a constraint is neither active, nor inactive, $x_j > 0$ is valid and the constraint is said to be violated. This is crucial, because only active constraints have an influence on the estimation process.

Step 2. Compute the search direction: The gradient

$$\boldsymbol{g} = \boldsymbol{N}\boldsymbol{x}^{(i)} - \boldsymbol{n} \tag{7.3}$$

in point $\boldsymbol{x}^{(i)}$ is determined, where $\boldsymbol{N}$ and $\boldsymbol{n}$ describe the normal equation matrix and the corresponding right-hand side (see Eq. 2.14). Subsequently, the negative gradient is projected in the nullspace of the set of active constraints to ensure that the boundary of the feasible set is followed, resulting in search direction

$$\boldsymbol{p}^{(i)} = -\Pi^N_{S^\perp(\boldsymbol{W})} \, \boldsymbol{g}, \tag{7.4}$$

where $\Pi^N_{S^\perp(\boldsymbol{W})}$ denotes a projection matrix (KOCH 1999, pp 64-66).

Step 3. Compute the step length: The distance to all inactive constraints in search direction is computed to determine the maximal feasible step length $q^{(i)}$.

Step 4. Update parameters and active set: With the search direction $\boldsymbol{p}$ and the step length q at hand, an update of the parameters can be computed,

$$\boldsymbol{x}^{(i+1)} = \boldsymbol{x}^{(i)} + q^{(i)}\boldsymbol{p}^{(i)}. \tag{7.5}$$

The corresponding Lagrange multipliers of the extended objective function

$$\Phi\left(\boldsymbol{x}, \boldsymbol{k}\right) = \boldsymbol{x}^T \boldsymbol{N} \boldsymbol{x} - 2\boldsymbol{n}^T \boldsymbol{x} + \boldsymbol{k}^T (\boldsymbol{B}^T \boldsymbol{x} - \boldsymbol{b}) \tag{7.6}$$

are determined (iteration indices were neglected). If all Lagrange multipliers linked with active constraints are non-negative, the optimal solution is found and the algorithm terminates. Otherwise all constraints with negative Lagrange multipliers are removed from the set of active constraints and the algorithm is repeated.

Stochastic Description

In contrast to classic adjustment procedures, there exists no analytic relationship between parameters and observation in the ICLS case. Therefore, variance propagation cannot be applied. In order to derive a measure for the quality of the estimated quantities, Monte Carlo methods can be utilized to derive a discrete approximation of the a posteriori probability density function (PDF, ROESE-KOERNER et al. 2012b). As the introduction of inequality constraints often leads to asymmetric PDFs, highest probability density (HPD) intervals are computed instead of (symmetric) standard deviations (ROESE-KOERNER et al. 2012b).

7.1.2   Analysis Settings

In total, 2333 VLBI sessions from 1993 to 2010 provided by the IVS (NOTHNAGEL et al. 2015) are processed using both, the classical and inequality constrained least squares adjustment. All observations are initially processed with the VLBI analysis software Calc/Solve (MA et al. 1990) which only implements the classical least squares adjustment. Calc/Solve was modified to export the equation system, which is, in a second step, used to perform the classical least squares adjustment and to implement and solve the ICLS problem in a C++ back-end. Later, the complete data analysis chain was incorporated into the VLBI analysis software package ivg::ASCOT (ARTZ et al. 2016; HALSIG et al. 2017).

In the following, the VLBI modeling and estimation settings will be briefly described. A typical parametrization for single session VLBI analysis has been chosen. The source positions are fixed to their positions in the current version of the International Celestial Reference Frame (ICRF2, FEY et al. 2015), while terrestrial station coordinates, Earth orientation parameters, the clock behavior and tropospheric delays are determined during the parameter estimation procedure.

First, the clock correction parameters are modeled by a quadratic polynomial and additional continuous piece-wise linear functions (CPWLF), i.e., linear splines (DE BOOR 1978), with a temporal resolution of 60 minutes. The zenith wet delays and troposphere gradients are parametrized as CPWLF with a temporal resolution of 60 minutes and 6 h, respectively. In order to stabilize the equation system, the clock and tropospheric parameters are supplemented by soft constraints in the form of pseudo observations, which are, compared to hard constraints, less heavily weighted (e.g., $\sigma_{clock} = 2 \cdot 10^{-14} \frac{s}{s}$, $\sigma_{ZWD} = 15 \frac{mm}{h}$, $\sigma_{grad_1} = 2 \frac{mm}{day}$, $\sigma_{grad_2} = 0.5$ mm).

Further, additional equations of hard constraints, including a no-net-translation (NNT) and a no-net-rotation (NNR) condition with three equations each, are needed to remove the natural VLBI rank deficiency and to prevent the system of equations from singularities (ANGERMANN et al. 2004). In the following of this section, the term constraint will always only refer to inequalities concerning the ICLS method and not to the measures for the stabilization of the equation system. The stabilizing pseudo observations are always applied, at least in the framework of the inequality constraint least squares adjustment.

Concerning the estimation of ZWDs, the Vienna mapping functions 1 (VMF1, BÖHM et al. 2006b) are used. To receive homogeneous time series of meteorological data, the hydrostatic delay is also modeled using reanalysis data of the numerical weather model of the European Centre for Medium-Range Weather Forecasts (ECMWF). This has been done although in-situ surface pressure is included in the vgosDB data files (the new data format to store data obtained from VLBI observations; BOLOTIN et al. 2016) or the former database format (see, e.g., GIPSON 2012), which,

however, could contain data gaps, outliers and incorrect meteorological data due to sensor failures. As the ECMWF data contain information only in intervals of six hours, we loose precision (from the pressure values at the epoch of each observation) but gain a higher accuracy.

In the following, an adequate a priori model is assumed and an inequality constrained least squares adjustment is applied to the VLBI modeling procedure, complementing the classical least squares solution described in Sec. 2.2. For this purpose, the constraint is imposed, that all ZWD estimates must be greater than or equal to 0 mm (i.e., $x_i \geq 0$ mm).

7.1.3 Results

The new methodology is applied to 17 years of VLBI observations in order to investigate the influence of the inequality constraints on typical VLBI parameters in a long term study. In 454 out of 2333 VLBI sessions the method automatically applied inequality constraints, that means in about 20 percent of cases at least one constraint is active. Generally, the quality of the determination of baseline lengths between different VLBI telescopes is assessed in terms of baseline length repeatabilities, which can be regarded as the standard deviation for an individual baseline after removing a linear trend from a time series of baseline lengths. For both the OLS (black) and the ICLS (red) adjustment, the baseline repeatabilities, which occur in at least 30 sessions, as well as the baseline repeatabilities for only those sessions, for which, in addition, inequality constraints are applied, are shown in Fig. 7.2(a) and Fig. 7.2(b), respectively. Further, a quadratic polynomial is fitted to the data for a better visualization. The ICLS solution (red line, Fig. 7.2(b)) is slightly more precise than the OLS solution (black line). The application of ICLS improves 9% of the baseline repeatabilities for at least 1 mm (black bars in Fig. 7.2(c)) while 1% get worse for at least 1 mm (dark gray bars) and 90% remain unchanged (light gray bars).

Concluding, the ICLS adjustment seems not to harm the estimation of the telescope positions, provided that the a priori hydrostatic component is modeled sufficiently. It is worth mentioning, that it was initially not intended to improve the determination of station coordinates, but to avoid negative tropospheric estimates and, therefore, to allow for a physically more reliable description of the atmospheric delays.

(a)

(b)

(c)
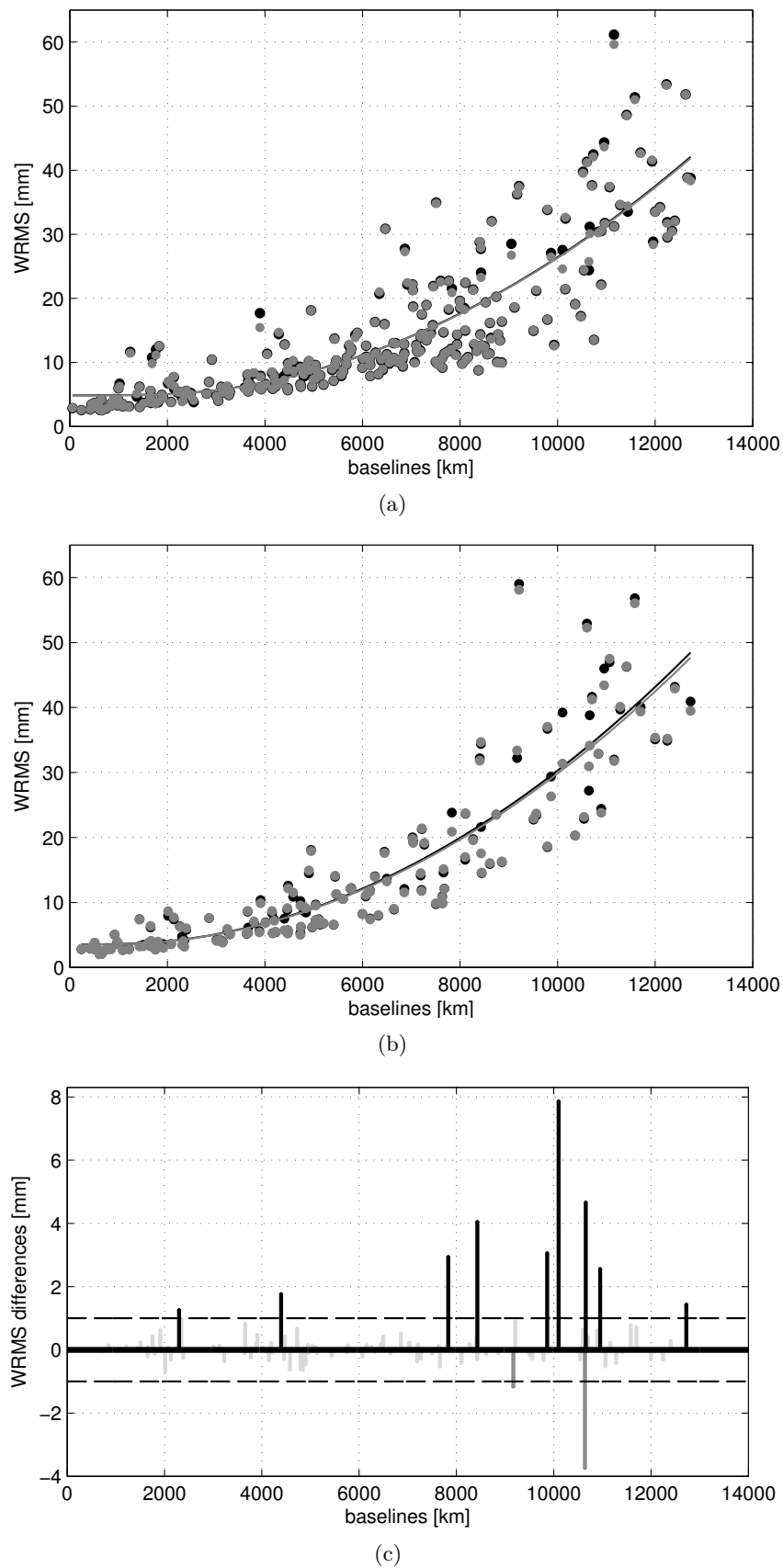
Figure 7.2: Baseline length repeatabilities for (a) VLBI data from 1993 to 2010 and (b) those sessions, for which constraints are active, w.r.t. the classical (black) and the ICLS (red) adjustment; and (c) difference (OLS minus ICLS) in baseline length repeatabilities (HALSIG et al. 2015B).

In the following, the effect of the new methodology on zenith wet delay estimates of a single VLBI session is investigated in more detail. Since negative ZWD estimates occur most frequently in cold regions, a VLBI station in Gilmore Creek, Alaska, was selected as an example. In Fig. 7.3, the zenith wet delay estimates are illustrated for a VLBI experiment in November 2001. The ZWD parameters derived from the classical least squares adjustment are represented in black while the ICLS estimates are depicted in red. Here, the parameter referring to the second piece-wise linear segment is negative by about 3 to 4 mm and is shifted to a non-negative value in the ICLS approach. Since continuous piece-wise linear functions are used for the parametrization of the atmospheric parameters, all zenith wet delay estimates of the same VLBI station are correlated. Although many of the ZWD estimates are also shifted, the ZWD differences between the classical and constrained adjustment are negligible, except for the parameter where the inequality constraint is active.
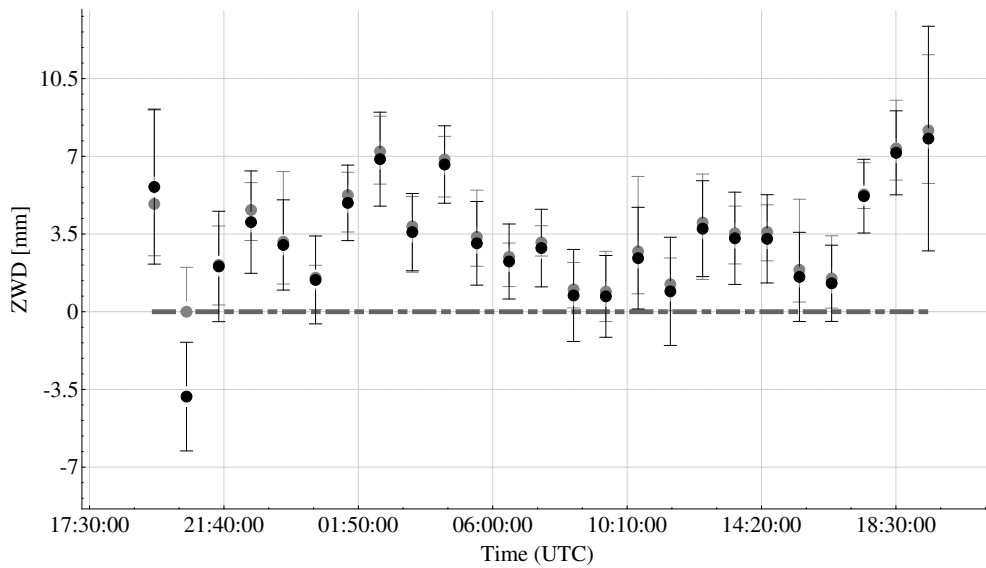
Figure 7.3: Zenith wet delay parameters for the VLBI station in Gilmore Creek, Alaska in November 2001. The classical least squares estimates are represented in black and the ICLS solution is depicted in red (HALSIG et al. 2016B).

Since different parameter types are possibly correlated, the influence of the single inequality constraint (blue) applied for one zenith wet delay on other parameter groups, such as station coordinates (black), clock model correction parameters (light gray) and the zenith wet delays (dark gray) of the same station, is shown in Fig. 7.4. While the maximum difference of about 1 mm can be found in one of the ZWD estimates, the remaining part is evenly distributed between the other parameters, although the differences are on the order of tenths of a millimeter and, consequently, negligible. The effect of the same inequality constraint on the ZWD estimates of another station, as an example for Matera in Italy, is depicted in Fig. 7.4(b). The differences between both solutions are again marginal, which was confirmed by investigating other sessions, concluding that the use of the ICLS method only leads to an effect on estimates of the same station for which inequality constraints are applied.

However, this is only true if the a priori hydrostatic calibrations are modeled correctly. If the assumption of an adequate a priori model is violated, the vertical component can change noticeably

(a)

(b)
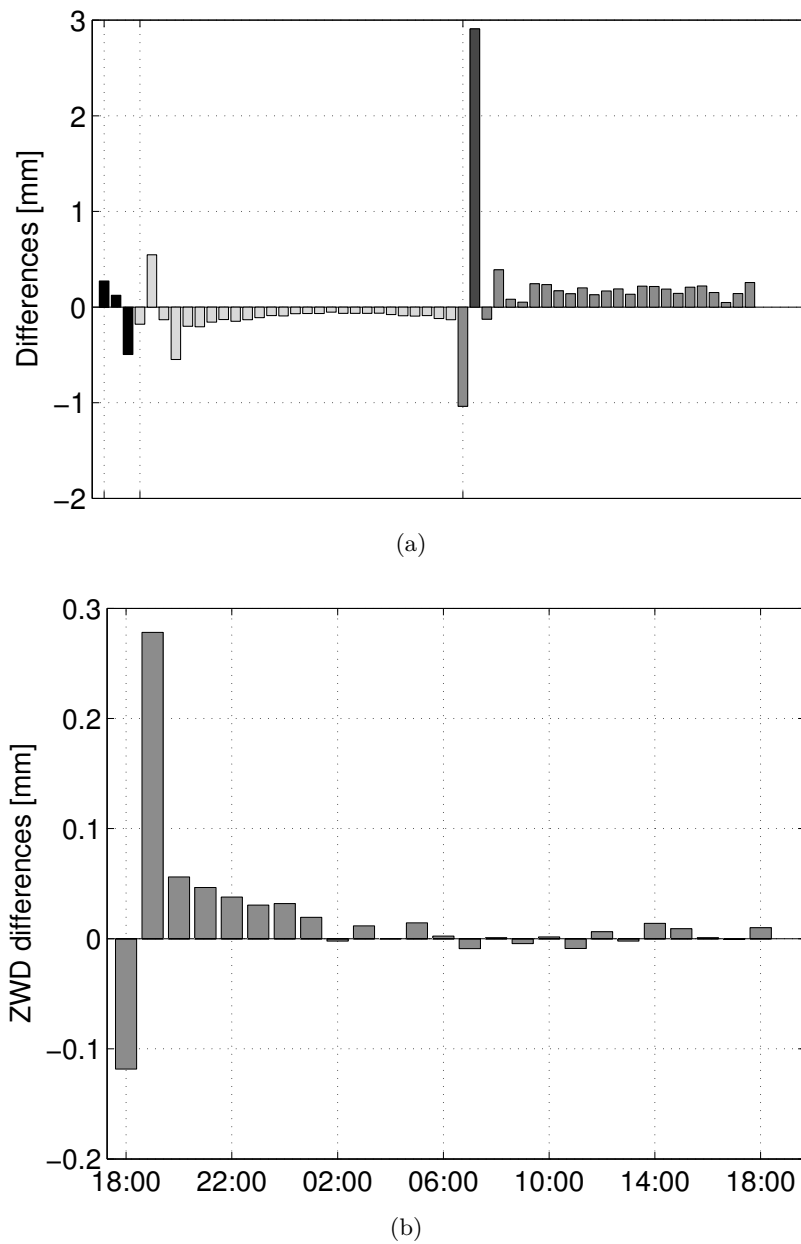
Figure 7.4: (a) The influence of a single ZWD inequality constraint (blue) on station coordinates (black), clocks (light gray) and zenith wet delays (dark gray) of the same station (Gilmore Creek, Alaska). (b) The influence of the same inequality constraint on zenith wet delay parameters (dark gray) of another station in Matera, Italy (Halsig et al. 2016b).

in the order of several millimeters. In order to validate the influence of the meteorological data on the results, two solutions have been determined for 125 VLBI sessions in 2002, which only differ in the hydrostatic calibrations: a solution with meteorological data only derived from in-situ observations is depicted in cyan, while a solution using the combined approach described above is represented in red in Fig. 7.5. Both solutions are validated in terms of the differences in baseline length repeatabilities with respect to the classical least squares adjustment.

For about 20% of these sessions automatically inequality constraints are applied for at least one station and one zenith wet delay parameter, and approximately the same number of inequality constraints is needed for both ICLS realizations, although the constrained parameters and the order of magnitude in the differences to the classical least squares solution can be different. Since outliers and data gaps may occur due to sensor failures in the in-situ measurements, and inequality constraints suppress the effect of compensating erroneous hydrostatic calibrations by the zenith wet delay estimates, the baseline length repeatabilities are degraded in the case of purely in-situ measurements compared to the classical least squares solution. The situation changes when introducing the strategy of combining model data and meteorological observations since the differences in baseline length repeatabilities are now negligible, although inequality constraints are introduced to allow for a more reliable estimation of tropospheric parameters.
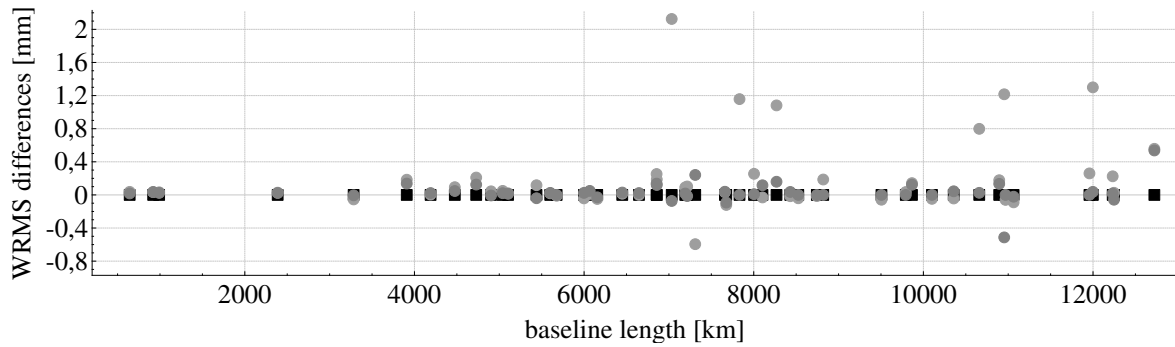
Figure 7.5: Baseline length repeatability differences with respect to the classical least squares solution. The cyan dots represent an ICLS solution, where the meteorological data used for the calculation of the hydrostatic delay only results from in-situ measurements, while red dots depict an ICLS solution using atmospheric a priori data derived from a combination of in-situ observations and a numerical weather model of the ECMWF (HALSIG et al. 2016B).

In conclusion, the application of the ICLS adjustment is, in principle, possible without harming the VLBI target parameters, provided that the a priori hydrostatic component is modeled sufficiently. However, the negative zenith wet delay estimates result not only from a priori mis-modeling, but could also be the result of several other issues, such as mis-modeling of geophysical effects as well as a certain impact due to instrumental delays or the clock parametrization. A sophisticated analysis on this topic, particularly on the stability of the hydrogen maser clocks feeding the local oscillators and other necessary electronics, is performed using close-range VLBI observations in the framework of the WHISP (Wettzell HIgh SPeed) project (see Ch. 6).

7.2 A Stochastic Description of Tropospheric Delays

In standard VLBI data analysis the zenith wet delays are not modeled but determined within the parameter estimation process, parametrized as continuous piece-wise linear functions in form of linear splines with a specific time interval. Routinely, the resolution of the piece-wise linear segments is 60 minutes, but can be reduced to 30 or even 15 to 20 minutes if the number of observations in the individual time segments is adequately high (cf. the discussion in Ch. 6 on this issue). The piece-wise linear representation is however not optimal, since the highly dynamic nature of the atmosphere, in particular the wet troposphere, can only be modeled to a limited extent. Moreover, the piece-wise linear functions represented as linear splines show a non-ideal characteristic in terms of their transfer function (cf. SCHUBERT 2017). Another deficit is the necessity of soft constraints in form of pseudo observations which are generally needed to stabilize the solution due to missing observations in some piece-wise linear segments. The pseudo-observations further distort the solution statistics as the (W)RMS due to an increasing number of degrees of freedom. In order to overcome both deficiencies and to allow for a fully stochastic description of the atmospheric behavior, a least squares collocation method is suggested, where the stochastic properties of the neutral atmosphere are reflected by suitable covariance functions.

In principle, the characteristics of the atmosphere could have also been described as a stochastic process in a filter estimation (e.g., a Kalman filter or a square-root information filter). Although the least squares collocation method lags behind the filter method concerning the computational effort, it directly provides the normal equation matrices, which could be used for combination purposes on the normal equation level in future VLBI global solutions. The covariance function used in the least squares collocation method could be easily transferred to a stochastic process in a filter estimation without loss of generality. The square-root information filter has already been implemented in the analysis software ivg::ASCOT (cf. SCHUBERT et al. 2017).

In Sec. 7.2.1, the theory of least squares collocation is presented, followed by Sec. 7.2.2 on the definition and discussion of different covariance functions. A case study is performed and the results are outlined in Sec. 7.2.3.

7.2.1 Least Squares Collocation Method

The general model of the least squares collocation (LSC, KRARUP 1969; MORITZ 1972) can be formulated as a generalization of Eq. (2.10),

$$\underbrace{\boldsymbol{l}}_{observation} = \underbrace{\boldsymbol{A}\boldsymbol{x}}_{deterministic} + \underbrace{\boldsymbol{s}}_{stochastic} + \underbrace{\boldsymbol{n}}_{noise}, \tag{7.7}$$

where $\boldsymbol{l}$ denotes the $n \times 1$ observation vector, $\boldsymbol{x}$ represents the $m \times 1$ vector of deterministic parameters, and the $n \times m$ Jacobian matrix is given by $\boldsymbol{A}$. In addition to the noise component $\boldsymbol{n}$ in Eq. (2.10), $\boldsymbol{s}$ denotes a second random quantity to describe the stochastic behavior of certain quantities, referred to as signal in the following.

Following SCHUH (2016), the estimates of $\boldsymbol{x}$ and $\boldsymbol{s}$ are supposed to comply with the requirements to be best linear estimates in the statistical sense. The linear dependency on the observations can be expressed by

$$\hat{\boldsymbol{x}} = \boldsymbol{G}^T \boldsymbol{l} \qquad \text{and} \qquad \hat{\boldsymbol{s}} = \boldsymbol{H}^T \boldsymbol{l}, \tag{7.8}$$

assuming $\boldsymbol{G}$ and $\boldsymbol{H}$ to be independent of the observations and describing the coefficients of the linear combination in order to receive the estimates directly from the observations. Second, the requirement of unbiased estimates is fulfilled, if the expectation value of the estimation error (ϵ_x and ϵ_s, respectively) is zero,

$$E\{\epsilon_x\} \overset{!}{=} 0 \qquad \text{and} \qquad E\{\epsilon_s\} \overset{!}{=} 0. \tag{7.9}$$

According to SCHUH (2016, pp 80ff) this is either fulfilled if the expectation value of the signal is zero,

$$E_s \overset{!}{=} 0, \tag{7.10}$$

or, additional constraints,

$$\boldsymbol{G}^T \boldsymbol{I_N} \overset{!}{=} \boldsymbol{0} \qquad \text{and} \qquad \boldsymbol{H}^T \boldsymbol{I_N} - \boldsymbol{I_N} \overset{!}{=} \boldsymbol{0}, \tag{7.11}$$

with $\boldsymbol{I_N} = \begin{bmatrix} 1 & 1 & \dots & 1 \end{bmatrix}^T_{[n \times 1]}$ needs to be included in the optimization task. Third, the estimates of $\boldsymbol{x}$ and $\boldsymbol{s}$ are supposed to minimize the estimation error

$$\Sigma\{\epsilon_x\} \dots Min. \qquad \text{and} \qquad \Sigma\{\epsilon_s\} \dots Min. \tag{7.12}$$

Finally, the optimal solution for the deterministic parameters can be written as

$$\widetilde{\boldsymbol{x}} = \left[\boldsymbol{A}^T \left(\boldsymbol{\Sigma}_{ss} + \boldsymbol{\Sigma}_{nn} \right)^{-1} \boldsymbol{A} \right]^{-1} \boldsymbol{A}^T \left(\boldsymbol{\Sigma}_{ss} + \boldsymbol{\Sigma}_{nn} \right)^{-1} \boldsymbol{l} \tag{7.13}$$

with the corresponding variance-covariance matrix

$$\boldsymbol{\Sigma}_{\widetilde{x}\widetilde{x}} = \left[\boldsymbol{A}^T \left(\boldsymbol{\Sigma}_{ss} + \boldsymbol{\Sigma}_{nn} \right)^{-1} \boldsymbol{A} \right]^{-1}, \tag{7.14}$$

where $\boldsymbol{\Sigma}_{ss}$ and $\boldsymbol{\Sigma}_{nn}$ are the variance-covariance matrices of the stochastic signal and the noise term, respectively. The matrix $\boldsymbol{\Sigma}_{ss}$ can be determined by suitable covariance functions (see Sec. 7.2.2). It is evident that Eq. (7.13) is equivalent to the classical least squares solution in Eq. (2.13) with the variance-covariance matrix $\boldsymbol{\Sigma} := \boldsymbol{\Sigma}_{ll} = \boldsymbol{\Sigma}_{ss} + \boldsymbol{\Sigma}_{nn}$. Consequently, $\boldsymbol{\Sigma}$ includes both the covariances of the signal and the observation noise.

After determining the deterministic parameters, the stochastic signal prediction can be formulated as

$$\widetilde{\boldsymbol{s}} = \boldsymbol{\Sigma}_{sl} \left(\boldsymbol{\Sigma}_{ss} + \boldsymbol{\Sigma}_{nn} \right)^{-1} \left(\boldsymbol{l} - \boldsymbol{A}\widetilde{\boldsymbol{x}} \right) \tag{7.15}$$

with the corresponding variance-covariance matrix

$$\boldsymbol{\Sigma}_{\widetilde{s}\widetilde{s}} = \boldsymbol{\Sigma}_{ss} - \boldsymbol{\Sigma}_{sl} \left(\boldsymbol{\Sigma}_{ss} + \boldsymbol{\Sigma}_{nn} \right)^{-1} \boldsymbol{\Sigma}_{sl}^T + \boldsymbol{\Sigma}_{sl} \left(\boldsymbol{\Sigma}_{ss} + \boldsymbol{\Sigma}_{nn} \right)^{-1} \boldsymbol{A} \boldsymbol{\Sigma}_{\widetilde{x}\widetilde{x}} \boldsymbol{A}^T \left(\boldsymbol{\Sigma}_{ss} + \boldsymbol{\Sigma}_{nn} \right)^{-1} \boldsymbol{\Sigma}_{sl}^T, \tag{7.16}$$

or

$$\boldsymbol{\Sigma}_{\widetilde{s}\widetilde{s}} = \boldsymbol{\Sigma}_{ss} - \boldsymbol{\Sigma}_{sl} \boldsymbol{\Sigma}^{-1} \boldsymbol{\Pi}_{\boldsymbol{S}^\perp(\boldsymbol{A})}^{\boldsymbol{\Sigma}^{-1}} \boldsymbol{\Sigma}^{-1} \boldsymbol{\Sigma}_{sl}^T. \tag{7.17}$$

with $\mathbf{\Sigma} = \mathbf{\Sigma}_{ss} + \mathbf{\Sigma}_{nn}$ and the projection matrix (SCHUH 2016)

$$\mathbf{\Pi}_{S^{\perp}(\boldsymbol{A})}^{\mathbf{\Sigma}^{-1}} = \mathbf{\Sigma} - \boldsymbol{A} \left(\boldsymbol{A}^T \mathbf{\Sigma}^{-1} \boldsymbol{A} \right)^{-1} \boldsymbol{A}^T. \tag{7.18}$$

In case of VLBI observations, two modifications are performed in Eq. (7.7). First, the stochastic component is augmented by a second Jacobian matrix $\boldsymbol{B}$ consisting of the partial derivatives of the observation equations with respect to the stochastic parameters, leading to

$$\boldsymbol{l} = \boldsymbol{A}\boldsymbol{x} + \boldsymbol{B}\boldsymbol{s} + \boldsymbol{n}. \tag{7.19}$$

More specifically, $\boldsymbol{B}$ contains the mapping functions as the partial derivatives with respect to the zenith wet delays. The mapping functions, which can be generally approximated by $\frac{1}{\sin(\varepsilon)}$, are not directly included in the signal component $\mathbf{\Sigma}_{ss}$ in order to ensure the positive definiteness of the covariance function and matrix, which generally may be violated with an additional sine term.

Second, the deterministic component of Eq. (7.19) is divided into

$$\boldsymbol{l} = \boldsymbol{A}_1 \boldsymbol{x}_1 + \boldsymbol{A}_2 \boldsymbol{x}_2 + \boldsymbol{B}\boldsymbol{s} + \boldsymbol{n}, \tag{7.20}$$

to separate the atmospheric and non-atmospheric components. Hence, $\boldsymbol{A}_1 \boldsymbol{x}_1$ contains the deterministic VLBI target parameters, such as station and source positions, Earth orientation parameters, and the clock model correction parameters, while $\boldsymbol{A}_2 \boldsymbol{x}_2$ only contains the parameters for the atmosphere, which only include an deterministic offset parameter estimated for each telescope and the duration of the complete session. This is necessary in order to guarantee that $E_s \overset{!}{=} 0$.

In case of the slightly modified model in Eq. (7.19), Eqs. (7.13) and (7.14) become

$$\widetilde{\boldsymbol{x}} = \left[\boldsymbol{A}^T \left(\boldsymbol{B}\mathbf{\Sigma}_{ss}\boldsymbol{B}^T + \mathbf{\Sigma}_{nn} \right)^{-1} \boldsymbol{A} \right]^{-1} \boldsymbol{A}^T \left(\boldsymbol{B}\mathbf{\Sigma}_{ss}\boldsymbol{B}^T + \mathbf{\Sigma}_{nn} \right) \boldsymbol{l}, \tag{7.21}$$

$$\mathbf{\Sigma}_{\widetilde{x}\widetilde{x}} = \left[\boldsymbol{A}^T \left(\boldsymbol{B}\mathbf{\Sigma}_{ss}\boldsymbol{B}^T + \mathbf{\Sigma}_{nn} \right)^{-1} \boldsymbol{A} \right]^{-1}, \tag{7.22}$$

and, defining $\mathbf{\Sigma} := \boldsymbol{B}\mathbf{\Sigma}_{ss}\boldsymbol{B}^T + \mathbf{\Sigma}_{nn}$ and using the projection matrix in Eq. (7.18), yields

$$\widetilde{\boldsymbol{s}} = \mathbf{\Sigma}_{ss}\boldsymbol{B}^T \left(\boldsymbol{B}\mathbf{\Sigma}_{ss}\boldsymbol{B}^T + \mathbf{\Sigma}_{nn} \right)^{-1} \left(\boldsymbol{l} - \boldsymbol{A}\widetilde{\boldsymbol{x}} \right), \tag{7.23}$$

$$\mathbf{\Sigma}_{\widetilde{s}\widetilde{s}} = \mathbf{\Sigma}_{ss} - \mathbf{\Sigma}_{ss}\boldsymbol{B}\mathbf{\Sigma}^{-1}\mathbf{\Pi}_{S^{\perp}(\boldsymbol{A})}^{\mathbf{\Sigma}^{-1}}\mathbf{\Sigma}^{-1}\boldsymbol{B}\mathbf{\Sigma}_{ss}^T, \tag{7.24}$$

instead of Eqs. (7.15) and (7.16).

7.2.2 Covariance Functions

Least squares collocation depends essentially on a priori information in form of appropriate (auto-) covariance functions used to describe the stochastic properties of the signal component in $\mathbf{\Sigma}_{ss}$. According to MORITZ (1976), the covariance functions are generally characterized by two parameters: the correlation length and the curvature or form parameter. While the correlation length defines the value of the argument for which the covariance function has decreased to half of its value, the form parameter is related to the curvature of the covariance function. In the following, several covariance models are presented and discussed, starting with the approach suggested by

TITOV (2000), which has already been successfully applied to VLBI observations before (TITOV 2000; TITOV and SCHUH 2000; ARTZ et al. 2012). It is demonstrated that this covariance function can be transferred to a second order Gauss Markov process (SOGM, MAYBECK 1979), which is used to analyze the covariance model in more detail. Additionally, further covariance functions are introduced (e.g., MATÉRN 1960; SANSÒ and SCHUH 1987; GASPARI and COHN 1999) and their properties are described.

Second Order Gauss Markov Process

The general model proposed by TITOV (2000) reads

$$\gamma(\tau) = \frac{\gamma(0)}{\cos(\varphi)} e^{-a|\tau|} \cos(b|\tau| + \varphi), \tag{7.25}$$

where $\gamma(0)$ is the variance and $\gamma(\tau)$ denotes the covariance for time difference τ. TITOV (2000) suggests the coefficients to be

$$a = 6.24, \qquad b = 6.48, \qquad \varphi = 0.82$$

for the atmospheric parameters. In addition, the author also proposed coefficients for the clock correction parameters with respect to the same covariance function, and a further covariance function and corresponding coefficients representing the behavior of the Earth orientation parameters. In this thesis, however, only the behavior of the zenith wet delays is modeled stochastically. Due to the highly dynamic character of the wet troposphere, the greatest potential in improving the data analysis of VLBI observations is expected, while the behavior of the clocks is assessed to be modeled sufficiently by piece-wise linear functions.

The covariance function in Eq. (7.25) consists of an oscillation part represented by a cosine term and a descending exponential function describing the attenuation effect. Concerning the coefficients in Eq. (7.25), a can be assigned to the attenuation while b defines the frequency in the cosine term, shifted by a phase φ.

Investigating this model in more detail, the covariance function seems not to be positive definite (cf. SCHUBERT 2017), which, however, is highly advisable (see, e.g., discussion in SANSÒ and SCHUH 1987). In order to verify this assumption, the initial model of TITOV (2000) is transferred to a second order Gauss Markov process (SOGM, MAYBECK 1979, p. 185) of the type

$$\gamma(\tau) = \frac{\gamma(0)}{\cos(\eta)} e^{-\zeta\omega_n|\tau|} \cos\left(\underbrace{\sqrt{1-\zeta^2}\omega_n}_{\overset{!}{=}\hat{\omega}} |\tau| - \eta\right). \tag{7.26}$$

Similar to the initial model, ζ represents the attenuation effect, ω_n the frequency, and η the phase shift. Comparing Eqs. (7.25) and (7.26) yields the following relationship between both covariance functions:

$$a = \zeta\omega_n, \tag{7.27}$$

$$b = \hat{\omega} = \sqrt{1-\zeta^2}\omega_n, \tag{7.28}$$

$$\eta = -\varphi, \tag{7.29}$$

$$\zeta = \frac{a}{\sqrt{a^2 + b^2}}, \tag{7.30}$$

$$\omega_n = \sqrt{a^2 + b^2}. \tag{7.31}$$

Consequently, the covariance function provided by TITOV (2000) could be reproduced by using a second order Gauss Markov process with the following coefficients (cf. SCHUBERT 2017):

$$\eta = -0.82, \qquad \zeta = 0.6936, \qquad \omega_n = 8.9960.$$

In Fig. 7.6, the resulting covariance function is depicted in black.

According to MAYBECK (1979, p 185f), the corresponding power spectral density of the covariance function in Eq. (7.26) reads

$$F(\omega) = \frac{\hat{c}_1^2 \omega^2 + \hat{c}_2^2}{\omega^4 + 2\omega_n^2 \left(2\zeta^2 - 1\right)\omega^2 + \omega_n^2} \tag{7.32}$$

with

$$\begin{aligned} \hat{c}_1^2 &= \sqrt{\left(\frac{2\sigma^2}{\cos(\eta)}\right)\omega_n sin(\alpha - \eta)}, \\ \hat{c}_2^2 &= \sqrt{\left(\frac{2\sigma^2}{\cos(\eta)}\right)\omega_n^3 sin(\alpha + \eta)} \end{aligned} \tag{7.33}$$

and the damping angle

$$\alpha = \arctan\left(\frac{\zeta}{\sqrt{1 - \zeta^2}}\right). \tag{7.34}$$

The power spectral density needs to be non-negative, and, satisfying this condition, it follows immediately from Eq. (7.33), that the argument of the sine may also not be negative, or, expressed mathematically (cf. SCHUBERT 2017),

$$\begin{aligned} \alpha + \eta &\geq 0, \\ \alpha - \eta &\geq 0. \end{aligned} \tag{7.35}$$

Using the coefficients suggested by TITOV (2000, see above) leads to

$$\eta = -\varphi = -0.82, \tag{7.36}$$

$$\alpha = \arctan\left(\frac{\zeta}{\sqrt{1 - \zeta^2}}\right) = \arctan\left(\frac{a}{b}\right) = 0.7665, \tag{7.37}$$

which violates the second condition in Eq. (7.35), and proves the assumption that the covariance function presented by TITOV (2000) is not positive definite (cf. SCHUBERT 2017).

However, it is possible to fulfill $\alpha + \eta = 0$ (positive (semi-) definiteness) by minor changes of the initial parameter set by TITOV (2000). According to SCHUBERT (2017), there are in total three possible alternatives, and the modified parameters are always marked by an asterisk (*). First, the coefficient for the phase η^* can be modified to be at least as large as the negative damping angle α,

$$\eta^* = -\varphi = -\alpha. \tag{7.38}$$

In Fig. 7.6, the corresponding covariance function is represented in blue.
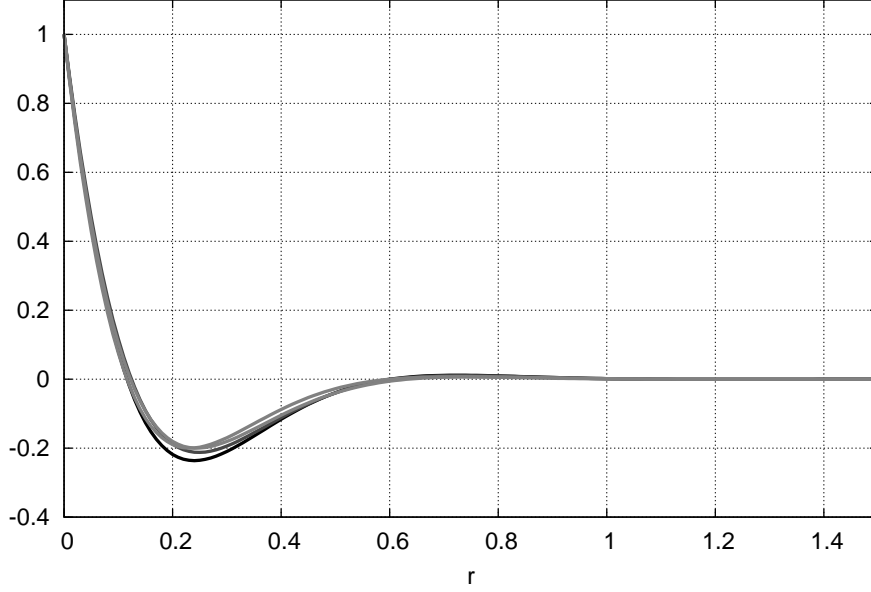
Figure 7.6: The second order Gauss Markov process reproducing the covariance function provided by TITOV (2000), referred to as the reference solution (black), and modifying the phase η^* (blue), the attenuation ζ^* (green) and the frequency ω_n^* (red).

Second, the attenuation ζ^* needs to be modified in a way that $\alpha = -\eta$ fulfills the same condition as before. Inverting Eq. (7.34) leads to $\zeta = \sin(\alpha)$ and $b = \hat{\omega} = \cos(\alpha)\,\omega_n$, and the modified coefficient of the attenuation can be expressed as

$$\zeta^* = \sin(-\eta) = \sin(\varphi). \tag{7.39}$$

In Fig. 7.6, the covariance function represented in green corresponds to the modification of the attenuation ζ^*.

Finally, it is also possible to perform a change in the frequency,

$$\omega_n^* = \frac{\hat{\omega}}{\cos(\eta)}, \tag{7.40}$$

which also modifies $\hat{\omega}^* = \sqrt{1 - \zeta^2}\,\omega_n^*$. Formulated in the notation of TITOV (2000), it follows

$$\omega_n^* = \frac{b}{\cos(\varphi)} \tag{7.41}$$

and

$$a^* = \hat{\omega}\tan(-\eta) = b\tan(\varphi). \tag{7.42}$$

Again, Fig. 7.6 shows the resulting covariance function (red).

In Tab. 7.1, the different coefficients of the initial covariance function by TITOV (2000) (a, b, φ) and the second order Gauss Markov process (η, ζ, ω_n) by modifying the phase η^* (3rd column),

Table 7.1: Different coefficients (1st column) of the initial covariance function by Titov (2000) and the second order Gauss Markov process (SOGM) by modifying the phase η^* (3rd column), the attenuation ζ^* (4th column) and the frequency ω_n^* (5th column). The 2nd column refers to initial coefficients (a, b, φ) suggested by Titov (2000) for his covariance function, and the equivalent coefficients (η, ζ, ω_n) necessary to reproduce the covariance function by Titov (2000) with a SOGM process (cf. Schubert 2017).

Coefficients	Reference: (Titov 2000)	change of phase η^*	change of attenuation ζ^*	change of frequency ω_n^*
SOGM				
η	-0.82	**-0.7665**	-0.82	-0.82
ζ	0.6939	0.6939	**0.7311**	**0.7311**
ω_n	8.9960	8.9960	8.9960	**9.4984**
$\hat{\omega}$	6.48	6.48	**6.1373**	6.48
α	0.7665	0.7665	**0.82**	**0.82**
TITOV (2000)				
a	6.24	6.24	**6.5774**	**6.9447**
b	6.48	6.48	**6.1373**	6.48
φ	0.82	**0.7665**	0.82	0.82

the attenuation ζ^* (4th column) and the frequency ω_n^* (5th column) are given. Further, a reference parameter set is defined (2nd column) describing the coefficients, which are initially suggested by Titov (2000), and the equivalent coefficients which are necessary to reproduce the covariance function by Titov (2000) with a SOGM process.

It is worth mentioning that the frequency remains unchanged when modifying either the phase η^* or the attenuation ζ^*, while a change in the frequency ω_n^* has the special characteristic of keeping the zeros of the covariance function, which is not true for the other cases. It is further recalled, that, in contrast to the original reference set, all covariance functions which have been subject to minor modifications in the selected coefficients are positive (semi-) definite.

Alternative Covariance functions

Additionally, further covariance functions have been used for validation purposes, which will be briefly described in the following. First, the finite covariance function $f_{GC}(r, a, R)$ of Gaspari and

COHN (1999) represents a fifth order piece-wise rational function, which is mathematically obtained by self-convolving the continuous piece-wise linear function

$$h(r, a, R) = \begin{cases} 2(a-1)\frac{r}{R} + 1 & : 0 \le r \le \frac{R}{2} \\ 2a\left(1 - \frac{r}{R}\right) & : \frac{R}{2} \le r \le R \\ 0 & : R \le r. \end{cases} \tag{7.43}$$
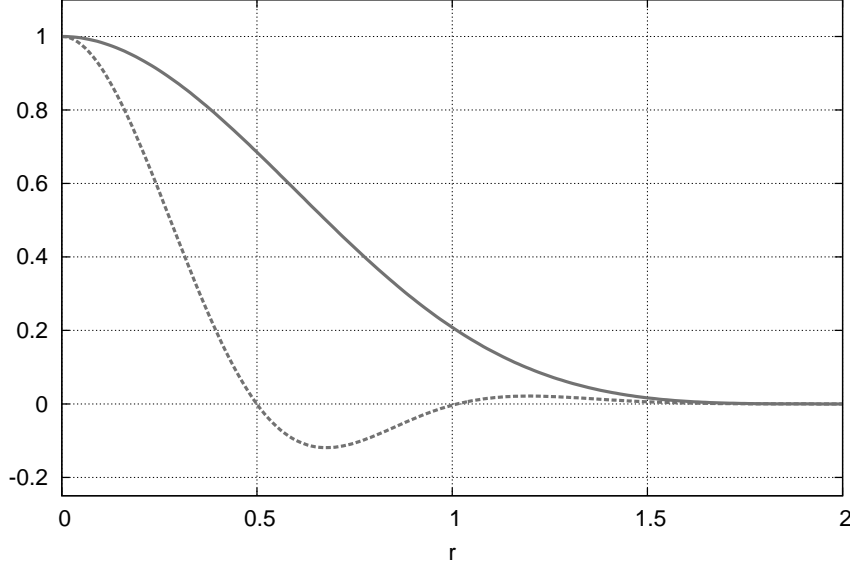
Figure 7.7: The covariance function $f_{GC}(r, a, R)$ proposed by GASPARI and COHN (1999) for $R = 1$ and two modifications of the form parameter: $a = 0.5$ (brown, solid line) and $a = -0.1$ (brown, dashed line).

The curvature or form parameter a determines the slope of the linear output function, r defines the Euclidean distance between two points separated in space or time, and R represents finite support. The extensive collection of equations for the resulting fifth order piece-wise polynomial is given in GASPARI et al. (2006, Eq. (33) and Appendix C.1 and C.2). The covariance function for $R = 1$ and two modifications of the form parameter, $a = 0.5$ (brown, solid line) and $a = -0.1$ (brown, dashed line), are depicted in Fig. 7.7.

SANSÒ and SCHUH (1987) proposed a covariance function as a convolution of a paraboloid function

$$h(r, R) = \begin{cases} R^2 - r^2 & : 0 \le r \le R \\ 0 & : R \le r \end{cases} \tag{7.44}$$

with itself, and obtained

$$f_{SS}(r, R) = \begin{cases} \frac{1}{3}R^6\pi - \frac{1}{2}R^4r^2\pi + \frac{1}{3}\left(R^4r + \frac{4}{3}R^2r^3 - \frac{1}{12}r^5\right) + \\ \sqrt{R^2 - \frac{r^2}{2}} + \left(R^4r^2 - \frac{2}{3}R^6\right)\arcsin\left(\frac{r}{2R}\right) & : 0 \le r \le 2R \\ 0 & : 2R \le r. \end{cases} \tag{7.45}$$

Since it is not possible to model negative correlations with the initial form in Eq. (7.45), a modified covariance function

$$f_{S2}(r, R) = 2R^4\pi - 4R^4 \arcsin\left(\frac{r}{2R}\right) - \left(6R^2r - r^3\right)\sqrt{R^2 - \left(\frac{r^2}{2}\right)}, \tag{7.46}$$

was defined, which allows the modeling of negative correlations, but does not have a form or curvature parameter. Both the original (orange) and the modified (cyan) form of the covariance function are shown in Fig. 7.8 for $R = 1$.
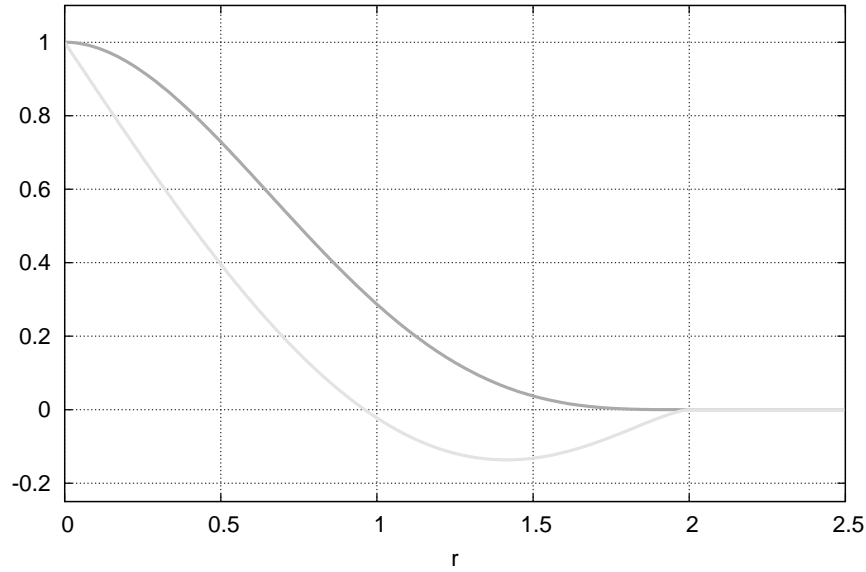
Figure 7.8: The covariance function $f_{SS}(r, R)$ proposed by SANSÒ and SCHUH (1987) in its original (orange) and modified (cyan) form for $R = 1$.

Additionally, a covariance function based on the so-called Matérn covariance family (MATÉRN 1960) is used which has the general form

$$\mathcal{C}(r) = \phi(\alpha r)^\nu K_\nu(\alpha r) \tag{7.47}$$

with the smoothness parameter ν and the correlation length $r = \frac{1}{\alpha}$. Here, $\phi > 0$ and $\alpha > 0$ are constant values, and K_ν represents the modified Bessel function of second kind (ABRAMOWITZ and STEGUN 1964, pp. 355ff). Special cases of the Matérn covariance function arise for specific smoothness parameters: $\nu = \frac{1}{2}$ leads to an exponential covariance function, $\nu = 1$ defines an autoregressive process of first order (also called a Markov process of first order), and $\nu = \infty$ is the squared exponential function or so-called Gauss type (KERMARREC and SCHÖN 2016). The resulting covariance functions for a fixed correlation length of $r = 0.2$ and specific smoothness parameters ($\nu = \frac{1}{2}$, black; $\nu = 1$, blue; $\nu = \infty$, green; $\nu = \frac{5}{6}$, magenta) are depicted in Fig. 7.9.

Finally, the atmospheric turbulence model developed within this thesis (see Sec. 5.1 for more details) is used to generate a covariance function. In this case, the covariance function depends on small-scale refractivity fluctuations due to turbulence-induced processes in the neutral atmosphere.
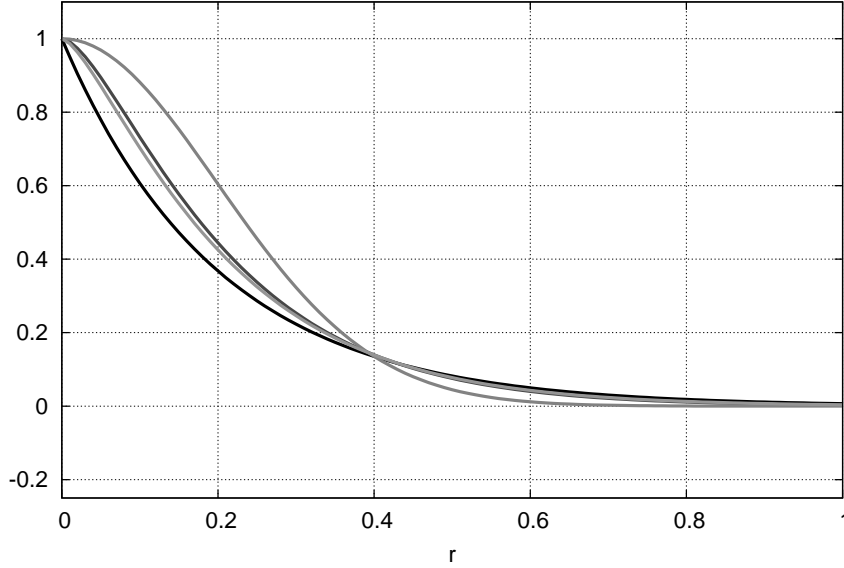
Figure 7.9: The Matérn covariance function (MATÉRN 1960) for a fixed correlation length of $r = 0.2$ and specific smoothness parameters: $\nu = \frac{1}{2}$ (exponential function, black), $\nu = 1$ (autoregressive process of first order, blue), $\nu = \infty$ (squared exponential function, green) and $\nu = \frac{5}{6}$ (magenta).

From a theoretical point of view, this model has the advantage of directly describing actual physical processes in the atmosphere, while the other functions presented here are related to empirical or mathematical models, not reflecting actual meteorological and physical conditions. The turbulence model follows a Matérn function with smoothness parameter $\nu = \frac{5}{6}$ and a correlation length depending on parameters with regard to atmospheric turbulence (see Eq. (5.16) and the description in the text).

7.2.3 Case Study: Least Squares Collocation in VLBI Data Analysis

In a case study, the classical least squares adjustment in the VLBI data analysis has been replaced by the least squares collocation approach, evaluated for different covariance functions and two specially designed VLBI sessions in the framework of the WHISP (Wettzell HIgh SPeed) project (see Ch. 6 for more details). Both experiments have been chosen since they stand out against other sessions, particularly in terms of the increased number of observations. Further, the sessions include observations on the European continent as well as short baselines of only about one hundred meter at the Wettzell Geodetic Observatory.

First, it should be clearly pointed out, that in the context of VLBI data analysis the least squares collocation approach only produces appropriate results if the number of observations is high enough. Remembering that, in case of the classical least squares adjustment, the lack of observations in specific piece-wise linear segments are counteracted by the introduction of less heavily weighted soft constraints in form of pseudo observations, and omitting these constraints would clearly degrade the quality of the results. Due to the fact, that this remedy is not foreseen for the least squares

collocation approach, the focus lies on future VGOS-like (VLBI Global Observing System, Niell et al. 2013) VLBI sessions with an increased number of observations as is the case for the WHISP sessions.

Data Analysis Settings

The data analysis of VLBI observations is performed using the VLBI software package ivg::ASCOT (Artz et al. 2016; Halsig et al. 2017). The target parameters are estimated in a least squares collocation adjustment according to Eq. (7.20), and the analysis of the observed group delays is performed following the conventions of the International Earth Rotation and Reference Systems Service (IERS, Petit and Luzum 2010).
The model and parametrization setup for single-session VLBI data analysis has been chosen with respect to the routine data analysis strategies of the IVS. Therefore, the station coordinates are estimated with respect to an ivg::ASCOT multi-session solution, and additional no-net-rotation (NNR) and no-net-translation (NNT) conditions (e.g., Angermann et al. 2004) have been applied to eliminate the datum defect. The Earth orientation parameters and radio source coordinates are not estimated, but fixed to a priori values of the IERS C04 series and the International Celestial Reference Frame (ICRF2, Fey et al. 2015), respectively.

Similar to the classical least squares adjustment, the clock parameters are modeled by a second order polynomial and additional continuous piece-wise linear functions (CPWLF) with a temporal resolution of 60 minutes. For the determination of the zenith wet delays, in contrast, the piece-wise linear functions are fully replaced to allow for a stochastic representation of the atmospheric parameters instead of the pseudo-stochastic behavior of the piece-wise linear functions. First, a deterministic offset valid for the entire duration of the session is estimated, and additionally, zenith wet delay corrections are predicted for each observation time period. Least squares collocation depends essentially on a priori information in form of appropriate covariance functions, which are needed to describe the stochastic properties of the signal component. In this case study, different covariance models presented in Sec. 7.2.2 have been applied: the two functions by Sansò and Schuh (1987), $f_{SS}(r, R)$ and $f_{SS}(r, R)$, with $R = 1$, the covariance function of Gaspari and Cohn (1999), $f_{GC}(r, a, R)$ with $R = 1$ and $a = -0.1$, the Matérn model (Matérn 1960) with a smoothness parameter $\nu = 1.6$ and a correlation length of $\tau = 1$, and finally, the second order Gauss Markov process (e.g, Maybeck 1979) similar to the covariance function provided by Titov (2000), but with modified attenuation parameter (see Eq. 7.39). The parameters characterizing the covariance functions are empirically derived and chosen to approximate the curve of the initial model by Titov (2000), which has already been applied to VLBI observations. Additionally, the covariance functions related to the turbulence model presented in Sec. 5.1 (see Eqs. 5.16 and 5.17) with $C_n^2 = 1 \cdot 10^{-14} \mathrm{m}^{-\frac{2}{3}}$, $H = 2000$ km, $v = 8 \frac{\mathrm{m}}{\mathrm{s}}$, and $a = b = 1 < c$ was used to describe the stochastic properties of the atmospheric parameters.

In order to provide a reference solution, an additional least squares adjustment is performed with the traditional piece-wise linear representation for the atmospheric parameters using interval lengths of 30 and 60 minutes, respectively, and soft constraints weighted by $\sigma_{ZWD} = 15 \frac{\mathrm{mm}}{\mathrm{h}}$. Here, both the clock and atmospheric model corrections are supplemented by additional constraints formulated as weighted pseudo observations to stabilize the equation system, whereas, in case of the least squares collocation approach, the zenith wet delays are not constrained any more.

In both cases, the Vienna mapping functions 1 (VMF1, Böhm et al. 2006b) are used for the mapping of the tropospheric wet delay from zenith to the slant direction.

Concerning the stochastic model of the observations, the weight matrix of the Gauss Markov model is a pure diagonal matrix only consisting of the pure observation weights derived from the correlation process and an additional noise term of about 15 ps to ensure $\chi^2 \approx 1$.

Results

Different covariance functions have been implemented and numerous adjustments based on the collocation model have been performed for the two WHISP sessions in November 2016 and July 2017. In order to obtain a reference solution, two classical least squares adjustments have been calculated, which only differ in the determination of the interval length of the piece-wise linear segments (30 and 60 minutes, respectively). The results in terms of the weighted root mean square (WRMS) error of post-fit residuals (see Eq. 5.23) are shown in Tab. 7.2. A distinction is made between a baseline-dependent WRMS to evaluate the influence of the individual baseline length, and an overall WRMS of post-fit residuals valid for the whole session. The covariance functions are determined with respect to a second order Gauss Markov process according to Eq. (7.26), the covariance function of GASPARI and COHN (1999), the initial model of SANSÒ and SCHUH (1987) and its modification (see Eqs. (7.45) and (7.46), respectively), the covariance function according to MATÉRN (1960, see Eq. 7.47), and, finally, the turbulence model presented in Sec. 5.1. Additionally, the two solutions following the classical least squares adjustment are given as a reference.

First, it is worth noting, that the different solutions lead to clearly different results in terms of WRMS of post-fit residuals, which are exclusively attributable to the corresponding covariance function used to describe the stochastic behavior of the atmospheric parameters. Generally, it seems that, compared to the classical least squares solutions (last two columns in Tab. 7.2), reasonable solutions may be obtained with respect to the second order Gauss Markov process, the modified function of SANSÒ and SCHUH (1987) and the turbulence model, while the WRMS of post-fit residuals already decreases for the MATÉRN (1960) case, and lead to unsatisfactory results using the function of GASPARI and COHN (1999) and the initial model of SANSÒ and SCHUH (1987). Possible reasons are given at a later stage, when directly looking at the zenith wet delay estimates and predictions, respectively. Concerning the overall WRMS of post-fit residuals, the best least squares collocation solution is obtained when modeling the stochastic properties by a second order Gauss Markov process. For both sessions, the results are better than the classical least squares solution with 60 minute piece-wise linear segments. Compared to the least squares solution reducing the interval lengths to 30 minutes, the SOGM solution lies in the same order of magnitude for WHISP5 and even leads to a slight improvement of about 8 ps in quadrature for WHISP7.

The analysis of the individual baselines reveals that the different strategies creating a covariance function also lead to a different behavior with respect to the extension of the baseline. For the adjacent European baselines between Onsala (On), Sweden, and the two radio telescopes (Wn and Wz) in Wettzell, Germany, (On-Wn, and On-Wz, respectively), the overall best solution is obtained by least squares collocation based on a second order Gauss Markov process, which is even slightly better than the classical least squares adjustment. Using the turbulence model or the modification of SANSÒ and SCHUH (1987) also yields suitable results, which are slightly worse than the least squares adjustment with a solution interval of 30 minutes, but are in the same order of magnitude or perform even slightly better than the solution with piece-wise linear segments of a resolution of 60 minutes.

Table 7.2: Overall and baseline-dependent WRMS of post-fit residuals [ps] based on different least squares adjustment strategies: the least squares collocation method based on different covariance functions (first row, from left to right: 2nd order Gauss Markov process; GASPARI and COHN 1999; SANSÒ and SCHUH 1987; second row, from left to right: MATÉRN 1960; turbulence model of HALSIG et al. 2016A), and the classical least squares adjustment using different interval lengths for the CPWL representation (second row, last two columns). In order to ensure $\chi^2 \approx 1$, a constant additional noise term is added to the standard deviations from the correlator process.

WHISP5

Baseline	2nd order Gauss process	GASPARI and COHN (1999)	SANSÒ and SCHUH (1987), Eq. (7.45)	SANSÒ and SCHUH (1987), Eq. (7.46)
Overall	27.52	35.69	47.89	28.15
On-Wn	30.02	37.74	50.26	30.21
On-Wz	28.80	38.94	53.08	30.03
Wn-Wz	12.42	12.89	12.26	12.19
	MATÉRN (1960)	Turbulence model HALSIG et al. (2016A)	Classical Least Squares Adjustment	
interval length			CPWL, 60 min.	CPWL, 30 min.
Overall	30.79	28.36	28.63	27.18
On-Wn	33,24	30.55	30.70	29.16
On-Wz	32.67	30.22	30.76	29.12
Wn-Wz	13.21	11.89	11.31	11.28

WHISP7

Baseline	2nd order Gauss process	GASPARI and COHN (1999)	SANSÒ and SCHUH (1987), Eq. (7.45)	SANSÒ and SCHUH (1987), Eq. (7.46)
Overall	24.44	32.32	34.66	26.69
On-Wn	29.39	37.41	41.25	31.85
On-Wz	26.57	36.72	38.49	29.32
Wn-Wz	8.29	9.90	10.24	8.85
	MATÉRN (1960)	Turbulence model HALSIG et al. (2016A)	Classical Least Squares Adjustment	
interval length			CPWL, 60 min.	CPWL, 30 min.
Overall	28.29	27.52	27.04	25.74
On-Wn	34.26	32.64	32.02	30.52
On-Wz	31.81	30.61	30.10	28.62
Wn-Wz	9.97	8.42	8.45	7.99

For the short baseline between the two Wettzell radio telescopes the assessment of the results is different. First, the difference between the WRMS of post-fit residuals of the different solutions is smaller compared to the traditional baseline lengths, and the turbulence model performs slightly better on the short baselines. Surprisingly perhaps, the Matérn covariance function does not lead to further improvements on the short baseline, although high-frequency variations, which are much more relevant on a local scale, should be modeled better by this model. Most likely, the daily cycle is however not ideally reflected by this function. Another explanation for the fact that the Matérn function lags behind the turbulence model, which generally also follows a Matérn function, is the capability to also consider spatial correlations with the turbulence model, which is not possible with the pure Matérn covariance function.

Table 7.3: Overall and baseline-dependent WRMS of post-fit residuals [ps] for different least squares adjustments with and without soft constraints/pseudo observations in the context of the piece-wise linear segments of different interval lengths. In order to ensure $\chi^2 \approx 1$, a constant additional noise term is added to the standard deviations from the correlator process.

WHISP5

Baseline	Classical Least Squares Adjustment			
	No pseudo observations/constraints		constraints with $\sigma_{ZWD} = 15 \frac{mm}{h}$	
interval length	CPWL, 60 min.	CPWL, 30 min.	CPWL, 60 min.	CPWL, 30 min.
Overall	29.74	31.25	28.63	27.18
On-Wn	31.85	33.62	30.70	29.16
On-Wz	32.05	33.59	30.76	29.12
Wn-Wz	11.33	11.37	11.31	11.28

WHISP7

Baseline	Classical Least Squares Adjustment			
	No pseudo observations/constraints		constraints with $\sigma_{ZWD} = 15 \frac{mm}{h}$	
interval length	CPWL, 60 min.	CPWL, 30 min.	CPWL, 60 min.	CPWL, 30 min.
Overall	29.88	32.85	27.04	25.74
On-Wn	35.43	38.89	32.02	30.52
On-Wz	33.36	36.86	30.10	28.62
Wn-Wz	8.57	8.53	8.45	7.99

As mentioned before, the least squares collocation approach requires a sufficient number of observations to describe the behavior of the target parameters for a specific time interval, such as the zenith wet delays within a 24 hour period. In case of the classical least squares adjustment, the lack of observations in specific piece-wise linear segments are counteracted by the introduction

of soft constraints in form of pseudo observations. Although the soft constraints are less heavily weighted in contrast to the actual observations, they directly influence the obtained WRMS of post-fit residuals as additional observations. Regardless of the number of observations per segment, the quality of the results would decrease when omitting these constraints, either due to the lack of observations in a piece-wise linear segment, or, in determining the degrees of freedom for the WRMS values. The overall and baseline-dependent WRMS of post-fit residuals for different least squares adjustments with and without soft constraints are given in Tab. 7.3 for the piece-wise linear segments of interval lengths of 30 or 60 minutes. As expected, the overall WRMS of post-fit residuals decreases for both solution intervals by neglecting the soft constraints, however, a much stronger effect occurs for the shorter piece-wise linear segment. One possible reason could be that in case of the 30 minute interval the number of observations per segment is smaller than in case of the hourly resolution, and the influence of the pseudo observations per time interval are considerably higher. Contrary, in case of the 60 minute interval length the pseudo observations could almost be neglected, at least for these WHISP sessions, where the observations are much higher compared to traditional 24 hour sessions of the IVS. Of course, also in this case the pseudo-observations distort the solution statistics as the (W)RMS due to an increasing number of degrees of freedom. Since the least squares collocation method completely avoids soft constraints in any form, the corresponding solutions should, strictly speaking, be compared to the classical adjustment without additional soft constraints, clearly emerging least squares collocation in connection with the second order Gauss Markov model as the best solution. In the following, however, soft constraints are always applied for the piece-wise linear representation, since this approach is the standard case of the IVS and, therefore, the reference solution.

Initially, the introduction of the least squares collocation approach was motivated by the idea of replacing the pseudo-stochastic character of the piece-wise linear representation by a fully stochastic description of the atmospheric behavior. In this context, it is justifiably assumed that also the behavior of the zenith wet delays could be represented more accurately, which now is investigated in more detail. For this purpose, the ZWD time series for both WHISP sessions and all solution strategies presented here are shown in Fig. 7.10. The two solutions obtained by a classical least squares adjustment with a CPWL interval length of 60 and 30 minutes are depicted as black and blue dots, respectively, which form the reference for the different least squares collocation solutions based on a second order Gauss Markov model (green), the model of SANSÒ and SCHUH (1987) and its modification (orange and cyan, respectively), the covariance function of GASPARI and COHN (1999, brown), the Matérn covariance function (magenta) and the turbulence model (red). From Fig. 7.10, it is apparent why the covariance functions of SANSÒ and SCHUH (1987) and GASPARI and COHN (1999) lead to worse results in terms of WRMS of post-fit residuals, compared to the other covariance models as well as the traditional least squares approach (cf. Tab. 7.2): the zenith wet delay time series for these functions are very smooth and follow only roughly the daily variations visible in case of the reference solutions. The reason for the smooth character lies directly in the form parameter of the covariance function, since the slope at the origin is almost zero, and the decrease of covariance functions is responsible for high frequencies and small-scale variations. Assuming the classical least squares solution with piece-wise linear segments of 30 minutes to be close to the "truth" the time series obtained by the second order Gauss Markov model, the turbulence model and the modified covariance model of SANSÒ and SCHUH (1987) show a very similar characteristic. The Matérn function generally follows a similar trend, however, for some peaks the deviation from other time series becomes larger.
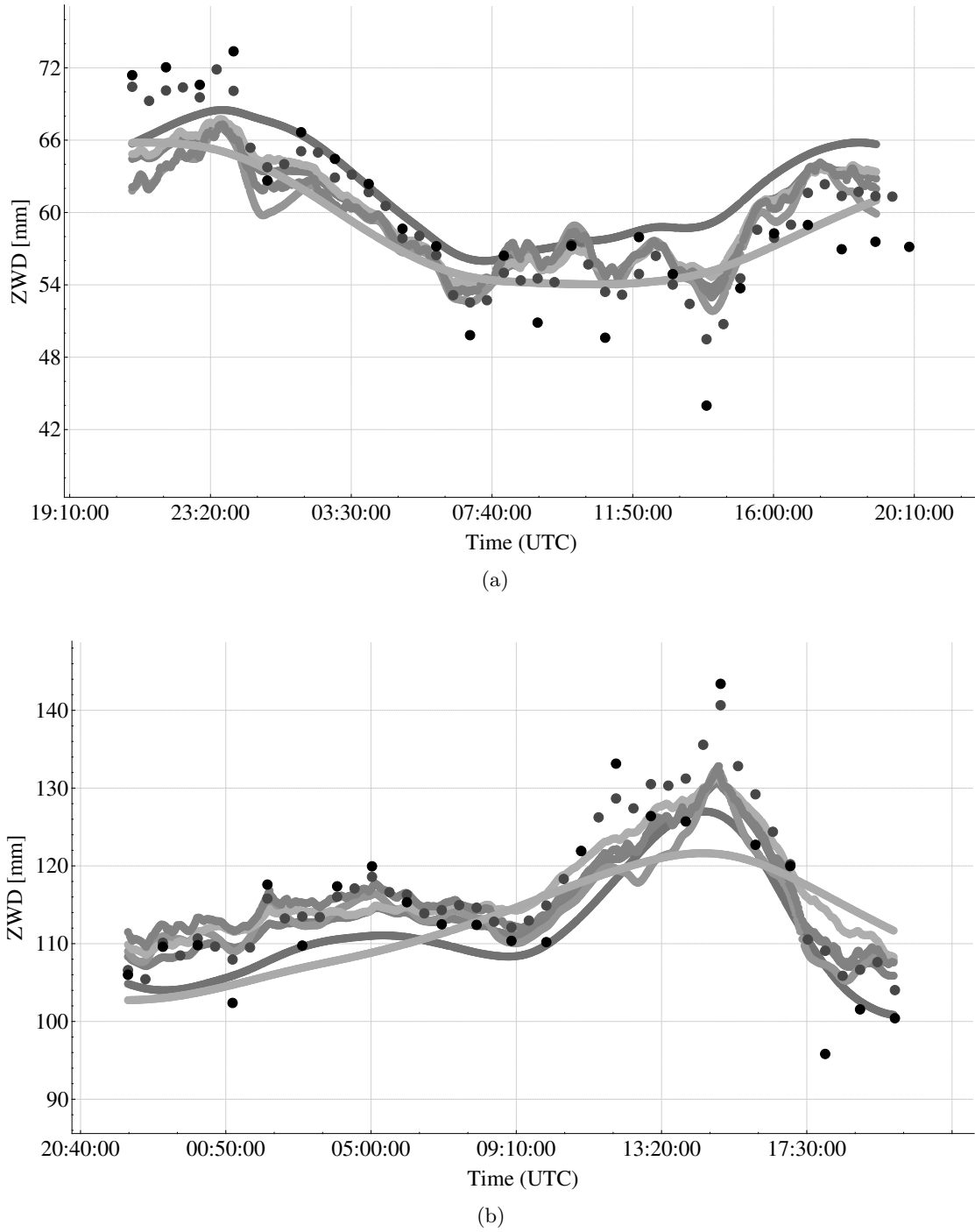
Figure 7.10: Zenith wet delay estimates for Wettzell during the WHISP5 (a) and WHISP7 (b) experiments obtained by a classical least squares adjustment with a CPWL interval length of 60 minutes (black dots) and 30 minutes (blue dots), and several least squares collocation solutions based on a second order Gauss Markov model (green), the model of SANSÒ and SCHUH (1987) and its modification (orange and cyan, respectively), the covariance function of GASPARI and COHN (1999, brown), the Matérn covariance function (magenta) and the turbulence model (red). The corresponding standard deviations are omitted for the sake of clarity.

In conclusion, the second order Gauss Markov process seems to perform best compared to the other covariance functions introduced here. For the longer baselines, this model even leads to better results than the classical least squares adjustment, independent whether using a 30 or 60 minute interval for the piece-wise linear representation.
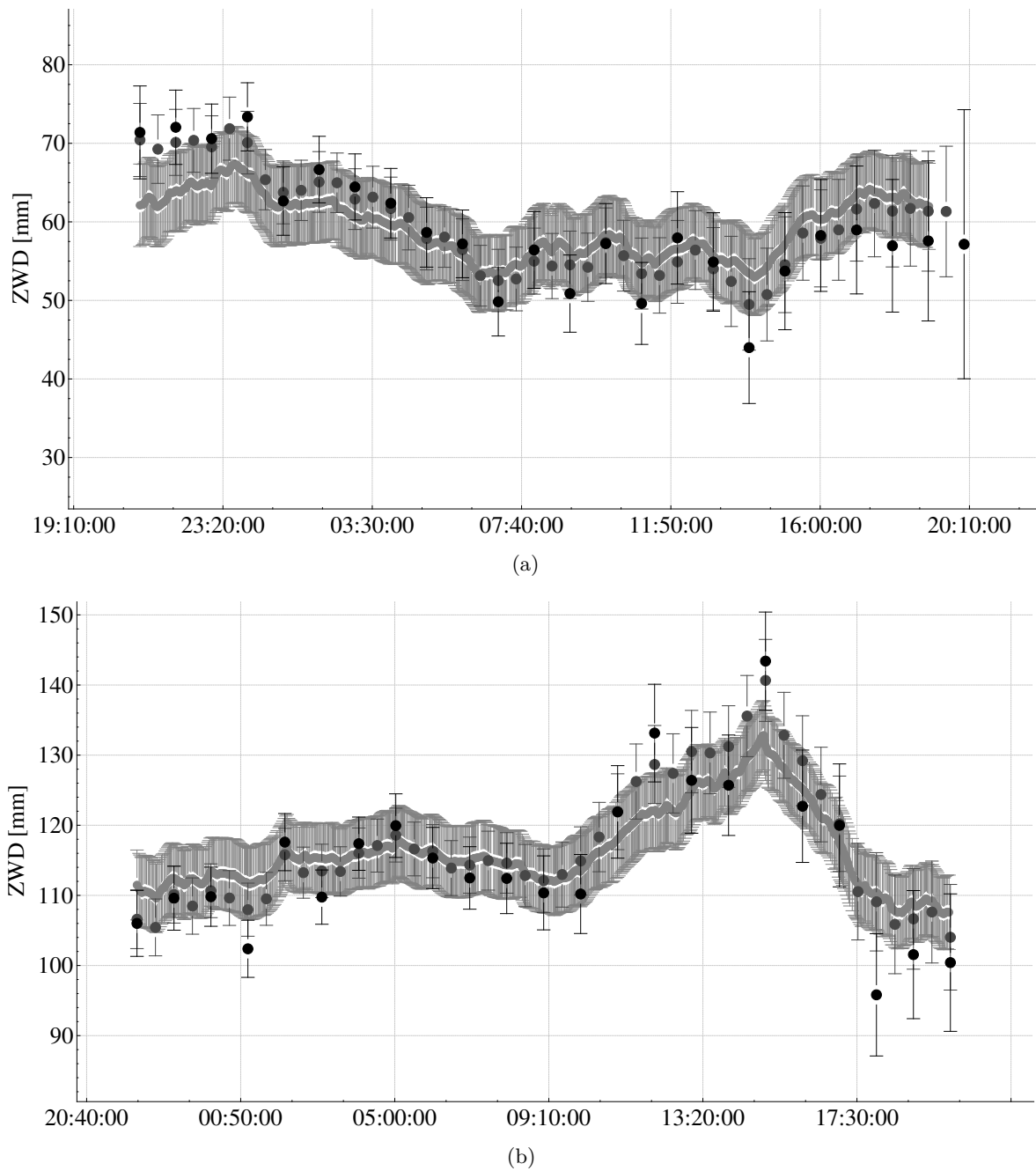
Figure 7.11: Zenith wet delay estimates for Wettzell during the WHISP5 (a) and WHISP7 (b) experiments obtained by a classical least squares adjustment with a CPWL interval length of 60 minutes (black dots) and 30 minutes (blue dots), and a least squares collocation solution (green dots).

For a better visualization, the ZWD estimates derived by the second order Gauss Markov model (green) are again depicted in Fig. 7.11 with respect to the behavior of the piece-wise linear oriented atmospheric parameters with different interval lengths (60 minutes, black dots and 30 minutes, blue dots). At first glance, all solutions fit very well to each other, since the general behavior of the atmospheric parameters is quite similar. However, a more detailed assessment reveals, that the least squares collocation solution shows a higher correlation to the least squares adjustment with a shorter solution interval, while the data set with a resolution of one hour results in a higher scatter of the zenith wet delay estimates, and compared to both other solutions some ZWD parameters can be assigned as outliers, in particular for certain peaks. It can be demonstrated that this effect is even growing with increasing piece-wise linear intervals (e.g., 120 minutes; for the sake of visibility not shown in Fig. 7.11). Consequently, the piece-wise linear representation is not optimal if the resolution is too low that the characteristics of the zenith wet delays cannot be represented accurately enough, but also if the solution interval is too small, that the influence of the pseudo observations becomes predominant over the current observations. The deficiency due to an inadequate number of observations cannot be healed by pseudo observations as long as the observation weights are less heavily weighted, at least for the time series of zenith wet delays. Another peculiarity occurs at the beginning and the end of the session, where either the least squares collocation solution differs from the two classical solutions (e.g., the first four hours of the WHISP5 session in Fig. 7.11(a)) or, more frequently, the hourly resolved ZWD estimates deviate from both the collocation and the least squares adjustment with higher resolution (e.g., the last three to four hours of both WHISP sessions in Fig 7.11(a) and 7.11(b), respectively). In this context, it should be pointed out, that also the standard deviations of some ZWD estimates at the end of the sessions increase disproportionately in case of the classical adjustment. One possible reason for this behavior could be the strength of the continuity condition in the framework of the continuous piece-wise linear segments. Therefore and due to the dependency of the scatter of the ZWD estimates on the solution interval of the piece-wise linear representation, the least squares collocation method should be the preferred solution, assuming the underlying covariance function to be suitable to reflect the behavior of the atmospheric parameters.

In this context, it should be emphasized, that on an overall basis, however, the least squares adjustment with the turbulence model presented in Sec. 5.1 leads to even better results (compare, for instance, Tab. 6.4 in Sec. 6.4.4 and Tab. 7.2 in Sec. 7.2.3), indicating the assumption that the corresponding covariance functions are not yet ideal. One possibility would be a combination of the second order Gauss Markov process with a turbulence-based approach to additionally model the small-scale fluctuations more properly.

7.3   Discussion

The current tropospheric model reveals severe deficiencies with respect to the estimation of atmospheric parameters, which are either reflected by the fact, that occasionally zenith wet delay estimates become negative, which does not correspond to actual physical conditions, or originate in the non-optimal pseudo-stochastic description of atmospheric parameters describing the stochastic behavior of the neutral atmosphere. Enhanced modeling and adjustment strategies have been introduced to address identified deficiencies of the tropospheric model and to allow for the estimation of zenith wet delays in a more meaningful and appropriate sense (objective 3).

First, an inequality constrained least squares (ICLS) approach of the field of convex optimization has been used to overcome the deficiency, that sometimes zenith wet delay estimates become negative, which, of course, does not reflect physical or meteorological conditions in a plausible way. However, deficiencies in the a priori hydrostatic delay, for instance due to missing or incomplete pressure data, are compensated by the zenith wet delay estimates to almost 100%. When constraining individual ZWD parameters to a positive value in the ICLS adjustment, mis-modeling effects in hydrostatic delays are not compensated for by the zenith wet delays anymore, but might affect correlated parameter groups. Homogeneous time series of meteorological data are absolutely necessary, since otherwise, the VLBI target parameters might be harmed. A first approach to ensure sufficiently modeled hydrostatic calibrations was based on numerical weather models, such as the ECMWF. Although the differences to meteorological in-situ observations could reach a few millimeters, which are possibly caused by the rather coarse time resolution of six hours and, therefore, neglecting actual variability, homogeneous time series of meteorological data are guaranteed. At a later stage, a homogenization strategy has been proposed, where a numerical weather model of the ECMWF is used to define the level of the meteorological data, while their variability is taken from in-situ observations derived at the VLBI sites after removing outliers and filling data gaps.

In conclusion, the application of the ICLS adjustment is, in principle, possible without harming the VLBI target parameters, provided that the a priori hydrostatic component is modeled sufficiently. But it should nevertheless be pointed out that the negative zenith wet delay estimates result not only from a priori mis-modeling, but could also be the result of several other issues, such as mis-modeling of geophysical effects as well as certain impact due to instrumental delays or the clock parametrization.
Due to the strong dependency on the a priori hydrostatic calibrations and the fact that sometimes an insufficient modeling of non-atmospheric quantities might be corrected by constraining atmospheric parameters, the inequality constrained least squares approach is not recommended for operational VLBI data analysis.

Alternatively to the application of inequality constraints, special emphasis was given to describe the atmospheric parameters by their stochastic properties. Since the pseudo-stochastic behavior of the piece-wise linear representation only models the stochastic character of the atmosphere to a limited extent, the piece-wise linear functions have been replaced by a least squares collocation method. Another benefit of least squares collocation over the classical least squares adjustment using piece-wise linear functions is that additional soft constraints in form of pseudo observations, which are generally needed to stabilize the solution due to missing observations in some piece-wise linear segments, are not required anymore. The stochastic properties of the zenith wet delay are completely described by appropriate covariance functions. In this chapter, different covariance models have been introduced and discussed. This includes, in particular, a covariance model already successfully applied to VLBI observations which has been transferred to a second order Gauss Markov process and reasonably modified.

A case study has been performed to compare the least squares collocation approach fed by different covariance functions to the classical least squares adjustment using piece-wise linear interval lengths of 30 and 60 minutes. Compared to the other covariance functions introduced, the second order Gauss Markov process seems to perform best in terms of the weighted root mean square (WRMS) error of post-fit residuals. For the longer baselines, this model leads to better results than the classical least squares adjustment, independent whether using a 30 or 60 minute piece-wise linear interval. An extensive analysis of the ZWD estimates reveals, that the least

squares collocation solution agrees better with the least squares adjustment with a shorter solution interval, while the data set with a resolution of one hour (or even higher) results in a higher scatter of the zenith wet delay estimates. The piece-wise linear representation is, thus, not optimal if the resolution is too low that the characteristics of the zenith wet delays cannot be represented accurately enough, but also if the solution interval is too small, that the influence of the pseudo observations prevail over the current observations. The deficiency due to an inadequate number of observations cannot be counteracted by pseudo observations as long as the observation weights are less heavily weighted. The behavior of the piece-wise linear functions has proven to be not optimal, particularly at the beginning and at the end of a session, where also the standard deviations of some ZWD estimates increase disproportionately in case of the classical adjustment. One possible reason for this behavior could be the strength of the continuity condition in the framework of the continuous piece-wise linear segments.

Although the inequality constrained least squares adjustment is generally not recommended for the routine data analysis of the IVS, the least squares collocation approach is very promising and the preferred adjustment strategy for VLBI observations, assuming the underlying covariance function to be suitable to reflect the behavior of the atmospheric parameters. First, it is possible to counteract the pseudo-stochastic character of the piece-wise linear model and its limitations in representing the stochastic behavior of the troposphere. Second, additional soft constraints are avoided, which not only influences the estimated zenith wet delay parameters, but also the solution statistic in terms of the WRMS, since the number of observations is artificially increased by the pseudo observations. Nonetheless, it has been demonstrated that the WRMS of post-fit residuals generally decreases in case of the collocation approach and the second order Gauss Markov process compared to the standard model of the IVS. In conclusion, the least squares collocation method ensures an improved modeling of the (stochastic) properties of the neutral atmosphere and allows for the estimation of zenith wet delays in a more meaningful and appropriate sense (objective 3).

8. Conclusions and Outlook

8.1   Conclusions

The main objective of this thesis is to characterize and model turbulence-based refractivity fluctuations and propose new modeling and adjustment strategies for space-geodetic observing techniques at radio frequency bands such as Very Long Baseline Interferometry (VLBI).

One main objective of this thesis was the development of an operationally efficient atmospheric turbulence model to stochastically describe small-scale refractivity variations in the neutral atmosphere in a meaningful and appropriate sense (objective 1). The results have produced an important contribution to the modeling of refraction effects in the neutral atmosphere now considering temporal and spatial correlations between the observations in a physical and meteorological way. From the turbulence model, a fully populated variance-covariance matrix is derived resulting in an enhanced stochastic model of VLBI observations. The achievements made in this thesis contribute considerably to an improvement of the stochastic modeling of VLBI observations. For validation purposes, in total, 2700 sessions between 1993 and 2014 were analyzed, which were provided by the International VLBI Service for Geodesy and Astrometry (IVS, Nothnagel et al. 2015; Nothnagel et al. 2016). The solutions of different VLBI observing networks, such as intercontinental, continental, local, and combinations thereof were generally improved by the new turbulence model compared to the routine data analysis of the IVS, where only diagonal variance-covariance information is used in the stochastic model, or other strategies refining the stochastic model of VLBI observations. This has been demonstrated in particular by the baseline length repeatabilities as a general measure of the accuracy of baseline length determinations, the WRMS of post-fit residuals, statistical tests, or the standard deviations of the derived estimates. First, the baseline length repeatabilities increase sharply. When using the turbulence-based solution in contrast to the routine IVS solution or a solution based on an empirical model, up to 50 % of all baselines are improved by at least 1 mm, whereas only a few baselines are degraded. The quality of the solutions also improves considerably with respect to statistical validation criteria. Modeling the turbulent behavior in the neutral atmosphere, the WRMS of post-fit residuals generally improves sharply by about 24 ps in quadrature compared to the reference solution of the IVS (as a mean value over all 2700 sessions). Generally, the turbulence model guarantees $\chi^2 \approx 1$ for almost all VLBI sessions without any re-weighting, confirming the stochastic model to be (almost) complete. It is worth mentioning that $\chi^2 \approx 1$ holds on both a global and local scale, while the other strategies evaluated here either lead to an over- or underestimation of the variances of the observations. The behavior is not necessarily identical, or even similar for a specific strategy applied to different VLBI experiments. Finally, the standard deviations of the derived target parameters become more realistic, which was validated against the average noise level of about 115 IVS sessions in terms of WRMS of single-session position estimates, computed after removing offset, rate and annual signal. Compared to other approaches addressing the issue of atmospheric turbulence, the model developed within this thesis has the advantage to be operationally efficient for routine mass analysis of VLBI observing sessions.

Thus, objective 1 of this thesis has been successfully implemented considering all formulated requirements: small-scale refractivity variations in the neutral atmosphere are stochastically described by an atmospheric turbulence model, and it has been demonstrated that the resulting fully populated variance-covariance matrix considering temporal and spatial correlations between

the observations can be incorporated in the stochastic model of VLBI observations without introducing too much additional computational effort. The turbulence model is now a standard component of the VLBI analysis software package ivg::ASCOT (ARTZ et al. 2016; HALSIG et al. 2017), which has been developed at the IGG.

In the near future, a clearly increased observation density will be achieved due to a new generation of fast and more precise VLBI instruments and, in particular, the commissioning phase of so-called twin radio telescopes, two more or less identically constructed adjacent antennas. The potential and importance of the twin telescopes is substantial to analyze atmospheric refraction effects. However, the behavior of atmospheric refraction cannot be analyzed before the stability of the VLBI observing system is understood sufficiently. Consequently, for an improved characterization of atmospheric refraction, the individual components of the observing system have to be carefully quantified, since the estimation of atmospheric parameters and the interpretation of the post-fit residuals in VLBI data analysis effects are closely linked to the stability issues of the VLBI observing system (objective 2). An optimal experimental setup for both, investigations of atmospheric refraction and system stability issues, was provided by close-range geodetic VLBI observations between two adjacent radio telescopes at the Wettzell Geodetic Observatory, where the completion of the first of the two new telescopes has provided an ample opportunity to carry out VLBI test observations on a baseline with a length of only about 120 m. This new opportunity was exploited within this thesis work through dedicated so-called WHISP (Wettzell HIgh SPeed) sessions. Special consideration was given to the so-called Two Way Optical Time Transfer method to evaluate the stability of the hydrogen maser clocks feeding the local oscillators and other necessary electronics. It was found that the agreement between the TWOTT measurements and the VLBI estimates of the same time interval is only at the tens of picosecond level (20-30 ps in the better case and up to 60 ps in the worst case). It is reasonable to assume that the clock estimates compensate for more than the clock effect. For the first time it was possible to identify and quantify the effect of applying manual phase calibration instead of scan-by-scan system calibration, which is on the order of about 20 ps, and therefore, not negligible.

Atmospheric refraction has been investigated on different stages. Differential zenith wet delays were estimated for one station relative to the other station, and the relative variations are found to be of the order of only 1-3 millimeters. While a non-zero offset is assumed to be the result of relative paraboloid deformation effects, the remaining variations are assigned to unmodeled random effects in the stochastic model of the observations, particularly refractivity fluctuations in the neutral atmosphere. This was confirmed by introducing the atmospheric turbulence model developed in this thesis, since the scatter of differential ZWDs reduce and the standard deviations became more realistic. Not only a temporal, but also a spatial relationship was found in the differential data analysis. Performing a residual analysis with respect to the separation distance of the signal paths, the post-fit residuals become larger with increasing ray distance. One reason is the loss of spatial correlations between observations of larger separations. Additional WHISP sessions have been designed with the purpose of having two independent baselines between the two Wettzell antennas and a telescope in Onsala, Sweden, and estimating zenith wet delays for the two Wettzell stations in an absolute sense. The correlation between the zenith wet delay parameters of the two adjacent telescopes has been found to be on the order of 0.94 to 0.99, e.g., when modeling small scale refractivity fluctuations with the turbulence model. Although this should have been expected, it is the first proof that the VLBI systems are capable to measure these effects reliably. For WHISP5 and WHISP7, the differences between the ZWDs of both stations generally vary only in the range of 1-3 millimeters, which fits very well the conclusions obtained for the single baseline WHISP

sessions. The WHISP6 experiment was hampered by the fact that manual phase calibration had to be applied for both Wettzell antennas, leading to much worse results compared to the other sessions.

In conclusion, all requirements formulated in objective 2 of this thesis have been successfully addressed and implemented. The individual components of the observing system, particularly the hydrogen maser clocks feeding the local oscillators and other necessary electronics, the uncertainties emerging from the VLBI correlation process, and the effect of phase calibration, have been quantified and their order of magnitude was specified, in part for the first time. The noise contribution of the clock variations and the correlation error level has been found to be within a few tens of seconds, but not more than 10 ps while, except of the unaccounted measurement noise, the rest of the observation to observation variations is purely atmosphere-driven. Atmospheric refraction effects have been found to be in the range of 1-3 millimeters as demonstrated by two different observing strategies pursued by independent specially designed experiments. In all these investigations the large number of observations has been necessary to guarantee a very stable estimation of the parameters and has warranted a reliable interpretation of the residuals. A number of noteworthy conclusions has been drawn which would not have been possible without the novel observing approach.

In order to better describe the behavior of the neutral atmosphere in the current tropospheric model and to allow for an optimal estimation of zenith wet delays, another focus has been laid to alternative modeling and adjustment strategies to address identified deficiencies of the tropospheric model (objective 3).

As a first measure, an inequality constrained least squares (ICLS) approach of the field of convex optimization has been used to overcome the deficiency, that occasionally zenith wet delay estimates become negative, which, of course, does not reflect meteorological conditions in a plausible way. However, deficiencies in the hydrostatic calibrations, for example due to missing or incomplete pressure data, are compensated by the zenith wet delay (ZWD) estimates to almost 100%. Constraining now individual ZWD parameters to a positive value in the ICLS adjustment, mis-modeling effects in hydrostatic delays are not compensated for by the zenith wet delays anymore, but might affect correlated parameter groups, such as the vertical component of the station coordinates or clock model corrections. Thus, homogeneous time series of meteorological data are of utmost importance in order to not distort the VLBI target parameters. To guarantee adequately modeled a priori information, the hydrostatic calibrations were first derived from numerical weather models. Although the differences to meteorological in-situ observations could reach a few millimeters, homogeneous time series of meteorological data could be guaranteed. Numerical weather models are, however, not optimal, since the time resolution of six hours is still rather coarse and actual variability is not taken into account. To overcome this issue, a homogenization strategy has been proposed, where a numerical weather model of the European Centre for Medium-Range Weather Forecasts (ECMWF) is used to define the level of the meteorological data, while their variability is taken from in-situ observations derived at the VLBI sites after removing outliers and filling data gaps. In conclusion, the application of the ICLS adjustment is, in principle, possible without harming the VLBI target parameters, provided that the a priori hydrostatic component is modeled sufficiently. But it should nevertheless be pointed out that the negative zenith wet delay estimates result not only from a priori mis-modeling, but could also be the result of several other issues, such as mis-modeling of geophysical effects as well as certain impact due to instrumental delays or the clock parametrization.

Due to the strong dependency on the a priori hydrostatic calibrations and the fact that sometimes an insufficient modeling of non-atmospheric quantities might be corrected by constraining

atmospheric parameters, the inequality constrained least squares approach is not recommended for operational VLBI data analysis.

Alternatively to the application of inequality constraints, special emphasis was given to describe the atmospheric parameters by their stochastic properties. Since the pseudo-stochastic behavior of the piece-wise linear representation only models the stochastic character of the atmosphere to a limited extent, the piece-wise linear functions have been replaced by a least squares collocation method. Another benefit of least squares collocation over the classical least squares adjustment using piece-wise linear functions is that additional soft constraints in form of pseudo observations, which are generally needed to stabilize the solution due to missing observations in some piece-wise linear segments, are not required anymore. The stochastic properties of the zenith wet delay are completely described by appropriate covariance functions. A model already applied to VLBI observations was transferred to a second order Gauss Markov process and reasonably modified. Several other covariance models have been applied for validation purposes. A case study was performed to compare the least squares collocation approach fed by different covariance functions to the classical least squares adjustment using piece-wise linear interval lengths of 30 and 60 minutes, respectively. In terms of the weighted root mean square (WRMS) error of post-fit residuals, the second order Gauss Markov process seems to perform best compared to the other covariance functions introduced here. For the longer baselines, this model even leads to better results than the classical least squares adjustment, independent whether using a 30 or 60 minute piece-wise linear interval. A more detailed assessment of the ZWD estimates reveals, that the least squares collocation solution agrees better with the least squares adjustment with a shorter solution interval, while the data set with a resolution of one hour (or even higher) results in a higher scatter of the zenith wet delay estimates. The piece-wise linear representation is not optimal if the resolution is too low that the characteristics of the zenith wet delays cannot be represented accurately enough, but also if the solution interval is too small, that the influence of the pseudo observations prevail over the current observations. It could further be demonstrated that the behavior of the piece-wise linear functions are particularly not optimal at the beginning and at the end of a session, where also the standard deviations of some ZWD estimates increase disproportionately in case of the classical adjustment. One possible reason for this behavior could be the strength of the continuity condition in the framework of the continuous piece-wise linear segments.

The least squares collocation approach is very promising and the preferred adjustment strategy for VLBI observations, assuming the underlying covariance function to be suitable to reflect the behavior of the atmospheric parameters. First, it is possible to counteract the pseudo-stochastic character of the piece-wise linear model and its limitations in representing the stochastic behavior of the troposphere. Second, additional soft constraints are avoided, which directly influence the results of the parameter estimation procedure. Finally, the WRMS of post-fit residuals decrease, when using the second order Gauss Markov process as the covariance model.

Although the inequality constrained least squares adjustment is generally not recommended for the routine data analysis of the IVS, the least squares collocation method, in contrast, ensures an improved modeling of the stochastic properties of the neutral atmosphere and allows for the estimation of zenith wet delays in a more meaningful and appropriate sense, and thus, objective 3 of this thesis has been successfully achieved.

8.2 Outlook

In the framework of this thesis, an atmospheric turbulence model has been developed to stochastically describe small-scale refractivity variations in the neutral atmosphere in a meaningful and appropriate sense, which are completely neglected in the current tropospheric model of the IVS. The enhanced stochastic has produced an important contribution to the modeling of refraction effects in the neutral atmosphere now considering temporal and spatial correlations between the observations in a physical and meteorological way. Although it could be demonstrated that the turbulence-based model is generally suitable for the different VLBI networks, not only for traditional long baselines, but also for observations on local scales, the results on local baselines are even better than those for global applications. In order to further improve the quality of the turbulence model on traditional baselines, it is intended to consider actual weather conditions for the turbulence parameters of the individual VLBI sites without harming the requirement for an operationally efficient modeling approach. The determination of the turbulence parameters from water vapor radiometers, radiosondes or GNSS observations is very time consuming and such sensors have to be available near to the radio telescope, which is generally only the case for GPS sensors, if at all. Instead, it will be possible to determine the turbulence parameters directly within the VLBI parameter estimation procedure due to the expected increase of observations and the better sky coverage with regard to the VLBI Global Observing System.

One major achievement results from the fact that the application of the turbulence model is operationally efficient, since the computational costs are kept to a limited extent for common VLBI sessions. However, for future applications, particularly in case of the new VGOS (VLBI Global Observing System, NIELL et al. 2013) networks providing a tenfold increased number of observations, and, therefore, a dramatically increased volume of data, the performance of the initial strategy is not sufficient anymore, and further optimization strategies have to be found to adapt the model to the new challenges. The most promising approach to reduce the computational costs could be achieved by introducing a parallel computing system, enabling a separated determination of the covariance matrices for the individual stations which will be merged into an overall variance covariance matrix for all observations in a next step. The corresponding necessary measures including different functionalities for the structure of the turbulence model have been already implemented in ivg::ASCOT.

Concerning the current approach to model and implement the tropospheric propagation delay, several deficiencies were identified. In particular, the concept of piece-wise linear functions is not suitable to fully describe the stochastic character of the troposphere, and further needs additional soft constraints in form of pseudo observations to stabilize the solution. The pseudo-stochastic piece-wise linear representation was replaced by a least squares collocation approach capable to model the stochastic properties of the neutral atmosphere. Generally, the least squares collocation approach is very promising and assigned to be the preferred adjustment strategy for VLBI observations, assuming the underlying covariance function to be suitable to reflect the behavior of the atmospheric parameters. Best results were obtained on the basis of a second order Gauss Markov process. On an overall basis, however, the least squares adjustment with turbulence model leads to even better results, indicating the assumption that the corresponding covariance functions need further investigations. One possibility would be a combination of the second order Gauss Markov process with a turbulence-based approach to additionally model the small-scale fluctuations more properly.

Abbreviations

ADEV	Allan Deviation
CONT	Continuous VLBI Campaign
CPWL	Continuous Piece-Wise Linear
CPWLF	Continuous Piece-Wise Linear Functions
CRF	Celestial Reference Frame
DAO	Data Assimilation Office
DORIS	Doppler Orbitography by Radiopositioning Integrated on Satellite
ECMWF	European Centre for Medium Weather Forecast
EOP	Earth Orientation Parameter
ERP	Earth rotation parameter
ET	Event Timer
GCRF	Geocentric Celestial Reference Frame
GGAO	Goddard Geophysical and Astronomical Observatory
GGOS	Global Geodetic Observing System
GLONASS	Globalnaja Nawigazionnaja Sputnikowaja Sistema
GMF	Global Mapping Functions
GNSS	Global Navigation Satellite Systems
GPS	Global Positioning System
GSFC	Goddard Space Flight Center
HPD	Highest Probability Density
IAG	International Association of Geodesy
IERS	International Earth Rotation and Reference Systems Service
IGG	Institute of Geodesy and Geoinformation
IGS	International GNSS Service
IMF	Isobaric Mapping Functions
ICLS	Inequality Constrained Least Squares
ICRF	International Celestial Reference Frame
ITRF	International Terrestrial Reference Frame

ITRS	International Terrestrial Reference System
ivg::ASCOT	(IGG VLBI Group) Analysis Scheduling COmbination Toolbox
IVS	International VLBI Service for Geodesy and Astrometry
IWV	Integrated Water Vapor
LEO	Low Earth Orbit
LLR	Lunar Laser Ranging
LSC	Least Squares Collocation
NMF	New Mapping Functions
NNR/NNT	No-Net Rotation / No-Net Translation
OLS	Ordinary (or classical) Least Squares
PDF	Probability Density Function
PW	Precipitable Water
SLR	Satellite Laser Ranging
SNR	Signal to Noise Ratio
SOGM	Second Order Gauss Markov process
SSB	Solar System Barycentric
TRF	terrestrial reference frame
TSG	Timing Signal Generator
TWOTT	Two-Way Optical Time Transfer
TWTT	Two-Way Time Transfer
UT1	Universal Time
UTC	Universal Time Coordinated
VCM	Variance-Covariance Matrix
VLBA	Very Long Baseline Array
VLBI	Very Long Baseline Interferometry
VGOS	VLBI Global Observing System
VGOSDB	VGOS database format
VMF1	Vienna Mapping Functions 1
VMF1-T	Total Vienna Mapping Functions 1
WHISP	Wettzell HIgh SPeed
(W)RMS	(Weighted) Root Mean Square error
ZHD	Zenith Hydrostatic Delay
ZWD	Zenith Wet Delay

List of Figures

List of Tables

Acknowledgements

Accomplishing the research and writing this thesis would not have been possible without the support of the following people.

First and foremost, I would like to express my gratitude to my Ph.D. supervisor PD Dr. Axel Nothnagel, who elicited my interest in geodetic VLBI and offered me the great chance to perform my Ph.D. studies in the VLBI group at the Institute of Geodesy and Geoinformation of the University of Bonn. Thank you for your guidance, the fruitful discussions and for providing me with the freedom to find my own line of research. I am very grateful for allowing me to promote my work at numerous international meetings and to get involved in the VLBI community. Finally, I have always appreciated the pleasant working atmosphere in our VLBI group.

My gratitude also goes to Prof. Dr. Heiner Kuhlmann (University of Bonn, Germany) and Prof. Dr. Johannes Böhm (Technical University of Vienna, Austria) for both agreeing to be a referee of this thesis and for your valuable discussions and kind support. Particularly, I am very grateful to Prof. Böhm for offering me the opportunity to visit him in Vienna for a personal discussion. I want to thank Prof. Jan-Henrik Haunert and Prof. Wolf-Dieter Schuh (University of Bonn, Germany) for being the chairperson and member of my examination board.

The content of this thesis has been already partly published before. Special thanks goes to my co-authors for their fruitful collaboration, their contributions, intensive discussions and proof reading the manuscripts: Thomas Artz, Alessandra Bertarini, Andreas Iddink, Frédéric Jaron, Judith Leek, Lutz Roese-Koerner, Wolf-Dieter Schuh (University of Bonn, Germany), Gerhard Kronschnabl, Christian Plötz, Torben Schüler (Federal Agency for Cartography and Geodesy, Geodetic Observatory Wettzell, Germany), Rüdiger Haas (Chalmers University of Technology, Sweden), Jan Kodet and Alexander Neidhardt (Technical University of Munich, Geodetic Observatory Wettzell, Germany). Additionally, I want to thank all students which were supervised by me in Bachelor- or Mastertheses, since their work often also contributed to my studies.

My special thanks go to Maike Schumacher (University of Bristol, UK) and Andreas Iddink for proof-reading my thesis.

Moreover, I want to thank my colleagues at the Institute of Geodesy and Geoinformation of the University of Bonn. I take particular pleasure in thanking my (former and current) colleagues in our VLBI group (IGG and Bonn Correlator): Thomas Artz, Simone Bernhardt, Alessandra Bertarini, Andreas Iddink, Frédéric Jaron, Maria Karbon, Laura La Porta, Judith Leek, Arno Müskens, Han Songtao and Zhang Zhongkai.

Especially my roommates Thomas Artz and Andreas Iddink are greatly acknowledged for the excellent cooperation and fruitful discussions, but also the (work- and non-work-related) time during numerous meetings. Without the two of you, we could never had initiated the development of our VLBI software package ivg::ASCOT. In this context I also would like to thank the entire ivg::ASCOT team.

The VLBI experiments used within this thesis were mainly provided by the International VLBI Service for Geodesy and Astrometry (NOTHNAGEL et al. 2016). A series of dedicated local and

References

Abramowitz, M. and I.Stegun (1964) *Handbook of Mathematical Functions: With Formulas, Graphs, and Mathematical Tables*. Applied mathematics series. Dover Publications.

Alizadeh, M. M., D.Wijaya, T.Hobiger, R.Weber and H.Schuh (2013) Ionospheric Effects on Microwave Signals. Böhm, J. and H.Schuh (Eds.), *Atmospheric Effects in Space Geodesy*, Springer Berlin Heidelberg, 35–71.

Altamimi, Z., P.Rebischung, L.Métivier and X.Collilieux (2016) ITRF2014: A new release of the International Terrestrial Reference Frame modeling nonlinear station motions. *Journal of Geophysical Research: Solid Earth*, 121(8):6109–6131, doi:10.1002/2016jb013098.

Angermann, D., H.Drewes, M.Krügel, B.Meisel, M.Gerstl, R.Kelm, H.Müller, W.Seemüller and V.Tesmer (2004) ITRS Combination Center at DGFI: a terrestrial reference frame realization 2003. *Deutsche Geodätische Kommission Bayer. Akad. Wiss. München, Reihe B*, 313:1–141. ISSN 3-7696-8593-8, ISBN 0065-5317.

Armstrong, J. W. and R. A.Sramek (1982) Observations of tropospheric phase scintillations at 5 GHz on vertical paths. *Radio Science*, 17(6):1579–1586, doi:10.1029/RS017i006p01579.

Artz, T., J.Leek, A.Nothnagel and M.Schumacher (2012) VLBI Intensive Sessions Revisited. In: Behrend, D. and K.Baver (Eds.), *IVS 2012 General Meeting Proceedings, "Launching the Next-Generation IVS Network"*, 4–9 March 2012, Madrid. NASA/CP-2012-217504, 276–280.

Artz, T., S.Halsig, A.Iddink and A.Nothnagel (2016) ivg::ASCOT: The Development of a new VLBI Software Package. In: Behrend, D., K. D.Baver and K.Armstrong (Eds.), *IVS 2016 General Meeting Proceedings, "New Horizons with VGOS", Johannesburg, South Africa, March 13-19 2016*, 217–221.

Artz, T. (2011) *Determination of Sub-daily Earth Rotation Parameters from VLBI Observations*. Dissertation, Schriftenreihe des Institutes für Geodäsie und Geoinformation, Heft Nr. 47, Universität Bonn.

Batchelor, G. K. (1950) The application of the similarity theory of turbulence to atmospheric diffusion. *Quarterly Journal of the Royal Meteorological Society*, 76:133–146, doi: 10.1002/qj.49707632804.

Bevis, M., S.Businger, T.Herring, C.Rocken, R.Anthes and R.Ware (1992) GPS Meteorology:Remote Sensing of Atmospheric Water Vapor Using the Global Positioning System. *Journal of Geophysical Research*, 97(D14):15787–15801.

Bevis, M., S.Businger, S.Chiswell, T. A.Herring, R. A.Anthes, C.Rocken and R. H.Ware (1994) GPS Meteorology: Mapping Zenith Wet Delays onto Precipitable Water. *Journal of applied meteorology*, 33(3):379–386.

Bierman, G. (1977) *Factorization Methods for Discrete Sequential Estimation*. Mathematics in Science and Engineering, volume 128, Academic Press, New York.

BISCHOFF, W., B.HECK, J.HOWIND and A.TEUSCH (2006) A Procedure for Estimating the Variance Function of Linear Models and for Checking the Appropriateness of Estimated Variances: A Case Study of GPS Carrier-phase Observations. *Journal of Geodesy*, 79(12):694–704, doi: 10.1007/s00190-006-0024-1.

BÖCKMANN, S., T.ARTZ, A.NOTHNAGEL and V.TESMER (2010) International VLBI Service for Geodesy and Astrometry: Earth orientation parameter combination methodology and quality of the combined products. *Journal of Geophysical Research*, 115(B14):4404, doi: 10.1029/2009JB006465.

BÖHM, J., A.NIELL, P.TREGONING and H.SCHUH (2006a) Global Mapping Function (GMF): A new empirical mapping function based on numerical weather model data. *Geophysical Research Letters*, 33(L07304), doi:10.1029/2005gl025546.

BÖHM, J., B.WERL and H.SCHUH (2006b) Troposphere mapping functions for GPS and very long baseline interferometry from European Centre for Medium-range Weather Forecasts operational analysis data. *Journal of Geophysical Research*, 111:B02406, doi:10.1029/2005JB003629.

BÖHM, J., P.MENDES CERVEIRA, H.SCHUH and P.TREGONING (2007a) The Impact of Mapping Functions for the Neutral Atmosphere Based on Numerical Weather Models in GPS Data Analysis. In: TREGONING, P. and C.RIZOS (Eds.), *IAG symposium series*, Volume 130, 837–843. ISBN 3-540-49349-5.

BÖHM, J., R.HEINKELMANN and H.SCHUH (2007b) Short Note: A global model of pressure and temperature for geodetic applications. *Journal of Geodesy*, 81(10):679–683, doi: 10.1007/s00190-007-0135-3.

BÖHM, J., S.BÖHM, T.NILSSON, A.PANY, L.PLANK, H.SPICAKOVA, K.TEKE and H.SCHUH (2012) The New Vienna VLBI Software VieVS. In: KENYON, S., M. C.PACINO and U.MARTI (Eds.), *Proceedings of IAG Scientific Assembly 2009, International Association of Geodesy Symposia Series*, Volume 136, 1007–1011.

BÖHM, J. (2004) *Troposphärische Laufzeitverzögerungen in der VLBI*. Dissertation, Geowissenschaftliche Mitteilungen, Heft Nr. 68, Schriftenreihe der Studienrichtung Vermessung und Geoinformation, Technische Universität Wien, ISSN 1811–8380 (in German).

BÖHM, J., D.SALSTEIN, M. M.ALIZADEH, D. D.WIJAYA and H.SCHUH (2013) Geodetic and Atmospheric Background. BÖHM, J. and H.SCHUH (Eds.), *Atmospheric Effects in Space Geodesy*, Springer Berlin Heidelberg, 73–136.

BOLOTIN, S., K.BAVER, J.GIPSON, D.GORDON and D.MACMILLAN (2016) Transition to the vgosDB Format. In: BEHREND, D., K. D.BAVER and K.ARMSTRONG (Eds.), *IVS 2016 General Meeting Proceedings, "New Horizons with VGOS", Johannesburg, South Africa, March 13-19 2016*, 222–224.

BOYD, S. and L.VANDENBERGHE (2004) *Convex Optimization*. Cambridge University Press.

BROTEN, N. W., T. H.LEGG, J. L.LOCKE, C. W.MCLEISH, R. S.RICHARDS, R. M.CHISHOLM, H. P.GUSH, J. L.YEN and J. A.GALT (1967) Long Base Line Interferometry: A New Technique. *Science*, 156(3782):1592–1593, doi:10.1126/science.156.3782.1592.

BRUNNER, F. and J.RÜEGER (1992) Theory of the local scale parameter method for EDM. *Bulletin Géodésique*, 66:355–364.

CAMPBELL, J. (1987) Very long baseline interferometry. TURNER, S. (Eds.), *Applied Geodesy*, Volume 12 of the series Lecture Notes in Earth Sciences, Springer Berlin Heidelberg, 67–87.

CHAO, C. C. (1971) The troposphere calibration model for Mariner Mars. *JPL Technical Report*, 32.

CHEN, G. and T. A.HERRING (1997) Effects of atmospheric azimuthal asymmetry on the analysis of space geodetic data. *Journal of Geophysical Research: Solid Earth*, 102(B9):20489–20502, doi:10.1029/97jb01739.

CLARK, T., B.COREY, J.DAVIS, G.ELGERED, T.HERRING, H. F.HINTEREGGER, C.KNIGHT, J.LEVINE, G.LUNDQVIST, C.MA, E.NESMAN, R.PHILLIPS, A.ROGERS, B.RONNANG, J.RYAN, B.SCHUPLER, D.SHAFFER, I.SHAPIRO, N.VANDENBERG, J.WEBBER and A.WHITNEY (1985) Precision Geodesy Using the Mark-III Very-Long-Baseline Interferometer System. *IEEE Transactions on Geoscience and Remote Sensing*, GE-23:438–449, doi:10.1109/TGRS.1985.289433.

CREWELL, S., M.MECH, T.REINHARDT, S.SELBACH, H.-D.BETZ, E.BROCARD, G.DICK, E. J.O'CONNOR, J.FISCHER, T.HANISCH, T.HAUF, A.HUENERBEIN, L.DELOBBE, A.MATHES, G.PETERS, H.WERNLI, M.WIEGNER and V.WULFMEYER (2008) The general observation period 2007 within the priority program on quantitative precipitation forecasting: concept and first results. *Meteorologische Zeitschrift*, 17(6):849–866.

DAVIS, J. L., T. A.HERRING, I. I.SHAPIRO, A. E. E.ROGERS and G.ELGERED (1985) Geodesy by radio interferometry - Effects of atmospheric modeling errors on estimates of baseline length. *Radio Science*, 20(6):1593–1607, doi:10.1029/RS020i006p01593.

DAVIS, J. L. (1992) The effect of turbulence on atmospheric gradient parameters estimated from ground-based radiometric and space geodetic measurements. *Geophysical Research Letters*, 19(21):2183–2186, doi:10.1029/92GL02510.

DAVIS, J., G.ELGERED, A.NIELL and C.KUEHN (1993) Ground-based measurement of gradients in the "wet" radio refractivity of air. *Radio Science*, 28(6):1003–1018.

DE BOOR, C. (1978) *A practical guide to splines*, Volume 27. Springer, New York.

DENG, Z., M.BENDER, F.ZUS, M.GE, G.DICK, M.RAMATSCHI, J.WICKERT, U.LÖHNERT and S.SCHÖN (2011) Validation of tropospheric slant path delays derived from single and dual frequency GPS receivers. *Radio Science*, 46:RS6007, doi:10.1029/2011RS004687.

DOUSA, J. and G. V.BENNITT (2013) Estimation and evaluation of hourly updated global GPS Zenith Total Delays over ten months. *GPS Solutions*, 17(4):453–464, doi:10.1007/s10291-012-0291-7.

DOW, J. M., R. E.NEILAN and C.RIZOS (2009) The International GNSS Service in a changing landscape of Global Navigation Satellite Systems. *Journal of Geodesy*, 83(3–4):191–198, doi:10.1007/s00190-008-0300-3.

DREWES, H., F.KUGLITSCH, J.ADÁM and S.RÓZSA (2016) *The Geodesist's Handbook 2016*, Volume 90. Springer Berlin Heidelberg.

EL-RABBANY, A. E.-S. (1994) *The Effect of Physical Correlations on the Ambiguity Resolution and Accuracy Estimation in GPS Differential Positioning.* Dissertation, Department of Geodesy and Geomatics Engineering, University of New Brunswick, Canada.

ELGERED, G. (1992) Refraction in the Troposphere. In: DE MUNCK, J. and T.SPOELSTRA (Eds.), *Proceedings of Symposium on Refraction of Transatmospheric Signals in Geodesy, 19-22 May 1992, The Hague, The Netherlands.* Delft, Netherlands, 13–19.

ELGERED, G. (1993) Tropospheric radio path delay from ground-based microwave radiometry. JANSSEN, M. (Eds.), *Atmospheric Remote Sensing by Microwave Radiometry*, John Wiley & Sons, Inc., New York.

ELGERED, G. K. (1982) Tropospheric wet path-delay measurements. *IEEE Trans. Antennas Prop.*, 30(3):502–505.

ELÓSEGUI, P., J. L.DAVIS, L. P.GRADINARSKY, G.ELGERED, J. M.JOHANSSON, D. A.TAHMOUSH and A.RIUS (1999) Sensing atmospheric structure using small-scale space geodetic networks. *Geophysical Research Letters*, 26(16):2445–2448.

EULER, H. J. and C. C.GOAD (1991) On optimal filtering of GPS dual frequency observations without using orbit information. *Bulletin Géodésique*, 65(2):130–143.

FEY, A. L., D.GORDON, C. S.JACOBS, C.MA, R. A.GAUME, E. F.ARIAS, G.BIANCO, D. A.BOBOLTZ, S.BÖCKMANN, S.BOLOTIN, P.CHARLOT, A.COLLIOUD, G.ENGELHARDT, J.GIPSON, A.-M.GONTIER, R.HEINKELMANN, S.KURDUBOV, S.LAMBERT, S.LYTVYN, D. S.MACMILLAN, Z.MALKIN, A.NOTHNAGEL, R.OJHA, E.SKURIKHINA, J.SOKOLOVA, J.SOUCHAY, O. J.SOVERS, V.TESMER, O.TITOV, G.WANG and V.ZHAROV (2015) THE SECOND REALIZATION OF THE INTERNATIONAL CELESTIAL REFERENCE FRAME BY VERY LONG BASELINE INTERFEROMETRY. *The Astronomical Journal*, 150(2)(58), doi:10.1088/0004-6256/150/2/58.

GASPARI, G. and S.COHN (1999) Construction of correlation functions in two and three dimensions. *Quarterly Journal of the Royal Meteorological Society*, 125(554):723–757.

GASPARI, G., S.COHN, L.GUO and S.PAWSON (2006) Construction and application of covariance functions with variable length-fields. *Quarterly Journal of the Royal Meteorological Society*, 132(27):1815–1838.

GILL, P., W.MURRAY and M.WRIGHT (1981) *Practical Optimazation.* Academic Press, San Diego.

GIPSON, J. (2012) IVS Working Group 4: VLBI Data Structures. In: BEHREND, D. and K.BAVER (Eds.), *IVS 2012 General Meeting Proceedings, "Launching the Next-Generation IVS Network",* 4 – 9 March 2012, Madrid. NASA/CP-2012-217504, 212 – 221.

GIPSON, J., D.MACMILLAN and L.PETROV (2008) Improved Estimation in VLBI through Better Modeling and Analysis. In: FINKELSTEIN, A. and D.BEHREND (Eds.), *IVS 2008 General Meeting Proceedings, "Measuring the Future",* 3 – 6 March 2008, St. Petersburg, Russia, 157–162.

GIPSON, J. M. (2007) Incorporating Correlated Station Dependent Noise Improves VLBI Estimates. In: BOEHM, J., A.PANY and H.SCHUH (Eds.), *Proceedings of the 18th European VLBI*

for Geodesy and Astrometry Working Meeting, 12-13 April 2007, Vienna. Geowissenschaftliche Mitteilungen, Heft Nr. 79, Schriftenreihe des Studienrichtung Vermessung und Geoinformation, Technische Universität Wien, ISSN 1811-8380, 129 – 134.

Gipson, J. M. (2006) Correlation Due to Station Dependent Noise in VLBI. In: Behrend, D. and K.Baver (Eds.), *International VLBI Service for Geodesy and Astrometry 2006 General Meeting Proceedings,* 9 – 11 January 2006, Concepción, Chile. NASA/CP-2006-214140, 286–290.

Gross, R., G.Beutler and H. P.Plag (2009) Integrated scientific and societal user requirements and functional specifications for the GGOS. Plag, H. and M.Pearlman (Eds.), *Global Geodetic Observing System*, Springer Berlin Heidelberg.

Haas, R. (1996) *Untersuchungen zu Erddeformationsmodellen für die Auswertung von geodätischen VLBI-Messungen.* Dissertation, Rheinische Friedrich-Wilhelms-Universität Bonn. Deutsche Geodätische Kommission bei der Bayerischen Akademie der Wissenschaften, Reihe C, Vol. 466, München, ISSN 0071-9196.

Halsig, S., T.Artz, J.Leek and A.Nothnagel (2014) VLBI analyses using covariance information from turbulence models. In: Behrend, D., K. D.Baver and K.Armstrong (Eds.), *IVS 2014 General Meeting Proceedings, "VGOS: The New VLBI Network",* 2 – 7 March 2014, Shanghai, China. Science Press (Beijing), 272 – 276. ISBN 978-7-03-042974-2.

Halsig, S., T.Artz, A.Iddink and A.Nothnagel (2016a) Using an atmospheric turbulence model for the stochastic model of geodetic VLBI data analysis. *Earth, Planets and Space*, 68:106, doi:10.1186/s40623-016-0482-5.

Halsig, S., T.Artz, A.Iddink and A.Nothnagel (2016b) An Inequality Constrained Least-Squares Approach as an Alternative Estimation Procedure for Atmospheric Parameters from VLBI Observations. In: Behrend, D., K. D.Baver and K.Armstrong (Eds.), *IVS 2016 General Meeting Proceedings, "New Horizons with VGOS", Johannesburg, South Africa, March 13-19 2016*, 326 – 330.

Halsig, S., A.Corbin, A.Iddink, F.Jaron, T.Schubert and A.Nothnagel (2017) Current development progress in ivg::ASCOT - A new VLBI analysis software. In: Haas, R. and G.Elgered (Eds.), *Proceedings of the 23th EVGA working meeting,* 15 – 19 May 2017, Gothenburg, Sweden, 167–171.

Halsig, S., T.Artz, A.Iddink and A.Nothnagel (2015a) Augmenting the stochastic model in VLBI data analysis by correlations from atmospheric turbulence models. In: Haas, R. and F.Colomer (Eds.), *Proceedings of the 22th EVGA working meeting,* 18 – 21 May 2015, Ponta Delgada, 201 – 204.

Halsig, S., L.Roese-Koerner, T.Artz, A.Nothnagel and W.-D.Schuh (2015b) Improved Parameter Estimation of Zenith Wet Delays Using an Inequality Constrained Least Squares Method. *International Association of Geodesy Symposia*, Springer Nature, 69–74.

Hase, H. and L.Petrov (1999) The First Campaign of Observations with the VLBI-Module of TIGO. In: Schlüter, W. and H.Hase (Eds.), *Proceedings of the 13th Working Meeting on European VLBI for Geodesy and Astrometry,* 12 – 13 February 1999, Viechtach/Wettzell. Bundesamt für Kartographie und Geodäsie, 19 – 24.

HAWAREY, M., T.HOBIGER and H.SCHUH (2005) Effects of the 2nd order ionospheric terms on VLBI measurements. *Geophysical Research Letters*, 32(L11304), doi:10.1029/2005GL022729.

HEINKELMANN, R., H.BÖHM, J. ABD SCHUH, S.BOLOTIN, G.ENGELHARDT, D. S.MACMILLAN, M.NEGUSINI, E.SKURIKHINA, V.TESMER and O.TITOV (2007) Combination of long time-series of troposphere zenith dealys observed by VLBI. *Journal of Geodesy*, 81:483–501, doi: 10.1007/s00190-007-0147-z.

HEINKELMANN, R., J.BÖHM, S.BOLOTIN, G.ENGELHARDT, R.HAAS, R.LANOTTE, D. S.MACMILLAN, M.NEGUSINI, E.SKURIKHINA, O.TITOV and S.H. (2011) VLBI-derived tropospheric parameters during CONT08. *Journal of Geodesy*, 85, doi:10.1007/s00190-011-0459-x.

HERRERA-PINZON, I., B.MÄNNEL, M.ROTHACHER, J.KODET, U.SCHREIBER and R.SCHMID (2017) Assessment of Local VLBI Baselines: the Wettzell Case (in preparation).

HERRING, T. A., J. L.DAVIS and I. I.SHAPIRO (1990) Geodesy by radio interferometry: The application of Kalman filtering to the analysis of very long baseline interferometry data. *Journal of Geophysical Research*, 95(B8):12561 – 12581, doi:10.1029/JB095iB08p12561.

HERRING, T. (1992) Modeling Atmospheric Delays in the Analysis of Space Geodetic Data. In: DE MUNCK, J. and T.SPOELSTRA (Eds.), *Refraction of Transatmospheric Signals in Geodesy*, Volume 36. Netherlands Geodetic Commission Publications on Geodesy, 157–164.

HOPFIELD, H. S. (1969) Two-quartic tropospheric refractivity profile for correcting satellite data. *Journal of Geophysical Research*, 74(18):4487–4499, doi:10.1029/jc074i018p04487.

HOWIND, J., H.KUTTERER and B.HECK (1999) Impact of temporal correlations on GPS-derived relative point positions. *Journal of Geodesy*, 73(5):246–258, doi:10.1007/s001900050241.

HOWIND, J. (2005) *Analyse des stochastischen Modells von GPS-Trägerphasenbeobachtungen*. Dissertation, Deutsche Geodätische Kommission bei der Bayerischen Akademie der Wissenschaften, Reihe C, Vol. 584, München, ISBN 3769650239, München.

ISHIMARU, A. (1991) Wave propagation and scattering in random media and rough surfaces. *Proceedings of the IEEE*, 79(10):1359–1366, doi:10.1109/5.104210.

IVS MASTER FILES. (2017) , International VLBI Service for Geodesy and Astrometry, multi-agency schedule files, https://ivscc.gsfc.nasa.gov/program/master.html, last access on 20 November 2017, 2017.

JACKSON, J. D. (1998) *Classical electrodynamics*. Wiley & Sons, Inc., New York.

JANES, H., R. B.LANGLEY and S.NEWBY (1991) Analysis of tropospheric delay prediction models: comparisons with ray-tracing and implications for GPS relative positioning. *Bulletin Géodésique*, 65:151–161.

KALMAN, R. (1960) A new approach to linear filtering and prediction problems. *Journal of Fluids Engineering*, 82(1):35–45, doi:10.1115/1.3662552.

KERMARREC, G. and S.SCHÖN (2014) On the Mátern covariance family: a proposal for modeling temporal correlations based on turbulence theory. *Journal of Geodesy*, 88(11):1061–1079, doi: 10.1007/s00190-014-0743-7.

KERMARREC, G. and S.SCHÖN (2016) Taking correlations in GPS least squares adjustments into account with a diagonal covariance matrix. *Journal of Geodesy*, 90(9):793–805, doi: 10.1007/s00190-016-0911-z.

KOCH, K.-R. (1999) *Parameter estimation and hypothesis testing in linear models*. Springer Verlag.

KODET, J., P.PANEK and I.PROCHAZKA (2016a) Two-way time transfer via optical fiber providing subpicosecond precision and high temperature stability. *Metrologia*, 53:18 – 26.

KODET, J., U.SCHREIBER, P.PANEK, I.PROCHAZKA, B.MÄNNEL and T.SCHÜLER (2016b) Optical two-way timing system for space geodesy applications. In: *2016 European Frequency and Time Forum*, 4 - 7 *April 2016, York, United Kingdom*.

KOLMOGOROV, A. (1941a) The Local Structure of Turbulence in Incompressible Viscous Fluid for Very Large Reynolds' Numbers. *Akademiia Nauk SSSR Doklady*, 30:301–305.

KOLMOGOROV, A. N. (1941b) Dissipation of Energy in Locally Isotropic Turbulence. *Akademiia Nauk SSSR Doklady*, 32:16.

KRARUP, T. (1969) A contribution to the mathematical foundation of physical geodesy. *Danish Geodetic Institute, Publication No. 4.*

KRAUS, H. (2004) *Die Atmosphäre der Erde - Eine Einführung in die Meteorologie*. Springer Berlin Heidelberg, 3. Auflage, ISBN: 978-3-540-20656-9.

LAGLER, K., M.SCHINDELEGGER, J.BÖHM, H.KRÁSNÁ and T.NILSSON (2013) GPT2: Empirical slant delay model for radio space geodetic techniques. *Geophysical Research Letters*, 40(6):1069–1073, doi:10.1002/grl.50288.

LANDSKRON, D. and J.BÖHM (2017) VMF3/GPT3: refined discrete and empirical troposphere mapping functions. *Journal of Geodesy*, doi:10.1007/s00190-017-1066-2.

LE BAIL, K. and J.GIPSON (2011) Strategy to Improve the Homogeneity of Meteorological Data in Mark3 Databases. In: ALEF, W., S.BERNHARD and A.NOTHNAGEL (Eds.), *Proceedings of the 20th EVGA working meeting*, 29 – 30 March 2011, Bonn, Germany, Volume 22. Institut für Geodäsie und Geoinformation der Universität Bonn, 138–141.

LIEBE, H. J. (1985) An Updated Model for Millimeter Wave Propagation in Moist Air. *Radio Science*, Vol. 20., No. 5:1069–1089.

LIEBE, H. J. (1989) MPM - an atmospheric millimeter-wave Propagation model. *International Journal of Infrared and Millimeter Waves*, 10(6):631–650, doi:doi:10.1007/BF01009565.

LIEBE, H. J., G. A.HUFFORD and M. G.COTTON (1993) Propagation modeling of moist air and suspended water/ice particles at frequencies below 1000 GHz. In: *AGARD 52d Specialists Meeting of the Electromagnetic Wave Propagation Panel, Palma de Mallorca, Spain*, 3.1–3.10.

LUCAS, J. R. and W. H.DILLINGER (1998) MINQUE for block diagonal bordered systems such as those encountered in VLBI data analysis. *Journal of Geodesy*, 72(6):343–349, doi: 10.1007/s001900050173.

LUO, X., M.MAYER and B.HECK (2011) A realistic and easy-to-implement weighting model for GNSS phase observations. In: *IUGG 2011 General Assembly, Earth on the Edge: Science for a Sustainable Planet, 27 June - 8 July 2011, Melbourne, Australia*.

Ma, C., J. M.Sauber, T. A.Clark, J. W.Ryan, L. J.Bell, D.Gordon and W. E.Himwich (1990) Measurement of horizontal motions in Alaska using very long baseline interferometry. *Journal of Geophysical Research*, 95(B13):21991–22011, doi:10.1029/JB095iB13p21991.

MacMillan, D. S. (1995) Atmospheric gradients from very long baseline interferometry observations. *Geophysical Research Letters*, 22(9):1041–1044, doi:10.1029/95gl00887.

MacMillan, D. S. and C.Ma (1997) Atmospheric gradients and the VLBI terrestrial and celestial reference frames. *Geophysical Research Letters*, 24(4):453–456, doi:10.1029/97GL00143.

MacMillan, D. and C.Ma (1998) Using meteorological data assimilation models in computing tropospheric delays at micrwave frequencies. *Physics and Chemistry of the Earth*, 23(1):97–102, doi:10.1016/s0079-1946(97)00249-8.

Marini, J. (1972) Correction of satellite tracking data for an arbitrary tropospheric profile. *Radio Science*, 7(2):223–231.

Martí-Vidal, I., T.Krichbaum, A.Marscher, W.Alef, A.Bertarini, U.Bach, F.Schinzel, H.Rottmann, J.Anderson, J.Zensus, M.Bremer, S.Sanchez, M.Lindqvist and A.Mujunen (2012) On the Calibration of Full-polarization 86 GHz Global VLBI Observations. *Astronomy & Astrophysics*, 542:A107, doi:10.1051/0004-6361/201218958.

Matérn, B. (1960) *Spatial Variation - Stochastic models and their application to some problems in forest ssurvey and other sampling investigations.* Meddelanden Från Statens Skogsforskningsinstitut.

Matveenko, L. I., N. S.Kardashev and G. B.Sholomitskii (1965) Large base-line radio interferometers. *Soviet Radiophysics*, 8(4):461–463, doi:10.1007/bf01038318.

Maybeck, P. (1979) *Stochastic models, estimation, and control.* Mathematics in Science and Engineering, Volume 141, Part 1, Academic Press, Inc., New York.

Mendes, V. B. (1999) *Modeling the neutral-atmosphere propagation delay in radiometric space techniques.* Dissertation, Geodesy and Geomatics Engineering, University of New Brunswick, Fredericton, New Brunswick, Canada, Technical Report No. 199.

Michelson, A. A. (1890) On the application of interference methods to astronomical measurements. *Philosophical Magazine, 5th Series.*

Moran, J. M., P. P.Crowther, B. F.Burke, A. H.Barrett, A. E. E.Rogers, J. A.Ball, J. C.Carter and C. C.Bare (1967) Spectral Line Interferometry with Independent Time Standards at Stations Separated by 845 Kilometers. *Science*, 157(3789):676–677, doi:10.1126/science.157.3789.676.

Moritz, H. (1972) Advanced Least-Squares Methods. *Reports of the Department of Geodetic Science, Ohio State University, Ohio*, Report No. 175.

Moritz, H. (1976) Covariance Functions in Least-Squares Collocation. *Reports of the Department of Geodetic Science, Ohio State University, Ohio*, Report No. 240.

Niell, A. (2015) Status report on the GGAO-Westford VGOS systems. In: Haas, R. and F.Colomer (Eds.), *Proceedings of the 22th EVGA working meeting,* 18 – 21 May 2015, Ponta Delgada, 80 – 84.

Niell, A., C.Beaudoin, R.Cappallo, B.Corey and M.Titus (2013) First results with the GGAO12M VGOS System. In: *21st Meeting of the European VLBI Group for Geodesy and Astronomy, held in Espoo, Finland, March 5-8, 2013, Eds: N. Zubko and M. Poutanen, Reports of the Finnish Geodetic Institute, p. 29-32.*, Volume 1, 29–32.

Niell, A., C.Beaudoin, S.Bolotin, R.Cappallo, B.Corey, J.Gipson, D.Gordon, R.McWhirter, C.Ruszczyk and J.SooHoo (2014) VGOS Operations and Geodetic Results. In: Behrend, D., K. D.Baver and K.Armstrong (Eds.), *IVS 2014 General Meeting Proceedings, "VGOS: The New VLBI Network"*, 2 – 7 March 2014, Shanghai, China. Science Press (Beijing), 97 – 101. ISBN 978-7-03-042974-2.

Niell, A., R.Cappallo, B.Corey, C.Eckert, P.Elosegui, R.McWhirter, G.Rajagopalan, C.Ruszczyk and M.Titus (2016) VGOS OObservations with Westford, GGAO, and the New Station at Kokee, Hawaii. In: Behrend, D., K. D.Baver and K.Armstrong (Eds.), *IVS 2016 General Meeting Proceedings, "New Horizons with VGOS"*, *Johannesburg, South Africa, March 13-19 2016*, 44 – 48.

Niell, A. E. (1996) Global mapping functions for the atmosphere delay at radio wavelengths. *Journal of Geophysical Research*, 101(B02):3227 – 3246, doi:10.1029/95JB03048.

Niell, A. E. (2000) Improved atmospheric mapping functions for VLBI and GPS. *Earth, Planets and Space*, 52(10):699–702, doi:10.1186/bf03352267.

Nilsson, T. and R.Haas (2010) Impact of atmospheric turbulence on geodetic very long baseline interferometry. *Journal of Geophysical Research*, 115(B03407), doi:10.1029/2009JB006579.

Nilsson, T., J. L.Davis and E. M.Hill (2009) Using ground-based GPS to characterize atmospheric turbulence. *Geophysical Research Letters*, 36(L16807), doi:10.1029/2009GL040090.

Nilsson, T., J.Böhm and H.Schuh (2010) Sub-Diurnal Earth Rotation Variations Observed by VLBI. *Artificial Satellites*, 45(2):49 – 55, doi:10.2478/v10018-010-0005-8.

Nilsson, T., J.Böhm, D. D.Wijaya, A.Tresch, V.Nafisi and H.Schuh (2013) Path Delays in the Neutral Atmosphere. Böhm, J. and H.Schuh (Eds.), *Atmospheric Effects in Space Geodesy*, Springer Berlin Heidelberg, 73–136.

Nilsson, T., R.Heinkelmann, M.Karbon, V.Raposo-Pulido, B.Soja and H.Schuh (2014) Earth orientation parameters estimated from VLBI during the CONT11 campaign. *Journal of Geodesy*, 88(5):491–502, doi:10.1007/s00190-014-0700-5.

Nilsson, T., M.Karbon, B.Soja, R.Heinkelmann, C.Lu and H.Schuh (2015) Atmospheric modeling for co-located VLBI antennas and twin telescopes. *Journal of Geodesy*, 89(7):655–665, doi:10.1007/s00190-015-0804-6.

Nothnagel, A. (1991) *Radiointerferometrische Beobachtungen zur Bestimmung der Polbewegung unter Benutzung langer Nord-Süd-Basislinien.* Dissertation, Rheinische Friedrich-Wilhelms-Universität Bonn. Deutsche Geodätische Kommission bei der Bayerischen Akademie der Wissenschaften, Reihe C, Vol. 368, ISSN 0071-9196.

Nothnagel, A. (2000) Der Einfluss des Wasserdampfes auf die modernen raumgestützten Messverfahren. *Mitteilungen des Bundesamtes für Kartographie und Geodäsie. Habilitationsschrift, Universität Bonn*, Band 16.

Nothnagel, A., T.Artz, D.Behrend and Z.Malkin (2016) International VLBI Service for Geodesy and Astrometry. *Journal of Geodesy*, doi:10.1007/s00190-016-0950-5.

Nothnagel, A., S.Bergstrand, R.Haas and C.Holst (2017) Modelling Gravitational Deformation Effects of the Onsala 20m Radio Telescope (in preparation).

Nothnagel, A., M.Vennebusch and J.Campbell (2002) On Correlations Between Parameters in Geodetic VLBI Data Analysis. In: Vandenberg, N. R. and K. D.Baver (Eds.), *International VLBI Service for Geodesy and Astrometry 2002 General Meeting Proceedings*, 04 – 07 February 2002, Tsukuba. NASA/CP-2002-210002, Greenbelt MD, 260 – 264.

Nothnagel, A., International VLBI Service for Geodesy and Astrometry (IVS), W.Alef, J.Amagai, P. H.Andersen, J.Anderson, T.Andreeva, T.Artz, S.Bachmann, K.Balidakis, C.Barache, A.Baudry, E.Bauernfeind, K.Baver, C.Beaudoin, D.Behrend, A.Bellanger, A.Berdnikov, P.Bergman, S.Bernhart, A.Bertarini, G.Bianco, E.Bielmaier, D.Boboltz, J.Böhm, S.Böhm, A.Boer, S.Bolotin, M.Bougeard, G.Bourda, S.Brazeau, S.Buttaccio, L.Cannizzaro, R.Cappallo, B.Carlson, M. S.Carter, P.Charlot, C.Chen, M.Chen, J.Cho, T.Clark, A.Collioud, F.Colomer, G.Colucci, L.Combrinck, J.Conway, B.Corey, R.Curtis, M.Daniels, R.Dassing, M.Davis, P.de Vicente, A.De Witt, A.Diakov, J.Dickey, C.Dieck, I.Diegel, K.Doi, H.Drewes, M.Dube, G.Elgered, G.Engelhardt, M.Evangelista, Q.Fan, S.Farley, L.Fedotov, A.Fey, R.Figueroa, Y.Fukuzaki, D.Gambis, S.Garcia-Espada, R.Gaume, N.Geiger, J.Gipson, S.Glaser, F.Gomez, J.Gomez-Gonzalez, D.Gordon, R.Govind, V.Gubanov, S.Gulyaev, R.Haas, D.Hall, S.Halsig, R.Hammargren, H.Hase, R.Heinkelmann, L.Helldner, C.Herrera, E.Himwich, T.Hobiger, C.Holst, X.Hong, M.Honma, X.Huang, U.Hugentobler, R.Ichikawa, A.Iddink, J.Ihde, G.Ilijin, R.Inniss, A.Ipatov, I.Ipatova, M.Ishihara, D. V.Ivanov, C.Jacobs, T.Jike, K.-A.Johansson, H.Johnson, K.Johnston, H.Ju, M.Karasawa, M.Karbon, P.Kaufmann, R.Kawabata, N.Kawaguchi, E.Kawai, M.Kaydanovsky, M.Kharinov, H.Kobayashi, K.Kokado, T.Kondo, E.Korkin, Y.Koyama, H.Krasna, G.Kronschnabl, S.Kurdubov, S.Kurihara, J.Kuroda, Y.Kwak, L.La Porta, R.Labelle, J.LaFrance, D.Lamb, S.Lambert, L.Langkaas, R.Lanotte, A.Lavrov, K.Le Bail, J.Leek, B.Li, H.Li, J.Li, L.Li, S.Liang, M.Lindqvist, X.Liu, M.Loesler, J.Long, C.Lonsdale, J.Lovell, S.Lowe, A.Lucena, B.Luzum, C.Ma, J.Ma, G.Maccaferri, M.Machida, D.MacMillan, M.Madzak, Z.Malkin, S.Manabe, F.Mantovani, V.Mardyshkin, D.Marshalov, G.Mathiassen, S.Matsuzaka, D.McCarthy, A.Melnikov, L.Messerschmitt, A.Mikhailov, N.Miller, D.Mitchell, J. A.Mora-Diaz, A.Mueskens, Y.Mukai, M.Nanni, T.Natusch, M.Negusini, A.Neidhardt, M.Nickola, G.Nicolson, A.Niell, P.Nikitin, T.Nilsson, T.Ning, T.Nishikawa, C.Noll, K.Nozawa, C.Ogaja, H.Oh, H.Olofsson, P. E.Opseth, S.Orfei, R.Pacione, K.Pazamickas, F.Pedreros, W.Petrachenko, L.Pettersson, P.Pino, L.Plank, C.Ploetz, M.Poirier, J.Popelar, M.Poutanen, Z.Qian, J.Quick, I.Rahimov, J.Redmond, B.Reid, J.Reynolds, B.Richter, M.Rioja, A.Romero-Wolf, C.Ruszczyk, A.Salnikov, P.Sarti, R.Schatz, H.-G.Scherneck, F.Schiavone, R.Schmid, U.Schreiber, H.Schuh, W.Schwarz, C.Sciarretta, A.Searle, M.Sekido, M.Seitz, S.Shabala, M.Shao, K.Shibuya, F.Shu, M.Sieber, A.Skjaeveland, E.Skurikhina, S.Smolentsev, D.Smythe, B.Soja, A.Sombra, D.Sousa, O.Sovers, J.Spitzak, L.Stanford, C.Stanghellini, A.Steppe, R.Strand, J.Sun, I.Surkis,

K.Takashima, K.Takefuji, H.Takiguchi, Y.Tamura, T.Tanabe, E.Tanir, A.Tao, C.Tateyama, K.Teke, C.Thomas, V.Thorandt, B.Thornton, C.Tierno Ros, O.Titov, M.Titus, P.Tomasi, V.Tornatore, C.Trigilio, D.Trofimov, M.Tsutsumi, G.Tuccari, T.Tzioumis, H.Ujihara, D.Ullrich, M.Uunila, D.Veillette, T.Venturi, F.Vespe, V.Vityazev, A.Volvach, A.Vytnov, G.Wang, J.Wang, L.Wang, N.Wang, S.Wang, W.Wei, S.Weston, A.Whitney, R.Wojdziak, Y.Yatskiv, W.Yang, S.Ye, S.Yi, A.Yusup, O.Zapata, R.Zeitlhoefler, H.Zhang, M.Zhang, X.Zhang, R.Zhao, W.Zheng, R.Zhou and N.Zubko (2015) The IVS data input to ITRF2014. doi:10.5880/GFZ.1.1.2015.002.

Owens, J. (1967) Optical Refractive Index of Air: Dependence on Pressure, Temperature and Composition. *Applied Optics*, Vol. 6, No. 1:51–59.

Pánek, P., J.Kodet and I.Procházka (2013) Accuracy of two-way time transfer via a single coaxial cable. *Metrologia*, 50(1):60.

Pany, A., J.Böhm, D.MacMillan, H.Schuh, T.Nilsson and J.Wresnik (2011) Monte Carlo simulations of the impact of troposphere, clock and measurement errors on the repeatability of VLBI positions. *Journal of Geodesy*, 85(1):39–50, doi:10.1007/s00190-010-0415-1.

Petit, G. and B.Luzum (2010) IERS Conventions 2010. IERS Technical Note 35, Verlag des Bundesamtes für Kartographie und Geodäsie, Frankfurt am Main. ISSN: 1019-4568.

Petrachenko, B., A.Niell, D.Behrend, B.Corey, J.Böm, P.Charlot, A.Collioud, J.Gipson, R.Haas, T.Hobiger, Y.Koyama, D.MacMillan, Z.Malkin, T.Nilsson, A.Pany, G.Tuccari, A.Whitney and J.Wresnik (2008) Design Aspects of the VLBI2010 System: Progress Report of the IVS VLBI2010 Committee. In: Behrend, D. and K.Baver (Eds.), *IVS 2008 Annual Report*. NASA/TP-2009-214183, 13–67.

Petrov, L. (1998) Memo about reweighting. *Web document, available at http://lacerta.gsfc.nasa.gov/mk5/help/upwei_02_hlp.ps.gz.*

Petrov, L. and J.Boy (2004) Study of the atmospheric pressure loading signal in very long baseline interferometry observations. *Journal of Geophysical Research*, 109(B18):B03405, doi: 10.1029/2003JB002500.

Plag, H. P., Z.Altamimi, S.Bettadpur, G.Beutler, G.Beyerle, A.Cazenave, D.Crossly, A.Donnellan, R.Forsberg, R.Gross, J.Hinderer, A.Komjathy, C.Ma, A.Mannucci, C.Noll, A.Nothnagel, E.Pavlis, M.Pearlman, P.Poli, U.Schreiber, K.Senior, P.Woodworth, S.Zerbini and C.Zuffada (2009) The goals, achievements, and ttool of modern geodesy. Plag, H. and M.Pearlman (Eds.), *Global Geodetic Observing System*, Springer, Berlin, Heidelberg.

Qian, Z.-H. (1985) The correlations between VLBI observables and its effects for the determinations of ERP. In: Müller, I. I. (Eds.), *Earth Rotation and the Terrestrial Reference Frame, 31 July–02 August 1985, Columbus.* MERIT-COTES Joint Working Groups, International Astronomical Union, International Association of Geodesy, International Association of Geodesy and Geophysics, 360–365.

Ray, J. and B.Corey (1991) Current Precision of VLBI Multi-Band Delay Observables. In: *Proceedings of the AGU Chapman Conference on Geodetic VLBI: Monitoring Global Change,*

NOAA Technical Report NOS 137 NGS 49. April 22-26, 1991, Washington, D. C., USA, 123–134.

Roese-Koerner, L., I.Krasbutter and W.-D.Schuh (2012a) A Constrained Quadratic Programming Technique for Data-Adaptive Design of Decorrelation Filters. Sneeuw, N., P.Novák, M.Crespi and F.Sansò (Eds.), *VII Hotine-Marussi Symposium on Mathematical Geodesy*, Volume 137 of the series International Association of Geodesy Symposia, Springer Berlin Heidelberg, 165–170.

Roese-Koerner, L., B.Devaraju, N.Sneeuw and W.-D.Schuh (2012b) A stochastic framework for inequality constrained estimation. *Journal of Geodesy*, 86(11):1005–1018, doi: 10.1007/s00190-012-0560-9.

Rogers, A. E. E. (1970) Very long baseline interferometry with large effective bandwidth for phase-delay measurements. *Radio Science*, 5(10):1239 – 1247, doi:10.1029/RS005i010p01239.

Romero-Wolf, A., C. S.Jacobs and J. T.Ratcliff (2012) Effects of Tropospheric Spatio-temporal Correlated Noise on the Analysis of Space Geodetic Data. In: Behrend, D. and K. D.Baver (Eds.), *IVS 2012 General Meeting Proceedings, "Launching the Next-Generation IVS Network",* 4 – 9 March 2012, Madrid, Spain, 231–235.

Rothacher, M., T.Springer, S.Schaer and G.Beutler (1998) Processing Strategies for Regional GPS Networks. In: Brunner, F. (Eds.), *Advances in Positioning and Reference Frames. International Association of Geodesy Symposia*, Volume 118.

Saastamoinen, J. (1972) Atmospheric correction for the troposphere and stratosphere in radio ranging of satellites. *In: The Use of Artificial Satellites for Geodesy, Geophysic. Monogr. Ser., Vol. 15, S. W. Henriksen et al. (Eds), American Geophysical Union, Washington DC.*

Saastamoinen, J. (1973) Contributions to the theory of atmospheric refraction. Part II - Refraction CCorrection in Satellite Geodesy. *Bulletin Géodésique*, 105(1):279–298, doi: 10.1007/BF02521844.

Sansò, F. and W.Schuh (1987) Finite covariance functions. *Bulletin Géodésique*, 61(4):331–347.

Schindelegger, M., S.Böhm, J.Böhm and H.Schuh (2013) Atmospheric Effects on Earth Rotation. Böhm, J. and H.Schuh (Eds.), *Atmospheric Effects in Space Geodesy*, Springer Berlin Heidelberg, 181–231.

Schön, S. and F. K.Brunner (2006) Modelling physical correlation of GPS phase observations: first results. In: Kahmen, H. and A.Chrzanowski (Eds.), *Proc. 3rd IAG Symp. Geodesy for Geotechnical and Structural Engineering / 12th FIG Symposium on Deformation Measurements, May 22-24, 2006, Baden, Austria*, PS–18.1–8.

Schön, S. and F. K.Brunner (2008a) Atmospheric turbulence theory applied to GPS carrier-phase data. *Journal of Geodesy*, 82(1):47–57, doi:10.1007/s00190-007-0156-y.

Schön, S. and F. K.Brunner (2008b) A proposal for modelling physical correlations of GPS phase observations. *Journal of Geodesy*, 82(10):601–612, doi:10.1007/s00190-008-0211-3.

Schön, S. and G.Kermarrec (2015) Turbulence Theory. Freeden, W., M. Z.Nashed and T.Sonar (Eds.), *Handbook of Geomathematics*, Springer Berlin Heidelberg, 1297–1348.

SCHÖN, S. and H.KUTTERER (2005) Realistic Uncertainty Measures for GPS Observations. SANSO, F. (Eds.), *A Window on the Future of Geodesy*, Volume 128 of the series International Association of Geodesy Symposia, Springer Berlin Heidelberg, 54–59.

SCHUBERT, T. (2017) Beschreibung des stochastischen Verhaltens der neneutral Atmosphäre im Rahmen der VLBI-Analyse. *Master thesis, Rheinische-Friedrich-Wilhelms-Universität Bonn, unpublished.*

SCHUBERT, T., S.HALSIG, A.IDDINK, F.JARON and A.NOTHNAGEL (2017) Stochastic estimation of ZWD parameter in VLBI data analysis using a Square-Root Information Filter. In: HAAS, R. and G.ELGERED (Eds.), *Proceedings of the 23th EVGA working meeting,* 15 – 19 May 2017, Gothenburg, Sweden, 261–264.

SCHUH, H. (1987) *Die Radiointerferometrie auf langen Basen zur Bestimmung von Punktverschiebungen und Erdrotationsparametern.* Dissertation, Rheinische Friedrich-Wilhelms-Universität Bonn. Deutsche Geodätische Kommission bei der Bayerischen Akademie der Wissenschaften, Reihe C, Vol. 328, ISBN 3-7696-9378-7.

SCHUH, H. and D.BEHREND (2012) VLBI: A fascinating technique for geodesy and astrometry. *Journal of Geodynamics*, 61:68–80, DOI 10.1016/j.jog.2012.07.007.

SCHUH, H. and J.BÖHM (2013) Very Long Baseline Interferometry for Geodesy and Astrometry. XU, G. (Eds.), *Sciences of Geodesy - II*, Springer Berlin Heidelberg, 339–376.

SCHUH, H. and S.BÖHM (2011) Earth Rotation. GUPTA, H. K. (Eds.), *Encyclopedia of Solid Earth Geophysics*, Encyclopedia of Earth Sciences Series, Springer Netherlands, 123–129.

SCHUH, H. and A.WILKIN (1989) Determination of Correlation Coefficients between VLBI-Observables. In: RIUS, A. (Eds.), *Proceedings of the 7th Working Meeting on European VLBI,* Madrid, 79 – 91.

SCHUH, W.-D. (2016) Signalverarbeitung in der Physikalischen Geodäsie. FREEDEN, W. and R.RUMMEL (Eds.), *Handbuch der Geodäsie*, Volume Erdmessung und Satellitengeodäsie, Springer Berlin Heidelberg.

SCHÜLER, T., G.HEIN and B.EISFELLER (2000) On the Use of Numerical Weather Fields for Troposphere Delay Estimation in Wide Area Augmentation Systems. In: *Proceedings of GNSS 2000, 1-4 May 2000, Royal Institute of Navigation, Edinburgh, Scotland*, 1077–1093.

SCHÜLER, T., G.KRONSCHNABEL, C.PLÖTZ, A.NEIDHARDT, A.BERTARINI, S.BERNHART, L.LA PORTA, S.HALSIG and A.NOTHNAGEL (2015) Initial Results Obtained with the First TWIN VLBI Radio Telescope at the Geodetic Observatory Wettzell. *SENSORS*, 15(8):18767–18800; doi:10.3390/s150818767.

SNAJDROVA, A., J.BÖHM, P.WILLIS, R.HAAS and S.H. (2006) Multi-technique comparison of tropospheric zenith delays derived during the CONT02 campaign. *Journal of Geodesy*, 79:613–623, doi:10.1007/s00190-005-0010-z.

SOVERS, O. J., J. L.FANSELOW and C. S.JACOBS (1998) Astrometry and geodesy with radio interferometry: experiments, models, results. *Rev Mod Phys*, 70:1393 – 1454, doi: 10.1103/RevModPhys.70.1393.

STOTSKII, A., K. G.ELGERED and I. M.STOTSKAYA (1998) Structure analysis of path delay variations in the neutralatmosphere. *Astronomical & Astrophysical Transactions*, 17(1):59–68, doi:10.1080/10556799808235425.

TAKAHASHI, F., T.KONDO, Y.TAKAHASHI and Y.KOYAMA (2000) *Very Long Baseline Interferometer*. Wave Summit Course. Ohmsha, Ltd. / IOS Press. ISBN 1-58603-076-0.

TATARSKII, V. (1971) *The effects of the Turbulent Atmosphere on Wave Propagation*. NOAA (TT-68-50464).

TAYLOR, G. I. (1938) The Spectrum of Turbulence. *Proceedings of the Royal Society of London A: Mathematical, Physical and Engineering Sciences*, 164(919):476–490, doi: 10.1098/rspa.1938.0032.

TEKE, K., T.NILSSON, J.BÖHM, T.HOBIGER, P.STEIGENBERGER, S.GARCÍA-ESPADA, R.HAAS and P.WILLIS (2013) Troposphere delays from space geodetic techniques, water vapor radiometers, and numerical weather models over a series of continuous VLBI campaigns. *Journal of Geodesy*, 87(10-12):981–1001, doi:10.1007/s00190-013-0662-z.

TESMER, V. and H.KUTTERER (2004) An Advanced Stochastic Model for VLBI Observations and its Application to VLBI Data Analysis. In: VANDENBERG, N. R. and K. D.BAVER (Eds.), *International VLBI Service for Geodesy and Astrometry 2004 General Meeting Proceedings*. NASA/CP-2004-212255, 296–300.

TESMER, V., J.BÖHM, R.HEINKELMANN and S.H. (2006) Impact of Analysis Options on the TRF, CRF and Position Time Series Estimated from VLBI. In: BEHREND, D. and K.BAVER (Eds.), *International VLBI Service for Geodesy and Astrometry 2006 General Meeting Proceedings*, 9 – 11 January 2006, Concepción, Chile. NASA/CP-2006-214140, 243 – 251.

TESMER, V. (2004) *Das stochastische Modell bei der VLBI-Auswertung*. Dissertation, Deutsche Geodätische Kommission bei der Bayerischen Akademie der Wissenschaften, Reihe C, Vol. 573, ISBN 3769650123.

TESMER, V., J.BOEHM, R.HEINKELMANN and H.SCHUH (2007) Effect of different tropospheric mapping functions on the TRF, CRF and position time-series estimated from VLBI. *Journal of Geodesy*, 81(6-8):409–421, doi:10.1007/s00190-006-0126-9.

THAYER, G. D. (1974) An improved equation for the radio refractive index of air. *Radio Science*, Vol. 9, No. 10:803–807.

THOMPSON, A., J.MORAN and G.SWENSON JR. (2001) *Interferometry and Synthesis in Radio Astronomy*. John Wiley and Sons Ltd. ISBN: 978-0-471-25492-8.

TIBERIUS, C. and F.KENSELAAR (2003) Variance Component Estimation and Precise GPS Positioning: Case Study. *Journal of Surveying Engineering*, 129(1):11–18, doi: 10.1061/(ASCE)0733-9453(2003)129:1(11).

TITOV, O. and H.SCHUH (2000) Short periods in Earth rotation seen in VLBI data analysed by least-squares collocation technique. In: KOLACZEK, B., H.SCHUH and D.GAMBIS (Eds.), *High frequency to subseasonal variations in Earth Rotation (IERS Technical Note No. 28)*, 33–41.

TITOV, O. A. (2000) Estimation of the subdiurnal UT1-UTC variations by the least squares collocation method. *Astronomical & Astrophysical Transactions*, 18(6):779–792, doi: 10.1080/10556790008208172.

TREUHAFT, R. N. and G. E.LANYI (1987) The effect of the dynamic wet troposphere on radio interferometric measurements. *RADIO SCI*, 22(2):251–265, doi:10.1029/RS022i002p00251.

TREUHAFT, R. N. and S. T.LOWE (1991) A measurement of planetary relativistic deflection. *The Astronomical Journal*, 102:1879–1888, doi:10.1086/116010.

VAN DAM, T. and J.WAHR (1987) Displacements of the Earth's surface due to atmospheric loading: Effects on gravity and baseline measurements. *Journal of Geophysical Research*, 92(B2):1281–1286, doi:10.1092/JB092iB02p01281.

VENNEBUSCH, M., S.SCHÖN and U.WEINBACH (2011) Temporal and spatial stochastic behaviour of high-frequency slant tropospheric delays from simulations and real GPS data. *Advances in Space Research*, 47(10):1681 – 1690, doi:http://dx.doi.org/10.1016/j.asr.2010.09.008.

VON KÁRMÁN, T. (1948) Progress in the Statistical Theory of Turbulence. In: *Proceedings of the National Academy of Sciences of the United States of America*, Volume 34, 530–539.

WANG, J., C.SATIRAPOD and C.RIZOS (2002) Stochastic assessment of GPS carrier phase measurements for precise static relative positioning. *Journal of Geodesy*, 76(2):95–104, doi: 10.1007/s00190-001-0225-6.

WHEELON, A. D. (2004) *Electromagnetic Scintillation*, Volume 1. Cambridge University Press. Cambridge Books Online.

WHITNEY, A. R. (2000) How Do VLBI Correlators Work? In: VANDENBERG, N. and K.BAVER (Eds.), *IVS 2000 General Meeting Proceedings, Bad Kötzting, Germany, February 21-24 2000*. NASA/CP-2000-209893, 187–205.

WIJAYA, D., J.BÖHM, M.KARBON, H.KRÁSNÁ and H.SCHUH (2013) Atmospheric Pressure Loading. BÖHM, J. and H.SCHUH (Eds.), *Atmospheric Effects in Space Geodesy*, Springer Berlin Heidelberg, 137–180.

ZUBKO, N., M.POUTANEN, J.BÖHM and T.NILSSON (2012) Analysis of VLBI Data with Different Stochastic Models. In: BEHREND, D. and K. D.BAVER (Eds.), *IVS 2012 General Meeting Proceedings, "Launching the Next-Generation IVS Network"*, 4 – 9 March 2012, Madrid, 236 – 240.

In der Schriftenreihe des Instituts für Geodäsie und Geoinformation
der Rheinischen Friedrich-Wilhelms-Universität Bonn sind erschienen: